ABSTRACT

Title of dissertation: AN ALL-SKY, THREE-FLAVOR SEARCH FOR NEUTRINOS FROM GAMMA-RAY BURSTS WITH THE ICECUBE NEUTRINO OBSERVATORY

Robert E. Hellauer III, Doctor of Philosophy, 2015

Dissertation directed by: Professor Gregory Sullivan
Department of Physics

Ultra high energy cosmic rays (UHECRs), defined by energy greater than 10^{18} eV, have been observed for decades, but their sources remain unknown. Protons and heavy ions, which comprise cosmic rays, interact with galactic and intergalactic magnetic fields and, consequently, do not point back to their sources upon measurement. Neutrinos, which are inevitably produced in photohadronic interactions, travel unimpeded through the universe and disclose the directions of their sources.

Among the most plausible candidates for the origins of UHECRs is a class of astrophysical phenomena known as gamma-ray bursts (GRBs). GRBs are the most violent and energetic events witnessed in the observable universe. The IceCube Neutrino Observatory, located in the glacial ice 1450 m to 2450 m below the South Pole surface, is the largest neutrino detector in operation. IceCube detects charged particles, such as those emitted in high energy neutrino interactions in the ice, by the Cherenkov light radiated by these particles. The measurement of neutrinos of 100 TeV energy or greater in IceCube correlated with gamma-ray photons from GRBs,

measured by spacecraft detectors, would provide evidence of hadronic interaction in these powerful phenomena and confirm their role in ultra high energy cosmic ray production.

This work presents the first IceCube GRB-neutrino coincidence search optimized for charged-current interactions of electron and tau neutrinos as well as neutral-current interactions of all neutrino flavors, which produce nearly spherical Cherenkov light showers in the ice. These results for three years of data are combined with the results of previous searches over four years of data optimized for charged-current muon neutrino interactions, which produce extended Cherenkov light tracks. Several low significance events correlated with GRBs were detected, but are consistent with the background expectation from atmospheric muons and neutrinos. The combined results produce limits that place the strongest constraints thus far on models of neutrino and UHECR production in GRB fireballs.

AN ALL-SKY, THREE-FLAVOR SEARCH FOR NEUTRINOS FROM GAMMA-RAY BURSTS WITH THE ICECUBE NEUTRINO OBSERVATORY

by

Robert Eugene Hellauer III

Dissertation submitted to the Faculty of the Graduate School of the
University of Maryland, College Park in partial fulfillment
of the requirements for the degree of
Doctor of Philosophy
2015

Advisory Committee:
Dr. Gregory Sullivan, Chair/Advisor
Dr. Erik Blaufuss
Dr. Kara Hoffman
Dr. Peter Shawhan
Dr. Cole Miller

Acknowledgments

Throughout my graduate school career I have benefited from and am thankful for the work, advice, and friendship of many people. I also acknowledge financial support from the University of Maryland and the National Science Foundation.

Firstly, I would like to thank my advisor Greg Sullivan for giving me the opportunity to work on a wonderful experiment with wonderful people. Thank you for always being available to discuss ideas and for all of your advice. Thank you also for allowing me to go to the South Pole. It will always be one of the best experiences of my life.

Many thanks to Erik Blaufuss for your help from the start. Your knowledge, patience, and humor were pivotal in my understanding of everything I strove to do in my research. Thanks to Kara Hoffman, Cole Miller, and Peter Shawhan for your guidance in my graduate research and classes. Thank you also for being on my committee.

Thanks to Peter Redl, Brian Christy, and Kevin Meagher for welcoming me into the group and helping me understand so much. Thank you Mike Richman for teaching me how to code, sharing your many insights, and helping generate myriad neologisms. Thank you Ryan Maunu, Elim Cheung, Josh Wood, and Ming Song for being awesome office mates and having so many helpful and fun conversations. Thank you John Felde for your positive, thoughtful, and helpful perspective on everything.

Thanks to Don La Dieu and Alex Olivas for your guidance and humor. Thank

you Don for your help in solving so many of my computer quandaries. I did my very best to fill a fraction of your boots on the ice. Thanks to John Kelley and all of my Antarctic coworkers for creating such a fun, enthusiastic, and productive atmosphere during my three weeks on the continent. Thank you Ignacio Taboada for your valuable input from the start of my analysis and Dawn Williams and Ryan for your very helpful review. Thank you Naomi Russo for coordinating numerous details of my research life. Thanks to all of my collaborators. I am lucky to have worked on an amazing detector with fantastic colleagues and friends.

I made a lot of great memories and have a lot of entertaining stories from studying for undergraduate and graduate school classes with friends. To Joffrey Peters, Mike Hischak, Jack Hellerstedt, Chris Najmi, Tom Langford, Matt Severson, Joyce Coppock, and many others, I could not have gotten through it all without you. To my roommates, your extraordinary swagger made each year so much fun.

Many thanks to Tom Gleason for taking the time to introduce me to the University of Maryland Physics Department when I was a senior in high school. Thanks also to Jordan Goodman for speaking with me that evening about a very interesting neutrino detector being built in the South Pole ice.

Finally, thanks to my family. To my parents and brother Matthew, thank you for all of your love, support, and encouragement. You mean more to me than everything else in the universe.

Table of Contents

List of Tables vii

List of Figures viii

1 Introduction: Cosmic Rays and Neutrinos 1
1.1 Cosmic Rays . . . 1
1.2 Neutrinos . . . 3

2 Gamma-Ray Bursts 7
2.1 Introduction . . . 7
2.2 Satellite Gamma-Ray Burst Detectors . . . 9
2.2.1 Fermi . . . 10
2.2.2 Swift . . . 11
2.2.3 Konus/Wind . . . 12
2.2.4 INTEGRAL . . . 12
2.2.5 MAXI . . . 13
2.2.6 SuzakuWAM . . . 13
2.2.7 SuperAGILE . . . 13
2.2.8 IPN3 . . . 14
2.3 GRBweb and GRB Data Compilation . . . 15
2.4 Fireball Model of Neutrino Production . . . 19
2.4.1 Prompt Photon Spectrum . . . 20
2.4.2 Internal Shock Fireball Model . . . 22
2.4.3 Normalizing to Observed Gamma-Ray Fluences . . . 27
2.4.4 Photospheric and ICMART Fireball Models . . . 32
2.4.5 Numerical Fireball Neutrino Spectra Predictions . . . 35
2.4.6 Cosmic Ray Connection: The Waxman & Bahcall Prediction . 37
2.4.7 Concerning Proton Escape . . . 38

3 IceCube: The Detector, Neutrino Detection, and Event Characteristics 42
3.1 The Detector . . . 42
3.1.1 Data Acquisition . . . 43
3.1.1.1 Digital Optical Modules and the PMT . . . 44
3.1.1.2 Waveform Digitization . . . 46
3.1.1.3 DOMHubs and the IceCube Laboratory . . . 48
3.1.1.4 Timing . . . 48
3.1.1.5 Data Triggering and Formatting . . . 49
3.1.2 Feature Extraction . . . 50
3.1.3 Pulse Cleaning . . . 51
3.1.4 Processing and Filtering . . . 51
3.1.5 Data Transmission to the North . . . 52
3.2 Particle Detection . . . 52
3.2.1 Signal Characteristics . . . 52

3.2.2 Background Characteristics 54

4 Simulation and Reconstruction Techniques 57
4.1 Simulation Methods and Description 57
4.2 Reconstruction Methods 58
4.2.1 Tensor of Inertia 59
4.2.2 LineFit 60
4.2.3 CascadeLlh 61
4.2.4 SPE 65
4.2.5 Analytic Energy Reconstruction - ACER 66
4.2.6 Credo 68
4.2.7 Monopod 69
4.2.8 Cramer-Rao 70

5 Event Selection 72
5.1 Level 1: Trigger at South Pole 73
5.2 Level 2: Cascade Event Filter at South Pole 73
5.3 Level 3 76
5.4 Final Event Selection 80
5.4.1 Machine Learning: Boosted Decision Tree Forests 82
5.4.2 BDT Input Signal - Background Discrimination Variables . . . 91
5.4.3 Loose Pre-BDT Cuts after Level 3 127
5.4.4 BDT Forest Training 129
5.4.5 Final Analysis Level 131

6 Unbinned Likelihood Method 142
6.1 The Test Statistic 143
6.2 Probability Distribution Functions 146
6.2.1 Time PDFs 146
6.2.2 Space PDFs 147
6.2.3 Energy PDFs 154
6.3 Pseudo-Experiment Methodology 157
6.4 Sensitivity and Discovery Potentials 158
6.5 Per-GRB Optimization Studies 163
6.6 Characteristics of a Discovery 165

7 Results 166
7.1 Three Year Cascade Coincidence Search Results 166
7.2 Systematic Errors 173
7.2.1 Ice Model 174
7.2.2 Optical Module Sensitivity 175
7.2.3 Neutrino Interactions 175
7.2.4 Seasonal Rate Variation 176
7.2.5 Total Systematic Error 177
7.3 GRB Neutrino Production Model Limits 178

7.3.1 Limits Normalized to Cosmic Ray Production in GRBs 179
7.3.2 Limits on GRB Fireball Models and Parameter Spaces 180

8 Conclusions and Outlook 184

A Gamma-Ray Burst Catalog 188

Bibliography 209

List of Tables

2.1 GRB Satellite Detector Contributions 10

5.1 Signal and Background Efficiencies 139

7.1 Most Significant Event and GRB Properties 169
7.2 Sources of Systematic Error 177

A.1 IC79 GRB Parameters 189
A.2 IC86I GRB Parameters 195
A.3 IC86II GRB Parameters 202

List of Figures

1.1 Cosmic Ray Energy Spectrum . . . 2

2.1 Localizations of BATSE GRBs . . . 8
2.2 Hillas Plot . . . 9
2.3 IPN Detection . . . 14
2.4 GRBweb Summary Table . . . 16
2.5 GRBweb Burst Table . . . 17
2.6 GRBweb Light Curve Display . . . 17
2.7 Analyzed GRB Localizations . . . 18
2.8 Fermi GBM GRB Light Curves . . . 21
2.9 Fireball Model GRB Neutrino Flux Predictions . . . 40
2.10 Guetta et al. Model Modifications . . . 41

3.1 The IceCube Detector . . . 43
3.2 The IceCube Laboratory . . . 44
3.3 DOM Main Board . . . 45
3.4 DOM Schematic . . . 46
3.5 DOMHub . . . 49
3.6 DIS Neutrino-Quark Scattering Diagrams . . . 53
3.7 Charged Current Neutrino Interaction Topologies . . . 54
3.8 Neutrino Cross Sections . . . 55
3.9 Cascade and Track Event Topologies . . . 56
3.10 Muon Energy Loss . . . 56

4.1 Cherenkov Light . . . 66
4.2 Angular Resolutions of Reconstructions . . . 70

5.1 L2 Efficiencies . . . 75
5.2 L2 Track-to-Cascade Likelihood Ratio . . . 78
5.3 L2 Cosine of SPE Zenith vs. ACER Energy . . . 78
5.4 L2 Fill-Ratio . . . 79
5.5 L3 Signal Efficiencies . . . 81
5.6 BDT Errors and Boost Factors . . . 86
5.7 Overtrained and Well-trained BDT Score Distributions . . . 92
5.8 BDT Variable Correlations . . . 93
5.9 track-cscd-llhratio . . . 98
5.10 cscdllh-rlogl . . . 100
5.11 lfv . . . 101
5.12 lfv-z . . . 102
5.13 t-lfv-z-sum . . . 104
5.14 t-lfv-z-diff . . . 106
5.15 spefit-zenith . . . 107
5.16 ratio-before-to-after-vertex . . . 109

5.17 fill-ratio . . . 110
5.18 evalratio . . . 111
5.19 qtot-eval-ratio . . . 113
5.20 max-qtot-ratio . . . 114
5.21 e-qtot-ratio . . . 115
5.22 charge-per-string . . . 116
5.23 Nch . . . 117
5.24 i3scale-inice-credo . . . 119
5.25 i3scale-inice-monopod . . . 120
5.26 credo-vertexdist . . . 121
5.27 t-cscdvertexdiff . . . 122
5.28 t-cscdllh-z-diff . . . 123
5.29 t-spevertexdiff . . . 125
5.30 vertexdiff . . . 126
5.31 track-cscd-llhratio Pre-BDT Cut Example . . . 128
5.32 lfv Pre-BDT Cut Example . . . 128
5.33 Pre-BDT Cuts Sensitivity Improvement . . . 129
5.34 IC86I First Tree . . . 133
5.35 IC86I Last Tree . . . 134
5.36 BDT Score Distribution . . . 135
5.37 Survival Rates vs. BDT Score . . . 136
5.38 Neutrino Flavor Signal Efficiencies . . . 137
5.39 Signal Efficiencies per BDT Score . . . 138
5.40 Signal Efficiency with Respect to L2 . . . 139
5.41 Effective Areas . . . 141

6.1 Time PDF Ratios . . . 147
6.2 Signal Space PDFs . . . 149
6.3 Background Space PDF . . . 149
6.4 Angular Resolutions of Neutrino Flavors . . . 150
6.5 Cramer-Rao Pull vs. Energy . . . 152
6.6 Corrected Cramer-Rao Pull vs. Energy . . . 153
6.7 Energy PDF Ratios . . . 155
6.8 Reconstructed vs. Simulated True Energy . . . 156
6.9 Energy Resolution . . . 156
6.10 E^{-2} Signal Limit Setting and Discovery Potentials . . . 160
6.11 Fireball Model Signal Limit Setting and Discovery Potentials . . . 161
6.12 Frequentist Plane . . . 162
6.13 Null Hypothesis Test Statistic Distributions . . . 164
6.14 Stacked and Per-Burst Discovery Potentials . . . 164
6.15 Discovery Potentials for Single Random Burst . . . 165

7.1 Three Year Cascade Test Statistic Distribution . . . 167
7.2 PDFs for Most Significant IC79 Events . . . 170
7.3 PDFs for Most Significant IC86I Events . . . 170

7.4 Time PDF Ratios and GRB Light Curves for Most Significant IC79 Events . . . 171
7.5 Time PDF Ratios and GRB Light Curves for Most Significant IC86I Events . . . 171
7.6 Detector Views for Most Significant IC79 Events . . . 172
7.7 Detector Views for Most Significant IC86I Events . . . 172
7.8 Seasonal Variation of Data Rate . . . 176
7.9 Best Possible Upper Limits with Systematic Errors . . . 178
7.10 Exclusion Contours for Cosmic-Ray-Normalized Models . . . 180
7.11 Benchmark Fireball Model Limits . . . 182
7.12 Exclusion Contours for Gamma-Ray-Normalized Models . . . 183

Chapter 1

Introduction: Cosmic Rays and Neutrinos

1.1 Cosmic Rays

Earth is constantly bombarded by a stream of astrophysical particles historically known as cosmic rays and discovered by Victor Hess in 1912. The cosmic particles consist of roughly 90% p, 9% He^{2+}, 1% heavier nuclei, and traces of single electrons. The observed cosmic ray spectrum follows a power law with several components of different indices due to their multiple origins. The tail of the spectrum is comprised of the highest energy particles ever observed, with energies over 10^{20} eV [1–3].

As seen in Figure 1.1, the first component of the spectrum up to about 10^{15} eV (the "knee") is characterized by the power law $\frac{dN}{dE} \sim E^{-2.7}$. The origins of cosmic rays up to the knee are widely agreed to be galactic supernova remnants (SNRs). Indeed, the Fermi Large Area Telescope recently measured the expected characteristic pion-decay "bump" feature in the gamma-ray spectra of two SNRs [4]. This signature is compelling evidence of proton acceleration in these objects. As accelerated protons encounter interstellar material, proton-proton interactions produce neutral pions, which quickly decay into gamma-rays.

The second component up to around $10^{18.6}$ eV (the "ankle") steepens to $\frac{dN}{dE} \sim E^{-3}$. Cosmic rays from the knee to the ankle of the spectrum are thought to be

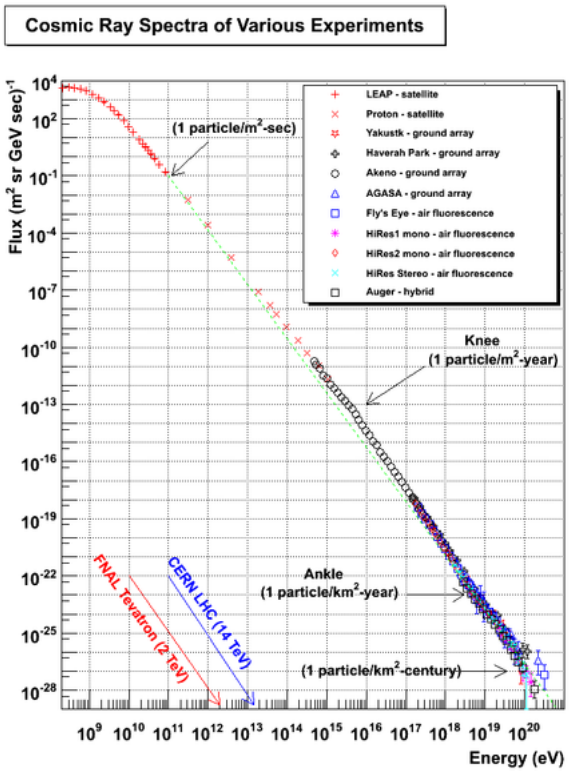

Figure 1.1: Measured cosmic ray energy spectrum [1]

from a mixture of both galactic and extragalactic sources. It can be reasoned that this softer spectral shape is due to cosmic rays from galactic accelerators reaching their maximum energy of propagation within the galaxy, as its size is exceeded by the particle's gyroradius [5].

The spectrum beyond the ankle hardens again to $\frac{dN}{dE} \sim E^{-2.7}$. These highest energy cosmic rays are most likely due to extragalactic accelerators. The spectrum drops off above $10^{20.5}$ eV because this is the energy where protons interact with the cosmic microwave background through the Δ resonance. This drop off is known as the GreisenZatsepinKuzmin (GZK) cutoff [1, 6].

The origins of cosmic rays are difficult to identify using these particles alone. The charged cosmic rays are deflected significantly by galactic and intergalactic

magnetic fields throughout nearly the entire spectrum. Source correlation with cosmic ray trajectory only becomes feasible at energies approaching GZK energies.

1.2 Neutrinos

Where there is high energy light and baryonic matter, neutrinos are inevitably produced in photohadronic interactions. While the charged cosmic rays are deflected electromagnetically, neutrinos travel unimpeded through the universe and disclose their source directions. Furthermore, the cross-section of the neutrino at all energies is extremely small and, as a result, these neutral leptons can travel billions of light years without interacting. Neutrinos are true cosmic messengers and they can be used to learn about otherwise currently unreachable astrophysical phenomena.

Neutrinos were first proposed by Wolfgang Pauli to solve the missing energy and momentum in the observed decay products of the neutron:

$$n \rightarrow p + e \tag{1.1}$$

This so-called beta decay was observed by a radioactive nucleus A transforming into a slightly lighter nucleus B and emitting an electron. If only an electron and the lighter nucleus resulted from this decay, then the measured electron energy in the center of momentum frame should be constant:

$$E_e = \frac{m_A^2 - m_B^2 + m_e^2}{2m_A} \cdot c^2 \tag{1.2}$$

However, researchers measured a wide range of electron energies. Therefore, another neutral particle, dubbed the the neutrino or "little neutral one" by Enrico Fermi, must be involved.

In 1953, Reines and Cowan proposed an experiment [7] to measure an effect of this neutrino through the crossed reaction:

$$\nu + p \rightarrow n + e^{+} \tag{1.3}$$

Using a stream of nuclear reactor emitted $\bar{\nu}_e$ they measured the emission of positrons through their annihilation with electrons and neutrons through their capture in cadmium dissolved in the scintillator. The delayed pulse pair in the photomultiplier tubes proved that the neutrino existed and was measurable [8, 9].

Since this pioneering work by Reines and Cowan, many more neutrino experiments have been proposed and conducted in order to explore the various properties of these subatomic particles. One such property being actively researched and which gives power to this work is flavor oscillation. Pontecorvo first proposed that a neutrino created with a certain lepton flavor (electron, muon, or tau) can convert to another of the three flavors [10]. This oscillation is possible due to the weak interaction eigenstates able to be described as superpositions of the mass eigenstates, each of which picks up a phase during propagation that develops with distance traveled [11]. Observation of this phenomenon, and thus evidence of neutrino mass, was first confirmed by the Super-Kamiokande collaboration in 1998 [12].

Neutrino oscillations over cosmic baselines are taken into consideration in this

work. The flavor ratio at the IceCube detector will be different form the flavor ratio generated at some astrophysical source. The expected neutrino flavor ratio produced in GRBs and explained in the next chapter is $(\nu_e : \nu_\tau : \nu_\mu)_{GRB} \approx 2 : 1 : 0$. At Earth, this ratio is expected to be $1 : 1 : 1$ due to the effect of oscillations over the extremely long distances to GRBs. An equal flavor ratio is important for this analysis because the event selection is tuned to shower-like events that can be produced by any neutrino flavor and, therefore, is sensitive to all neutrino flavors.

The IceCube collaboration has instrumented over one billion tons of ice in order to have a reasonable probability of observing an extraterrestrial high energy neutrino flux. This analysis searches for such a flux coincident with the gamma-ray emission of gamma-ray bursts (GRBs) to show first evidence of their hypothesized hadronic makeup. To date, no neutrino signal has been detected in searches for muon neutrinos from GRBs in multiple years of data from AMANDA, the partially-instrumented IceCube, and the completed IceCube detector [13–17], nor in four years of data by the ANTARES collaboration [18–20]. High energy ν_μ charged-current interactions produce high energy muons that manifest as extended Cherenkov light patterns in the South Pole glacial ice, referred to as "tracks"; and Southern Hemisphere bursts were often excluded from searches for this signal in order to remove the dominant cosmic-ray-induced muon background.

The absence of charged-current ν_μ signal from GRBs motivates this search for nearly spherical Cherenkov light patterns, referred to as "showers" or "cascades", produced by all neutrino flavors correlated with GRBs. Charged-current interactions of electron and tau neutrinos along with neutral current interactions of all neutrino

flavors generate electromagnetic and hadronic showers. The asymmetrical timing distributions of the Cherenkov photons in these showers is elicited to reconstruct the direction of the primary particle and calculate the likelihood that any were neutrinos emitted from observed GRBs over the entire sky.

This dissertation is organized as follows. Chapter 2 discusses the neutrino spectra predicted by the different fireball models on which limits are placed. Chapter 3 describes the IceCube detector and data acquisition system. The simulation and reconstruction of events in IceCube are detailed in Chapter 4. The event selection techniques and likelihood analysis are covered in Chapters 5 and 6. Finally, Chapter 7 presents the results of this all-sky, three-flavor search in combination with those from the Northern Hemisphere ν_μ searches, and Chapter 8 concludes with an outlook on the field.

Chapter 2

Gamma-Ray Bursts

2.1 Introduction

GRBs are the most concentrated and luminous explosions observed in the universe and occur isotropically at an average rate of a few per day [21]. A large dynamic range of burst durations, from milliseconds to thousands of seconds, has been observed. During their lifespan, they outshine the rest of the gamma-ray sky.

GRBs were discovered in 1967 by the Vela satellites, which were designed by the US Department of Defense to detect nuclear detonations in violation of the 1963 Nuclear Test Ban Treaty [22]. The Russian IMP-6 satellite then confirmed the discovery once the Vela data was released in 1973 [23]. Due to the difficulty in resolving the source direction of gamma-rays, the satellites could only confirm that the flashes did not originate from the direction of the Earth. For the next two decades, myriad theories on GRB origins were proposed [24]. Little experimental progress was achieved, though, until the Compton Gamma-Ray Observatory (CGRO) was launched in 1991 [25]. The Burst And Transient Source Experiment (BATSE) on board CGRO [26] revealed an isotropic distribution of 2704 GRBs as shown in Figure 2.1. This distribution was the first strong evidence of the cosmological origin of GRBs.

In 1997 the Beppo-SAX satellite detected GRBs in x-rays for the first time,

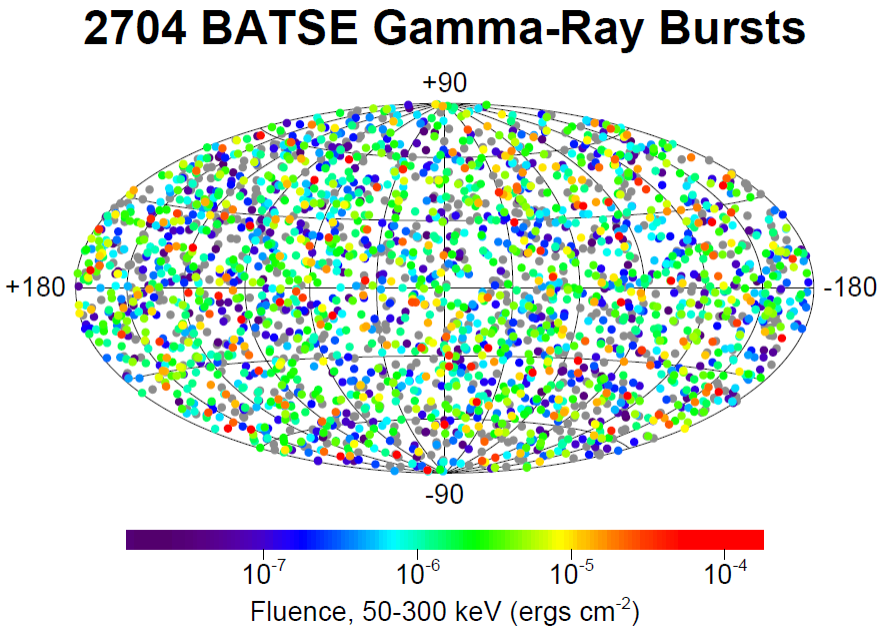

Figure 2.1: Distribution of GRBs detected by BATSE [27]

yielding much more accurate position measurements than had been previously achieved [28]. Large ground-based telescopes were then able to carry out follow up studies on the GRB progenitor distances from Earth, proving their existence on an extra-galactic scale [29].

The origins of these remarkable phenomena are still unknown; however, progenitor scenarios can be deduced from the light curves and energy output. GRBs are typically classified into two categories: long (greater than 2 seconds in duration) and short (less than 2 seconds in duration). Long bursts are thought to be associated with collapsars [30], while short bursts are thought to be associated with the mergers of compact objects [31].

Figure 2.2 shows the conditions necessary for UHECR production and where astrophysical phenomena lie in terms of these conditions. UHECR production ne-

cessitates a source to either be of sufficient size to accelerate particles to the given energies or possess a sufficient magnetic field to confine particles during acceleration. GRBs appear to be prime candidates to accelerate protons up to 10^{21} eV.

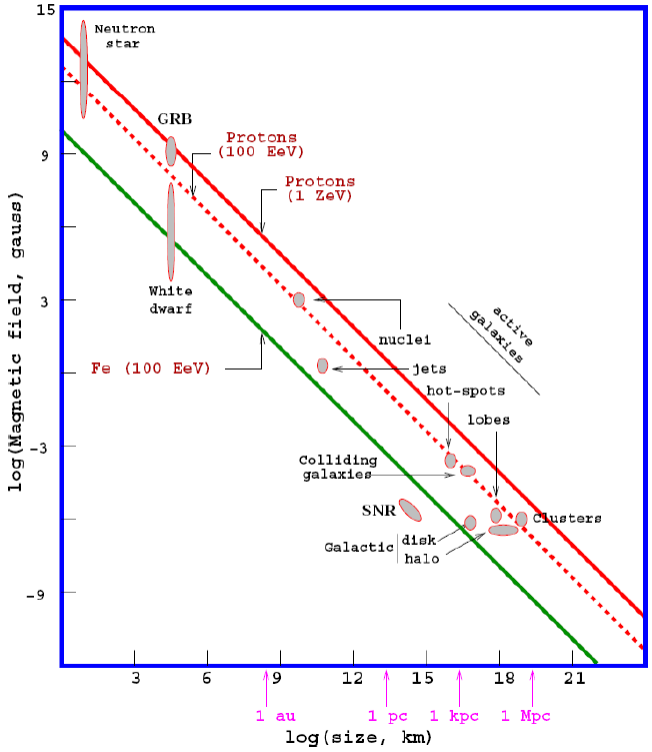

Figure 2.2: The Hillas Plot. Solid red marks the conditions necessary to accelerate protons up to 10^{21} eV. Dotted red is for proton acceleration to 10^{20} eV. Green is for iron acceleration to 10^{20} eV [32].

2.2 Satellite Gamma-Ray Burst Detectors

Spacecraft are in operation with instruments designed to detect and observe GRBs. The teams operating the instruments and analyzing their data all share the high priority goal of the high energy astrophysical community to explain the physical mechanisms behind these powerful transient phenomena. Many of these instruments build off of the work of the BATSE instrument which operated from

1991 to 2000.

Table 2.1 summarizes the angular resolutions, fields of view, energy ranges, and contributions to this search for each of the satellite GRB detectors described in this section.

Team	Ang. Resolution	Field of View	Energy Range	T1	T2	Direction	Spectrum
FermiGBM	1° - 15°	3π sr	8 keV - 40 MeV	524 (64.9%)	509 (63.1%)	480 (59.5%)	464 (57.5%)
FermiLAT	0.1° - 1°	0.8π sr	20 MeV - 300 GeV	–	–	13 (1.6%)	-
SwiftBAT	$1'$ - $4'$	0.5π sr	15 - 150 keV	188 (23.3%)	203 (25.2%)	63 (7.8%)	137 (17.0%)
SwiftXRT	$\sim 3.5''$	–	0.2 - 10 keV	–	–	154 (19.1)	–
SwiftUVOT	$\sim 0.5''$	–	optical (170 - 650 nm)	–	–	15 (1.9%)	–
KonusWind	–	4π sr	10 keV - 10 MeV	45 (5.6%)	60 (7.4%)	–	73 (9.0%)
INTEGRAL	$1'$ - $2'$	0.5π sr	8 keV - 40 MeV	14 (1.7%)	13 (1.6%)	13 (1.6%)	8 (1.0%)
MAXI	$1'$ - $2'$	0.5π sr	8 keV - 40 MeV	7 (0.9%)	7 (0.9%)	12 (1.5%)	–
SuzakuWAM	–	2π sr	50 keV - 5 MeV	25 (3.1%)	12 (1.5%)	–	3 (0.4%)
SuperAGILE	$1'$ - $2'$	0.5π sr	15 - 45 keV	2 (0.2%)	2 (0.2%)	3 (0.4%)	3 (0.4%)
IPN3	.1° - 5°	4π sr	keV - MeV	–	–	51 (6.3%)	–

Table 2.1: Data for GRB detectors contributing to this analysis and contribution number and percentage for analysis parameters.

2.2.1 Fermi

The Fermi Gamma-ray Space Telescope launched in 2008 with the goal of studying the universe at high energies. The spacecraft has two instruments that detect GRBs at different energy ranges: the Gamma-ray Burst Monitor (GBM) and the Large Area Telescope (LAT). These instruments detect high energy gamma-rays through scintillators and pair production measurement. The combined energy range of the two instruments is the broadest of all GRB detectors in operation.

The FermiGBM [33–36] is the most prodigious detector of GRBs among all spacecraft GRB-detecting instruments. The instrument is made up of 12 sodium iodide (NaI) detectors, with energy range 8 keV to 1 MeV, and two bismuth germanate (BGO) detectors, with energy range 200 keV to 40 MeV. The detectors'

positions and orientations achieves a ~ 9.5 sr field of view. Localization of a burst is determined to an accuracy of 1° to 15° degrees using the relative event rates of the detectors with different orientations with respect to the burst. Upon detection of GRB prompt emission, GBM provides quick notification to Fermi's main instrument, LAT.

The FermiLAT [37] is pair production telescope that consists of a 4x4 array of identical towers of silicon strips, interleaved tungsten converter foils, and a cesium iodide calorimeter. An anti-coincidence plastic scintillator detector covers the array and rejects charged particle background. This arrangement achieves a ~ 2.4 sr field of view and $\lesssim 1^\circ$ burst localization accuracy. The detector covers a much higher energy range compared to GBM and is sensitive to 20 MeV to 300 GeV gamma rays.

2.2.2 Swift

The Swift satellite [38] launched in 2004 with its primary mission to study GRBs. The spacecraft has three instruments that detect different wavelengths of light: the Burst Alert Telescope (BAT) [39], the X-Ray Telescope (XRT) [40], and the Ultraviolet/Optical Telescope (UVOT) [41]. The BAT instrument continuously scans the sky using a coded aperture mask overlaid on a gamma sensitive CCD array that has a 1.4 sr field of view and 15 - 150 keV energy range. The mask is an arrangement of lead tiles and when gamma rays are detected, the on-board computer reads out the array charge pattern and then reconstructs the direction

based on the coded arrangement with an angular resolution of $1'$ to $4'$.

When BAT detects a previously unmeasured gamma-ray transient, the Swift spacecraft slews over 20 to 75 seconds to point XRT and UVOT at the source. XRT searches for an X-ray point source in the same location as the gamma-ray source, with an energy range of 0.2 - 10 keV and angular resolution of $\sim 3.5''$. If XRT observes an x-ray source, UVOT searches for an 170 - 650 nm optical afterglow and can localize this point source with an angular resolution of $\sim 0.5''$.

2.2.3 Konus/Wind

Konus [42] is the gamma-ray detector on the Wind spacecraft which launched in 1994. Wind consists of two NaI crystal detectors oriented perpendicular to the ecliptic with an energy range of 10 keV - 10 MeV. The detector has no localization capabilities on its own, but is part of the IPN3 network described below. Lastly, the Wind spacecraft lies at Lagrange point L1, which is about seven light seconds from Earth; however its timing information is converted to UTC in its published circulars and before use in this search.

2.2.4 INTEGRAL

INTEGRAL [43] is a gamma-ray detecting satellite launched in 2002. The spacecraft consists of three coded aperture mask detectors with a total energy range of 15 keV - 10 MeV. The detectors on board contribute to the IPN3 collective GRB localizations described below, while the field of view for burst localizations made by

this spacecraft only is $\sim 0.5\pi$.

2.2.5 MAXI

The Monitor of All-sky X-ray Image (MAXI) [44] is an X-ray detector installed on the International Space Station in 2009. The instrument localizes bursts based on their X-ray afterglow using two detector types: (1) gas proportional counters with an energy range of 2 - 30 keV and (2) X-ray charge-couple devices with an energy range of 0.5 - 12 keV. MAXI also discovers bursts by extrapolating a hard X-ray spectrum into the gamma-ray spectrum.

2.2.6 SuzakuWAM

The Suzaku satellite Wide-band All-sky Monitor (WAM) [45] launched in 2005. This instrument detects GRBs with its 20 thick BGO anti-coincidence shields of its hard X-ray detectors. The BGO detectors have an energy range of 50 keV - 5 MeV. SuzakuWAM has no localization capabilities on its own, but is part of the IPN3 network described below.

2.2.7 SuperAGILE

The Super spacecraft launched in 2007. Its AGILE instrument [46] consists of four independent silicon detectors that are equipped with tungsten coded aperture masks. The instrument measures gamma rays in the range of 10 - 40 keV, and has a $\sim 0.3\pi$ sr field of view with an angular resolution around $1'$.

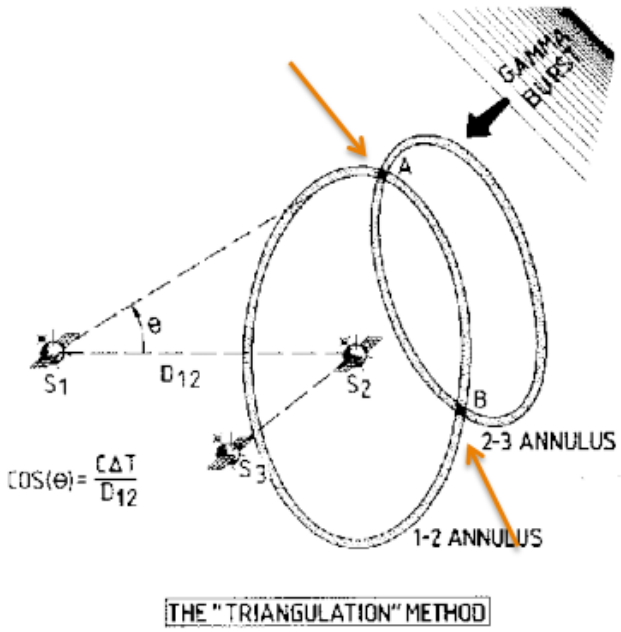

Figure 2.3: IPN detection mechanism, taken from [47]. The crossings of two annuli calculated from the different GRB-detecting satellite positions are marked by orange arrows.

2.2.8 IPN3

The Third Interplanetary Network (IPN3) [47] is a collection of gamma-ray detecting satellites. IPN3 uses the timing information from multiple satellite measurements of the same GRB to triangulate an error box for the burst localization, as pictured in Figure 2.3. Degeneracy of the annuli crossings can be lifted by Earth occultation or detections by other satellites. For the years of this GRB search, the network consisted of the following nine spacecraft: AGILE, Fermi, RHESSI, Suzaku, and Swift, in low Earth orbit; INTEGRAL, in eccentric Earth orbit with apogee 0.5 light-seconds; Wind, up to 7 light-seconds from Earth; MESSENGER, en route to and then in orbit around Mercury; and Mars Odyssey, in orbit around Mars.

2.3 GRBweb and GRB Data Compilation

All of the spacecraft GRB detectors detailed in section 2.2 publish circulars on each detected GRB to the Gamma-ray Coordinates Network (GCN) [48]. The relevant temporal, spatial, and spectral parameters used in this analysis are extracted autonomously with PHP scripts from these circulars and imported to an IceCube MySQL database. Much of the Fermi GBM burst data is located only in their database and so is extracted separately and imported to the same IceCube database.

The compiled relevant GRB parameters are then presented on a publicly-available interactive website, GRBweb [49] [50]. This website contains a summary table, shown in Figure 2.4 which presents the parameters used in this analysis for each GRB and the satellite detectors from which they came. For multiple burst measurements by different detectors, the prompt photon emission time (T_{100}) is defined by the most inclusive start and end times (T_1 and T_2) reported by any satellite. The most precise localization available is used as well, with all reported error circle radii scaled to 1σ containment. Thirdly, the hierarchy of spectral parameters used is ordered by the widest to narrowest energy ranges, given in Table 2.1.

In addition to the summary table, GRBweb has individual GRB pages, detailing the measured parameters from each detector and links to the relevant GCN circulars. Light curves of normalized photon counts per time from FermiGBM, SwiftBAT, KonusWind, and INTEGRAL are also presented, if available. An example of an individual GRB page and its measured light curves are shown in Figures

GRB		Position			Time			Spectrum						Other					Neutrino Spectrum					
Name	RA	Decl	ERR	T100	T90	UTT	UT Frac Sec	T1	T2	$T_{fluence}$	α_γ	β_γ	ε_γ	F_γ	E_{min}	E_{max}	z	Position GCN	T1 GCN	T2 GCN	$T_{fluence}$ GCN	Light Curve	Num. Circulars
		No filter		No filter																			
120519A	178.366	22.407	0.634	5.7	0.72	2012-05-19 17:18:14	0.64	-0.5	5.2	1.2	0.5	**2.5**	740	3.7E-6	0.02	10	**2.15**	ipn 13313	suzaku 13350	konuswind 13315	konuswind 13315	YES	4
120520A	45.86	35.28	8.3	5.76	5.76	2012-05-20 22:46:24	0.663	-4.74	1.02	5.76	1.05	2.25	205	4.409E-7	0.008	1	**2.15**	GBMDb	GBMDb	GBMDb	GBMDb	YES	1
120521A	148.725	-49.417	0.0003	0.54	0.45	2012-05-21 05:59:42	0	0.02	0.56	0.54	0.98	**1.98**	**1000**	7.8E-8	0.015	0.15	**0.5**	swiftxrt 13304	swiftbat 13310	swiftbat 13310	swiftbat 13310	NO	9
120521B	197.01	-52.755	0.0003	96.53	31.4	2012-05-21 09:07:48	0	-1.39	95.14	34	0.34	**2.34**	213	3.11E-6	0.01	1	**2.15**	swiftxrt 13311	swiftbat 13317	GBMDb	fermigbm 13339	YES	13
120521C	214.286	42.145	0.0003	32.87	26.7	2012-05-21 23:22:07	0	-1.03	31.84	32.87	1.73	**2.73**	**200**	1.1E-6	0.015	0.15	6.0	swiftxrt 13324	swiftbat 13333	swiftbat 13333	swiftbat 13333	NO	18
120522A	165.996	-62.094	0.0773	78.086	13	2012-05-22 03:11:07	0.377	0	78.086	78.086	0.88	**2.88**	381	2.5E-5	0.02	10	**2.15**	ipn 13340	konuswind 13341	konuswind 13341	konuswind 13341	YES	2
120522B	56.07	54.85	2.02	28.16	28.16	2012-05-22 08:39:16	0.839	-11.52	16.64	28.16	1.05	2.25	205	9.324E-6	0.008	1	**2.15**	GBMDb	GBMDb	GBMDb	GBMDb	YES	1

Figure 2.4:]
GRBweb summary table of GRB parameters.

2.5 and 2.6. A table of all bursts analyzed in this analysis and their parameters compiled by GRBweb is in Appendix A.

807 GRBs during IceCube data taken from May 2010 through May 2013 were analyzed in this neutrino search. The right ascension and declination coordinates of these bursts are plotted in Figure 2.7 with colors corresponding to the detector configuration during which they occurred. Searches over each detector configuration were optimized separately with very similar event selections and sensitivities, detailed in Chapters 5 and 6.

GRB: 110903A

Summary:

GRBNAME	RA	DECL	ERR	T100	UTT1	T1	UTT2	T2	ALPHA	BETA	EPEAK	FLUENCE	Emin	Emax	Z
110903A	197.061	58.985	0.0333	422	2011-09-03 02:39:33	0	2011-09-03 02:39:55	400	0.69	2.7	295	4.2E-5	0.02	10	-

Notice:

GRB_RA	GRB_DEC	GRB_TIME	DETECTOR
197.037	58.9956	2011-09-03 02:39:55	INTEGRAL

Fermi GBM:

GRBNAME	UTTIME	TRIG1	TRIG2	RA	DECL	ERR	T90	T1	T2	ALPHA	BETA	EPEAK	POWINDX	EMIN	EMAX	FLUENCE	FTEXT	Edit?	Delete?
110903A	2011-09-03 02:39:34	336710376	110903111	-	-	-	339.9	-0	339	-	-	281.3	-0.88	10	1000	3.3E-5	Full Text	Edit Values	Delete

Konus-Wind:

GRBNAME	UTTIME	T90	T2	ALPHA	BETA	EPEAK	FLUENCE	EMIN	EMAX	FTEXT	Edit?	Delete?
110903A	2011-09-03 02:39:33	370	368.896	-0.69	-2.7	295	4.2E-5	20	10000	Full Text	Edit Values	Delete

Suzaku WAM:

GRBNAME	UTTIME	T90	T1	T2	ALPHA	BETA	EPEAK	POWINDX	FLUENCE	EMIN	EMAX	FTEXT	Edit?	Delete?
110903A	2011-09-03 02:39:34	340	-	364	-	-	281	1.19	2.18E-5	100	1000	Full Text	Edit Values	Delete

INTEGRAL:

GRBNAME	UTTIME	RA	DECL	ERR	T90	FLUENCE	FTEXT	Edit?	Delete?
110903A	2011-09-03 02:39:55	197.0614	58.9852	0.03333333	400	-	Full Text	Edit Values	Delete

Fermi GBM Db:

GRBNAME	UTTIME	TRIG1	TRIG2	RA	DECL	ERR	T90	T1	T2	ALPHA	BETA	EPEAK	POWINDX	EMIN	EMAX	FLUENCE	DURATION	PLOT	Edit?	Delete?
110903A	2011-09-03 02:39:34	336710376	110903111	197.061	58.9852	10.4	341.26	-0.26	341.0	1.05	2.25	205	-	8	1000	3.470e-05		Link	Edit Values	Delete

IceCube:

RUN	UTTIMESTART	UTTIMEEND	DUR	INICETRIGS	ICETOPTRIGS	AMANDATRIGS	EVENTS	FILES	FTEXT
118636	2011-09-03 01:44:16	2011-09-03 03:28:30	01:44:14	16100975	420453	1479873	16439345	119	Full Info

Figure 2.5: GRBweb individual burst page example.

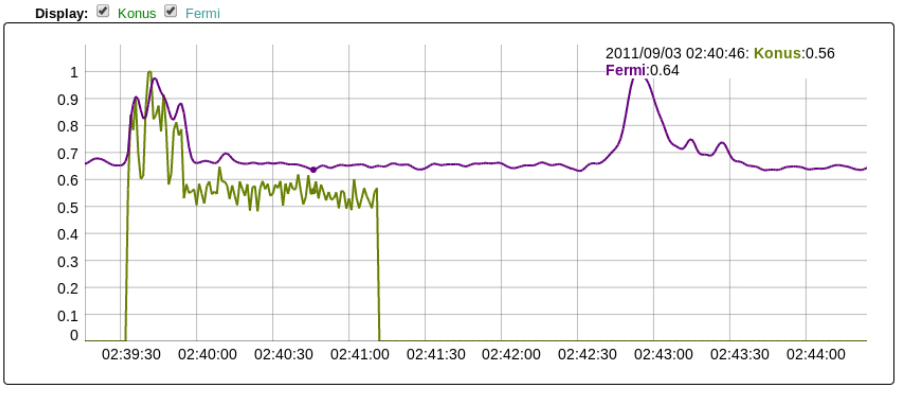

Figure 2.6: GRBweb light curve display example.

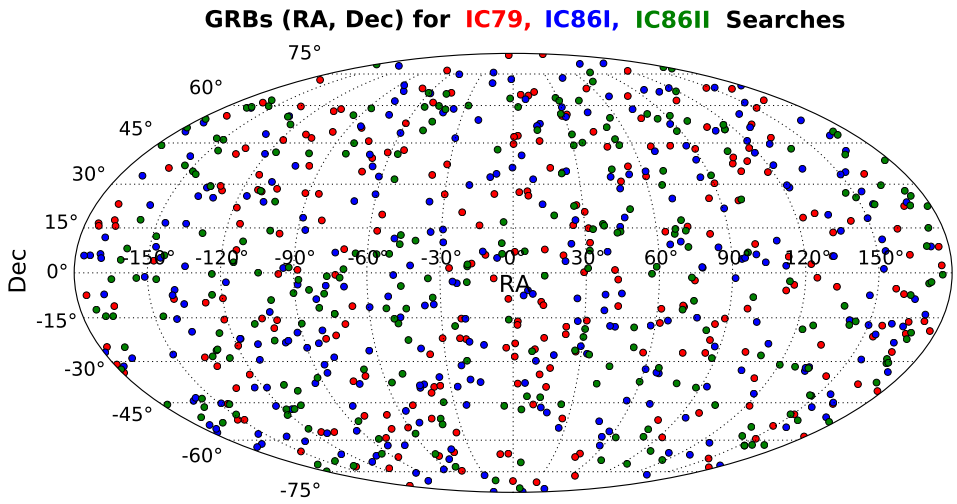

Figure 2.7: Localizations of the 255 IC79, 288 IC86I, and 264 IC86II GRBs in equatorial coordinates analyzed during these three IceCube detector configuration seasons of approximately one year each.

2.4 Fireball Model of Neutrino Production

The prevailing phenomenology that successfully describes GRB observations is that of a relativistically expanding fireball of electrons, photons, and protons [21, 51, 52]. The two main engines of the GRB fireball model are the central engine, that converts roughly a solar rest mass of gravitational energy into kinetic energy; and the internal shocks between the fireball ejecta and the external medium, that convert kinetic energy into the observed gamma-rays. These engines allow GRBs to attain the energies necessary to reconcile their measured luminosities and their vast distances from us. Additionally, GRB emission must be beamed since their observed isotropic luminosities exceed the energies that would be available in their theorized progenitor scenarios [21].

As noted in Section 1.2, no neutrino signal has yet been detected in searches for neutrinos from GRBs. The resulting limits presented in prior IceCube publications [14–17] and Chapter 7 focus on two genres of GRB neutrino spectral predictions for this fireball scenario: models normalized to the observed UHECR flux [53] and models normalized to the observed gamma-ray flux for each burst. Cosmic-ray-normalized models [54–56] assume protons emitted by GRBs are the dominant sources of the highest energy cosmic rays observed, and with these models limits are placed on this assumption. Gamma-ray-normalized models [57, 58] assume protons from GRBs are only a source of cosmic-rays, and with these models limits are placed on internal fireball parameters.

Three types of gamma-ray-spectrum-normalized fireball models are considered

in this analysis, calculated on a burst-by-burst basis, that differ in their neutrino emission sites. The internal shock model relates the neutrino production radius to the variability time scale of the gamma-ray light curves [54,57,58]. The photospheric model places the radius at the photosphere through combinations of processes such as internal shocks, magnetic reconnection, and neutron-proton collisions [59–61]. The internal collision-induced magnetic reconnection and turbulence (ICMART) model favors a neutrino production radius $\sim$ 10 times larger than the standard internal shock model due to a Poynting-flux-dominated outflow that remains undissipated until internal shocks destroy the ordered magnetic fields [58, 61]. In these models, the regions where photons are generated through electron synchrotron radiation and where protons are accelerated are taken to be equivalent. This equivalence is not necessarily true for scenarios other than the internal shock model and multiple emission zones can exist [62], but one emission zone allows the predicted neutrino flux to scale linearly with the proton-to-electron energy ratio in the fireball. For all GRBs, standard flavor mixing from the source over cosmic baselines to the earth is assumed.

2.4.1 Prompt Photon Spectrum

Gamma-rays from GRBs are observed on a daily basis by a number of detectors in space, e.g. those in section 2.2. These missions report on the time, location, fluence, and spectral information of each burst. GRB output is extremely varied. Light curves plotted using data from the Fermi GBM mission shown in Figure 2.8

below illustrate the wide range of emission GRBs exhibit.

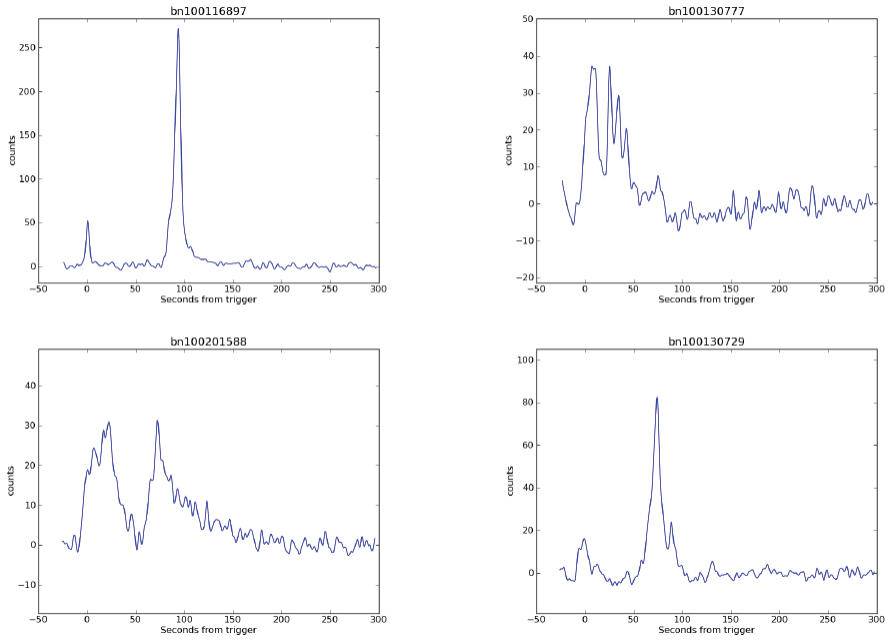

Figure 2.8: GRB light curves generated from the Fermi GBM detector data.

The gamma-ray signal observed by satellites in the keV to MeV range is generated in the outflow of the fireball scenario by synchrotron radiation or inverse Compton scattering of electrons accelerated in the internal shocks [63] [64]. This prompt GRB photon spectrum is typically modeled by a single power law, a power law with an exponential cut-off, a smoothly broken power law, or the Band function [34]. The Band function has become the standard for fitting GRB spectra, and was formulated using time-averaged spectra measured by the BATSE spectroscopy detectors [65]. The spectral parameters α, β, and E_0 vary from burst to burst. The break energy can range from tens of keV to over 1 MeV.

A broken power law approximation (Equation 2.1) based on the Band function is typically used in neutrino astrophysics to describe the average photon flux of the

GRB prompt emission [66].

$$F_\gamma(E_\gamma) = \frac{dN(E_\gamma)}{dE_\gamma}$$
$$= f_\gamma \times \begin{cases} \left(\frac{\epsilon_\gamma}{MeV}\right)^{\alpha_\gamma} \left(\frac{E_\gamma}{MeV}\right)^{-\alpha_\gamma}, & E_\gamma < \epsilon_\gamma \\ \left(\frac{\epsilon_\gamma}{MeV}\right)^{\beta_\gamma} \left(\frac{E_\gamma}{MeV}\right)^{-\beta_\gamma}, & E_\gamma \geq \epsilon_\gamma \end{cases} \tag{2.1}$$

2.4.2 Internal Shock Fireball Model

The current standard fireball phenomenology in the literature involves internal shock waves with varying boost factors [21]. The fireball plasma is initially opaque to radiation and expands by radiation pressure until it becomes optically thin and produces the measured gamma-ray emission. From this manifestation of optical thinness onward, the growing bulk Lorentz factor Γ becomes constant and its value depends on the baryonic load of the fireball [56].

The existence of internal shocks is supported by observations of the rapid time structure of GRBs [67]. The variability time scale of the measured light curves on the order of milliseconds suggests that the internal shocks collide. These collisions would be due to the varying baryonic loads and thus differing bulk Lorentz factors. Also, spikes in the burst spectra on the order of seconds are from synchrotron radiation electrons accelerated in the strong internal magnetic field [68]. Baryons must also be accelerated with the electrons in the expanding fireball. The resulting photohadronic interactions would then produce neutrinos.

As noted above, there are two branches of neutrino production models for the GRB fireball scenario, and the split is due to the assumptions they make about the

relationship between GRBs and UHECRs. The first class of model assumes GRBs are the dominant sources of the highest energy cosmic rays and allows one to draw conclusions on this hypothesis. The second type of model assumes that GRBs are only a source of UHECRs without any relation to the observed CR flux and allows one to draw conclusions on the makeup of GRBs themselves.

In either case, protons must be accelerated along with the electrons. The mechanism believed to be responsible for accelerating the protons and giving them their characteristic power law spectrum shown in Figure 1.1 is that of Fermi acceleration. This acceleration process transfers "macroscopic kinetic energy of moving magnetized plasma to individual charged particles, thereby increasing the energy per particle to many times its original value and achieving the nonthermal energy distribution characteristic of particle acceleration" [69]. Following the argument from chapter 11 of [69], upon each encounter with the magnetized plasma, a charged particle gains an amount of energy proportional to its energy:

$$\Delta E = \xi E \tag{2.2}$$

So after n encounters, the particle's energy is

$$E = E_0(1 + \xi)^n \tag{2.3}$$

and the number of encounters needed to reach energy E is

$$n = \frac{\ln(\frac{E}{E_0})}{\ln(1+\xi)} \tag{2.4}$$

Next, if the probability of escape from the acceleration region at each encounter is P_{esc}, then the probability of a particle remaining after n encounters is $(1 - P_{esc})^n$. Consequently, the number of particles accelerated to energies greater than or equal to E is proportional to

$$N(> E) \propto \sum_{m=n}^{\infty} (1 - P_{esc})^m = \frac{(1 - P_{esc})^n}{P_{esc}} \tag{2.5}$$

After taking the natural logarithm of both sides and exponentiating, one can write

$$N(> E) \propto \frac{1}{P_{esc}} \left(\frac{E}{E_0}\right)^{\frac{\ln(1-P_{esc})}{\ln(1+\xi)}} \tag{2.6}$$

Let

$$\gamma = \frac{\ln((1 - P_{esc})^{-1})}{\ln(1+\xi)} \approx \frac{P_{esc}}{\xi} \tag{2.7}$$

The above approximation can be made if one assumes P_{esc} and ξ are small. So now

$$N(> E) \propto \frac{1}{P_{esc}} \left(\frac{E}{E_0}\right)^{-\gamma} \tag{2.8}$$

and it is clear that the Fermi mechanism naturally leads to the power law spectrum observed for cosmic rays. The shape of the observed high energy cosmic ray spectrum

motivates the common choice of an E^{-2} power law [69]. Further, one can introduce the characteristic acceleration cycle and escape times. The ratio of T_{cycle} to T_{esc} is equal to P_{esc}. Thus γ can also be approximated as

$$\gamma \approx \frac{1}{\xi} \times \frac{T_{cycle}}{T_{esc}} \tag{2.9}$$

Fermi acceleration can be divided into two types based on the proportionality of the energy gain of a particle when encountering a shock front to the velocity of the shock front. Second order Fermi acceleration was the original mechanism proposed by Fermi for energy gains of charged particles in moving plasma among turbulent magnetic fields [70]. This type of acceleration is thought to occur in particles encountering a moving gas cloud. When a charged particle encounters the cloud, it moves into and out of it and gains an amount of energy proportional to β^2. In first order Fermi acceleration, a planar shock wave moves with a velocity v through a magnetized plasma. When a charged particle encounters the shock, it moves back and forth across it and gains an amount of energy proportional to $\beta = v/c$. First order Fermi acceleration is presumed to be the process through which very high energy protons and electrons are accelerated in the fireball internal shock model.

After protons have been Fermi accelerated in the expanding fireball, they interact with gamma-rays radiated by electrons. Charged and neutral pions are then produced via the delta resonance shown below.

$$p + \gamma \rightarrow \Delta^+ \rightarrow n + \pi^+$$

$$p + \gamma \rightarrow \Delta^+ \rightarrow p + \pi^0$$

In the comoving (primed) fireball frame, the threshold for this interaction is given by

$$E'_p E'_\gamma \geq \frac{m_\Delta^2 - m_p^2}{4} \tag{2.10}$$

In the (unprimed) reference frame of an observer on Earth, the minimum proton energy for photo-pion production is then

$$E_p \geq \frac{\Gamma^2}{(1+z)^2} \frac{m_\Delta^2 - m_p^2}{4E_\gamma} \tag{2.11}$$

High energy gamma rays are produced by the decay of the π^0, while neutrinos are produced by the decay of the charged π^+ and product μ^+.

$$\pi^0 \rightarrow \gamma + \gamma$$

$$\pi^+ \rightarrow \mu^+ + \nu_\mu \rightarrow e^+ + \nu_e + \bar{\nu}_\mu + \nu_\mu$$

The extremely long baselines from GRBs to the Earth cause the source flavor ratio of

$$(\nu_\mu : \nu_e : \nu_\tau)_{source} \approx (2 : 1 : 0)$$

to oscillate to

$$(\nu_\mu : \nu_e : \nu_\tau)_{earth} \approx (1 : 1 : 1)$$

2.4.3 Normalizing to Observed Gamma-Ray Fluences

The GRB neutrino spectrum predicted by Guetta et al. [71] is not built on the assumption that GRBs are *the* source of UHECRs. Instead, the prediction assumes that GRBs are *a* source of UHECRs, and is a per-burst fluence based on measured and predicted values of GRB parameters. Photopion production from collisions of accelerated protons and the observed gamma-rays in the fireball internal shock scenario results in neutrino emission. The neutrino emission therefore is predicted to occur during the same gamma-ray emission time window and to follow the gamma-ray spectrum up to the second break energy.

During photopion production, the peak cross section at the Δ resonance and the associated photon energy are used to approximate the fraction of energy lost by protons to pions f_π [54]. The mean fraction of energy lost to the pion at this resonance is approximately $\langle x_{p\to\pi}\rangle \simeq 0.2$ [54]. If this energy is evenly distributed between the four decay leptons of the charged pion described above, then following Eq. 2.11 the neutrino energy in the observer frame is

$$E_\nu = \frac{1}{4}\langle x_{p\to\pi}\rangle E_p \geq \frac{1}{4}\langle x_{p\to\pi}\rangle \frac{\Gamma^2}{(1+z)^2}\frac{m_\Delta^2 - m_p^2}{4E_\gamma} \tag{2.12}$$

The first break energy $\epsilon_{\nu,1}$ of the predicted double broken power law neutrino spectrum is obtained from the Δ resonance threshold condition in Eq. 2.12. Given

the photon spectrum break energy ϵ_γ and taking the geometric mean of 100 and 1000 as a standard bulk Lorentz factor value, $\epsilon_{\nu,1}$ can be written as

$$\begin{aligned}\epsilon_{\nu,1} &= \frac{1}{4}\langle x_{p\to\pi}\rangle \frac{\Gamma^2}{(1+z)^2}\frac{m_\Delta^2 - m_p^2}{4E_\gamma} \\ &= 7\times 10^5 GeV \frac{1}{(1+z)^2}\left(\frac{\Gamma}{10^{2.5}}\right)^2\left(\frac{MeV}{\epsilon_\gamma}\right)\end{aligned} \tag{2.13}$$

The second break energy $\epsilon_{\nu,2}$, which again results from synchrotron cooling of the high energy π^+ and μ^+ before they decay, is relevant when the synchrotron loss time approaches the particle lifetime [71].

$$t'_{sync} = \frac{3m_\pi^4 c^3}{4\sigma_T m_e^2 E_\pi U'_B} \to \tau'_\pi = \tau_\pi^0 \frac{E'_\pi}{m_\pi c^2} \tag{2.14}$$

where $U'_B = \frac{B'^2}{8\pi}$ is the energy density of the shocked plasma magnetic field and the Thompson cross section $\sigma_T = 6.65\times 10^{-25} cm^2$. Following the kinematics of [71] and [72], the fraction of internal energy carried by the magnetic field ϵ_B is given by

$$\epsilon_B L_{int} = 4\pi R^2 c\Gamma^2 U'_B \tag{2.15}$$

where $R \sim 2\Gamma^2 c t_{var}$ is the collision radius of two shock fronts in the plasma that have a difference in velocities of $\Delta v \sim \frac{c}{2\Gamma^2}$ and the variability time of the source is the previously introduced t_{var}. Additionally, the internal luminosity is related to the observed gamma-ray isotropic-equivalent luminosity by

$$\epsilon_e L_{int} = L_\gamma^{iso} \tag{2.16}$$

where the fraction of internal energy converted by accelerating electrons is ϵ_e. For simplicity, ϵ_e and ϵ_B are both taken to be 0.1 [71].

Now, if the ratio $\frac{t'_{sync}}{\tau'_\pi}$ approaches unity and the energy of the pion is distributed evenly among the four resultant leptons, then the break energy of the pion decay product muon neutrinos is

$$\begin{aligned} \epsilon_{\nu_\mu} &= \sqrt{\frac{t'_{sync}}{\tau'_\pi}} \\ &= \frac{1}{4}\sqrt{\frac{12\pi m_\pi^5 c^8 \epsilon_e \Gamma^6 t_{var}^2}{\sigma_T m_e^2 \tau_\pi^0 \epsilon_B L_{iso}(1+z)^2}} \end{aligned} \tag{2.17}$$

or more usefully

$$\epsilon_{\nu_\mu} = 10^8 GeV \frac{1}{(1+z)^2}\sqrt{\frac{\epsilon_e}{\epsilon_B}}\left(\frac{\Gamma}{10^{2.5}}\right)^4\left(\frac{t_{var}}{0.01s}\right)\sqrt{\frac{10^{52}\mathrm{erg}s^{-1}}{L_\gamma^{iso}}} \tag{2.18}$$

The muon decay product neutrinos have a lifetime 100 times longer than those from the charged pion and because $\frac{t'_{sync}}{\tau'} \propto E_\nu^{-2}$ as is described above, their break energy is 10 times smaller

$$\epsilon_{\bar{\nu}_\mu,\nu_e} = \epsilon_{\nu,2} = 10^7 GeV \frac{1}{(1+z)^2}\sqrt{\frac{\epsilon_e}{\epsilon_B}}\left(\frac{\Gamma}{10^{2.5}}\right)^4\left(\frac{t_{var}}{0.01s}\right)\sqrt{\frac{10^{52}\mathrm{erg}s^{-1}}{L_\gamma^{iso}}} \tag{2.19}$$

A further result of the $\frac{t'_{sync}}{\tau'} \propto E_\nu^{-2}$ relationship is that the corresponding high energy spectral index steepens by two powers. The final form of the neutrino spectrum is

then

$$F_\nu(E_\nu) = \frac{dN(E_\nu)}{dE_\nu}$$
$$= f_\nu \times \begin{cases} \left(\frac{\epsilon_{\nu,1}}{GeV}\right)^{\alpha_\nu} \left(\frac{E_\nu}{GeV}\right)^{-\alpha_\nu}, & E_\nu < \epsilon_{\nu,1} \\ \left(\frac{\epsilon_{\nu,1}}{GeV}\right)^{\beta_\nu} \left(\frac{E_\nu}{GeV}\right)^{-\beta_\nu}, & \epsilon_{\nu,1} \leq E_\nu < \epsilon_{\nu,2} \\ \left(\frac{\epsilon_{\nu,1}}{GeV}\right)^{\beta_\nu} \left(\frac{\epsilon_{\nu,2}}{GeV}\right)^{\gamma_\nu - \beta_\nu} \left(\frac{E_\nu}{GeV}\right)^{-\gamma_\nu}, & E_\nu \geq \epsilon_{\nu,2} \end{cases} \tag{2.20}$$

and the spectral indices are related to the gamma-ray indices and each other by

$$\alpha_\nu = 3 - \beta_\gamma, \quad \beta_{nu} = 3 - \alpha_\gamma, \quad \gamma_\nu = \beta_\nu + 2 \tag{2.21}$$

The above neutrino spectrum is then normalized to the observed GRB gamma-ray fluence [71] [14]. The gamma-ray fluence is assumed to be proportional to the neutrino fluence. This proportionality is argued to be

$$\int_0^\infty dE_\nu E_\nu F_\nu(E_\nu) = \frac{1}{8}\frac{1}{f_e} f_\pi \int_{1keV}^{10MeV} dE_\gamma E_\gamma F_\gamma(E_\gamma) \tag{2.22}$$

The gamma-ray fluence is defined with finite limits because some GRBs are reported with divergent F_γ if integrated from zero to infinity. The factor of $\frac{1}{8}$ represents that roughly half of the photohadronic interactions result in π^+ (and thus leptons), and the energy is taken to be distributed evenly among the four leptons. In truth, as can be calculated using isospin arguments, the probability that a Δ^+ decays into a π^+ is 1/3, but 1/2 is taken by [71] and [55] for an approximation. f_e is the fraction of fireball energy carried by electrons compared to protons, and is assumed to be

0.1 [14].

Finally, f_π estimates the overall fraction of the proton energy going into the pions [14]. This fraction is calculated from the size of the shock ΔR, the mean free path of a proton for photohadronic interactions $\lambda_{p\gamma}$, and the average fraction of proton energy transferred to a pion in a single interaction, which is assumed to be $\langle x_{p\to\pi}\rangle = 0.2$. Altogether, the expression for f_π is

$$f_\pi = 1 - (1 - \langle x_{p\to\pi}\rangle)^{\Delta R'/\lambda_{p\gamma}} \tag{2.23}$$

which ensures that the transferred energy fraction is ≤ 1. $\Delta R'/\lambda_{p\gamma}$ yields the expected number of photohadronic interactions given the size of the shock and the interaction mean free path. $\lambda_{p\gamma} = \frac{1}{n_\gamma \sigma_\Delta}$, where the number density of photons n_γ in the expanding fireball is in turn given by the ratio of the photon energy density and the photon energy in the comoving frame

$$n_\gamma = \frac{U'_\gamma}{\epsilon'_\gamma} \simeq \left(\frac{L_\gamma^{iso} t_{var}/\Gamma}{4\pi R^2 \Delta R'}\right) \Big/ \left(\frac{\epsilon_\gamma}{\Gamma}\right) \simeq \frac{L_\gamma^{iso}}{16\pi c^2 t_{var} \Gamma^4 \Delta R' \epsilon_\gamma} \tag{2.24}$$

The number of photohadronic interactions can then be usefully written as

$$\frac{\Delta R'}{\lambda_{p\gamma}} = N_{int} = \left(L_\gamma^{iso}\right) \left(\frac{0.01s}{t_{var}}\right) \left(\frac{10^{2.5}}{\Gamma}\right)^4 \left(\frac{MeV}{\epsilon_\gamma}\right) \tag{2.25}$$

where $\Delta R'$ is the comoving width of the causally connected region of the jet.

The benefit of the Guetta et al. approach is clearly in its ability to tailor to measured parameters of individual bursts. However, each prediction still depends

on a number of tenuous assumptions on these internal variables, including the bulk Lorentz factor, the smallest observed variability time of the light curve, the equipartition fractions ϵ_B and ϵ_e, photopion production efficiency, the luminosity of bursts with no measured redshift, and the ratio of energy carried by electrons to that of protons. Moreover, conclusions on the GRB contribution to UHECRs cannot be drawn because there is no intrinsic relation to the observed flux in UHECRs using this normalization method.

Null results from IceCube [14] [73] [16] have brought about revisions of the above γ-normalized prompt models of GRB neutrino emission. New and revised models, both analytically calculated and Monte Carlo-based numerically calculated, of GRB prompt neutrino emission address the assumptions discussed above as well as implement more complete particle physics. Further, some models invoke scenarios that force proton acceleration at different radii compared to the usual internal shock radius. A sample of these predictions using the northern hemisphere GRB samples of each season are presented below.

2.4.4 Photospheric and ICMART Fireball Models

As is shown in Chapter 7, any model that invokes high energy proton acceleration at the photosphere is already disfavored by the present limits. If deeper limits are placed on the internal shock model, then it is argued that the neutrino emission site is at a much larger radius than the internal shock radius or high energy protons are not at the site where γ-ray photons are produced [58]. Magnetic dissipation

models [61] [74] invoke a larger-radius of proton acceleration and gamma-ray production. Such models could be the explanation for the unobserved GRB neutrino flux.

The per-GRB neutrino flux for two different mechanisms of prompt emission are shown below and provide alternatives to the fireball internal shock model [58]. These models are normalized to the observed gamma-ray spectra of each GRB. The differences in the models manifest in the radius of gamma-ray prompt emission. The dissipative photosphere (photospheric) model requires gamma-ray generation and proton acceleration at the photosphere, where the fireball becomes optically thin to $\gamma\gamma$ interactions [59] [75].

The general formalism used by Zhang and Kumar mostly follows that of the Guetta-based prediction in Section 2.4.3. One difference between the two is the consideration of the radius of the proton acceleration site R and the bulk Lorentz factor Γ as the primary parameters instead of t_{var} and Γ. This paradigm is chosen to allow one to probe the resulting neutrino production of models with different emission radii. Another addition to the formalism is the introduction of the ratio of the photon luminosity to the non-thermal proton luminosity $f_{\gamma/p}$. This parameter acts as a more general electron-to-proton energy ratio f_e and allows for gamma-ray generation and proton acceleration to occur at different locations. If photon production and proton acceleration are invoked at the same sight, then $f_{\gamma/p}$ reduces to f_e. The usual scheme for calculating the neutrino flux is followed, with the observed photon spectrum fit to a broken power law (Equation 2.1) and the neutrino spectrum assumed to follow a double broken power law (Equation 2.20).

The photospheric model proposes that the prompt GRB spectrum is formed near the Thomson scattering photosphere given by

$$R_{ph} \simeq 3.7 \times 10^{11} cm \frac{1}{\epsilon_e} \left(\frac{L_\gamma^{iso}}{10^{52} ergs^{-1}} \right) \left(\frac{\Gamma}{10^{2.5}} \right)^{-3} \tag{2.26}$$

[58] considers it likely that both photons are generated and protons are accelerated at R_{ph} such that $f_{\gamma/p}$ can be set to f_e. Thus, compared to the Guetta-based prediction, N_{int} increases by a factor of $R_{IS}(\ 10^{14} cm)/R_{ph}$ and $\epsilon_{\nu,2}$ decreases by the same factor. Compared to other GRB emission models, the photospheric model has the smallest possible dissipation scale and, as a result, the highest photon density [76]. Altogether, this scenario leads to an enhancement in neutrino production from the conventional internal shock model.

The internal collision-induced magnetic reconnection and turbulence (ICMART) model is presented in [58] as a typical large-radius magnetic dissipation model of GRB neutrino production. This model invokes a highly magnetized outflow, which remains undissipated up to a distance of $R_{ICMART}(\ 10^{15} cm) > R_{IS}$. At this radius, internal shocks help to destroy the ordered magnetic fields and a strong runaway magnetic dissipation process occurs. Photon generation and proton acceleration are again in the same region, so $f_{\gamma/p} = f_e$. Thus, compared to the Guetta-based prediction, N_{int} decreases by a factor of R_{IS}/R_{ICMART} and $\epsilon_{\nu,2}$ increases by the same factor. Altogether, this model leads to a reduction in neutrino production.

2.4.5 Numerical Fireball Neutrino Spectra Predictions

The per-GRB gamma-ray-normalized predictions used in the likelihood analysis and limit calculations are calculated numerically with a wrapper of the Monte-Carlo generator SOPHIA [77]. This code was written by a colleague in IceCube [76]. The calculation includes the full particle production chain and synchrotron losses of all intermediate mesons and leptons of the $p\gamma$-interaction cascade before their decay in the fireball, which must be added to the original SOPHIA setup. The author notes that this is not a new model, "but simply a direct application of the fireball model" [76].

For these calculations, the reported gamma-ray spectrum of each GRB is parametrized as a broken power-law approximation of the Band function, following the formula in [58, 65, 66]. As described in Section 2.3, GRB parameters from the GCN circulars and the Fermi GBM database [35, 36] are compiled on the GRB-web database. Average values of γ fluence 10^{-5} erg cm^{-2}, redshift 2.15 for long bursts with durations > 2 s and redshift 0.5 for shorter bursts are used if these parameters are unmeasured, following the same prescription of IceCube's previous model limit calculations [15–17].

The neutrino flux predictions depend on several unnmeasured quantities; variability time scale 0.01 s and isotropic luminosity 10^{52} erg cm^{-2} are used for long bursts and variability time scale 0.001 s and isotropic luminosity 10^{51} erg cm^{-2} are used for short bursts, which are consistent with the literature [57, 58, 78]. If the redshift is known for a particular burst, the approximate isotropic luminosity from

the redshift, photon fluence, and T_{100} is calculated [57].

The top plot of Figure 2.9 shows neutrino spectra from the three models with benchmark fireball parameters. These benchmark parameters are bulk Lorentz boost factor $\Gamma = 300$ and proton-to-electron energy ratio, or baryonic loading, $f_p = 10$. The middle and bottom plots show neutrino spectra from the three models with larger boost factors, requiring larger proton energy thresholds for pion, and hence neutrino, production in the observer frame. These spectra are presented as per-flavor quasi-diffuse fluxes, in which we divide the total fluence from all GRBs in the sample by the full sky 4π steradians and one year in seconds, and scale the total number of bursts to a predicted average 667 observable bursts per year, which has been used in our previous publications. The actual number of bursts observed by satellite detectors in each year is less than the prediction because of detector field of view limitations and obstruction by the sun, moon, and Earth.

The fireball model neutrino spectra calculations in these figures compare with a numerical model first presented as an improvement to the analytic approximations outlined above [57]. The changes lead to an overall reduction in the predicted flux, shown in Figure 2.10 for an example GRB. In this plot, f_{C_γ} comes from removing the assumption that all photons have an energy at the break energy of the photon spectrum. The photons are consequently distributed according to the photon spectrum. $f_\approx$ comes from correcting some rounding errors in the Guetta et al. calculation. f_σ results from considering the width of the Δ resonance and integrating over the photon spectrum rather than just the resonance peak. C_S follows from the inclusion of the proton energy in the interaction rate of the photons within the energy range

of the Δ resonance. Finally, the addition of kaon and multi-pion production modes to the photomeson interactions increases the neutrino flux by the amount seen in the "full $p\gamma$" labeled correction to the numerical calculation in the right panel of Figure 2.10.

2.4.6 Cosmic Ray Connection: The Waxman & Bahcall Prediction

The GRB neutrino flux derived by Waxman and Bahcall assumes GRBs are the major source of UHECRs (above 10^{19} eV) [54]. A relativistic expanding fireball scenario is assumed with protons and electrons Fermi accelerated by interaction with internal shocks, as described above. The internal shocks arise from fluctuations in the expanding wind bulk Lorentz factor Γ, which themselves are a result of the variability of the source [54]. If the time scale of the variability of the source is t_{var}, then the internal shocks in the ejecta form at comoving radius $R' \approx \Gamma^2 c t_{var}$. The kinetic energy converted by the central engine is then reconverted by the shocks to acceleration of protons and electrons with similar efficiency for both particles. Similarity in the two efficiencies is necessary if cosmological GRBs are the sources of UHECRs.

The energy in protons accelerated in the fireball is normalized to the energy production rate required to produce the observed flux of cosmic rays at energies 10^{19} - 10^{20} eV, which in this case is taken to be about 3×10^{44} erg Mpc^{-3} yr^{-1} [55]. This rate is comparable to the energy production rate of GRBs through gamma rays using the BATSE energy range [79]. Assuming an E_p^{-2} power law for the proton

differential energy spectrum generated at the source, and that each product neutrino carries about 5% of the primary proton energy, an upper limit to the neutrino flux is obtained [55]

$$E_\nu^2 \Phi_\nu \leq 4.5 \times 10^{-8} \frac{GeV}{cm^2 ssr} \tag{2.27}$$

A $\Gamma \approx 300$ is assumed and for typical $E_\gamma = 1MeV$, using Eq. 2.11, one gets characteristic proton energies of $\sim 10^7$ GeV required for pion production. This required proton energy leads to an expected production of $\sim 10^5$ GeV neutrinos. This value is taken as the first break in the neutrino spectrum. The second break energy is reasoned to be $\sim 10^7$ GeV. The suppression beyond this energy is due to energy loss of the pions and muons before they decay.

2.4.7 Concerning Proton Escape

Because protons are magnetically confined to the expanding fireball and the maximum proton energy is significantly reduced due to the fireball's adiabatic cooling [80], the notion of direct proton escape as UHECRs is problematic. However, secondary neutrons from photopion production escape the fireball unhindered. Cosmic ray protons thus could be identified as protons from the β-decayed escaped neutrinos, and "a smoking-gun test of this scenario is the production of PeV neutrinos from the decay of the charged pions inevitably produced along with the neutrons" [56].

In [56], Ahlers et al. present an alternative approach to the per-burst photon fluence normalized spectra. Instead, their approach directly fits the proton spectra

from the β decay of escaped fireball neutrons to HiRes I and II data [81] [82]. Their analysis assumes that UHECRs above the 4 EeV ankle in the measured spectrum consists of neutrons emitted from $p\gamma$ interactions in internal shocks of the GRB fireball model. The diffuse flux of neutrinos produced in association with these GRB cosmic rays is then calculated. The authors conclude that the predicted diffuse neutrino flux associated with GRB-produced cosmic rays exceeds the upper bound on a diffuse flux of cosmic neutrinos obtained by IceCube with the IC40 detector [83]. As seen in their Figure 3, the results show that predicted prompt neutrino fluxes from typical "benchmark" fireball environments with the associated proton spectrum fit to CR data are ruled out by the IC40 diffuse neutrino limits. "Atypical" fireball environments with different relative synchrotron and dynamical scales have some allowed parameter space. The predicted spectrum from secondary neutrino production during CR propagation in the form of GZK neutrinos was also considered under two assumptions: (1) that the comoving density of GRBs follows the star formation rate (SFR evolution) and (2) that GRBs do not follow the SFR and may have been stronger in the past (strong evolution).

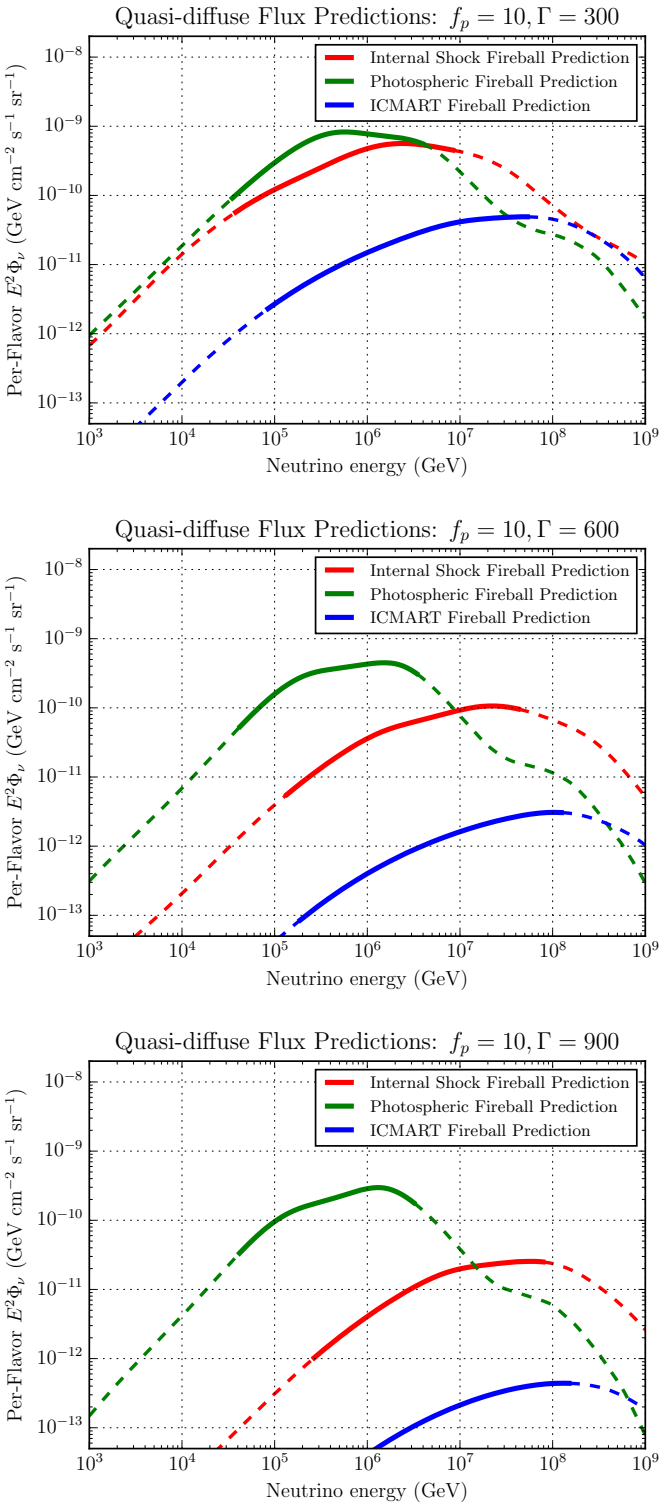

Figure 2.9: Per-flavor quasi-diffuse all-sky flux predictions for different models of fireball neutrino production, assuming $f_p = 10$, full flavor mixing at Earth, 667 total GRBs per year and three different Γ values (300, 600, 900). Red, green, and blue curves are the internal shock, photospheric, and ICMART models, which differ in the radius at which photohadronic interactions occur. The solid segments indicate the central 90% energies of neutrinos that could be detected by IceCube.

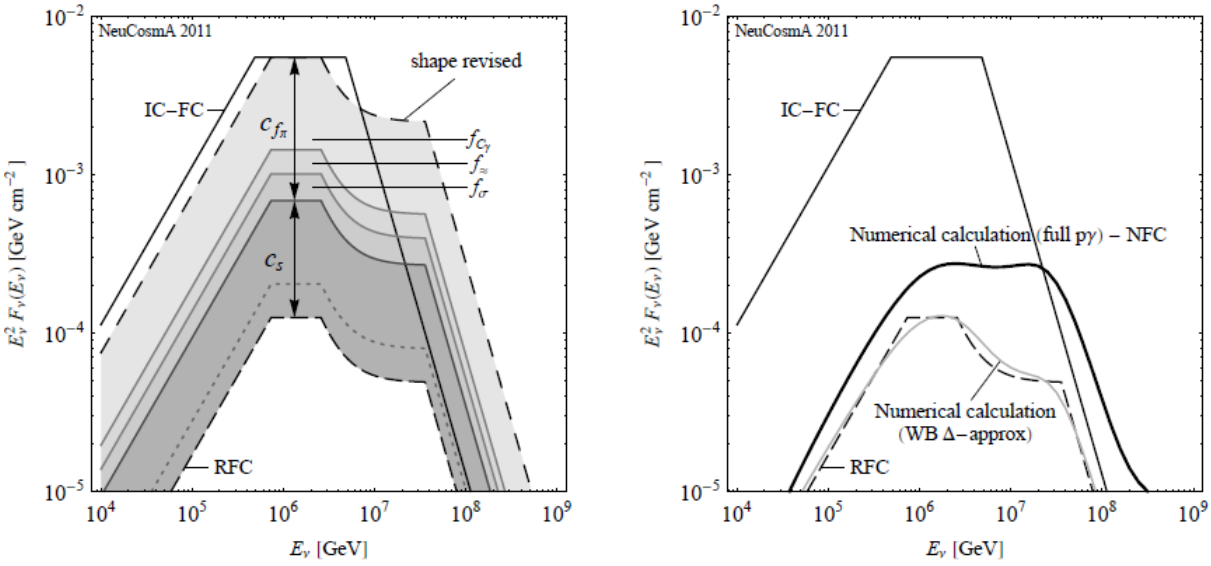

Figure 2.10: Left panel: Step-by-step modifications to the Guetta et al.-based prediction. Right panel: Numerical code applied [57]

Chapter 3

IceCube: The Detector, Neutrino Detection, and Event Characteristics

3.1 The Detector

The IceCube detector [84] consists of 5160 digital optical modules (DOMs) instrumented over 1 km^3 of clear glacial ice 1450 m to 2450 m below the surface at the geographic South Pole and is the largest neutrino detector in operation. The detector consists of 86 "strings" of copper twisted wire pairs, each with 60 DOMs [85] positioned vertically at 17 m intervals. Adjacent strings are separated by about 125 m. These sensors detect the Cherenkov radiation of relativistic charged particles produced in neutrino-nucleon interactions in the ice and bedrock below. The DeepCore array [86] is made up of a more densely spaced subset of these strings that are located in the clearest ice at depths below 2100 m and contain higher quantum efficiency photomultiplier tubes (PMTs). The IceTop array consists of 81 stations located at the top of IceCube strings and detects cosmic ray air showers. Each IceTop station has two tanks of two downward-facing DOMs. Data from IceTop DOMs are not used in this analysis.

Sensor deployment began during the 2004-2005 austral summer. Physics data collection began in 2006 with the nine-string iteration and continued with partial

detector configurations through completion of the 86 strings in December 2010. This work uses data taken from May 2010 through May 2013, with one year using 79 strings and two years using all 86 strings. Model limits presented in Chapter 7 combine the results of this analysis with those of analyses of data extending back to May 2008, taken with 40 instrumented strings.

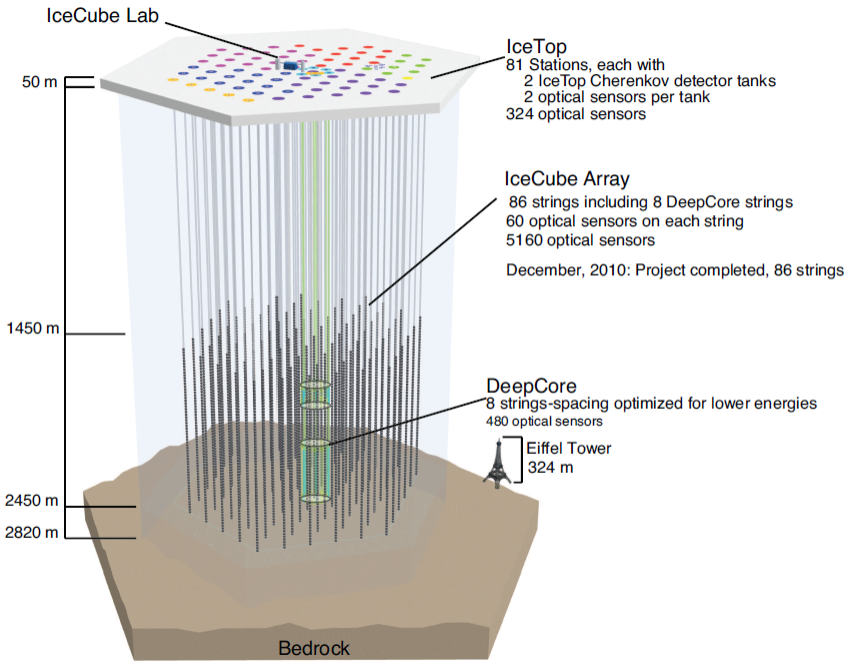

Figure 3.1: The IceCube detector

3.1.1 Data Acquisition

The data acquisition (DAQ) software in IceCube analyzes the packet of data, assembled by each DOM, and checks if any of the configured trigger conditions (Section 3.1.1.5) are met. The DAQ was designed "to capture and timestamp with high accuracy, the complex, widely varying optical signals over the maximum dynamic range provided by the PMT" [85]. This goal is accomplished over a decentralized

system, with the signal digitization done inside each DOM Main Board (MB) and then sent to the counting house in the IceCube Laboratory (ICL) computers on the surface. The ICL is shown in Figure 3.2. A diagram of the DOM Main Board, with components described in the following sections, is shown in Figure 3.3.

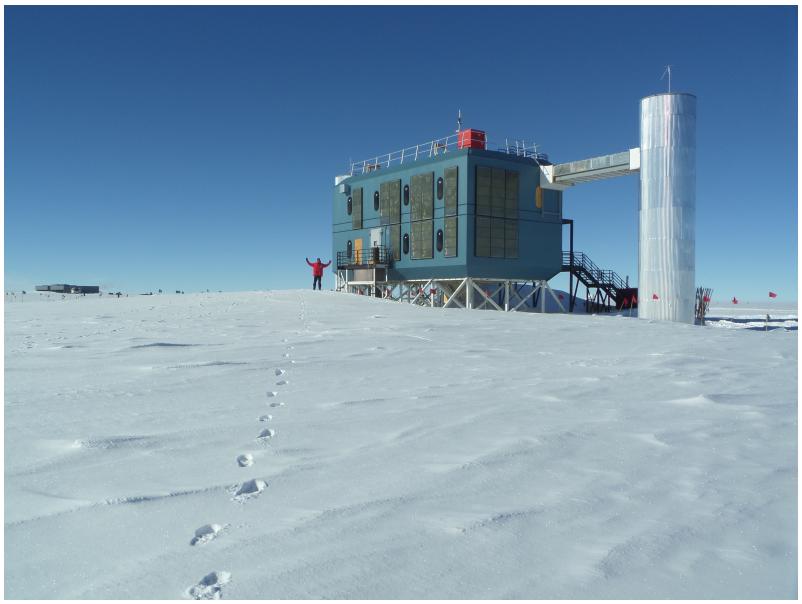

Figure 3.2: The IceCube Laboratory (ICL). There is a cylinder on each side through which all of the twisted copper wire pair "strings" traverse, connecting the DOMHubs to the detector below.

3.1.1.1 Digital Optical Modules and the PMT

The first element of the IceCube DAQ is the DOM itself. Each DOM contains a 10 in. diameter R7081-02 photomultiplier tube made by Hamamatsu Photonics [85]. The PMT detects the blue and near-UV Cherenkov photons and the signal waveforms are then time-stamped, digitized, and sent from the DOM to the ICL. At the heart of IceCube, in the clearest ice below 2100 m, the DeepCore array consists of 360 more densely spaced DOMs deployed over 8 additional strings. These

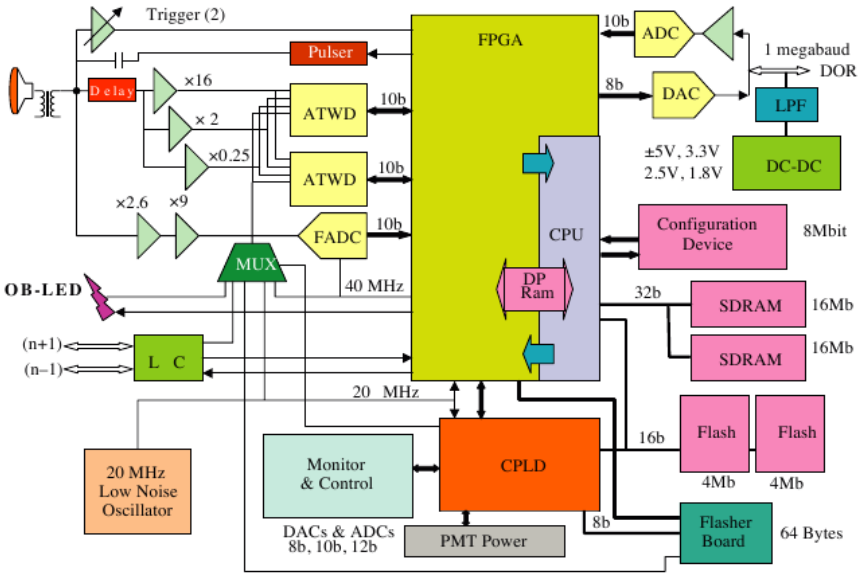

Figure 3.3: Diagram of the DOM Main Board. The PMT, CPU, digitizers, FPGA, and clock are shown.

DOMs contain Hamamatsu R7081MOD PMTs, which have a quantum efficiency that is about 40% higher than that of the otherwise identical R7081-02 at the photon wavelength 390 nm. DeepCore provides improved acceptance for neutrinos at energies as low as about 10 GeV [86].

A photon incident on the grounded PMT cathode that overcomes the cathode's electron binding energy results in the emission of a photoelectron. The photoelectron accelerates over the potential differences between the cathode and the first dynode, knocking off electrons, which in turn knock off more electrons throughout a series of 10 linear focused dynode stages. The PMT achieves a nominal gain in signal of 10^7 at about 1300 V from cathode to anode [85]. An illustration of the IceCube DOM can be seen in Figure 3.4.

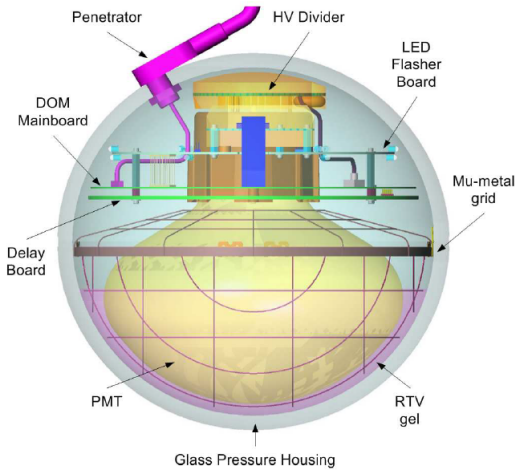

Figure 3.4: Schematic of a DOM

3.1.1.2 Waveform Digitization

The analog signal is presented to the DOM MB signal path where it is split to a high-bandwidth discriminator path and to a 75 ns delay line [87]. If the measured current exceeds the discriminator threshold of 0.25 times the single photoelectron peak, then the field programmable gate array (FPGA) initiates the capture of the waveform. Waveform capture is accomplished by two digitization systems: the Fast Analog to Digital Converter (fADC) and the Analog Transient Waveform Digitizer (ATWD) [88]. The fADC digitizes the PMT signal every clock cycle (25 ns), and determines whether the signal passes the discriminator threshold. If the 0.25 photoelectron threshold is surpassed, then the ATWD begins capturing the delayed signal. The ATWD is a custom designed application specific integrated circuit (ASIC) and has three separate channels, which receive the input from three separate wide-band amplifiers [87] The three amplifiers are characterized by progressively lower gains of x 16, x 2, and x 0.25. In order to increase the dynamic range of the readout, the

next lower gain channel is read out if the previous higher-gain channel saturates. There is also a fourth channel used only for calibration. Furthermore, "to minimize dead time, the DOM is equipped with two ATWDs such that while one is processing input signals, the other is available for signal capture" [87]. Each ATWD has an array of 128 low-capacitance capacitors, which are connected to the signal for 3.3 ns each in sequence and thus hold a time series of the signal in their charge.

The ATWD is only engaged for photon signals that satisfy an imposed local coincidence constraint. The Hard Local Coincidence (HLC) condition causes ATWD data to be read out in a DOM only if it receives a local-coincidence-tagged pulse from one of its neighboring or next-to-neighboring DOMs within 1 μs [87]. This procedure allows for a high level of background rejection and reduction in data flow. Once the HLC requirement is met, then these data is read out through the highest, unsaturated, gain channel by the ATWD. The process of digitizing the waveform takes 29 μs if all three channels need to be read out [87]. Data from DOMs failing the local coincidence condition report a short summary of their recorded waveform for inclusion in data records, and these events are colloquially known as Soft Local Coincidences (SLC) in IceCube.

The DOM MB can be thought of as its central processor. Upon detection of one or more photons, the MB digitizes the received PMT signals. The MB then formats these data into the fundamental IceCube datum, the "hit." Each hit compiled by a DOM is made up of a timestamp and waveform information. Such waveform information contains a coarse measure of charge and several bits defining the hit origin. [87].

3.1.1.3 DOMHubs and the IceCube Laboratory

The second and third elements of the IceCube DAQ are the cable network and DOMHub. The cable network connects adjacent DOMs to each other and DOMs on a string to a DOMHub computer in the ICL. There is a hub computer in the ICL for each string of the detector. Each hub contains a hard disk, power source, and single board computer, which buffers packets of data sent to them by the DOMs. Each cable carries power and data signal through the copper twisted-pair wires bundled together [85].

Data rates reach $\sim$ 900 kb/s for the DOMs most remote from the ICL [87]. One DOMHub machine controls an entire string of 60 DOMs (or 8 stations of 32 IceTop DOMs) and stores their packets of data sent to it. The machine supplies power and communicates with its host DOMs using several custom PCI cards, called DOR (DOM Readout) cards. A picture of an open DOMHub is shown in Figure 3.5.

3.1.1.4 Timing

The fourth element of the IceCube DAQ is the timing calibration process. This background-running process consists of the Master Clock and the Reciprocal Active Pulsing Calibration (RAPCal) system. "The Master Clock makes use of the Global Positioning System (GPS) satellite radio-navigation system, which disseminates precision time from the UTC master clock at the US Naval Observatory to our GPS receiver in the ICL" [87] [89]. The RAPcal procedure establishes a com-

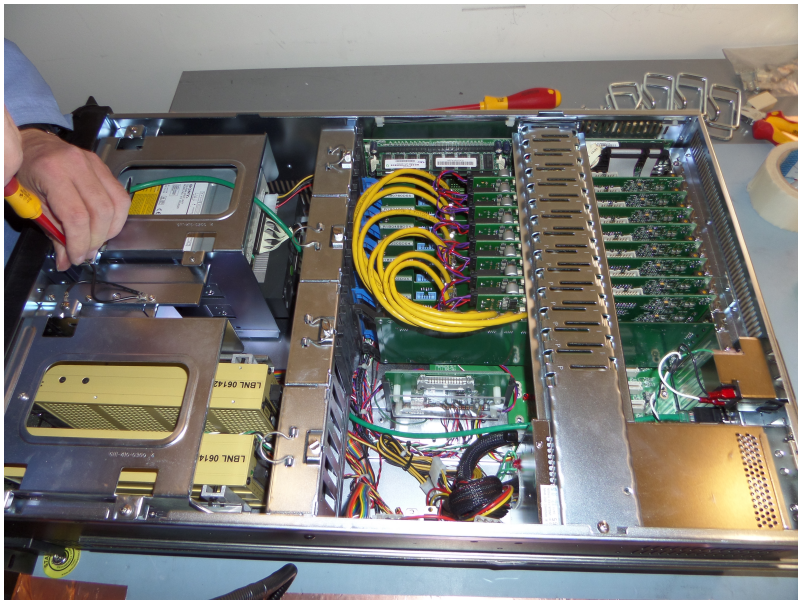

Figure 3.5: An open DOMHub with hard disk, power source, DOR cards, and single board computer shown.

mon time-base for all DOM hits. This calibration is accomplished by the DOM and DOMHub sending and receiving precisely-timed RAPCal pulses to each other using identical hardware [87]. The DOMHub calculates the travel time offset of the pulses and the clock drift of the 40 MHz oscillator and sends the appropriate correction instructions. This procedure is performed periodically at a frequency of 1 Hz.

3.1.1.5 Data Triggering and Formatting

The fifth and final element of the IceCube DAQ is the Stringhub program. Stringhub resides in the DOMHub CPUs and "converts the flow of DOM hits into physics-ready hits that are suitable at both trigger and event-building stages of the surface DAQ" [87]. The program transforms the timestamps accompanying all received hits into a UTC-based time domain, orders DOM hits from multiple DOMs

on a string, and then applies string-wide trigger filters as necessary. Stringhub communicates with the multi-string trigger handlers and, upon receiving the specified hit criteria, sends a list of all matching hits and then flushes the cached information. All of these data are buffered until the DOM MB receives a request to transfer data to the ICL.

There are several in-ice trigger conditions checked by the IceCube DAQ. The trigger used for the base event selection of this analysis is the requirement of 8 local coincidences within 5 μs. Time windows for any other triggers optimized for different signal types that overlap with this 5 μs window are combined. Finally, the waveforms of all hits recorded within -4 μs and +6 μs of this global trigger window are combined into an "event." The minimum energy to trigger an event in IceCube is around 10 GeV.

3.1.2 Feature Extraction

The number and arrival times of Cherenkov photons are then extracted by reconstructing each waveform as a series of pulses. The best fit pulse series amplitudes and times for each triggered PMT's waveform are determined from the linear combination that minimizes the fit error [90]. The relative timing resolution of photons within an event is 1 ns [84].

An improved feature extraction algorithm called wavedeform [91] is used in IC86II. Wavedeform avoids the problem of adding large positive and negative pulses together in the fit by using the Lawson-Hanson algorithm which is a non-negative

least squares fit. This algorithm also avoids over-fitting by only using the most error-reducing pulse at each iteration.

3.1.3 Pulse Cleaning

Early and late noise hits that may make some reconstructions less accurate are cleaned after the pulse series are produced. Two different cleaning algorithms are employed. The first, called time window cleaning, keeps only the $6\mu s$ of data that contain the most pulses out of the triggered event. The second, called seeded RT cleaning, removes all hits that had no other hit within $1\mu s$ and 150 m. The "seeded" part refers to the algorithm only using mostly-signal-like HLC events. Then all other hits (SLC) in the event are included if they satifsy the RT requirements with respect to the seeded hits.

3.1.4 Processing and Filtering

Various physics filters choose events based on different signal types. The filters are implemented by the Processing and Filtering (PnF) system, which receives events from the DAQ. The PnF system performs the various computationally-light reconstructions required for the online filters using a computer cluster. The server monitors the the events being dispatched by the DAQ and distributes the events to the clients, which are then chronologically recombined into larger files. In this analysis, the cascade filter-passing events are used. This filter is described in Section 5.2 and uses the LineFit and Tensor-of-Inertia reconstructions.

3.1.5 Data Transmission to the North

The DAQ Dispatch sends the triggered data to the processing and filtering system which reconstructs and filters events to send to the north via communications satellites. All events are written to tape at the pole for data recovery contingency. These backups are physically sent to Wisconsin each year and stored.

3.2 Particle Detection

IceCube detects neutrinos by their deep inelastic scattering products traveling through the ice. Charged particles traversing a dielectric medium faster than the speed at which light can traverse that medium produce Cherenkov radiation. This light is emitted in a cone about the particle's trajectory as illustrated in Figure 3.9. The angle of the wave front is given by

$$\theta_C = \cos^{-1}(\frac{1}{\beta n}) \tag{3.1}$$

where n is the index of refraction of the medium and $\beta = v/c > 1/n$. In the deep South Pole ice, an electron or muon traveling with $\beta \approx 1$ emits 300 to 600 nm wavelength photons.

3.2.1 Signal Characteristics

The signal in this search is astrophysical electron, tau, and muon neutrinos interacting in the ice with energies above 1 TeV. The Feynman diagrams for deep

inelastic neutrino-quark scattering that constitute these interactions are given in Figure 3.6. In charged current interactions, a W boson is exchanged and the charged lepton corresponding to the neutrino flavor is emitted. In neutral current interactions, a Z boson is exchanged and a neutrino of the same flavor is emitted.

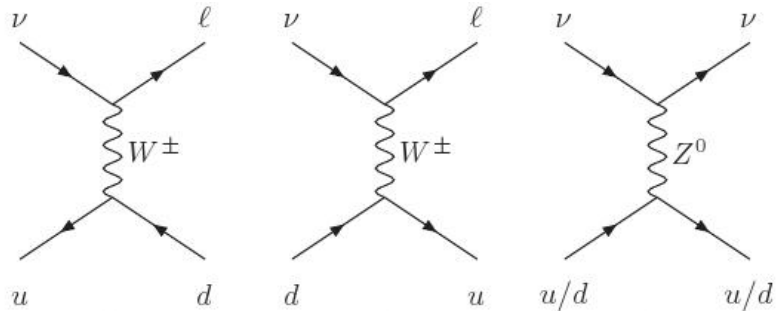

Figure 3.6: Charged current and neutral current deep inelastic neutrino-quark scattering.

The three flavors of neutrino all exhibit similar Cherenkov patterns through Z boson exchange. In this interaction at high energies, only the hadronic shower of baryons and mesons produced by the recoiling nucleus manifest in the detector. The three flavors of neutrinos all exhibit different Cherenkov patterns through W boson exchange. The three different Cherenkov light topologies in IceCube are illustrated in Figure 3.7.

Electrons lose their energies as they emit high energy bremsstrahlung photons, which then create an e^+ e^- pair. This pair, in turn, emits photons, and so on. The resulting electromagnetic "shower" or "cascade" manifests as a spherical light pattern. Tau neutrino charged current interactions produce a hadronic cascade at the interaction vertex and a tau. The short tau lifetime usually means that it decays within the initial cascade. At energies beyond a few PeV, the tau travels a long

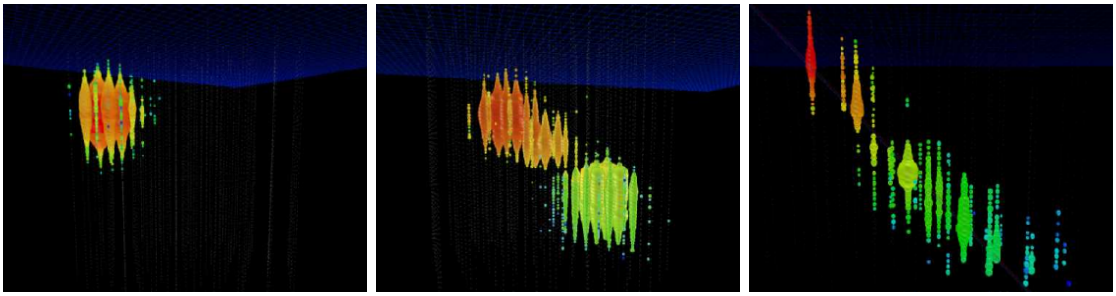

Figure 3.7: Electron (left), tau (middle), and muon (right) flavored neutrino high energy charged current interaction topologies in IceCube.

enough distance to show a "double bang" topology. This type of event has yet to be observed in IceCube data. Muons traversing the detector produce "tracks" of Cherenkov light as they lose their energies much more slowly than electromagnetic cascades. The signal for this search is all neutrino interactions that produce cascades, which means all of the above except for charged current ν_μ and PeV energy charged current ν_τ.

Another possible high energy neutrino interaction that can be observed is the Glashow resonance, which occurs when a $\bar{\nu}_e$ with energy $\approx \frac{M_W^2}{2m_e} = 6.3$ PeV resonantly scatters off of an electron to produce a W^- [92]. The cross section for this resonance is much larger than the charged-current cross section at this energy as shown in Figure 3.8. The Glashow resonance has yet to be observed but the decay leptons and hadrons would induce PeV-scale cascades in the ice [93] [94].

3.2.2 Background Characteristics

The primary background of this analysis is muons catastrophically losing their energies through stochastic processes with little apparent Cherenkov track tail.

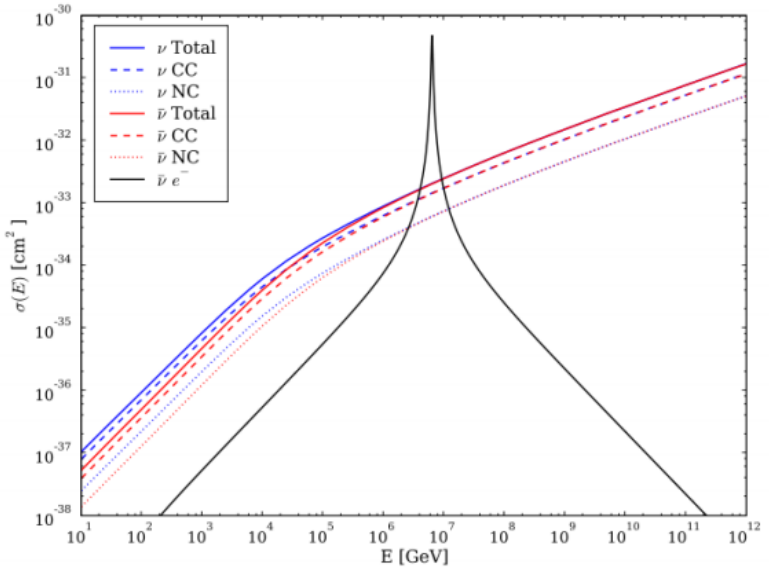

Figure 3.8: Cross sections of neutrino and anti-neutrino charged-current and neutral-current interactions as a function of neutrino energy. The Glashow resonance is also plotted. Plot from [95].

These muons are produced by cosmic rays interacting with the atmosphere. Muons can lose their energies in the ice through ionization, bremsstrahlung, photo-nuclear interactions, and pair production. The energy and loss profiles of these processes are shown in Figure 3.10.

Another background of this search is neutrinos also from cosmic ray air showers. This background is nearly irreducible because the signal is neutrinos as well. Atmospheric neutrinos can be weighted down to some extent in the likelihood analysis by their lower energies on-average than the expected astrophysical signal.

Muons dominate the data rate at all event selection levels of this search. Therefore, data events not within two hours of any reported GRB γ emission are used for the background dataset in this analysis.

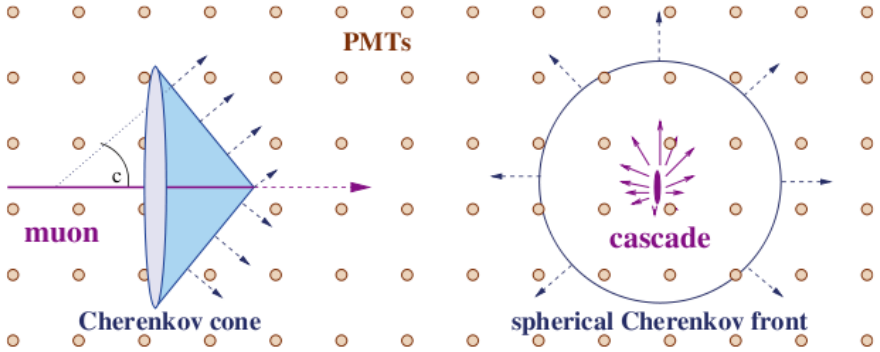

Figure 3.9: Two-dimensional schematic of cascade and track event topologies in the detector

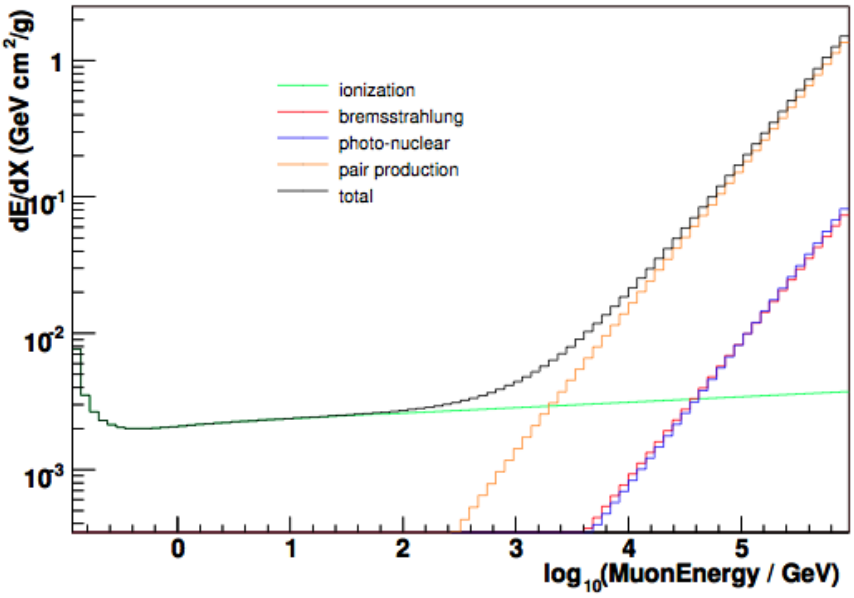

Figure 3.10: The different processes for muon energy loss in IceCube. From [96].

Chapter 4

Simulation and Reconstruction Techniques

This chapter describes the simulation of particle interactions in and around the detector as well as the techniques used to describe real and simulated events. Monte Carlo simulations model the detector response to both neutrino signal and muon background. These simulated data allow for accurate estimations of signal sensitivity and better understanding of the actual data. Event reconstructions use the timing, position, and intensity of Cherenkov light recorded by the DOMs to better describe the events that generated the light. Many features are calculated from these reconstruction algorithms and then are used for particle identification.

4.1 Simulation Methods and Description

Monte Carlo simulations of signal neutrinos interacting in the IceCube detector are used for the signal hypothesis in the event selection and optimization for this search. Although data outside of GRB gamma-ray emission time windows are used for the background, simulated neutrinos and muons generated in cosmic-ray air showers are useful checks for background characterization and estimating the signal purity of the final data sample. Neutrinos are generated with the `NEUTRINO-GENERATOR` program, a port of the `ANIS` code [97]. `NEUTRINO-GENERATOR` is used to distribute neutrinos with a power-law spectrum uniformly over the entire

sky and propagate them through the earth and ice. The simulated neutrino-nucleon interactions take cross sections from CTEQ5 [98]. The Earth's density profile is modeled with the Preliminary Reference Earth Model [99]. The propagation code takes into account absorption, scattering, and neutral-current regeneration.

Each generated neutrino is given an interaction vertex in or near the detector volume and a probabilistic weight for this interaction. This weight can then be manipulated further through multiplication by a model energy spectrum, e.g. E^{-2} for the optimization of this analysis. For the atmospheric neutrino background, the Honda et al. spectrum [100] is applied. For electromagnetic and hadronic showers greater than 1 TeV, the longitudinal profile of the Cherenkov light output is taken into account. Muons from cosmic-ray air showers, using the `CORSIKA` simulation package [101], and ν_μ interactions are traced through the Antarctic ice and bedrock incorporating continuous and stochastic energy losses [96]. The PMT detection of Cherenkov light from showers and muon tracks is simulated using ice and dust layer properties determined in detailed studies and simulations [102] [103]. Finally, the DOM triggering and signal is simulated from the aforementioned interactions.

4.2 Reconstruction Methods

The reconstruction methods described below identify physical parameters that can be used to classify events. The neutrino-induced cascades for which this analysis searches exhibit different values for these physical parameters compared to muon-induced tracks. Thus, these reconstructed features are used to identify potential

astrophysical neutrinos in Chapter 5 in order to then test the hypothesis that GRBs emit these particles in Chapter 6.

4.2.1 Tensor of Inertia

The tensor of inertia algorithm [104] involves an analytic calculation of a "center of mass", where the mass terms correspond to the number of photoelectrons (PMT amplitude) a recorded by each DOM at position $\overrightarrow{r}$ with respect to the center of the detector:

$$\overrightarrow{R}_{com} = \sum_{i=1}^{N_{hitDOMs}} (a_i) \cdot \overrightarrow{r}_i \tag{4.1}$$

The inertia tensor is calculated using the PMT amplitudes and DOM positions $\left\{ \overrightarrow{x}_i = \overrightarrow{r}_i - \overrightarrow{R}_{com} \right\}$ with respect to the center of mass:

$$I^{j,k} = \sum_{i}^{N_{hitDOMs}} a_i \cdot (\delta^{k,j} |\overrightarrow{x}_i|^2 - x_i^j x_i^k) \tag{4.2}$$

where x_i^l refers to the $\hat{x}$, $\hat{y}$, or $\hat{z}$ component of the i'th DOM position.

Furthering the rigid body analogy, the smallest eigenvalue corresponds to rotation about the longest principal axis. This axis provides a reasonable guess for muon track trajectory. The direction of the primary particle is inferred from the direction in which the average DOM hit time is latest. An electromagnetic or hadronic cascade yields nearly equal eigenvalues.

4.2.2 LineFit

The line-fit algorithm [104] is an analytic calculation that approximates a charged particle producing Cherenkov light as a planar wavefront traveling with some constant velocity through the ice. Given the position $\overrightarrow{r}_i$ and leading pulse time t_i of each hit DOM in an event, the best-fit track and velocity of the particle are calculated.

This calculation entails minimizing a function of residuals:

$$\min_{t_0, \overrightarrow{x}_0, \overrightarrow{v}} \sum_{i=1}^{N_{hitDOMs}} \rho_i(t_0, \overrightarrow{x}_0, \overrightarrow{v})^2 \tag{4.3}$$

where

$$\rho_i(t_0, \overrightarrow{x}_0, \overrightarrow{v}) = |\overrightarrow{x}_i - \overrightarrow{x}_0 - \overrightarrow{v}(t_i - t_0)| \tag{4.4}$$

for the reconstructed track passing through a point $\overrightarrow{x}_0$ at time t_0 with velocity $\overrightarrow{v}$. Solving this minimization gives

$$\overrightarrow{r}_0 = \langle \overrightarrow{r}_i \rangle - \overrightarrow{v} \cdot \langle t_i \rangle \tag{4.5}$$

and

$$\overrightarrow{v} = \frac{\langle \overrightarrow{r}_i \cdot t_i \rangle - \langle \overrightarrow{r}_i \rangle \cdot \langle t_i \rangle}{\langle t_i^2 \rangle - \langle t_i \rangle^2} \tag{4.6}$$

where the angle brackets denote an average over all hit DOMs, e.g.

$$\langle \overrightarrow{r}_i \rangle \equiv \frac{1}{N_{hitDOMs}} \sum_{i=1}^{N_{hitDOMS}} \overrightarrow{r}_i \tag{4.7}$$

This algorithm was improved recently [105] to (1) filter and discard late-arriving hits that occur over 778ns later than any other hits within a 156 m radius and (2) perform a Huber fit [106] that penalizes potential outlier hits over 153 m from the source before performing the above least-squares fit with the outlier hits removed. The parameters in (1) and (2) were optimized using simulated muons. These improvements effectively discard hits from scattering in the ice and noise that degraded the quality of the initial result.

While this fast algorithm is tuned to track-like events, the calculated speed of the assumed track often provides a good indicator for spherical showers. Low speeds correspond to spherical events, while near-speed-of-light speeds correspond to minimally ionizing muon tracks.

4.2.3 CascadeLlh

CascadeLlh is a likelihood-based reconstruction of the time, vertex position, and energy of a neutrino interacting in the ice, assuming a neutrino-induced cascade hypothesis. The likelihood problem to solve is as follows: What is the set of cascade parameters $\overrightarrow{a} = \{a_1, a_2, ..., a_m\}$ that maximizes the likelihood function

$$\mathcal{L}(\{\overrightarrow{x}\}\,|\,\overrightarrow{a}) = \prod_{i=1}^{n} p(\overrightarrow{x_i}; \overrightarrow{a}) \tag{4.8}$$

for given sets of observables $\{\overrightarrow{x}\} = \{\overrightarrow{x_1}, \overrightarrow{x_2}, ..., \overrightarrow{x_n}\}$ of an event? Maximizing $\mathcal{L}$ for the set of hit DOMs of an event lets one solve for the time, vertex position, direction, and energy ($\overrightarrow{a} = \{t, x, y, z, \theta, \phi, E\}$) of the hypothesized cascade-inducing neutrino.

No probability distribution functions (PDFs) describing directionality or energy are used for this reconstruction in this analysis and so the angles θ and ϕ and the energy are fixed to the values taken from their seeds, which are described below.

For this reconstruction, the event observable $\overrightarrow{x_i} = \{t_i, x_i, y_i, z_i\}$ are the time corresponding to the leading edge of the waveform and the position of the i'th hit DOM. Specifically, the $\overrightarrow{x_i}$ for each DOM's PDF is parametrized in terms of the *time residual*:

$$t_{res} \equiv t_i - t_{direct} = t_i - \left(t_v + \frac{|\overrightarrow{r}_i - \overrightarrow{r}_v|}{c_{ice}} \right) \tag{4.9}$$

where t_v and $\overrightarrow{r}_v$ are the interaction vertex time and position. t_{res} does peak near zero for DOMs close to the vertex, but is often positive especially for farther DOMs since photons often experience scattering in the ice, as discussed in Section 4.1. t_{res} can also be negative due to PMT jitter [85] and random dark noise hits. The vertex position is seeded by the center of mass $\overrightarrow{R}_{com}$ calculated in Equation 4.1. The seed vertex time is determined by the following steps: (1) pick one hit DOM and calculate a trial vertex time $\left(t_{hit} - \frac{|\overrightarrow{r}_i - \overrightarrow{R}_{COM}|}{c_{ice}} \right)$; (2) calculate t_{res} for all other hit DOMs using the trial vertex; (3) repeat steps (1) and (2) for all hit DOMs; and (4) choose the seed vertex time as the earliest trial t_v such that there are greater than 4 "direct hits" in which $0 \leq t_{res} \leq 200$ ns.

Thus, $p(t_{res,i}|\overrightarrow{a})$ gives the probability of measuring a single photoelectron generated in a cascade with parameters $\overrightarrow{a}$ at a given DOM i. This probability can be calculated by using photon hit probability and arrival time distribution look-up tables. However, as noted in [104], an analytic function can be calculated for this

probability much more quickly than using the archived tables and with good results. This analytic function that parametrizes $p(t_{res,i}|\overrightarrow{a})$ as a function of the distance d from the cascade vertex is named the "Pandel function" after the researcher who derived it in an analysis of laser light signals in the BAIKAL experiment. This function is expressed as follows:

$$p(t_{res}|d) \equiv \frac{1}{N(d)} \frac{\tau^{-(d/\lambda)} t_{res}^{(d/\lambda-1)}}{\Gamma(d/\lambda)} \times \mathrm{e}^{-\left(t_{res}\left(\frac{1}{\tau}+\frac{c_{ice}}{\lambda_a}\right)+\frac{d}{\lambda_a}\right)} \tag{4.10}$$

where the normalization factor

$$N(d) = \mathrm{e}^{-d/\lambda_a} \left(1 + \frac{\tau c_{ice}}{\lambda_a}\right)^{-d/\lambda} \tag{4.11}$$

and the speed of light in ice $c_{ice} = \frac{c_{vac}}{1.31}$ and the absorption length $\lambda_a = 98.0$ m. There are also two empirically determined free parameters used for this likelihood reconstruction $\tau = 450.0$ ns $\lambda = 47.0$ m [107].

Further, $p(t_{res}|d)$ is modified in order to more accurately describe the detector. First, negative values of t_{res} are accommodated to account for the DOMs' imperfect timing resolution with a half Gaussian function in this regime. Mean $\mu = 0$ ns and $\sigma_{jitter} = 15$ ns are chosen for this Gaussian because $10 \leq \sigma_{jitter} \leq 20$ ns yield the best reconstruction results. The original Pandel function is used for $t_{res} > \sqrt{2\pi}\sigma_{jitter}$ and a spline interpolation to connect these two domains. Second, a small flat probability of 10^{-10} is added to the function to account for noise hits. This modifed Pandel function is refered to as the UPandel, which as the form:

$$p_U(d, t_{res}) = \begin{cases} p_1 & \text{for } t_{res} < 0; \\ p_2 & \text{for } 0 \leq t_{res} < \sqrt{2\pi}\sigma_{jitter}; \\ p_3 & \text{for } \sqrt{2\pi}\sigma_{jitter} \leq t_{res}. \end{cases} \tag{4.12}$$

where the functions p_1, p_2, p_3 are:

$$p_1 = A \frac{1}{\sqrt{2\,\pi}\,\sigma_{jitter}} \exp(-t_{res}^2/2\sigma_{jitter}^2) \ , \tag{4.13}$$

$$p_2 = c_0 + c_1 t_{res} + c_2 t_{res}^2 + c_3 t_{res}^3 \tag{4.14}$$

and

$$p_3 = p(t_{res}|a) \tag{4.15}$$

The parameters A, c_0, c_1, c_2, and c_3 are determined by requiring that the UPandel function is continuous and differentiable at $t_{res} = 0$ and $t_{res} = \sqrt{2\pi}\sigma_{jitter}$, the slope is zero at $t_{res} = 0$, and the integral over time from $t_{res} = -\infty$ to $t_{res} = \infty$ equals 1. Therefore, the final likelihood to maximize for this reconstruction is:

$$\mathcal{L}(\{\overrightarrow{x}\}\,|\,\overrightarrow{a}) = \prod_{i=1}^{n} p_U(\overrightarrow{x_i}; \overrightarrow{a}) \tag{4.16}$$

Using a minimization software package [108], the likelihood function is maximized by minimizing $-\log(\mathcal{L})$ with respect to the parameters $\overrightarrow{a}$. In order to aid the minimizer and improve reconstruction performance, this reconstruction is seeded with a first guess interaction vertex, interaction time, and energy The seed vertex is the center of mass calculation in Equation 4.1. The seed vertex time is the earliest

time such that there are greater than 4 direct hits on DOMs within 100 m of the vertex. A direct hit for this calculation is defined as a DOM hit with a time residual less than 200 ns For a DOM at location $\overrightarrow{r}_i$ hit at time t_i, this time residual is defined as the difference between an unscattered-light trial vertex time $\left(t_i - \frac{|\overrightarrow{r}_i - \overrightarrow{R}_{COM}|}{c_{ice}}\right)$ and the interaction vertex time.

4.2.4 SPE

The single photoelectron or SPE fit is a maximum likelihood fit based on a muon track hypothesis [104]. A likelihood function is maximized, expressed by Equation 4.8, the same way as described for CascadeVertexLlh above. The likelihood function used for this reconstruction is the modified Pandel function of Equation 4.12 as well. The empirically determined free parameters of the Pandel function take the values $\tau = 557.0$ ns and $\lambda = 33.3$ m. These parameters have different values for track and cascade hypotheses because The time residual for this reconstruction is

$$t_{res} = t_i - t_{geo} = t_i - \left(t_0 + \frac{\hat{\mathbf{p}} \cdot (\mathbf{r}_i - \mathbf{r}_0) + d \tan \theta_c}{c_{vac}}\right) \tag{4.17}$$

The geometry in figure 4.1 illustrates the time residual calculation. In this reconstruction, an arbitrary vertex position is chosen and a time along the track is specified by the direction $\hat{p}$. This reconstruction is seeded with the results of the line-fit algorithm. Although this reconstruction is primarily used for track directions, it is useful in this analysis in its ability to sift out track-like topologies in the muon background. The SPE reconstruction values after four iterations are used in this

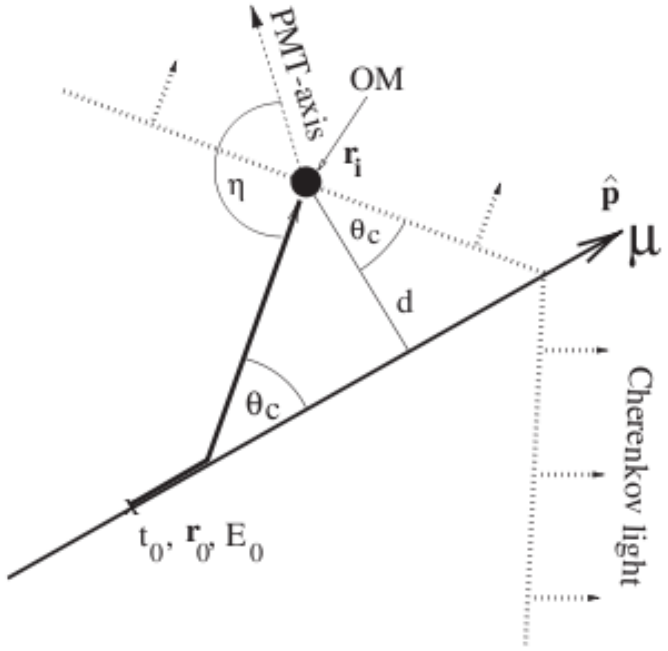

Figure 4.1: Schematic of Cherenkov light front interacting with an optical module (OM) in the ice

analysis.

4.2.5 Analytic Energy Reconstruction - ACER

For a fast analytic dedicated energy reconstruction [109] for cascades, a Poissonian distribution for the total number of detected photons by a DOM from a point-like source is taken. The likelihood function then for a given energy E, observed number of photoelectrons k, and expectation λ:

$$\mathcal{L}(E) = \prod_{i=1}^{N_{DOMs}} \frac{\lambda_i(E)^{k_i}}{k_i!} \mathrm{e}^{-\lambda_i(E)} \tag{4.18}$$

An expected number of photoelectrons in a DOM from a shower event is defined with some reference energy (1 GeV here) as Λ. Λ is an amplitude that corresponds to the amount of photoelectrons that reach the PMT. The expectation λ can then be expressed as $(E/(1\text{GeV})\Lambda = E_1\Lambda$ due to the linear relationship between Cherenkov light emission and deposited energy..

After first taking the log of $\mathcal{L}$, this likelihood is maximized with respect to energy:

$$0 = \frac{\partial \mathcal{L}(\mathcal{E})}{\partial E} = \frac{\partial}{\partial E} \sum_{i=1}^{N_{DOMs}} (k_i \log(E_1\Lambda_i) - (E_1\Lambda_i) - \log(k_i!)) \tag{4.19a}$$

$$= \sum_{i=1}^{N_{DOMs}} (\frac{k_i\Lambda_i}{E_1\Lambda_i} - \Lambda_i) \tag{4.19b}$$

$$= \sum_{i=1}^{N_{DOMs}} \frac{k_i}{E_1} - \sum_{i=1}^{N_{DOMs}} \Lambda_i \tag{4.19c}$$

and therefore

$$E = 1\text{GeV} \times \frac{\sum k_i}{\sum \Lambda_i} \tag{4.20}$$

An intuitive energy calculation is left. The total energy deposited by a neutrino-induced electromagnetic cascade is the number of photoelectrons recorded divided by the number of photoelectrons expected by a 1 GeV neutrino, times 1 GeV.

The template function, Λ, used to calculate the expected number of photoelectrons from a reference point source is evaluated with tabulated Monte Carlo simulation of light propagation through the ice [85, 110, 111]. The energy reconstruction described in this section was developed for the first cascade analysis in IceCube designed to detect atmospheric neutrino interactions [112], and so is named

AtmCscdEnergyReco, and hereafter referred to as ACER. The primary purpose of ACER in this analysis is to provide an energy to the following more computationally intensive cascade-hypothesis reconstruction.

4.2.6 Credo

Once the filtered data is transmitted beyond the South Pole via satellite, more computationally expensive likelihood-based reconstructions are calculated. The first of these reconstructions is performed over the complete seven parameter (E, t, x, y, z, θ, ϕ) cascade. This reconstruction was developed for prior atmospheric cascade searches is called Credo [113, 114]. The detection of light follows a Poisson distribution and thus the likelihood function to maximize is

$$\mathcal{L}(k|E,t,x,y,z,\theta,\phi) = \prod_{i=1}^{N_{DOM}} \frac{\lambda_i^{k_i}}{k_i!} \mathrm{e}^{-\lambda_i} \tag{4.21}$$

for the observed and expected number of photoelectrons k and λ in each DOM from a neutrino traveling in direction θ,ϕ and depositing energy E at time t and vertex (x, y, z) [109].

Due to the linear relationship between Cherenkov light emission and deposited energy the energy is still estimated by comparing to a template event of 1 GeV. The seed is composed of different prior reconstructions: the tensor-of-inertia direction, CascadeLlh interaction vertex and time, and ACER energy. Given the shower vertex and orientation, and the same ice model-dependent tables of photon amplitudes and time delays used with ACER, the negative log-likelihood is minimized using

MINUIT [115] and the best-fit particle parameters are extracted.

4.2.7 Monopod

Another likelihood-based algorithm is run with the Credo results used as the seed. This reconstruction is called Monopod, and is the the single source specialization of the general Millipede likelihood [109] which considers multiple light sources, e.g. for stochastic muon losses along a path through the detector. Because the signal of this search is defined to be neutrino-induced showers, and showers act as point-like light sources at all energy scales in IceCube [116], only the single source hypothesis is necessary.

The likelihood function is the same Equation 4.21 above, but spline-fit tables of photon amplitudes and time delays are used instead of coarse photon tables. Additionally, unlike the above reconstructions, an explicit noise rate input (450 Hz used for ACER and Credo) is not required as Monopod handles noise on its own, reading in the hardware calibration from each simulation or data run. The minimization is iterated five times to achieve $\sim 30^{\circ}$ angular resolution, which, with three flavor acceptance, allows for sensitivities comparable to previous ν_{μ} track-optimized GRB neutrino flux searches. Consequently, the five-iteration Monopod reconstructed direction and energy are used for each event in the likelihood analysis detailed in Chapter 6.

The angular resolution capabilities for the different reconstruction techniques described in this chapter are shown in Figure 4.2 for simulated astrophysical ν_e at

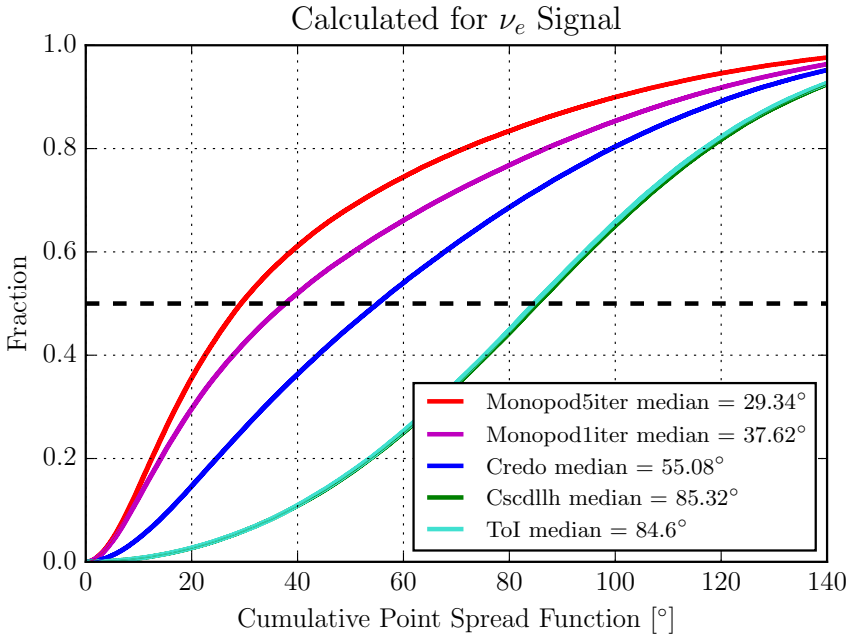

Figure 4.2: Cumulative point spread functions with median angular resolutions shown for different reconstructions of simulated astrophysical ν_e at final event selection.

final event selection. This figure shows the cumulative point spread function, where each y-axis value is the percentage of events that yield less than or equal to the corresponding angular difference between truth and reconstruction on the x-axis. Five iterations of Monopod clearly achieves the best directional reconstruction of the set.

4.2.8 Cramer-Rao

A lower bound on the error in the reconstructed directions is estimated by the Cramer-Rao relation [117–119] between the covariance of each fit parameter $\mathrm{cov}(a_m, a_n)$ and the inverted Fisher information matrix $J(\overrightarrow{a})$. For the unbinned likelihood analysis, detailed in Chapter 6, five iterations of the Monopod reconstruc-

tion is used for the estimated direction of each event. Thus, the Fisher information matrix is given by

$$J_{m,n}(\overrightarrow{a}) = -\left\langle \frac{\partial^2 \ln \mathcal{L}(\overrightarrow{a})}{\partial a_m \partial a_n} \right\rangle \tag{4.22}$$

where $\mathcal{L}$ and $\overrightarrow{a}$ are the likelihood and fit parameters of the five iterations Monopod reconstruction and only hit DOMs are considered.

Because the Cramer-Rao bound is used in this analysis for estimating the error in the direction, the variances of the zenith $\sigma_\theta = \sqrt{(J^{-1})_{\theta\theta}}$ and azimuth $\sigma_\theta = \sqrt{(J^{-1})_{\theta\theta}}$ are taken. Finally, the circularized per-event error is calculated as follows:

$$\sigma_{CR} = \frac{1}{\sqrt{2}} \sqrt{\sigma_\theta^2 + \sigma_\phi^2 \sin^2(\theta_{\text{Monopod5}})} \tag{4.23}$$

Chapter 5

Event Selection

The signal in this search is one or more high energy neutrino-induced showers coincident in space and time with one or more GRBs. Before one can analyze the likelihood that an event is a GRB-emitted neutrino, one must reduce the over 2.5 kHz triggered data that is dominated by cosmic ray air shower muons to a much smaller 0.2 mHz selection of possible signal. The geometric pattern, timing, and amount of recorded photons are used to reconstruct the time, location, direction, and energy of interacting neutrinos and muons, remove background, and realize the final sample of signal-like events.

Searches for neutrino-induced showers from astrophysical and atmospheric sources have been conducted previously in IceCube [112, 120–122]. The predominant difference between these and the search presented in this paper is that this search assumes neutrinos come from known transient sources. The previous shower-like event selections assume a diffuse signal or constantly emitting sources and, as a result, require much more stringent background reduction that leads to data rates nearly a factor of 100 smaller than what is needed in this search. Cascade containment constraints in the detector were imposed to reach these low backgrounds, which are achieved in this search by the effective cuts in time and space around each GRB in the unbinned likelihood analysis presented in the next chapter.

5.1 Level 1: Trigger at South Pole

This analysis starts with the SMT8 trigger requirement of 8 local coincidences of DOM neighbors or next-to-nearest neighbors within 5 μs. As described in Section 3.1.1.5, the time windows of other signal-specific triggers that overlap with this 5 μs are included as well. Finally, the waveforms of all hits recorded within -4 μs and +6 μs of the global trigger window are combined into an "event."

Under this triggering system, IceCube assembles events at a rate of over 2.5 kHz. Most of these events are muons produced in air showers from cosmic rays bombarding the atmosphere. The task of the following event selection stages is to reduce this dominating background to a sample of events that could be astrophysical neutrinos. The final sample does not need to achieve near 100% neutrino purity because further discrimination is achieved through the unbinned likelihood probability distribution functions, detailed in Chapter 6.

5.2 Level 2: Cascade Event Filter at South Pole

The first class of background to remove is track-like events generated by muons losing their energy through continuous ionization processes. This background of muon tracks is relatively easily separated from the shower-like neutrino signal by use of a filter run online at the computer farm located above the buried detector. During the 79-string configuration, two analytic reconstructions described in Section 4.2 are used to select events with spherical DOM hit topology, indicative of electromagnetic or hadronic neutrino-induced showers. The CascadeLlh reconstruction is used for

the slightly more sophisticated 86-string filter. Both filters reduce the data rate to around 30 Hz, which is still comprised almost entirely of atmospheric muons that shower through stochastic processes.

The two calculated parameters used for this initial selection in IC79 are the tensor-of-inertia eigenvalue ratio and line-fit absolute speed. Using the rigid body analogy, a spherical shower should provide nearly even tensor-of-inertia eigenvalues, while an elongated track should have one eigenvalue much smaller than the other two. Additionally from line-fit, showers typically provide slower best-fit planar wavefront speeds than the near speed of light fit tracks.

The online cascade filter for the first two years of the 86-string configuration imposes SPE reconstructed zenith-dependent cuts to allow more events with energies below 10 TeV. A cut on the reduced log-likelihood value from CascadeLlh is implemented to remove many of the muons misreconstructed as upgoing. The down-going region, which has a greater number of events than the up-going region, requires a harder reduced log-likelihood cut in combination with the same online 79-string filter selection from above.

The cut parameters for the IC79 cascade filter are as follows:

1. **evalratio** > 0.05
2. **linefit-speed** < 0.10 m/ns

The cut parameters for the IC86I and IC86II cascade filters are as follows:

1. Up-going ($\mathbf{\cos\left(\theta_{zen}\right)} < 0.20$):

(a) **cscdllh-rlogl** < 11.75

2. Down-going ($\mathbf{\cos(\theta_{zen})} \geq 0.20$):

   (a) **cscdllh-rlogl** < 9.50

   (b) **evalratio** > 0.10

   (c) **linefit-speed** < 0.12 m/ns

Below are the E^{-2}-weighted ν_e signal efficiencies with respect to the SMT8 trigger per energy bin for the 79-string (left) and 86-string (right) detector cascade event filter selections. The Monte-Carlo truth ν_e energy distributions at trigger and filter levels are also shown. Both energy distributions peak at about 10 TeV and the Glashow Resonance, described in Section 3.2.1, at 6.3 PeV is apparent as well.

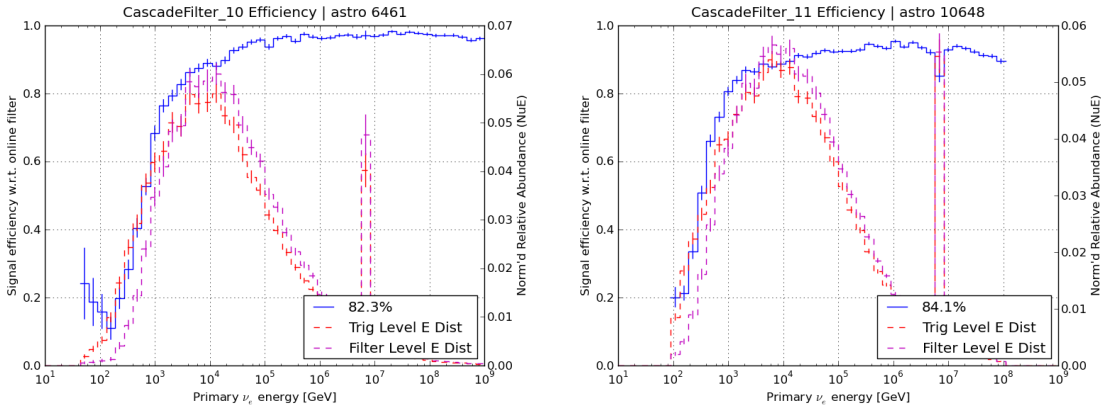

Figure 5.1: Left axis: IC79 (left) and IC86I (right) Cascade Filter E^{-2}-weighted ν_e signal efficiency with respect to the SMT8 trigger per energy bin. Right axis: Monte-Carlo truth ν_e energy distributions at trigger-level and filter-level. The IC86II (left) Cascade Filter selection is equivalent to the IC86I selection.

5.3 Level 3

Upon transmission via satellite from the South Pole, the ∼30 Hz filtered data of spherically shaped events can be further reduced to about 1 Hz using cuts developed visually from background and signal distributions. The background at this Level 3 is still dominated by atmospheric muons that lose their energy through bremsstrahlung, photonuclear interactions, and pair production, but allows for sensible performance with the BDT forest algorithm described in Section 5.4.4. These stochastic energy loss mechanisms in muons create nearly spherical hit patterns that are difficult to differentiate with the neutrino-induced shower signal when the muon track is at the edge or outside of the detector and therefore not observed. Even though the background muons after the online filter selection are shower-like in topology, the Cherenkov light hit patterns of the minimally ionizing muon track are exploited when possible to differentiate from neutrino-produced electromagnetic or hadronic showers.

The discrimination variables at this level are derived from the more CPU-intensive reconstructions run offline. The cut values were optimized on IC79 data by a colleague for the collaboration with the aim of providing a sub-1 Hz shower-like data sample on which to develop more sophisticated neutrino-level event selections. This analysis takes advantage of this sample's separation of stochastic energy-loss muons from high energy neutrinos for eventual machine-learning input. A different Level 3 event selection was developed using IC86I data, but sacrificed signal efficiency for higher neutrino purity, needed by diffuse astrophysical neutrino flux

searches. This stricter selection reduced this search's sensitivity because high purity is achieved in this search by using the transient nature of the hypothesized GRB signal. As a result, the IC79-optimized Level 3 event selection is used on all three seasons of this search, with slight alterations in IC86I and IC86II.

The further separation of signal from muon track background is achieved through two levels of cuts using the fast track hypothesis, SPE, and cascade hypothesis, CascadeLlh, analytic likelihood function reconstructions. The first Level 3 cut is on events for which the logarithm of the ratio of the track likelihood to the cascade likelihood heavily favors the track hypothesis. Two other background muon features that are taken advantage of are their down-going directions and typically lower energies. Consequently, the track likelihood reconstructed zenith is parametrized in terms of the ACER reconstructed energy, removing low energy down-going events from the sample. Events imparting at least 10 TeV are kept regardless of their likelihood ratios and reconstructed zeniths. This first selection stage of Level 3 reduces the 30 Hz Level 2 online filter rate to around 5 Hz. The distributions of 79-string data and simulated astrophysical and atmospheric ν_e for each selection variable are shown with the respective cut values in Figures 5.2 and 5.3. The 86-string data and simulation distributions are similar to those of IC79.

Lastly at this level, signal-like events that exhibit a large fraction of hit DOMs inside of a sphere centered on the reconstructed vertex with a radius determined by the mean hit distance are selected. This calculation is referred to as the fill-ratio, and the radius and fraction filled of the sphere are optimized separately for reconstructed vertices inside and outside of the instrumented volume. Both volume regions are

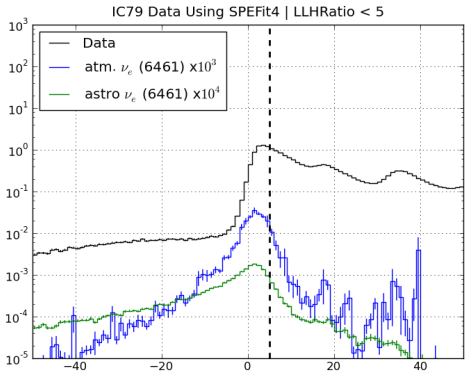

Figure 5.2: Track-to-cascade likelihood ratio distribution at Level 2 for background muon-dominated data, atmospheric ν_e, and astrophysical ν_e. Level 3 events are kept to the left of the vertical line.

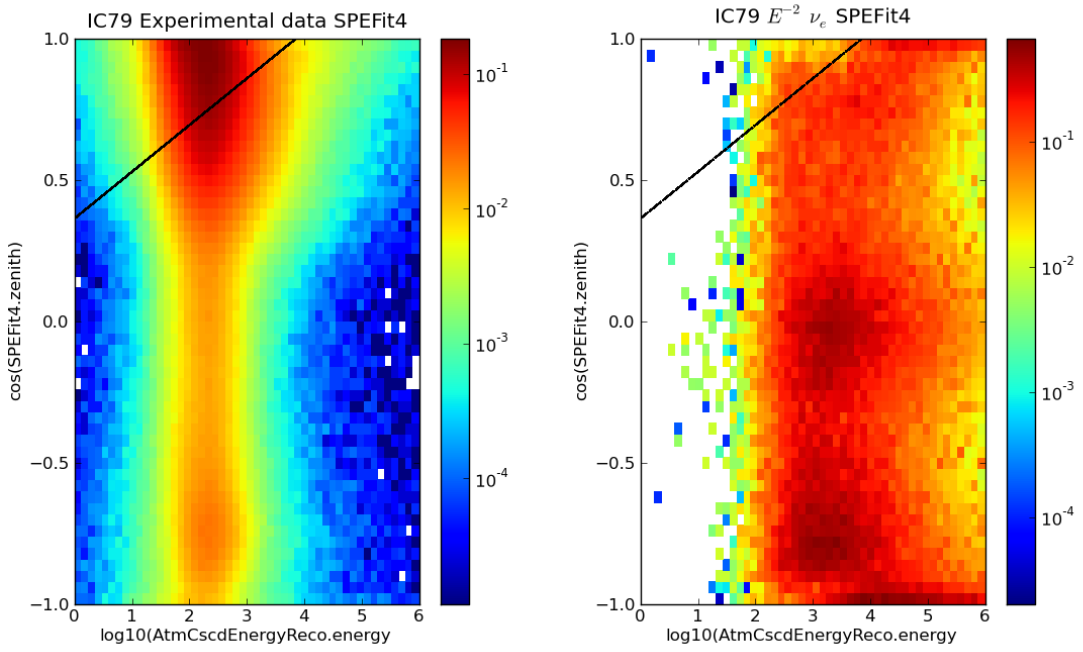

Figure 5.3: Cosine of SPE zenith versus ACER energy distribution at L2 for background muon-dominated data (left) and astrophysical ν_e (right). Level 3 events are kept below the parametrized line.

incorporated in this search. This second stage of cuts yields a combined contained and uncontained data rate of about .7 Hz. The distributions of 79-string data and simulated astrophysical and atmospheric ν_e for both the contained and uncontained fill-ratio are shown with the respective cut values in Figure 5.4. As with the previous selection variable distributions above, the 86-string detector distributions are similar.

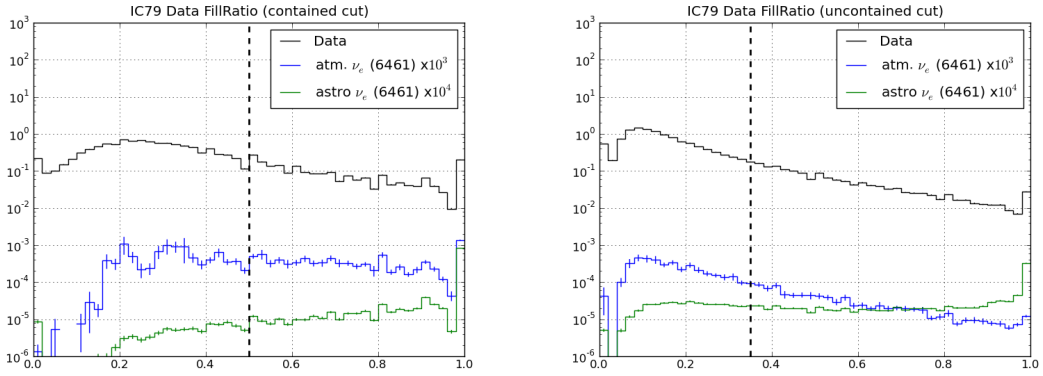

Figure 5.4: Fill-ratio distributions at Level 2 for the contained (left) and uncontained (right) branches for background muon-dominated data, atmospheric ν_e, and astrophysical ν_e. Level 3 events are kept to the right of the vertical line.

The cut parameters for the Level 3 event selection are given below. The track-to-cascade likelihood ratio and uncontained fill-ratio cut values were loosened slightly for the IC86I and IC86II data compared to IC79 in order to achieve similar signal rates. The 86-string detector cut values are in parentheses.

1. Stage 1:

   (a) **track-cscd-llhratio** < 5 (6)

   (b) **cos (SPE.zenith)** $< \theta_{\text{param}} \equiv 0.36 + 0.16 \log 10(E_{\text{ACER}}/\text{GeV})$

2. Stage 2:

   (a) **fill-ratio, contained events** > 0.50

   (b) **fill-ratio, uncontained events** > 0.35 (0.30)

Figure 5.5 shows the IC79, IC86I, IC86II E^{-2}-weighted ν_e efficiencies per energy bin for Level 3 and each of its stages, detailed above. The relatively lower percentage of 86-string signal kept from the Level 2 filter at 10 TeV and lower energies compared to 79-string signal is attributed to the relatively higher amount of signal kept at these energies at Level 2. The different data rates in the figures from those in Table 5.1 are due to the fact that these rates are calculated from one eight-hour data-taking run for each season, and rates can vary by a few percent.

5.4 Final Event Selection

After the data rate is reduced to below 1 Hz, the final event selection employs a machine learning algorithm to optimize the signal-background separation over a many parameter space. At the Level 3 data rate, stochastic muon losses with little or no tail in and around the detector volume still dominate the data and strongly resemble neutrinos. The problem of separating these two types of events is ideal for a supervised machine learning classification algorithm.

Generally, supervised learning involves constructing a statistical model for predicting an output based on one or more inputs [123]. In this case, the inputs are muon-dominated data background events and simulated neutrino signal events. Each event input includes its background / signal classification, which the statistical

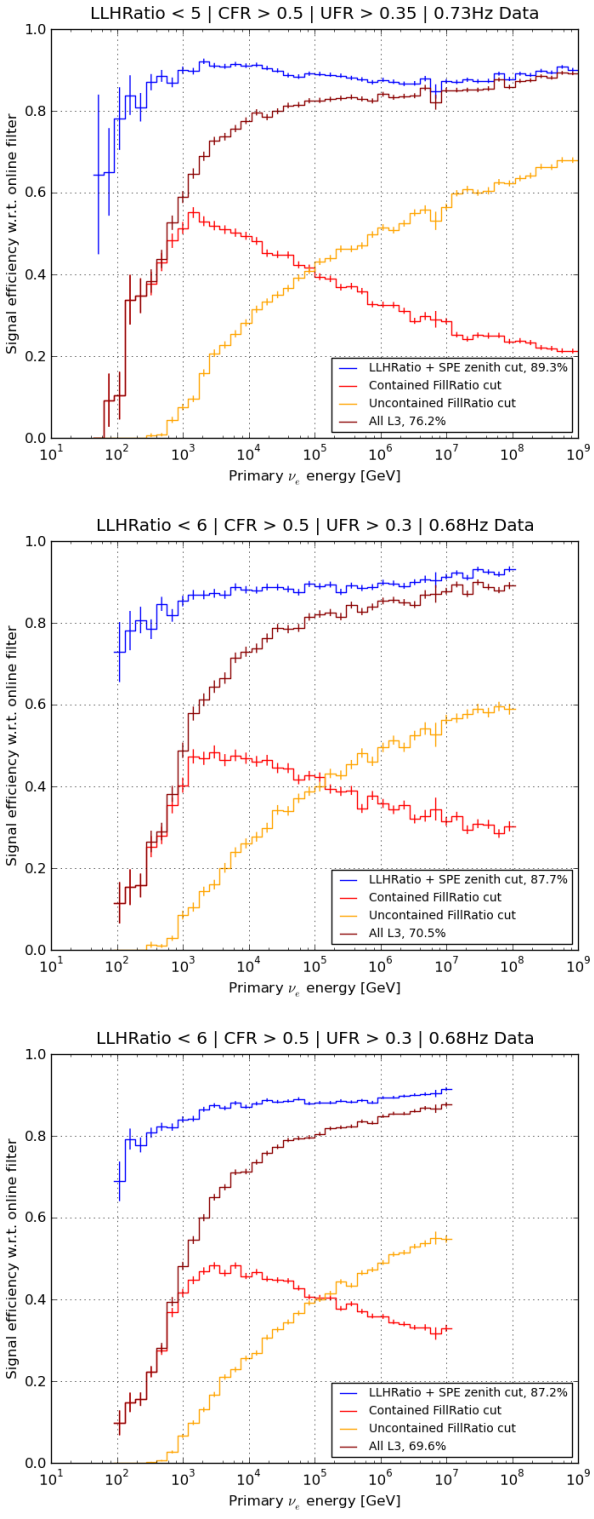

Figure 5.5: Components of Level 3 ν_e signal efficiency with respect to the Level 2 Cascade Filter per energy bin for IC79 (top), IC86I (middle), IC86II (bottom). The magenta line is the total Level 3 efficiency curve.

model aims to predict, as well as values for discriminator variables, which the model uses to predict the classification. In such a problem, the inputs are separated into training and testing sets. The training set is used to develop the model while the testing set is used to ensure the model is not overly fit to peculiarities in the training set [123]. The model is designed to separate the signal and background events in the multivariate space as much as possible. The model implemented in this analysis assigns a score that denotes whether a particular event is background muon-like or signal neutrino-like.

The algorithm used to create this statistical model is a boosted decision tree forest (BDT) [124], that also has been used in Northern Hemisphere ν_μ track GRB coincidence searches in IceCube [16, 17]. The forest takes as input a collection of signal and background discrimination variables, many of which were influenced by past neutrino-induced shower searches conducted in IceCube. A separate BDT is trained with configuration-specific signal simulation and background data for each of the three year-long detector configurations of this search. The BDT software used for this work is a Python-based package written by a colleague and is now the standard tool for machine-learning-based classification in the IceCube collaboration [125].

5.4.1 Machine Learning: Boosted Decision Tree Forests

The BDT machine learning algorithm used in this search for astrophysical neutrino-induced cascades involves a collection of sequentially trained classifiers, or a "forest of trees." The training begins with designated signal events and designated

background events. The signal used for this analysis is a flux of simulated ν_e events with an E^{-2}-weighted spectrum distributed evenly over the sky. The background is a collection of events from IceCube data that did not occur within two hours of any reported GRB γ emission to prevent bias. These off-time data events were chosen as background because, as shown in Section 5.3, the atmospheric muon rate still dominates any presence of astrophysical neutrinos at the 1 Hz level.

The algorithm takes as input a collection of signal and background discrimination variables, described in Section 5.4.2. A tree begins with a root node. The discrimination variable values for signal and background events are each histogrammed with a user-defined bin size at this node. The cut choice at a variable bin boundary that best separates the signal and background events into child nodes is determined. The best separation can be defined different ways using the signal purity of the child nodes.

For this analysis, the Gini separation criterion is used to judge cut effectiveness at a tree node. Let the weight of a simulated signal event s, discussed in Section 4.1, be defined as w_s; and let the weight of a background off-time data event b, which is the background rate at pre-BDT event selection, be defined as w_b; and let the sum of all signal and background event rates at a given node be defined as

$$\sum_s w_s + \sum_b w_b = W \tag{5.1}$$

The Gini separation criterion is defined as

$$S_{Gini}(p) = p \cdot (1 - p) \tag{5.2}$$

where

$$p = \frac{\sum_s w_s}{W}, (1 - p) = \frac{\sum_b w_b}{W} \tag{5.3}$$

are the signal and background purity of a given node, respectively. Thus, a purely signal or purely background node has a S_{Gini} of 0.

At each node the algorithm chooses the cut on a variable bin boundary that maximizes the signal-background separation into its child nodes. The separation gain from the parent node to the child nodes L and R is calculated as follows:

$$\Delta S = W \cdot S_{Gini}(p) - (W_L \cdot S_{Gini}(p_L) + W_R \cdot S_{Gini}(p_R)) \tag{5.4}$$

This procedure is repeated for the child nodes, their children, and so on until one of several user-defined stopping criteria is fulfilled. The stopping criteria defined for this analysis are a S_{Gini} of 0 in a node or a maximum depth of five levels of nodes. The final classifying nodes in a tree are called "leaves." If $p_{leaf} > 0.5$, all events in that leaf are classified as signal and given a value of 1. If $p_{leaf} < 0.5$, all events in that leaf are classified as background and given a value of -1.

The BDT algorithm consists of a forest of trees trained sequentially. After the growth of one tree ends, the classification performance of that tree is assessed, and incorrectly classified events are weighted more heavily so in effect "boosting"

the subsequent tree's performance. This analysis uses the AdaBoost, or "adaptive boosting," algorithm [124]. The event reweighting is calculated in the following way. For event i, define the true classification y_i that equals +1 for signal and -1 for background. Similarly, define the tree-scored classification s_i. Let the identity test function for each event in a tree be

$$I_t(y_i, s_i) = \begin{cases} 0, & y_i = s_i \\ 1, & \text{otherwise} \end{cases} \tag{5.5}$$

For each tree t, define the tree error as

$$e_t = \sum_i \frac{w_i I_t(y_i, s_i)}{W} \tag{5.6}$$

and the boost factor as

$$\alpha_t = \beta \ln\left(\frac{1 - e_t}{e_t}\right) \tag{5.7}$$

where β is the user-defined boost strength. Finally, the signal and background events are reweighted for tree $t + 1$ with the factor

$$w_i \to \mathrm{e}^{\alpha_t I_t(y_i, s_i)} w_i \tag{5.8}$$

The error e_t and boost α_t for each tree in the IC86I BDT are given in Figure 5.6. The boost factors correspond to the tree weight in the final scoring. Later trees that attempt to classify the toughest events have less weight than earlier trees.

The sum of all signal and background event weights are normalized to one

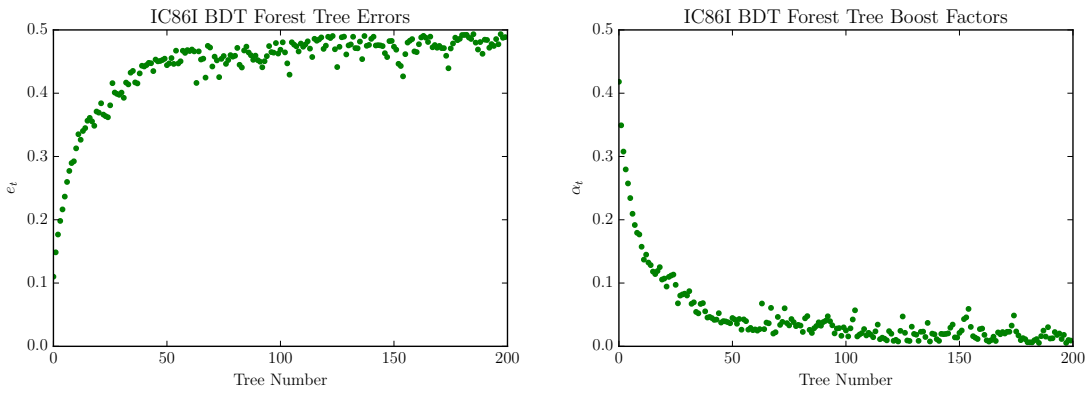

Figure 5.6: Per-tree errors (e_t, left) and boost factors (α_t, right) for the IC86I BDT.

before each tree is trained such that $\sum_u w_i = W = 1$. The boosting method outlined above is cumulative and forces exaggerated signal/background purity of nodes with previously misclassified events. This boosting consequently assists the maximization of ΔS for proper classification. The overall score of each event by the forest, s_i is an average of the individual tree classifications, $(s_i)_t$ weighted by the tree-specific boost factors, α_t:

$$s_i = \frac{\sum_t \alpha_t (s_i)_t}{\sum_t \alpha_t} \tag{5.9}$$

It is important to keep a set of signal and background events separate from the training set, but originally from the same distributions, in order to test the trained BDT model. Upon reaching sufficient signal/background separation, one may find that the BDT score distributions of the training and testing samples differ substantially. This difference would be due to overtraining. A model may be trained so precisely on a dataset, that statistical fluctuations and outlier characteristics in

those data are part of the model. As a result, data from the same distribution as the training set will be classified differently.

This type of overtraining that leads to disparity in the training and testing data BDT score distributions can be identified by a Kolmogorov-Smirnov (KS) test [126,127]. The KS test calculates the probability the null hypothesis - that two data samples are drawn from the same distribution - is rejected. The KS statistic $D_{n,m}$ is the maximum of the difference between the cumulative distribution functions of two data samples 1 and 2 of sizes n and m, respectively:

$$D_{n,m} = \left| F_n^1(s) - F_m^2(s) \right| \tag{5.10}$$

Given $D_{n,m}$ and the limiting cumulative distribution function $L(z)$ of $\sqrt{\frac{nm}{n+m}} D_{n,m}$, the null hypothesis is rejected at level z if

$$D_{n,m} > L(z) \sqrt{\frac{n+m}{nm}}. \tag{5.11}$$

Training for each BDT of the three detector configurations was tuned until the KS p-value was above 10% for each sample. The BDT score distributions of the training (solid lines) and testing (dashed lines) of the signal (blue) and background (red) data samples are shown below for an overtrained BDT and the final BDT for IC86I. The KS p-values (z above) are given in the legends of the figures.

In order to reduce overtraining, one may apply the process of pruning to each tree in the BDT forest. This process is called pruning because it involves removing

leaf nodes from a tree. Upon their removal, the respective parent nodes are then turned into leaves. Pruning is performed for each tree before the boost factor α_t is calculated and the succeeding tree is created.

A simple pruning procedure occurs automatically in the BDT algorithm and so is used for all three detector configuration BDTs. If a node cut creates two children signal leaves or two children background leaves, those leaves are removed and the parent node becomes a leaf. These pruned leaves would offer no further separation themselves and are expendable.

A slightly more involved pruning procedure is also used in the IC79 BDT training in order to maximize the KS p-value for both the signal and background samples. With this procedure, the cost of pruning is calculated at each parent node of leaf nodes. This pruning cost ρ is defined using ΔS of Equation 5.4:

$$\rho = \frac{\Delta S}{n_{subleaves}} \tag{5.12}$$

where $n_{subleaves}$ refers to the total number of leaves below this split node. This cost value quantifies the effect on the tree. The larger the separation gain and the greater number of subleaves, the larger the effect of pruning at that node.

This "cost-complexity" pruning algorithm creates a copy of the tree and prunes the copy, starting with the lowest ρ value node and continuing until the root node is reached. The pruning order and the percentage of the entire sequence is recorded for each pruned node. The percentage of the pruning sequence to be executed for all trees is specified by the user and is called the "pruning strength" in this text.

As seen above, there are several parameters one may tune to optimize BDT performance: (1) the number of trees **N-trees**, (2) the maximum depth of each tree **max-depth**, (3) the boosting strength $\boldsymbol{\beta}$, (4) the number of cuts to test for each variable at a node **N-cuts**, (5) and the pruning strength **prune-strength**. These parameters are listed below with descriptions and their values used in this work.

1. **N-trees** = 200 for each of the three seasons' BDTs

   More trees in the forest allow for more cumulative boosting and more classification trials of events. There are diminishing returns when increasing the size of the forest, however, due to the most signal-like background events continuing to be difficult to classify while exploring the parameter space. Search sensitivity remained nearly constant beyond 200 trees.

2. **max-depth** = 5 for each of the three seasons' BDTs

   The maximum depth controls the number of node levels in each tree. A too large tree depth can lead to overtraining, while a too small tree depth will not allow sufficient signal/background separation.

3. $\boldsymbol{\beta} = 0.2$ for each of the three seasons' BDTs

   The boosting factor β controls the weight of misclassified events, as shown in Equation 5.7. A too large β can lead to overtraining and reduces the discriminating power of the forest as misclassified events will dominate the node purity in most of the trees. Search sensitivity remained nearly constant up to $\beta = 0.5$; overtraining arose beyond this value.

4. **N-cuts** = 20 for each of the three seasons' BDTs

This parameter determines the number of bins for each variable histogram constructed at each node. The optimal number of bins depends on the signal and background event statistics. Each bin must contain a representative amount of events for the histogram to convey meaningful signal/background separation.

5. **prune-strength** = 10% for the IC79 BDT; **prune-strength** = 0% for the IC86I and IC86II BDTs

   As described above, the pruning strength is the percentage of the cost-complexity pruning sequence to be executed for all trees in the BDT.

For each node in each tree in the BDT algorithm, every variable is histogrammed with an equal number of bins and a single variable cut value is chosen that yields the best separation between the signal and background hypotheses. Signal and background data to the left and right of this cut are separated into two different child nodes. This histogramming and separating continues until five levels of child nodes are created or if 100% signal or background purity is reached. Events in each tree are scored +(-)1 if they end up in a signal(background) node. Each subsequent tree incorporates higher weights, or boosting, for incorrectly categorized data. Several hundred trees are trained for each season's BDT. The final BDT score of each event is a weighted average of its scores in each tree, with the weight corresponding to the boost factor of each tree.

5.4.2 BDT Input Signal - Background Discrimination Variables

The BDT discrimination variables take advantage of topological and energetic differences between astrophysical neutrino and atmospheric muon spectra. Figure 5.36 shows the distributions of simulation and data with respect to BDT score. The vertical dashed line corresponds to the optimized final cut described in the next section. The ν_μ in these plots is already preselected to be shower-like from Level 2 and Level 3 and has minimal overlap with the Northern Hemisphere track search. Additionally, the muon background is preselected to be shower-like and with these variables the BDT is able to effectively discriminate between these events and signal.

Nearly two dozen variables are used in the BDT. While a few of them clearly dominate in the algorithm, the correlations between the variables are small and all exhibit effective separation above the 1% level in different areas of the parameter space. The only strongly correlated variables are the interaction vertex containment variables, which convey the same idea but are still used by different amounts in the trees. The correlation matrix for signal (top) and background (bottom) is shown in Figure 5.8.

The relative importance of each variable in the IC79 BDT is shown below for different definitions of importance. The values are similar for IC86I and IC86II with the main difference being less usage of Nch. This energy proxy is used less in the 86-string BDTs because of the limited high energy statistics in their available simulated signal datasets relative to IC79.

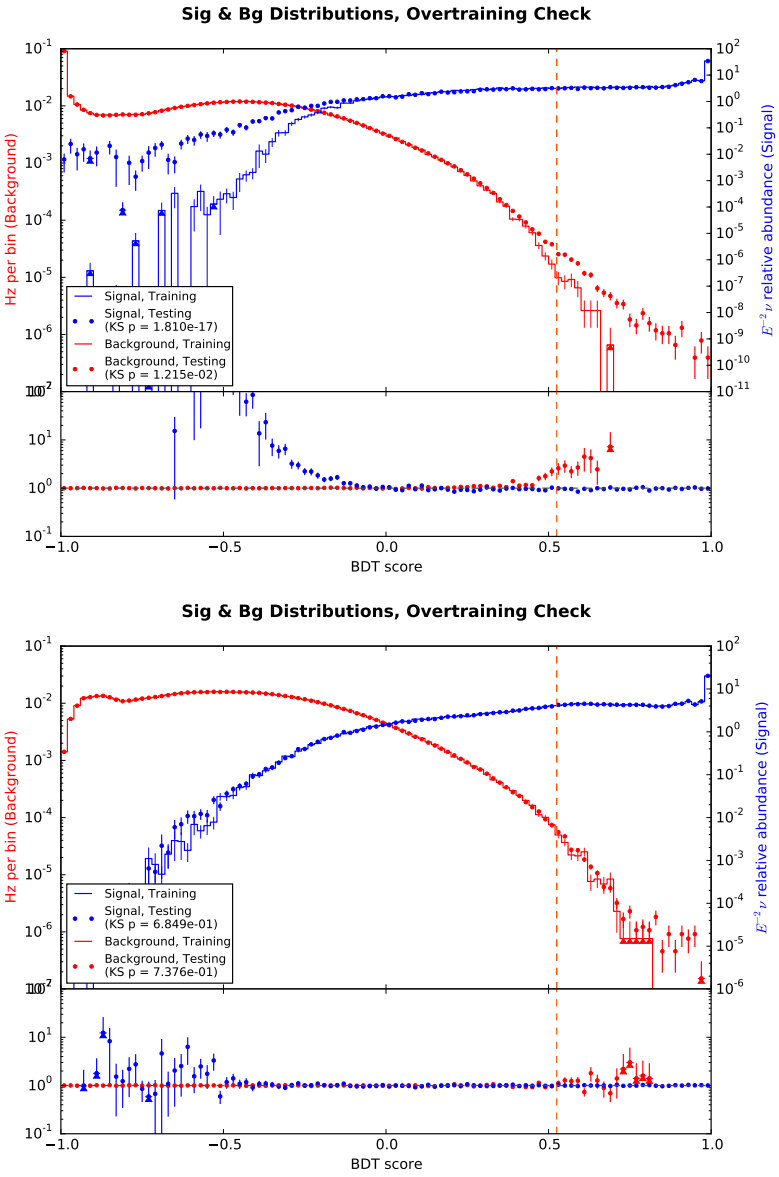

Figure 5.7: Overtrained (top) and well-trained (bottom) BDT score distributions for signal (blue) and background (red).

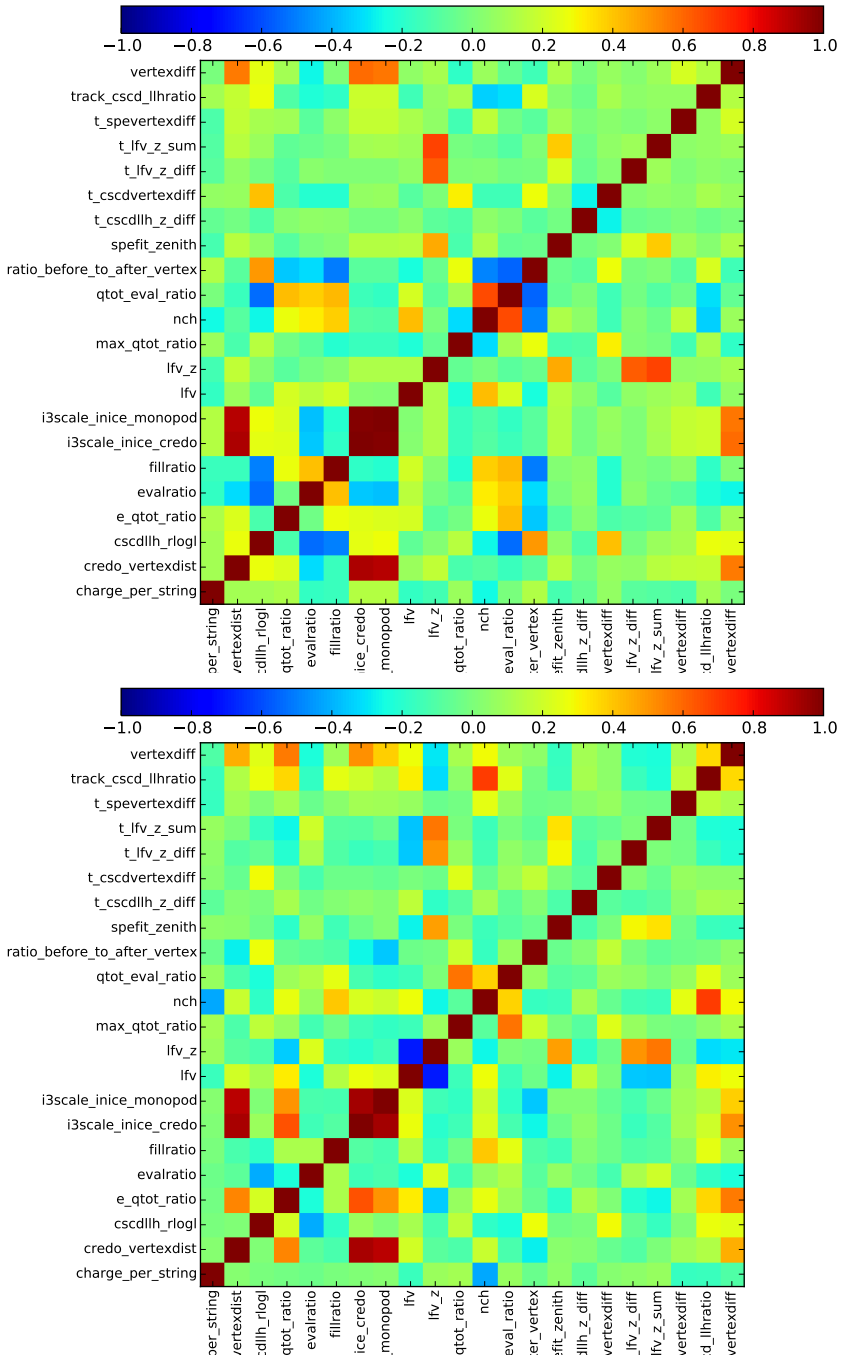

Figure 5.8: Variable correlation matrix for signal (top) and background (bottom).

The following variable importance list weights by separation per node. This ranking shows which variables drive the majority of the separation.

```
 1. nch                          : 0.263219
 2. qtot_eval_ratio              : 0.206007
 3. track_cscd_llhratio          : 0.169659
 4. cscdllh_rlogl                : 0.068819
 5. max_qtot_ratio               : 0.046522
 6. t_lfv_z_diff                 : 0.037657
 7. t_lfv_z_sum                  : 0.031459
 8. t_cscdllh_z_diff             : 0.028757
 9. lfv_z                        : 0.021912
10. e_qtot_ratio                 : 0.018711
11. i3scale_inice_monopod        : 0.018262
12. fillratio                    : 0.017134
13. ratio_before_to_after_vertex : 0.012300
14. spefit_zenith                : 0.011471
15. lfv                          : 0.011163
16. vertexdiff                   : 0.008894
17. credo_vertexdist             : 0.008630
18. i3scale_inice_credo          : 0.007794
19. t_spevertexdiff              : 0.005102
20. charge_per_string            : 0.002859
21. t_cscdvertexdiff             : 0.002262
22. evalratio                    : 0.001406
```

The following variable importance list weights by tree weight. This ranking shows which variables separate the easiest events in the early trees.

```
 1. ratio_before_to_after_vertex : 0.101122
 2. spefit_zenith                : 0.085615
 3. track_cscd_llhratio          : 0.083146
 4. qtot_eval_ratio              : 0.080421
 5. e_qtot_ratio                 : 0.072368
 6. lfv_z                        : 0.068617
 7. max_qtot_ratio               : 0.063828
 8. i3scale_inice_monopod        : 0.053032
 9. cscdllh_rlogl                : 0.049083
10. t_cscdvertexdiff             : 0.048363
11. t_lfv_z_diff                 : 0.042257
12. fillratio                    : 0.041723
13. lfv                          : 0.040528
14. nch                          : 0.031168
15. t_lfv_z_sum                  : 0.028530
16. credo_vertexdist             : 0.025968
17. t_cscdllh_z_diff             : 0.020933
18. t_spevertexdiff              : 0.018946
19. vertexdiff                   : 0.015740
20. charge_per_string            : 0.013126
21. i3scale_inice_credo          : 0.011495
22. evalratio                    : 0.003988
```

The following variable importance list based on the number of uses only. This ranking shows which variables were used in separating the hard events in the later trees.

```
 1. ratio_before_to_after_vertex : 0.104993
 2. track_cscd_llhratio          : 0.102712
 3. max_qtot_ratio               : 0.082781
 4. qtot_eval_ratio              : 0.078517
 5. i3scale_inice_monopod        : 0.068034
 6. spefit_zenith                : 0.065309
 7. e_qtot_ratio                 : 0.059480
 8. t_cscdvertexdiff             : 0.051972
 9. t_lfv_z_diff                 : 0.045436
10. nch                          : 0.044225
11. lfv_z                        : 0.043940
12. t_lfv_z_sum                  : 0.042579
13. cscdllh_rlogl                : 0.030139
14. t_spevertexdiff              : 0.025493
15. lfv                          : 0.025215
16. t_cscdllh_z_diff             : 0.024855
17. vertexdiff                   : 0.021481
18. fillratio                    : 0.019964
19. i3scale_inice_credo          : 0.019936
20. charge_per_string            : 0.019010
21. credo_vertexdist             : 0.018340
22. evalratio                    : 0.005590
```

The BDT variables are separated into three classes below. The first class of variables **Topology Separators** separate the spherical-like signal from track-like background topologies. The second class **Energy Separators** separates signal from background using various energy proxies. In general, high energy neutrino showers impart their energy uniformly over a more contained volume than lower energy atmospheric muons. The third class **Vertex Location Separators** separates signal from background using the location of the reconstructed event vertex. While no requirements of containment within the detector are imposed on the desired signal, interaction location in the detector can further elicit differences in muon and neutrino-induced showers.

Topology Separators

track-cscd-llhratio One of the most effective BDT variables is the same ratio of the track likelihood to the cascade likelihood used in Level 3. Even though the analysis selected on this parameter before the BDT cut, the high energy background muons that passed in spite of it are successfully distinguished from signal with the BDT algorithm. Note that high energy neutrino-induced showers can yield large, track-like values. Both analytic likelihood-based reconstructions, SPE and CascadeLlh, give large log-likelihood values to events with high numbers of hit DOMs. Because SPE's $\mathcal{L}$ range peaks at much higher values than CascadeLlh, high-energy events tend to yield large positive $\log(\mathcal{L}_{\text{track}}/\mathcal{L}_{\text{cscd}})$ values.

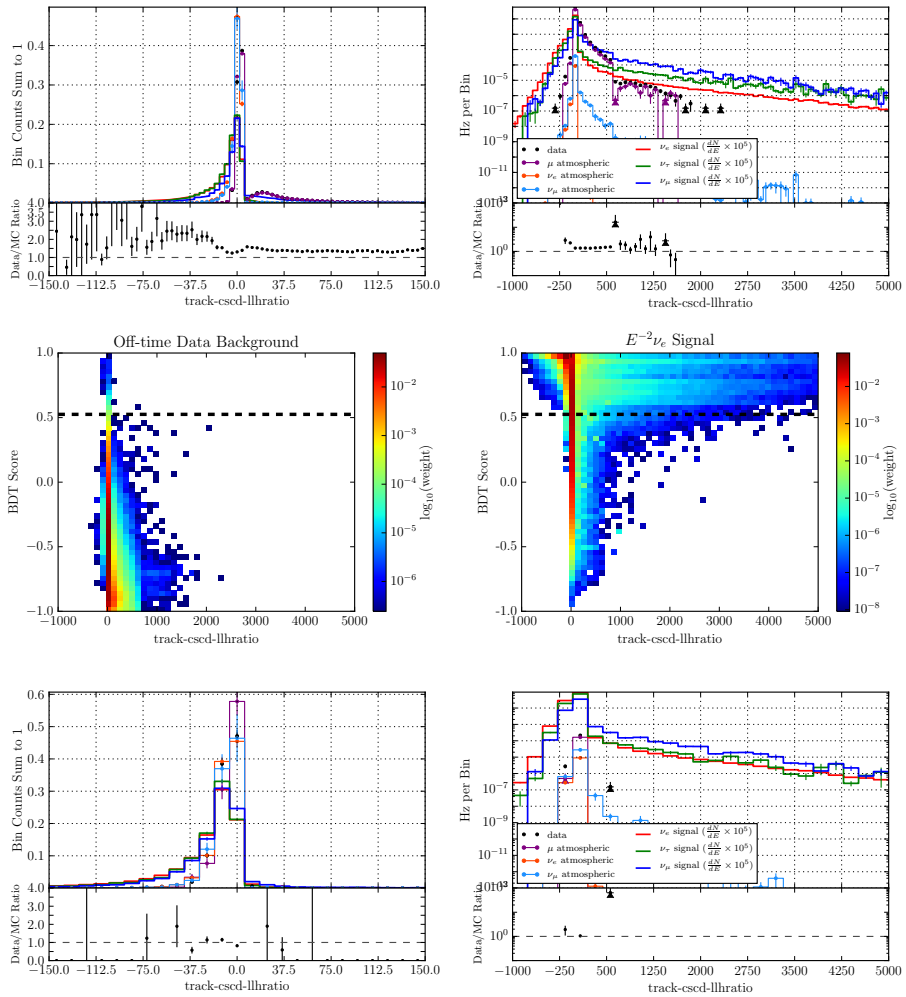

Figure 5.9: track-cscd-llhratio. Top: linear (left) and logarithmic (right) Level 3 distributions. Middle: BDT score vs. background (left) and signal (right) distributions. Bottom: final cut level distributions.

cscdllh-rlogl Another powerful separator is the reduced negative log-likelihood value from CascadeLlh likelihood maximization. Events with more hit DOMs will have a larger log-likelihood value because it is calculated as the sum of the PDFs of all hits, taking the logarithm of Equation 4.16. The number of free parameters in CascadeLlh are the number of hit DOMs (Nch) minus the number of degrees of freedom in the fit (one temporal, three positional, and two directional). Therefore, if the log-likelihood is divided by the number of degrees of freedom, events with different Nch values can be compared. The linear distributions are zoomed in to better see the neutrino-muon separation.

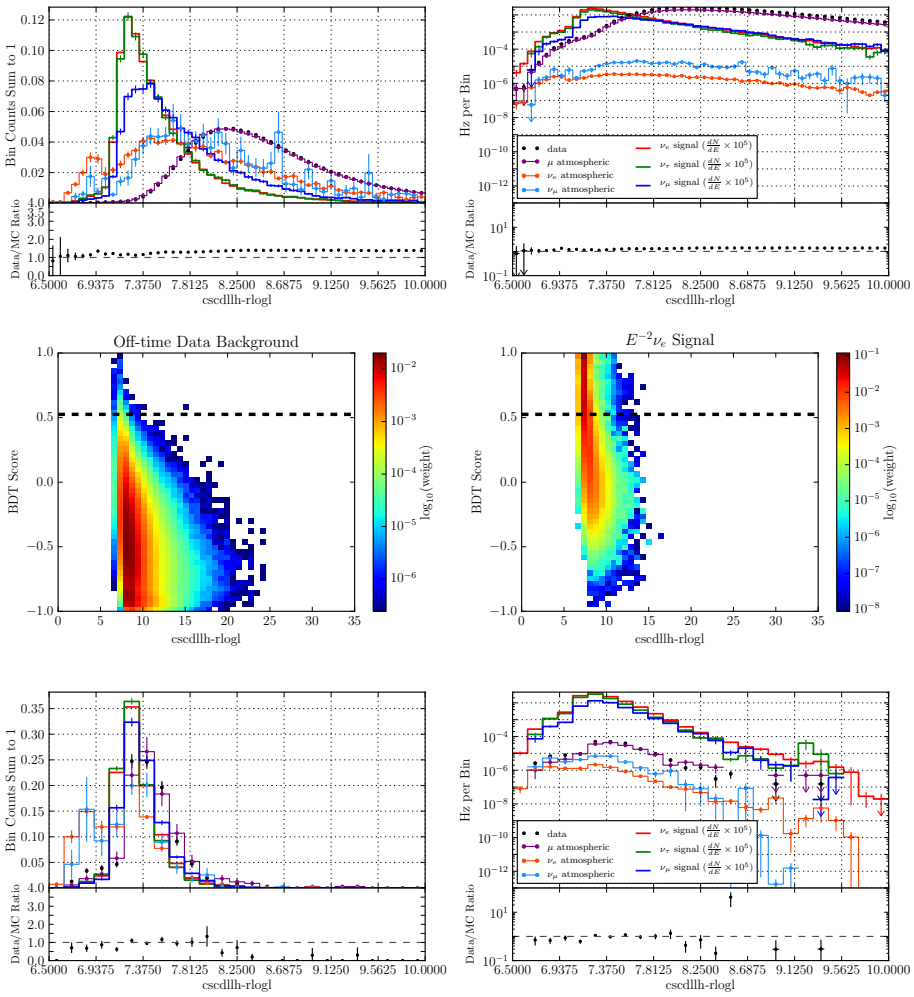

Figure 5.10: cscdllh-rlogl. Top: linear (left) and logarithmic (right) Level 3 distributions. Middle: BDT score vs. background (left) and signal (right) distributions. Bottom: final cut level distributions.

lfv This variable is the reconstructed speed from the improved LineFit algorithm. Muon tracks should be reconstructed close to the speed of light. A cascade, on the other hand, is comprised of light diffusing out from the interaction point, and therefore should exhibit a relatively slow reconstructed LineFit speed.

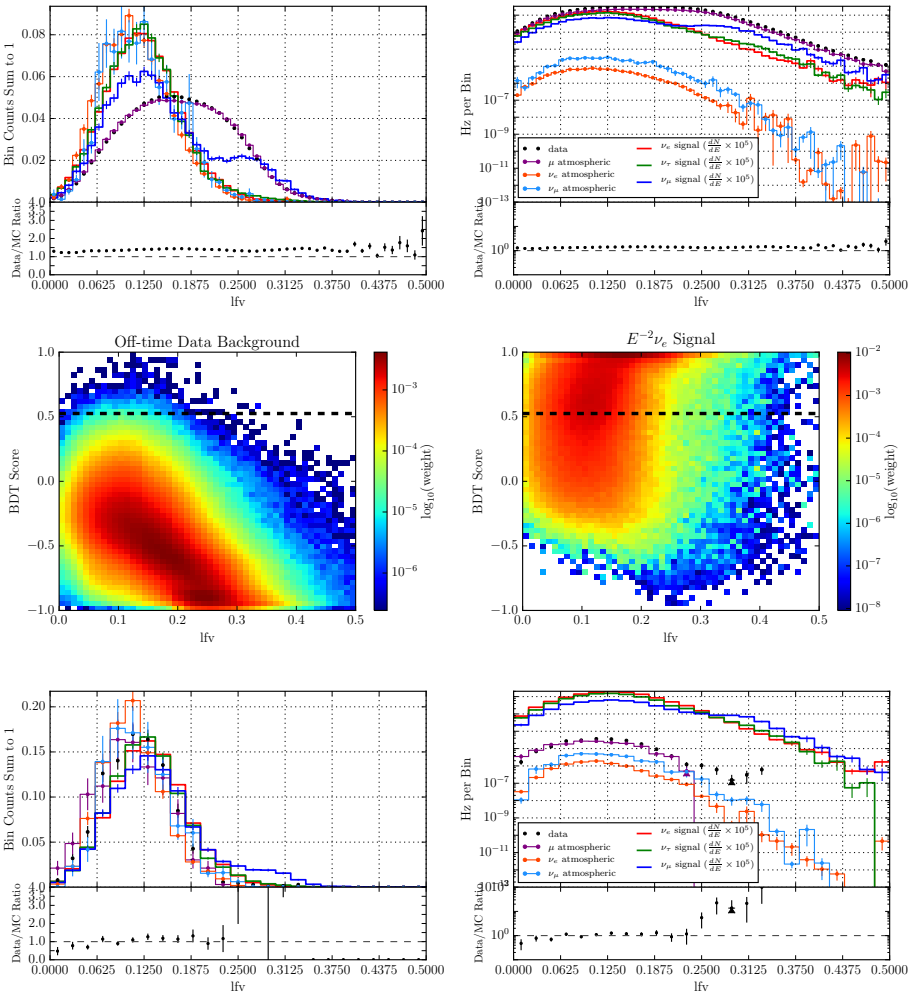

Figure 5.11: lfv. Top: linear (left) and logarithmic (right) Level 3 distributions. Middle: BDT score vs. background (left) and signal (right) distributions. Bottom: final cut level distributions.

lfv-z Background muons originate from above the detector, while astrophysical neutrinos should have near-isotropic origins. The (vertical) z-component of the reconstructed LineFit speed exhibits this directionality difference.

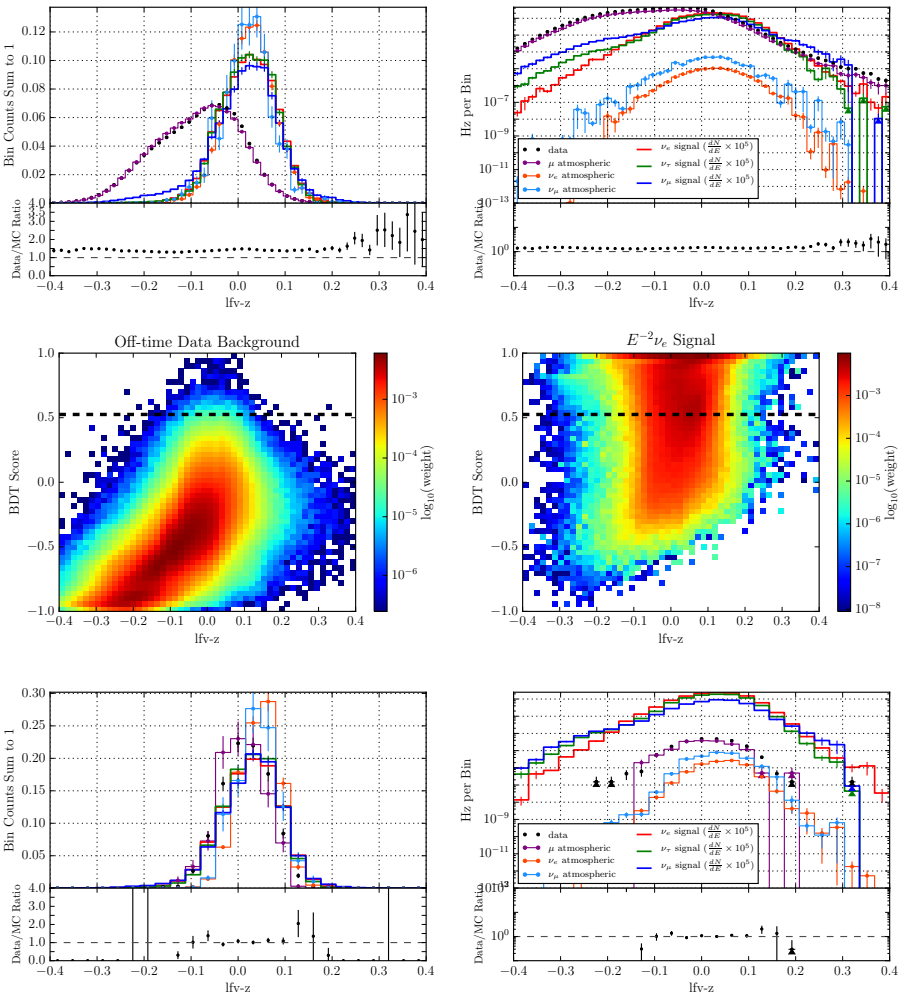

Figure 5.12: lfv-z. Top: linear (left) and logarithmic (right) Level 3 distributions. Middle: BDT score vs. background (left) and signal (right) distributions. Bottom: final cut level distributions.

t-lfv-z-sum Each event has a charge-weighted mean time calculated and is split on this mean time. The LineFit reconstruction is calculated for each half. A cascading neutrino interaction covers a relatively localized volume in the detector and thus its two event halves are much closer together than the two halves of a muon event. The sum of the z-component LineFit speeds of the two halves tends to be near zero for neutrino signal and negative for down-going muon background. Some muon event halves can be misreconstructed as upgoing, however, and yield near-zero or positive t-lf-z-sum values. The difference between the z-component speeds, which is also included and described below, catches and separates background events where one half is misreconstructed as up-going.

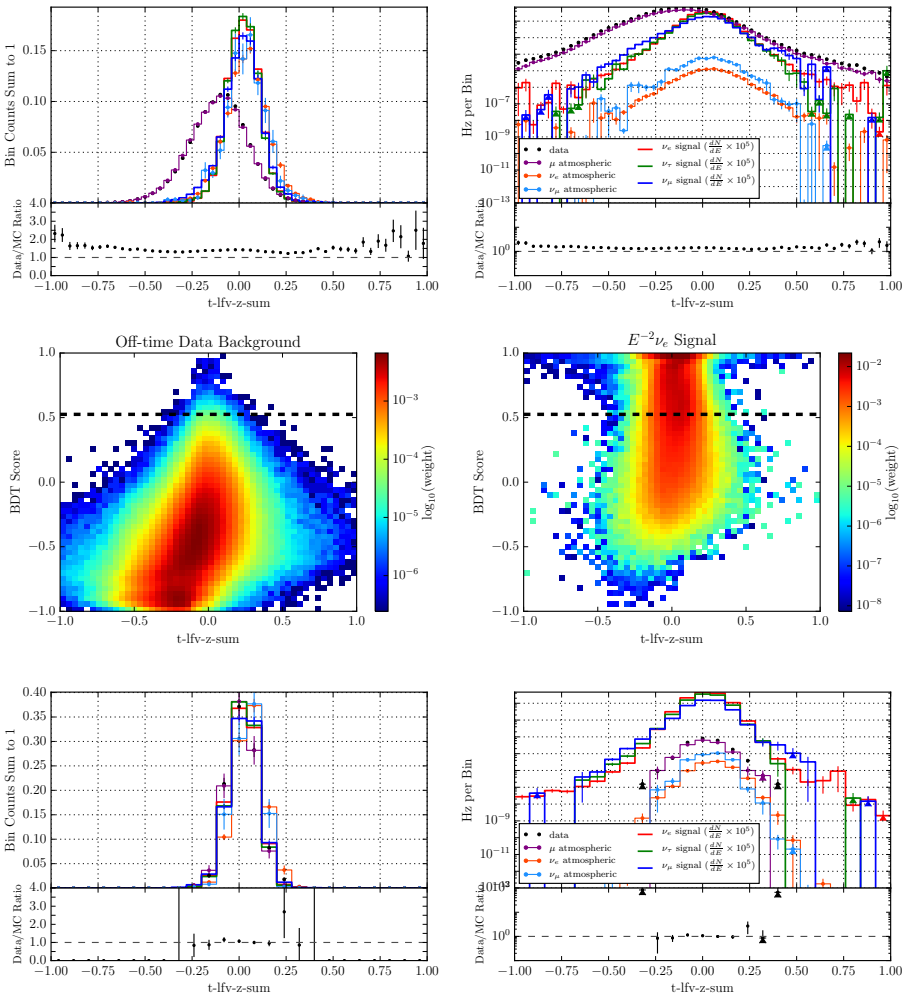

Figure 5.13: t-lfv-z-sum. Top: linear (left) and logarithmic (right) Level 3 distributions. Middle: BDT score vs. background (left) and signal (right) distributions. Bottom: final cut level distributions.

t-lfv-z-diff This variable is the difference between the z-component LineFit speeds of the two charge-weighted mean time-split halves of an event. The sum of the two halves' z-component speeds is described above. This difference catches and separates background events where one half is misreconstructed as up-going. t-lfv-z-diff and t-lfv-z-sum show little correlation in Figure 5.8 because they are used by the BDT for different events, depending on LineFit's success in reconstructing the direction of each event half.

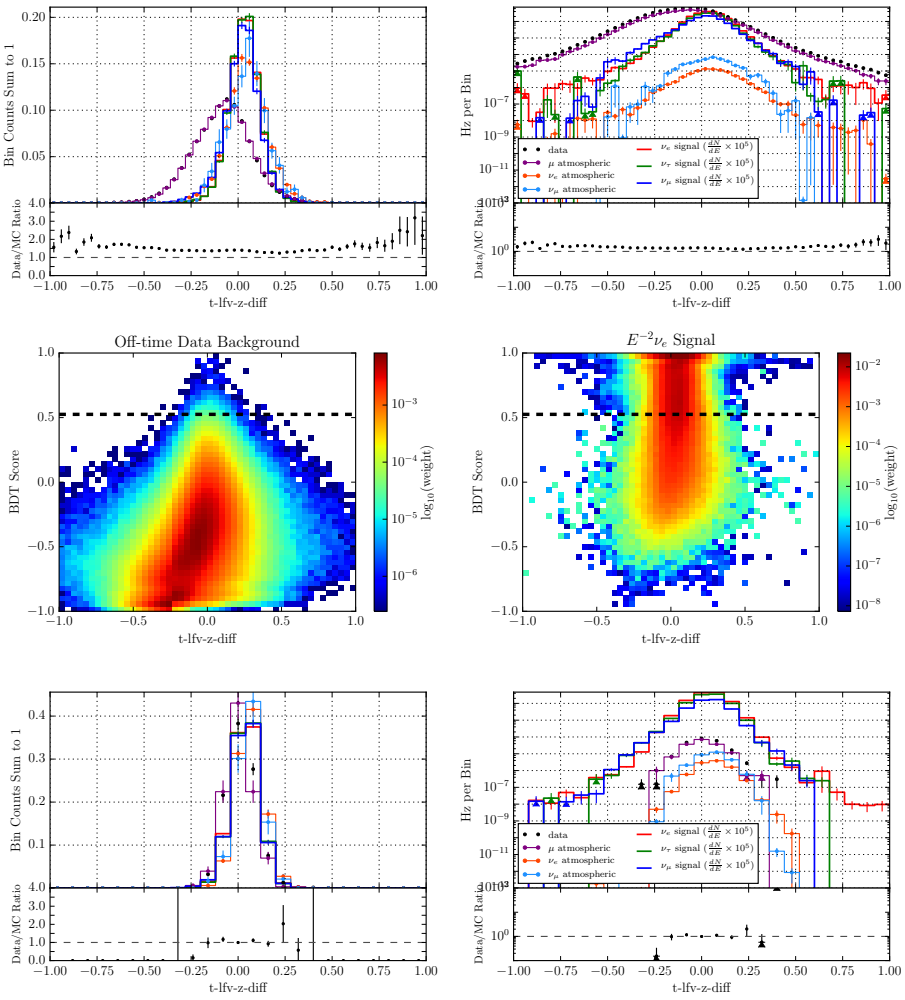

Figure 5.14: t-lfv-z-diff. Top: linear (left) and logarithmic (right) Level 3 distributions. Middle: BDT score vs. background (left) and signal (right) distributions. Bottom: final cut level distributions.

spefit-zenith The event zenith reconstructed by SPE. Background muons are mostly reconstructed as down-going whereas signal neutrinos are nearly isotropic in their reconstructed zenith distributions.

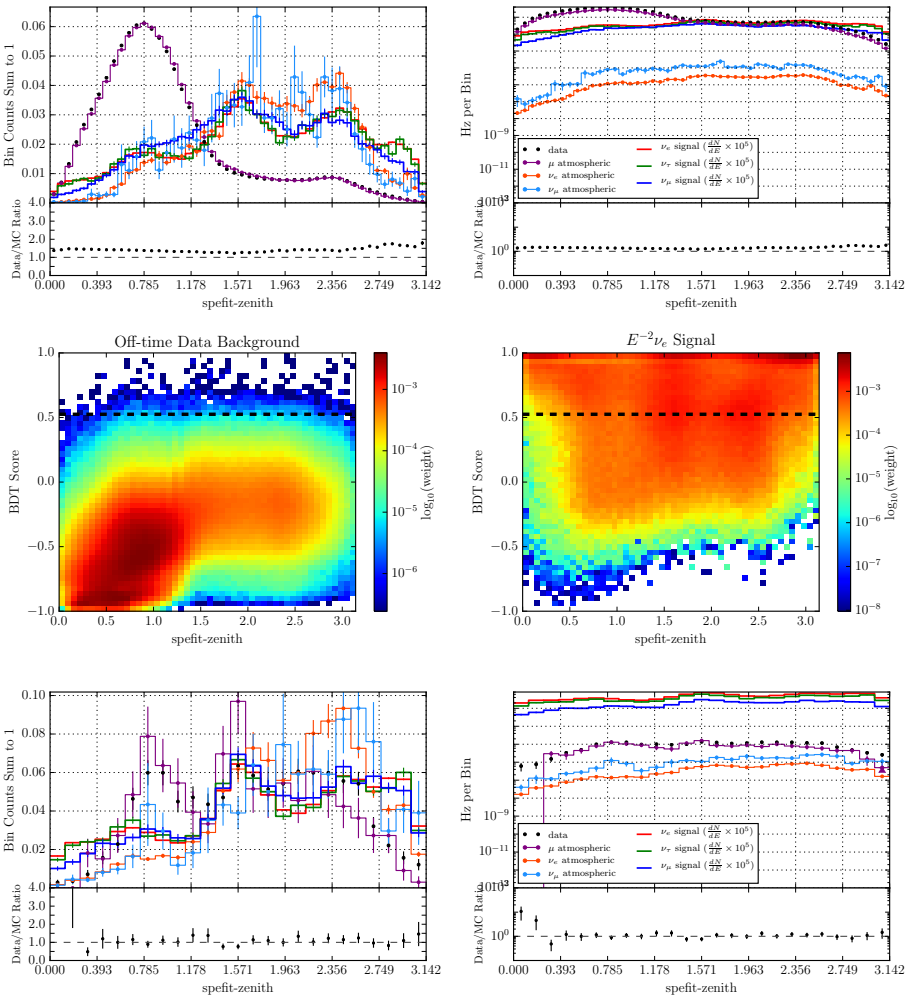

Figure 5.15: spefit-zenith. Top: linear (left) and logarithmic (right) Level 3 distributions. Middle: BDT score vs. background (left) and signal (right) distributions. Bottom: final cut level distributions.

ratio-before-to-after-vertex Ignoring noise hits, a cascade ideally should have all of their DOM hits take place in time after the interaction vertex. A track event should have about half of their hits take place before and half after its reconstructed "vertex," even with the fact that the background muon tracks are already preselected to be cascade-like at Level 3. This variable equals the total hit times of the DOMs hit before the Monopod-reconstructed vertex time divided by the total hit times of the DOMs hit after the Monopod-reconstructed vertex time. Using the time values instead of the hit counts brings out more separation from signal for background events with early hits.

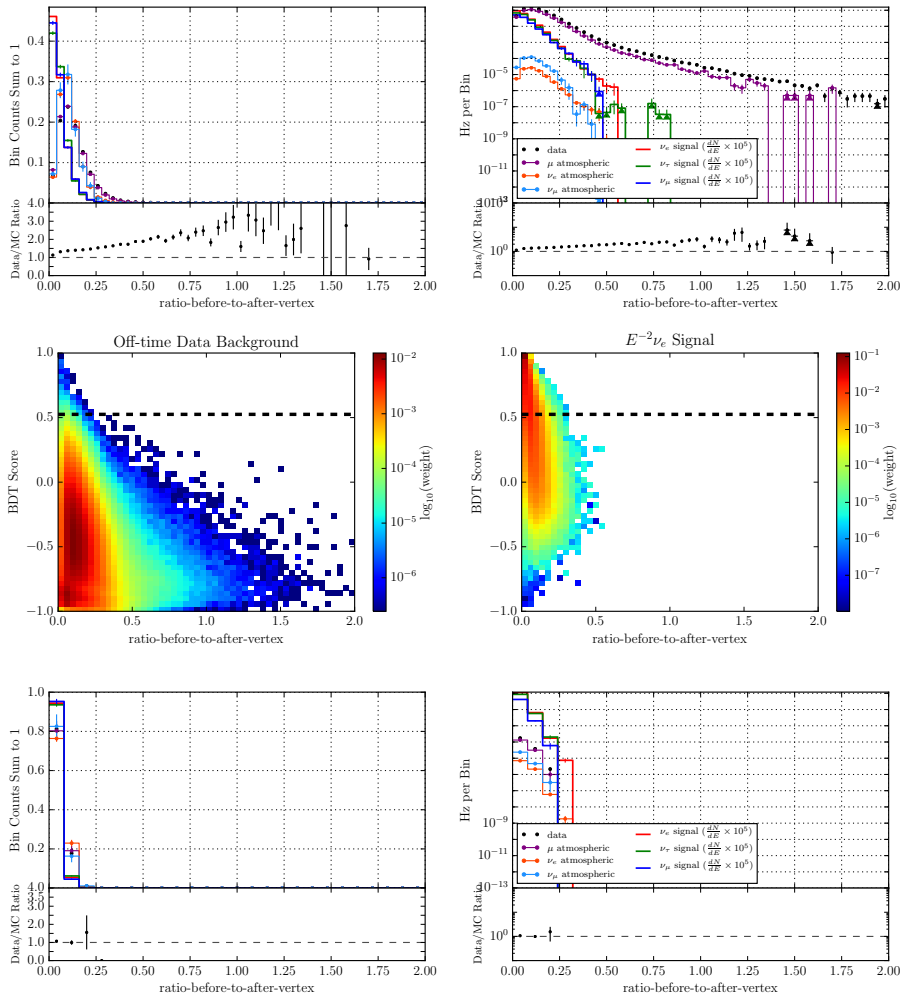

Figure 5.16: ratio-before-to-after-vertex. Top: linear (left) and logarithmic (right) Level 3 distributions. Middle: BDT score vs. background (left) and signal (right) distributions. Bottom: final cut level distributions.

fill-ratio The fill-ratio is the same as used in the Level 3 selection. Signal-like events exhibit a large fraction of hit DOMs inside of a sphere centered on the reconstructed vertex with a radius determined by the mean hit distance. Background tracks exhibit a less-filled sphere. The BDT is able to use this variable to some extent even though it was employed at Level 3.

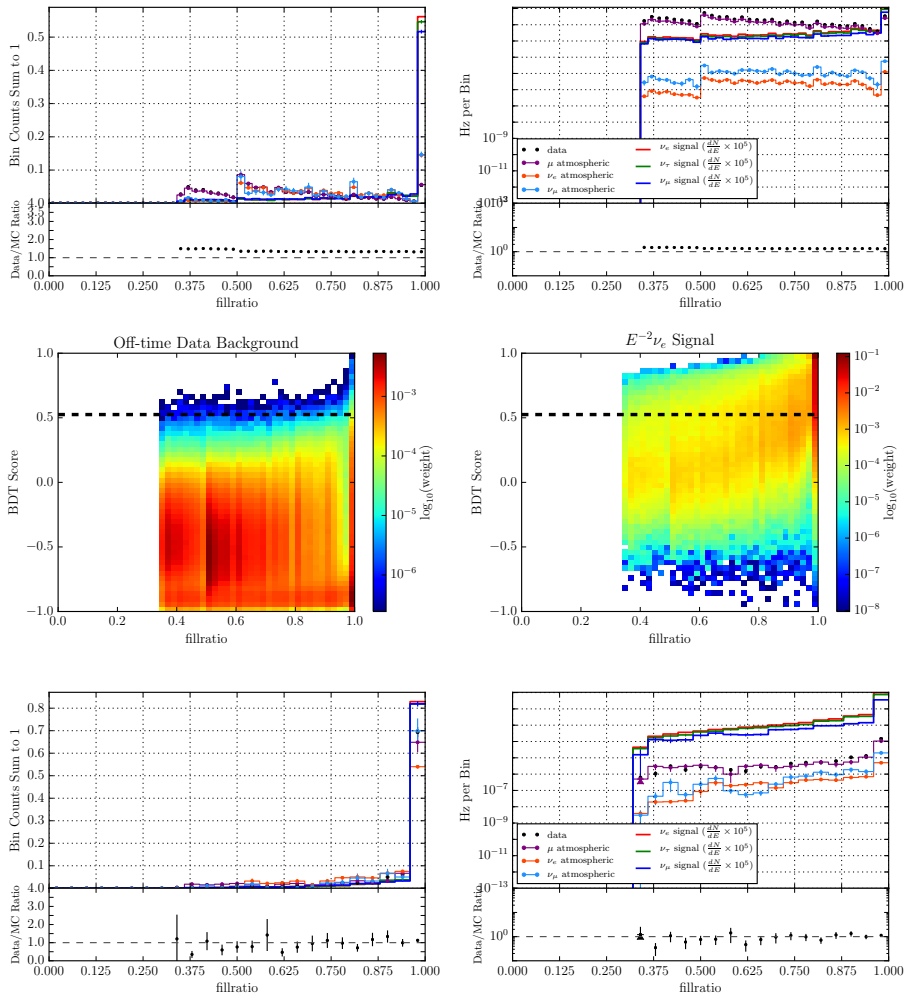

Figure 5.17: fill-ratio. Top: linear (left) and logarithmic (right) Level 3 distributions. Middle: BDT score vs. background (left) and signal (right) distributions. Bottom: final cut level distributions.

evalratio This variable is the tensor-of-inertia eigenvalue ratio employed at Level 2.

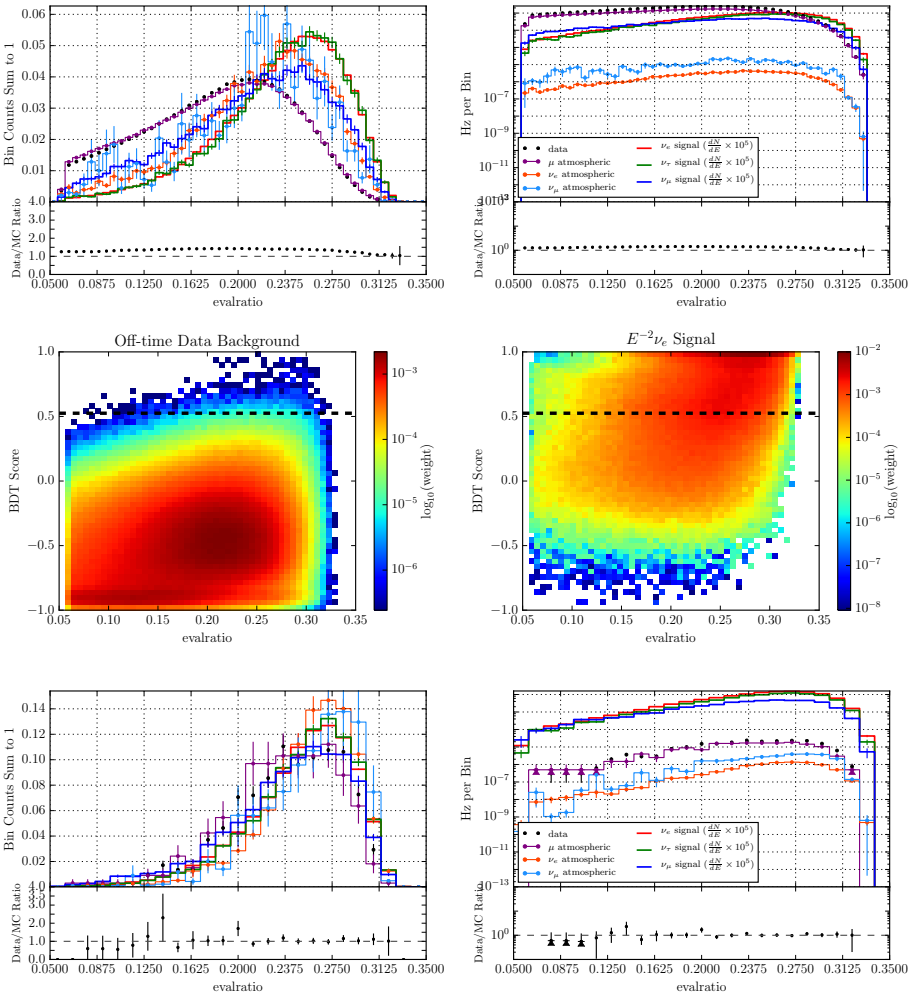

Figure 5.18: evalratio. Top: linear (left) and logarithmic (right) Level 3 distributions. Middle: BDT score vs. background (left) and signal (right) distributions. Bottom: final cut level distributions.

Energy Separators

qtot-eval-ratio Another potent variable is the total amount of Cherenkov light imparted in the DOMs divided by the tensor-of-inertia derived elongation of an event. The numerator separates lower energy background atmospheric muons from higher energy astrophysical signal neutrinos, while the denominator separates elongated background atmospheric muons from spherical neutrino-induced showers. As shown in Figure 5.19, the ratio of these two observables effectively separates the lower energy atmospheric neutrino background from the signal as well.

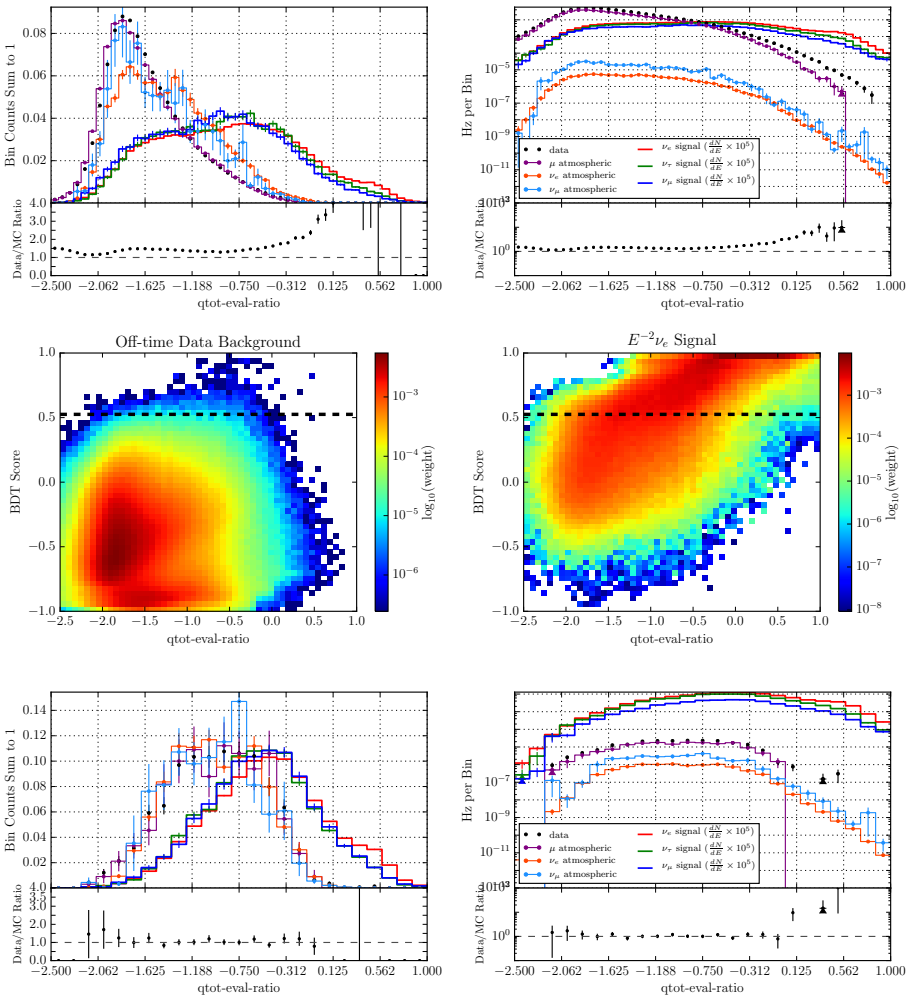

Figure 5.19: qtot-eval-ratio. Top: linear (left) and logarithmic (right) Level 3 distributions. Middle: BDT score vs. background (left) and signal (right) distributions. Bottom: final cut level distributions.

max-qtot-ratio The maximum imparted charge to a DOM to the total imparted charge in an event removes so-called "balloon events," in which a muon loses its energy catastrophically close to a DOM.

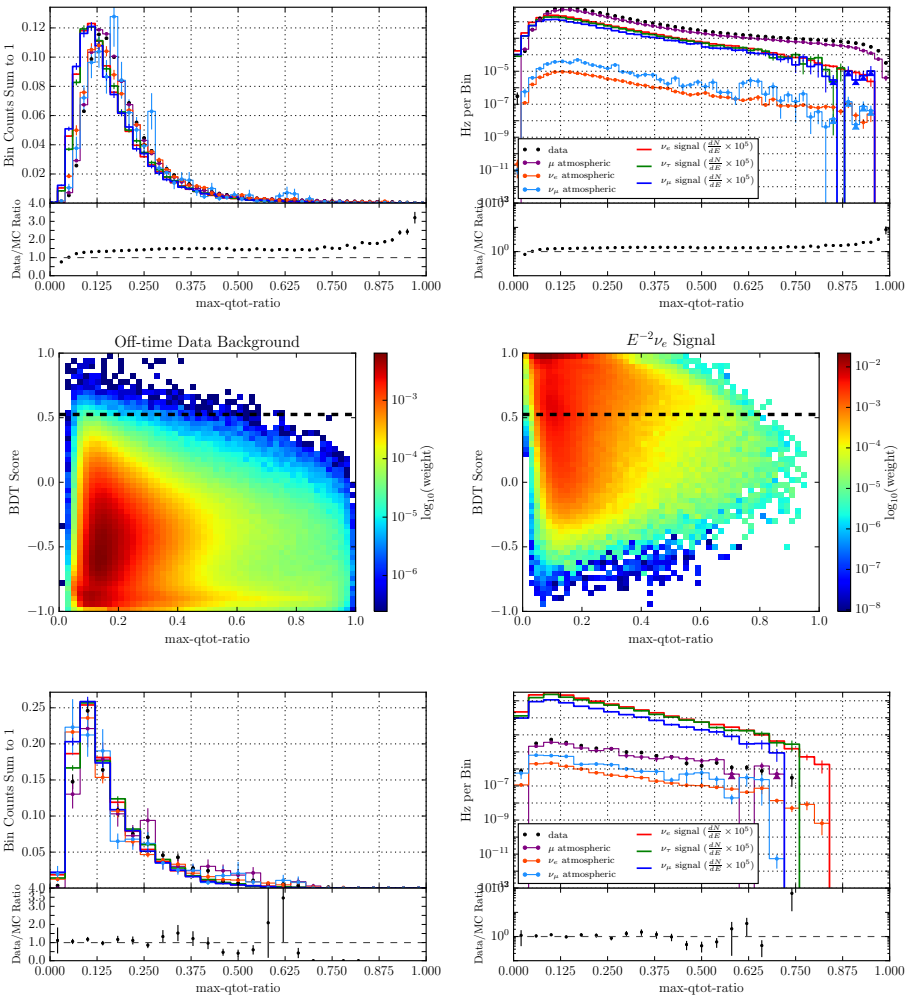

Figure 5.20: max-qtot-ratio. Top: linear (left) and logarithmic (right) Level 3 distributions. Middle: BDT score vs. background (left) and signal (right) distributions. Bottom: final cut level distributions.

e-qtot-ratio The logarithm of the ratio of the ACER reconstructed energy divided by the total imparted charge in an event removes interactions in which the total charge is much smaller than the reconstructed energy.

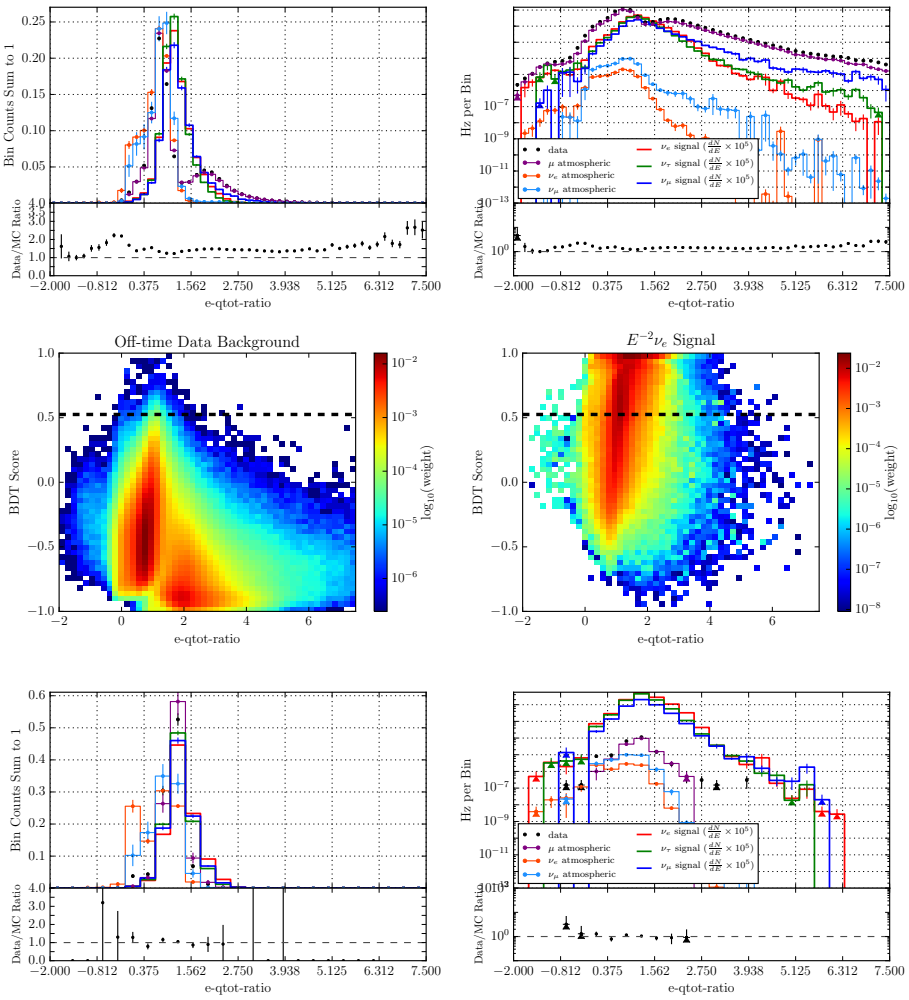

Figure 5.21: e-qtot-ratio. Top: linear (left) and logarithmic (right) Level 3 distributions. Middle: BDT score vs. background (left) and signal (right) distributions. Bottom: final cut level distributions.

charge-per-string The total charge in an event divided by the number of strings whose DOMs trigger during an event. Cascades have fewer hit strings than tracks and, therefore, greater charge per string.

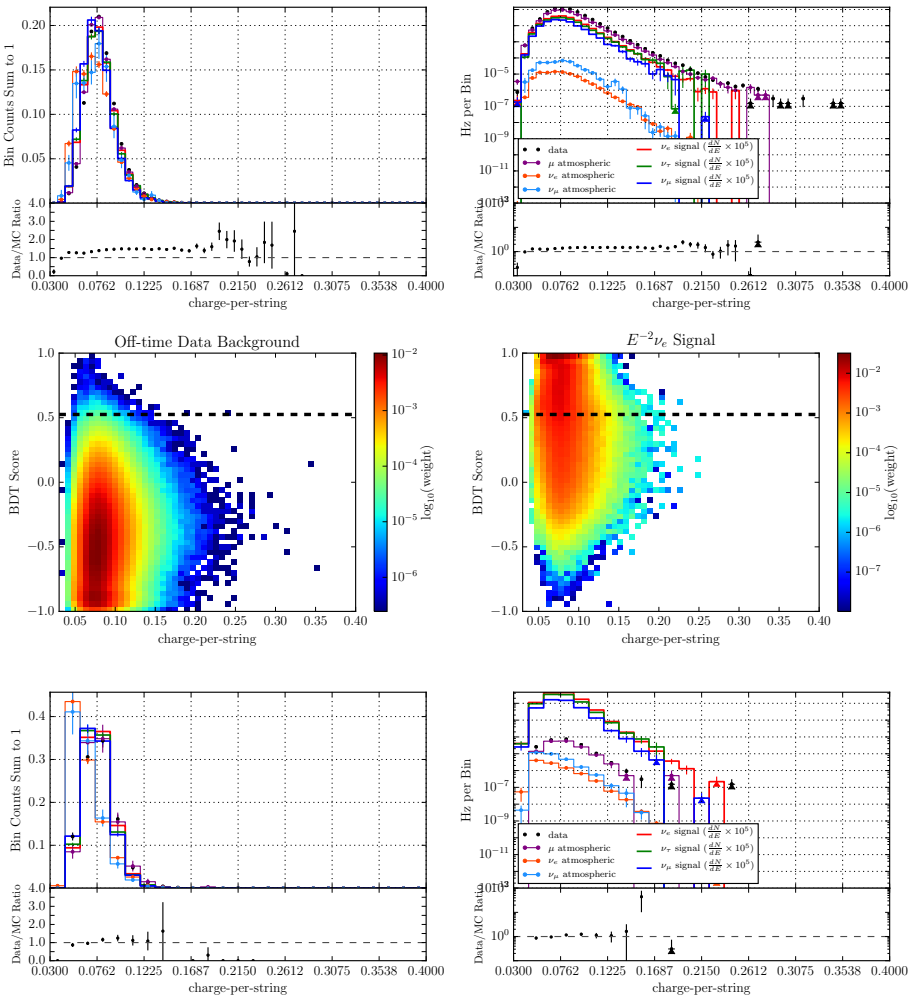

Figure 5.22: charge-per-string. Top: linear (left) and logarithmic (right) Level 3 distributions. Middle: BDT score vs. background (left) and signal (right) distributions. Bottom: final cut level distributions.

Nch Nch is the number of channels, or equivalently DOMs, that trigger during an event. An astrophysical neutrino flux reaches higher energies, and larger Nch values, than atmospheric muons.

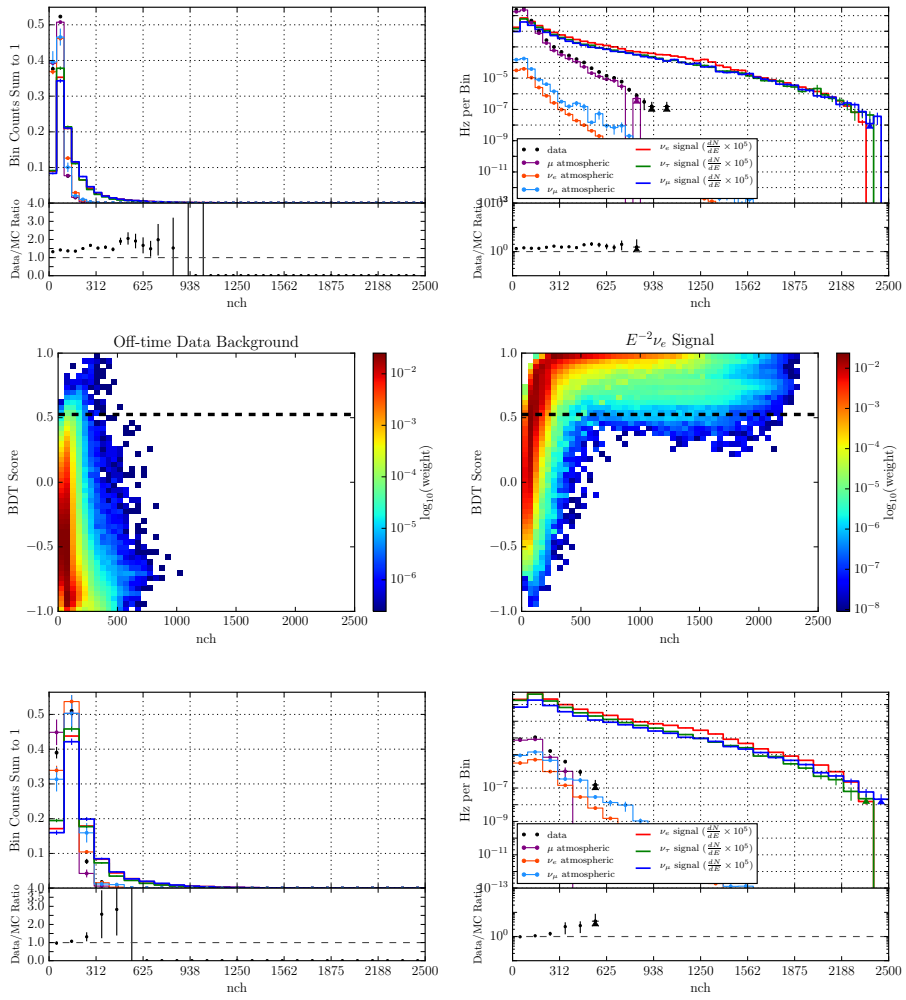

Figure 5.23: Nch. Top: linear (left) and logarithmic (right) Level 3 distributions. Middle: BDT score vs. background (left) and signal (right) distributions. Bottom: final cut level distributions.

Vertex Location Separators

i3scale-inice-credo The I3Scale calculation is the factor by which the nearest edge of the detector must scale in order to be at the reconstructed vertex. For example, a vertex with a value of 1 is at the edge of the detector, a vertex with a value less than one is contained within the detector volume, and a vertex with a value greater than one is outside of the detector volume. This specific variable is the measure of containment using the Credo reconstructed vertex.

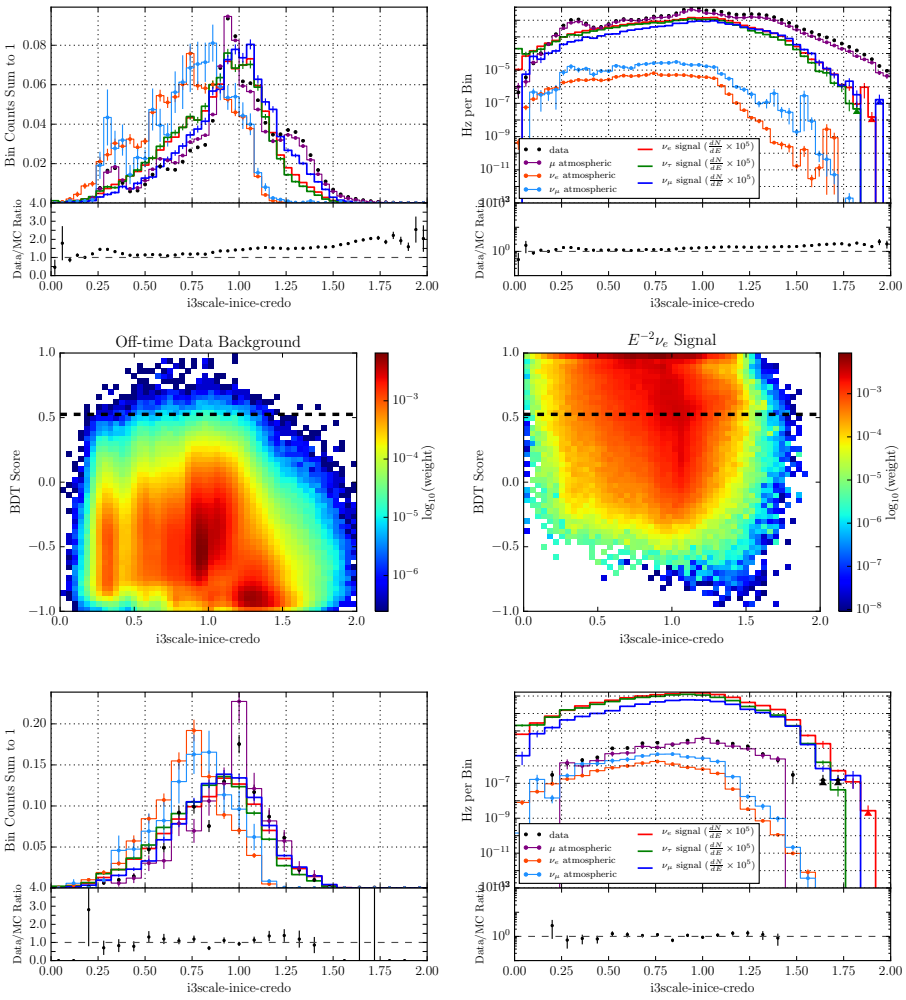

Figure 5.24: i3scale-inice-credo. Top: linear (left) and logarithmic (right) Level 3 distributions. Middle: BDT score vs. background (left) and signal (right) distributions. Bottom: final cut level distributions.

i3scale-inice-monopod This variable is a measure of containment using the I3Scale calculation, described for i3scale-inice-credo above, on the Monopdo reconstructed vertex. i3scale-inice-monopod is quite correlated with i3scale-inice-credo, but both are used by the BDT in varying degrees as depicted in the variable importance lists at the beginning of this section.

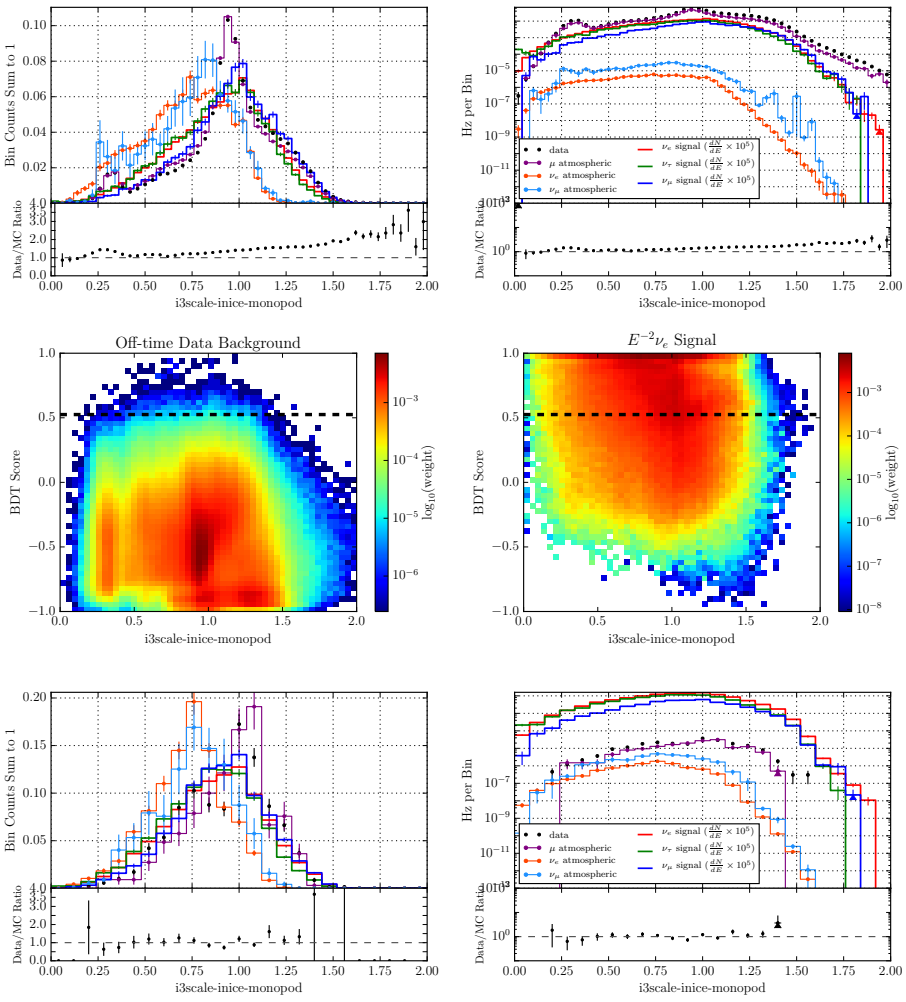

Figure 5.25: i3scale-inice-monopod. Top: linear (left) and logarithmic (right) Level 3 distributions. Middle: BDT score vs. background (left) and signal (right) distributions. Bottom: final cut level distributions.

credo-vertexdist Similar to i3scale-inice-credo above, this variable is a measure of containment and is the distance in meters of the Credo reconstructed vertex from the center of the detector volume.

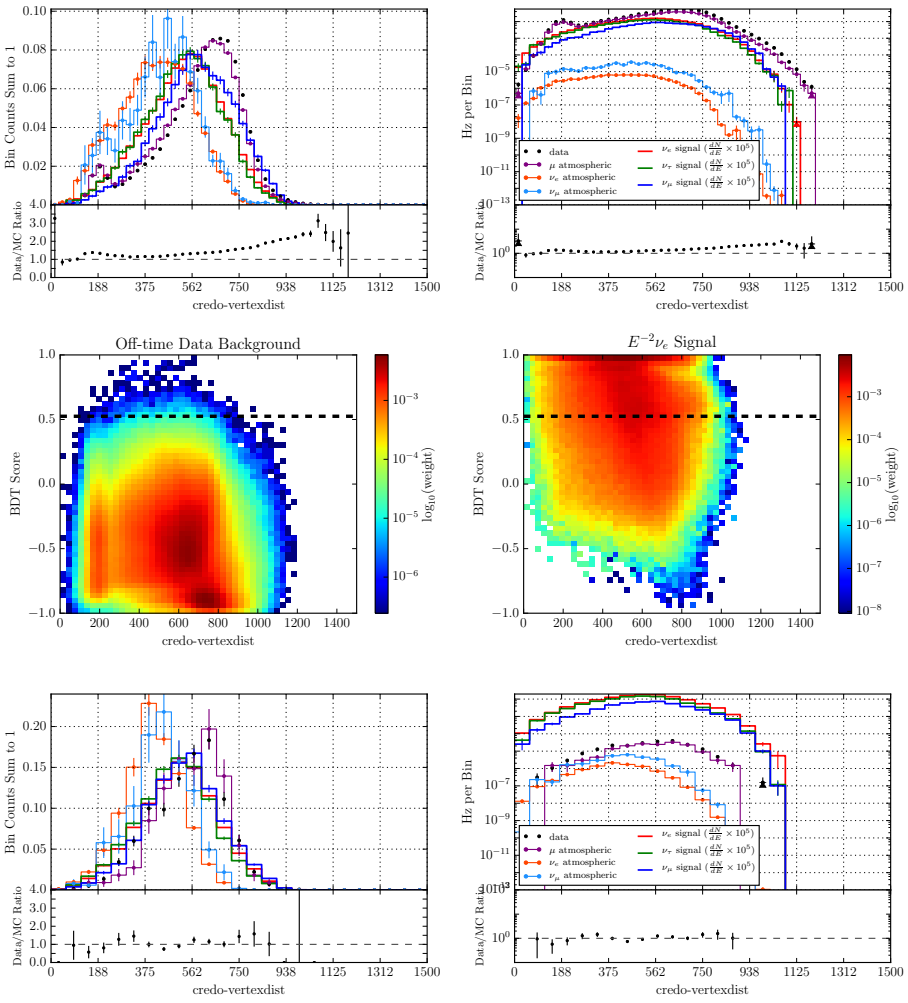

Figure 5.26: credo-vertexdist. Top: linear (left) and logarithmic (right) Level 3 distributions. Middle: BDT score vs. background (left) and signal (right) distributions. Bottom: final cut level distributions.

t-cscdvertexdiff Each event has a charge-weighted mean time calculated and is split on this mean time. The CascadeLlh reconstruction is performed on both halves and the distance between their reconstructed vertices is calculated. A cascading neutrino interaction covers a relatively localized volume in the detector and thus its two event halves are much closer together than the two halves of a muon event, and thus signal events are expected to have smaller t-cscdvertexdiff values.

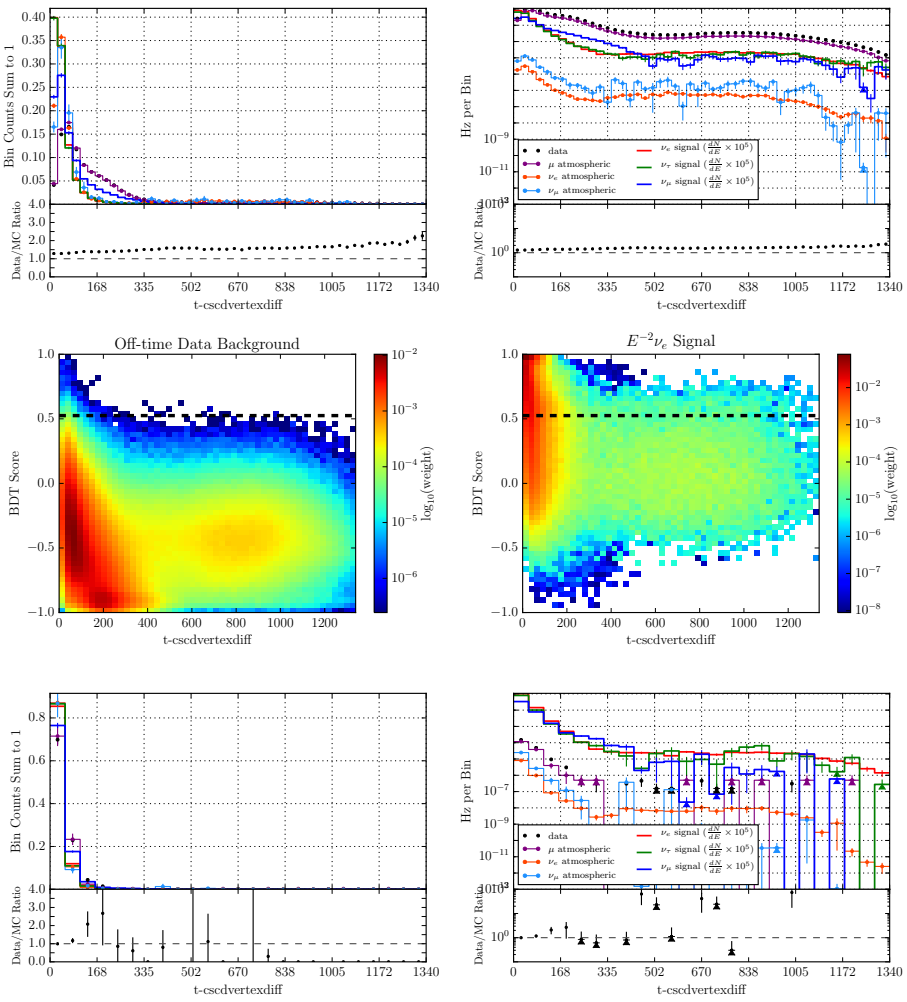

Figure 5.27: t-cscdvertexdiff. Top: linear (left) and logarithmic (right) Level 3 distributions. Middle: BDT score vs. background (left) and signal (right) distributions. Bottom: final cut level distributions.

t-cscdllh-z-diff Each event has a charge-weighted mean time calculated and is split on this mean time. The CascadeLlh reconstruction is performed on both halves and the distance between their reconstructed vertex (vertical axis) z values is calculated. The difference in the z components of the vertices reveals additional separation between signal and background because of the down-going nature of atmospheric muons.

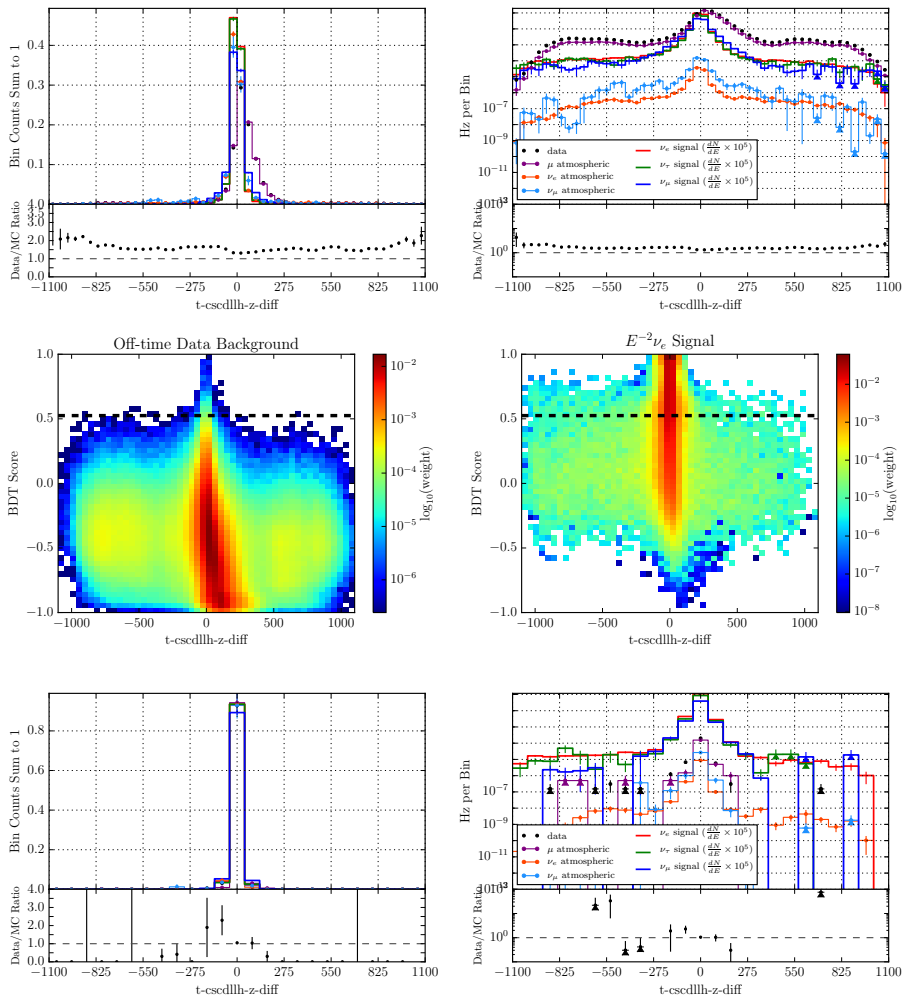

Figure 5.28: t-cscdllh-z-diff. Top: linear (left) and logarithmic (right) Level 3 distributions. Middle: BDT score vs. background (left) and signal (right) distributions. Bottom: final cut level distributions.

t-spevertexdiff Like with t-cscdvertexdiff above, the SPE reconstruction is performed on both halves of an event and the distance between their reconstructed vertices is calculated. In general the distance between the vertices is less in a localized cascade compared to more track-like background, but interestingly high energy signal events display a large spread in the distribution of this variable. This spread is likely due to the fact that SPE is built on a track hypothesis and often does not converge on the true shower interaction vertex.

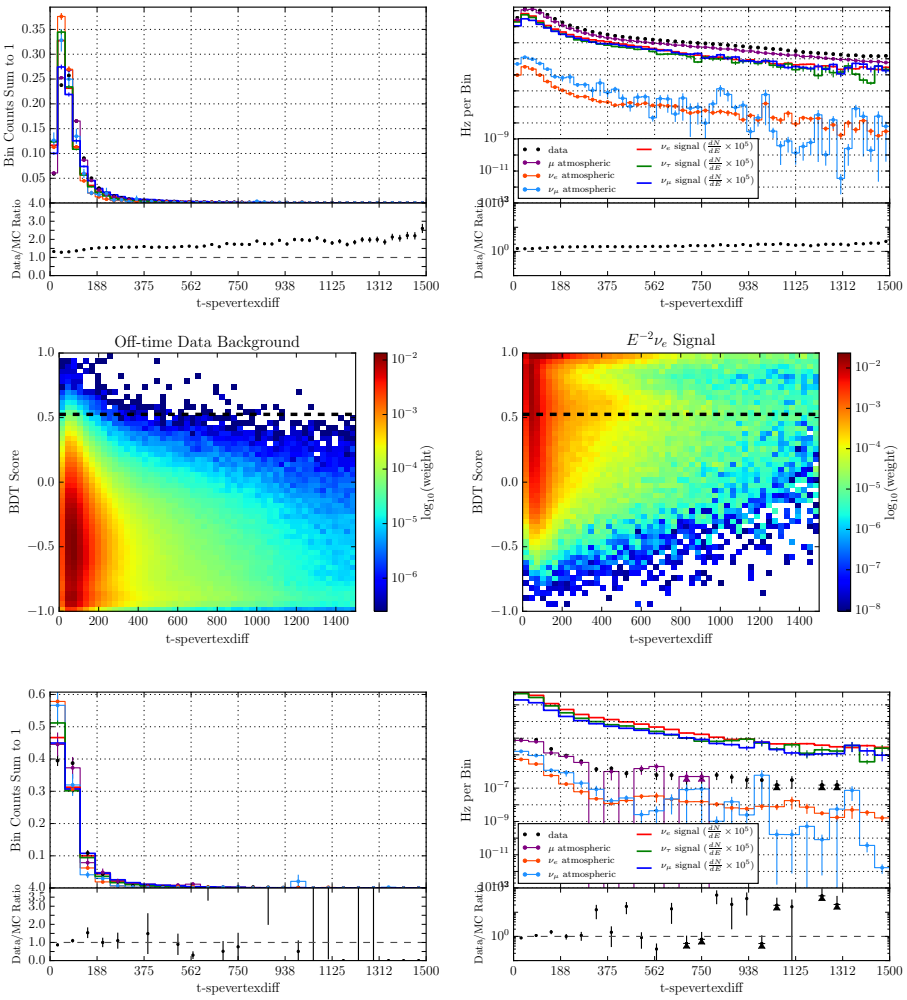

Figure 5.29: t-spevertexdiff. Top: linear (left) and logarithmic (right) Level 3 distributions. Middle: BDT score vs. background (left) and signal (right) distributions. Bottom: final cut level distributions.

vertexdiff This variable is the difference in vertex positions calculated by the Credo and CascadeLlh reconstructions. This variable identifies the track-like muon background by the larger distance between the vertices on which these two reconstructions converge, compared with the neutrino-induced cascade signal.

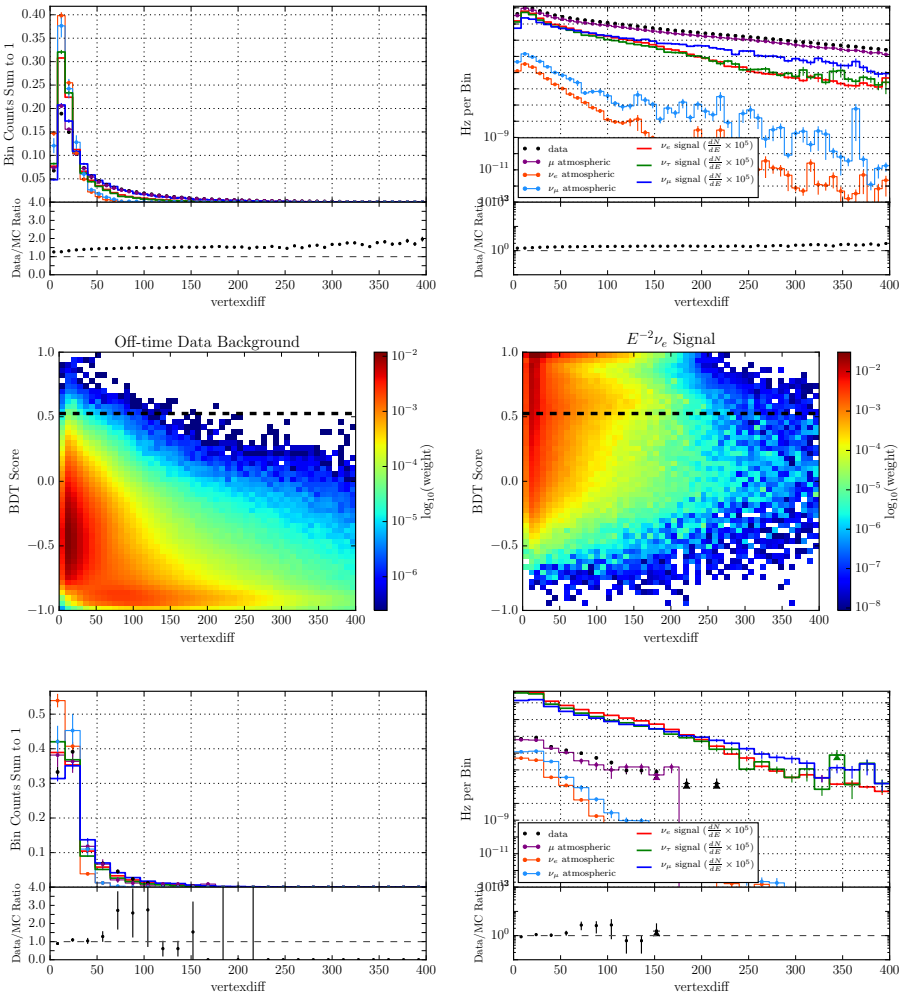

Figure 5.30: vertexdiff. Top: linear (left) and logarithmic (right) Level 3 distributions. Middle: BDT score vs. background (left) and signal (right) distributions. Bottom: final cut level distributions.

5.4.3 Loose Pre-BDT Cuts after Level 3

Before training the BDT, deep tail values of some variables were removed. Because the BDT algorithm uses constant bin widths for each variable histogram at each tree node, bins with poor statistics at outlier values can diminish the separating power of the given variable. Removing these few outlying events from the signal and background datasets allows the BDT to identify the separation where the majority of events in each distribution lie. A possible improvement of the BDT algorithm that would circumvent this step would be to allow varying bin widths by imposing constant total signal and background weights in each bin.

Additionally, and as described above in Section 5.4.2, the track versus cascade likelihood ratio has a very wide range. High energy signal events can end up in the track-like region of the range. This variable's separation power can be strengthened by removing lower-energy background where there is little signal, and this is done before the BDT training as well.

These loose pre-BDT training cuts are as follows:

1. $\mathbf{lfv} \leq 0.5$
2. $-1 \leq \mathbf{t\_lfv\_z\_diff} \leq 1$
3. $-1 \leq \mathbf{t\_lfv\_z\_sum} \leq 1$
4. $\mathbf{ratio\_before\_to\_after\_vertex} \leq 2$
5. $\mathbf{ln}\left(\boldsymbol{L}_{\mathbf{track}}/\boldsymbol{L}_{\mathbf{cscd}}\right) \leq 0.5$ OR $\mathbf{log\,(Qtot)} > 4$

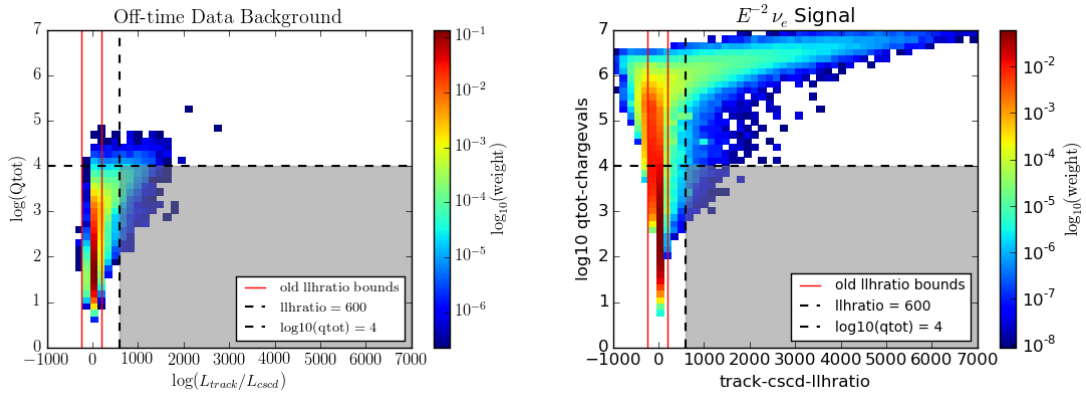

Figure 5.31: Background (left) and signal (right) distributions of the total charge versus track-to-cascade likelihood.

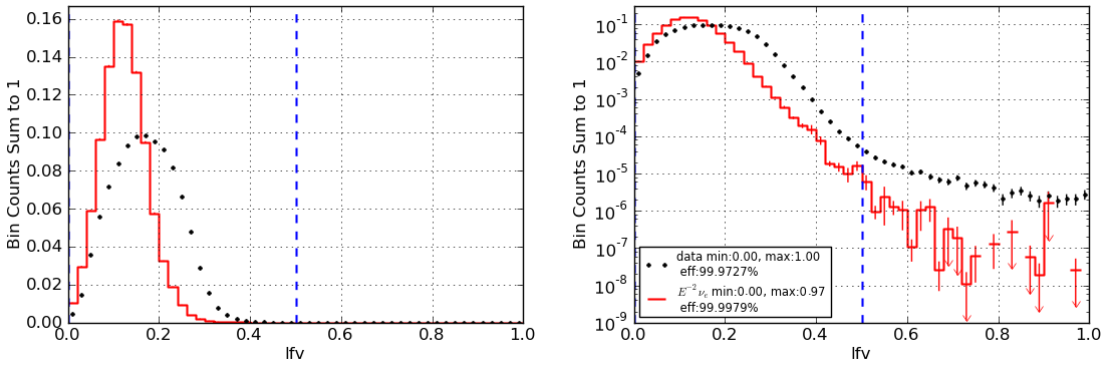

Figure 5.32: Linear (left) and logarithmic (right) distributions of the LineFit speed at L3 for background off-time data and astrophysical ν_e, with the loose pre-BDT cuts as vertical lines.

The removal of this class of events reduces the signal sample by less than 0.3%. The signal and background distributions of the likelihood ratio versus total charge imparted to the DOMs and LineFit speed at Level 3 and their cut values are shown in Figures 5.31 and 5.32.

Two additional pre-BDT cuts are made as well on events that will not contribute to the likelihood analysis. The first of which are those with failed Monopod reconstructions. This reconstruction fails to converge on about 1% of the highest

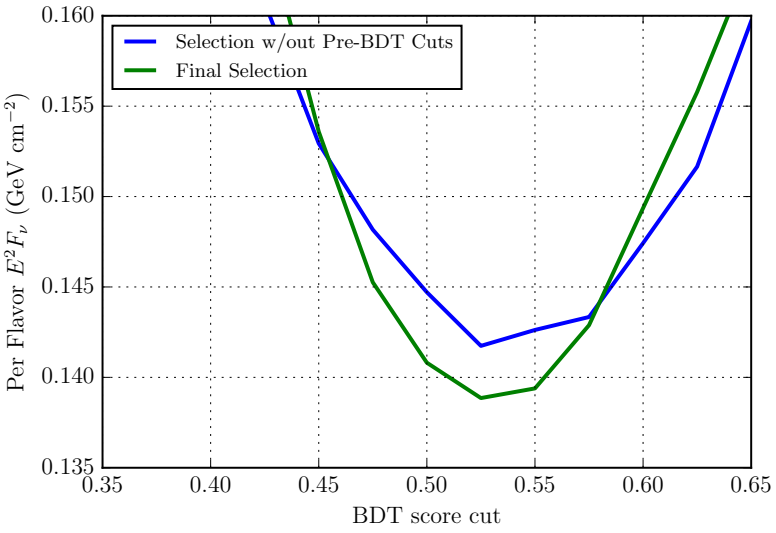

Figure 5.33: Improvement in sensitivity to an E^{-2}-weighted per-flavor neutrino flux with pre-BDT cuts versus without.

energy simulated neutrinos that interact outside of the detector. The second additional cut is on the Cramer-Rao estimated directional error, before the energy-based pull correction that is described in Section 4.2.8. All events that have a Cramer-Rao $\sigma > \pi$ are removed as none would contribute appreciably to a discovery. These discarded events account for less than 1% of all neutrino signal and are typically TeV neutrinos that interaction outside of the detector and so cannot allow very certain reconstructed directions. The improvement in sensitivity, see Chapter 6 for its calculation, is shown in Figure 5.33.

5.4.4 BDT Forest Training

Once the data rate has been reduced to around 0.7 Hz from Trigger to Level 3, and outlier misreconstructed events have been removed, a boosted decision tree

forest is trained and a final collection of data events that very closely resemble astrophysical neutrino interactions in IceCube is attained. The training parameters used are outlined in Section 5.4.1. Simulated E^{-2}-weighted ν_e events were used as known signal and atmospheric muon-dominated data events that occur outside of two hours from any GRB prompt flux were used as known background. A different BDT was trained on each of the three detector configurations' data and simulation due to differences in feature extraction algorithms and event selection at the South Pole.

Half of the available simulated ν_e signal was used for training the BDT model while the other half was used for overtraining testing for each detector configuration. 515391, 131661, and 161555 signal events were used for training in IC79, IC86I, and IC86II, respectively. 793050, 829870, and 745510 background events distributed evenly throughout the year were used for training in IC79, IC86I, and IC86II, respectively. A full-year sample of data was necessary to minimize the effects of the seasonal variation in atmospheric muon and neutrino interaction rates in the detector, described in Section 3.2.2.

The first tree and the last tree with variable cut and purity values at each node for the IC86I forest are shown in Figures 5.34 and 5.35.

Figure 5.36 shows the distributions of IC79 simulation and data with respect to BDT score. The vertical dashed line corresponds to the optimized final cut described in the next section. Also, the survival rates of different backgrounds from data and simulation per cut in BDT score are shown in Figure 5.37. The ν_μ in these plots is already preselected through Levels 2 and 3 to be shower-like and has

minimal overlap with the Northern Hemisphere track search. The overlap is at the level of .05% for background data and 2% for signal ν_μ.

5.4.5 Final Analysis Level

Once each BDT has been sufficiently trained, a final selection on the score is made. This optimal selection is determined by performing the unbinned likelihood analysis, described in the next chapter, on different (BDT score > minimum value) cuts. The chosen selection for each BDT is the minimum score that requires the least amount of signal to surpass thresholds set by the background-only hypothesis.

For each BDT, the optimal final event selection is those events with a score > 0.525. The fact that each detector configuration search yielded the same optimal score cut is not surprising given the very similar event selection levels leading to the machine learning input as well as the fact that the same variables were used in all three BDTs. The ν_e signal efficiency per energy bin with respect to Level 3 for different possible final cuts on the BDT score are shown for the IC79, IC86I, and IC86II searches in Figure 5.39. The energy cutoffs in the 86-string plots are only due to the simulation availability for those configurations. The integrated efficiency and background data rate are given in the legend for each score. The optimal score curves are in bold orange.

The ν_e, ν_τ, and ν_μ efficiency per energy bin for charged-current and neutral-current interactions with respect to Level 3 are shown in Figure 5.38 along with their energy distributions. Hadronic cascades from deep-inelastic neutral current

interactions produce similar spherical Cherenkov light patterns for all neutrino flavors, and therefore exhibit similar efficiency curves. The decrease in high energy astrophysical ν_τ charged-current events at the final level compared to Level 3 is due to the fact that the resulting tau lepton can travel an appreciable in-IceCube distance before decaying. These type of events yield the so-called "double bang" topology. The BDT-based selection of this search is less accepting of these types of tau neutrino events than lower energy ones, where the two cascades are so close together that they are indistinguishable from a single cascade. The efficiency of astrophysical ν_μ charged current events is lower than the other two flavors because, besides the requirement of a large initial hadronic cascade, the resulting muon must catastrophically lose its energy with little observable Cherenkov tail in order to pass the cut. This requirement is reflected in the larger peak ν_μ energy compared to the other flavors.

Table 5.1 shows efficiences and data rates at each event selection level. Figure 5.40 presents the signal efficiency of each event selection level relative to the online Level 2 filter as a function of neutrino energy. The data rate is calculated for one eight hour detector run during the summer and so is at a higher rate than the average. As illustrated in this figure and the others like it above, the efficiency improves dramatically for neutrinos with energies beyond 10 TeV. Many energy-based variables drive the BDT model for this search so that signal neutrinos can be lifted out of the generally lower energy atmospheric muon background.

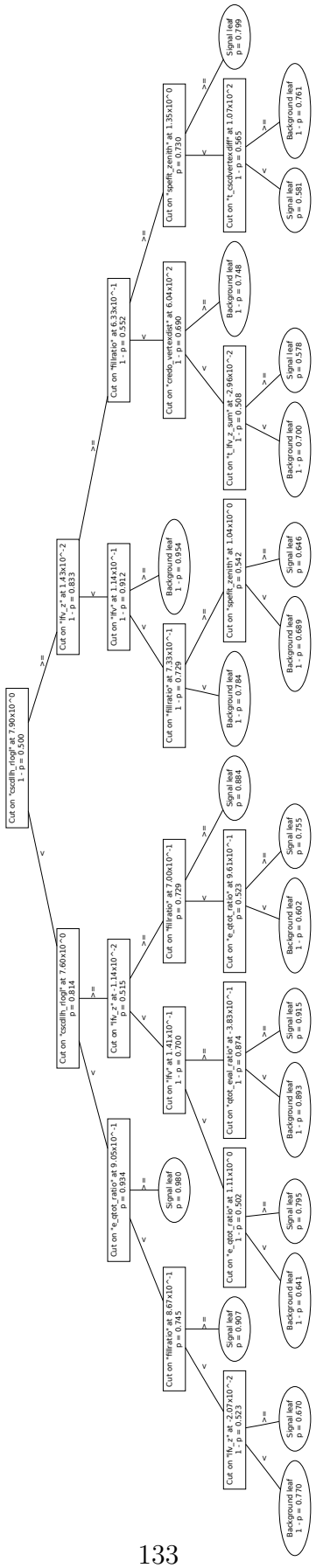

Figure 5.34: First tree in the IC86I BDT forest

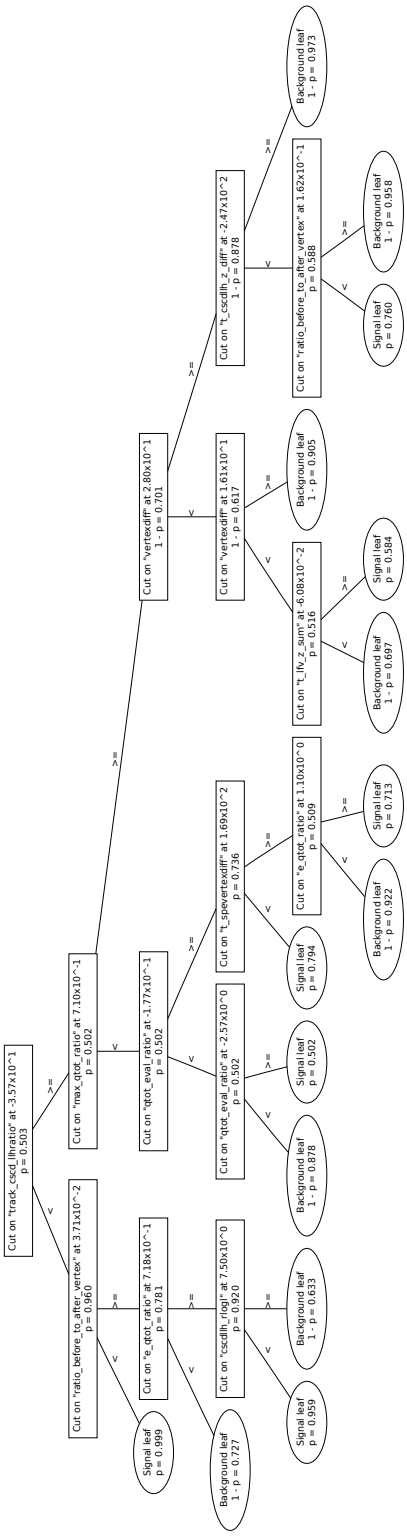

Figure 5.35: Last tree in the IC86I BDT forest

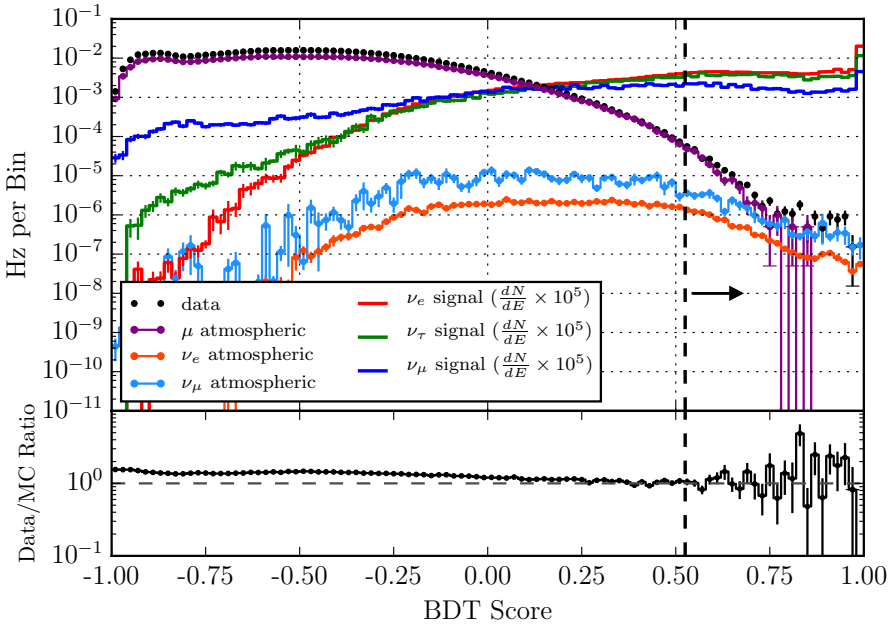

Figure 5.36: Distribution of data, simulated muon background, simulated atmospheric neutrino background, simulated E^{-2}-weighted neutrino signal (where $\frac{dN}{dE} = 10^{-8}\text{GeV}^{-1}\text{cm}^{-2}\text{s}^{-1}\text{sr}^{-1}(\frac{E}{GeV})^{-2}$) with respect to BDT score. The vertical dashed line represents the final analysis cut of > 0.525.

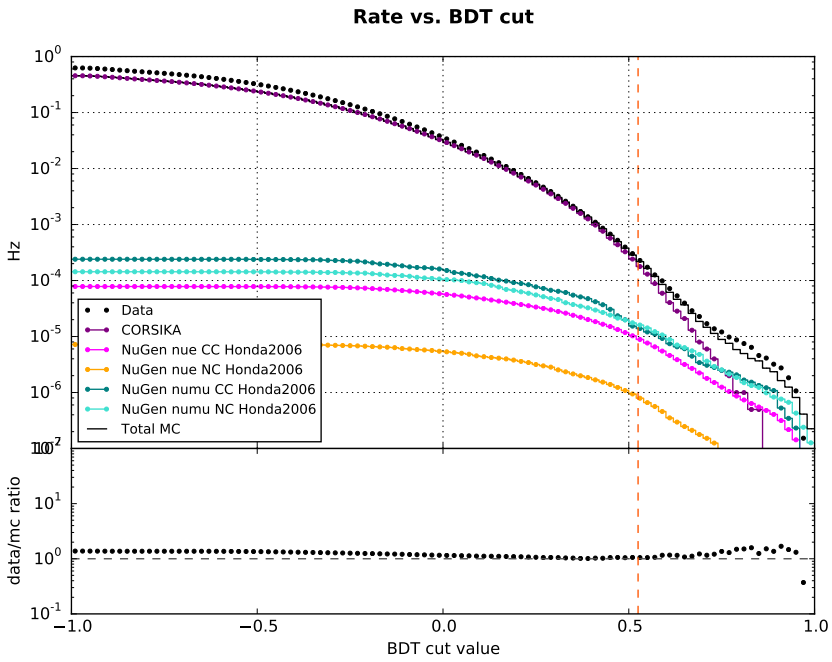

Figure 5.37: Survival rates of different backgrounds as a function of cut on BDT score.

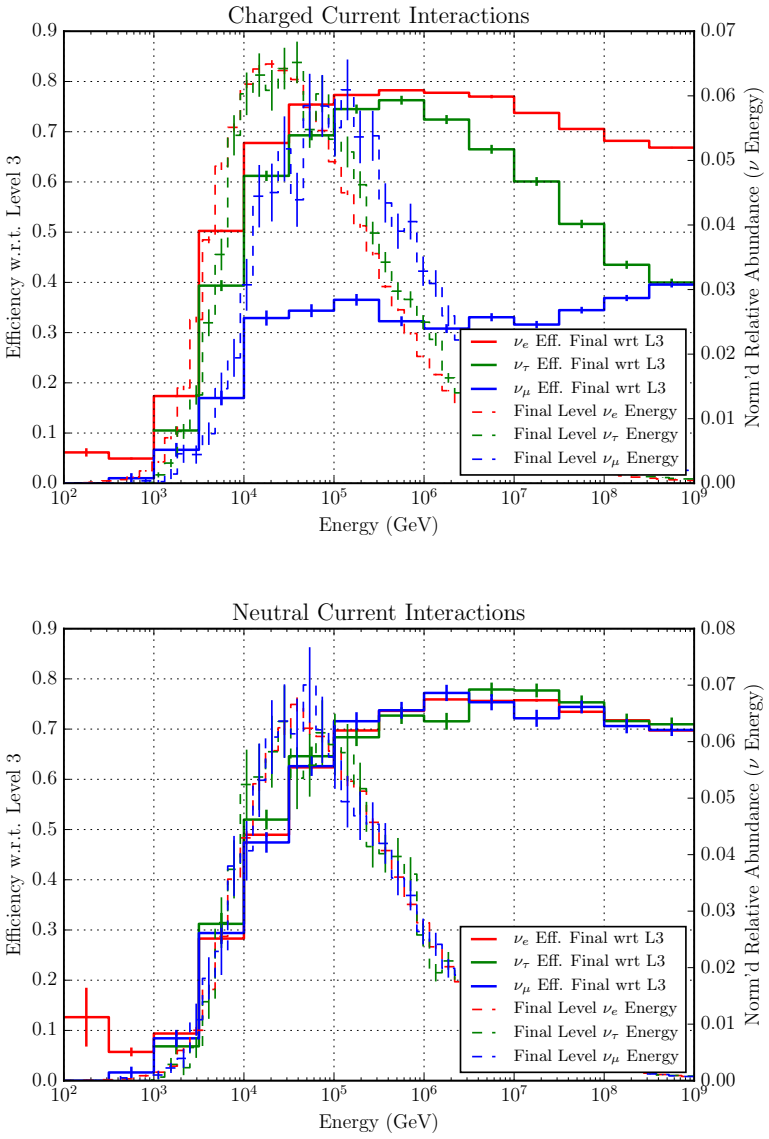

Figure 5.38: E^{-2}-weighted ν_e, ν_τ, and ν_μ efficiency per energy bin for charged-current (left) and neutral-current (right) interactions with respect to Level 3. The normalized energy distributions are also shown.

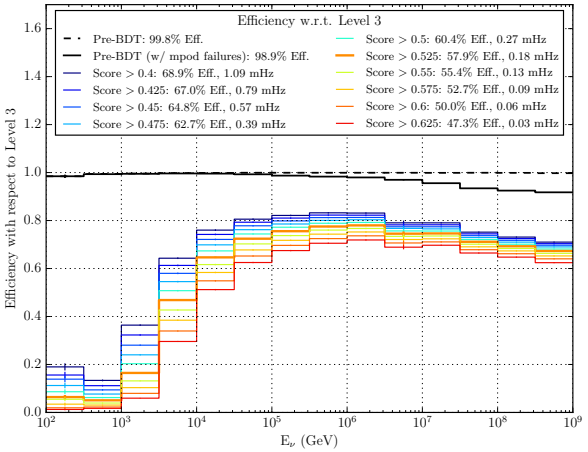

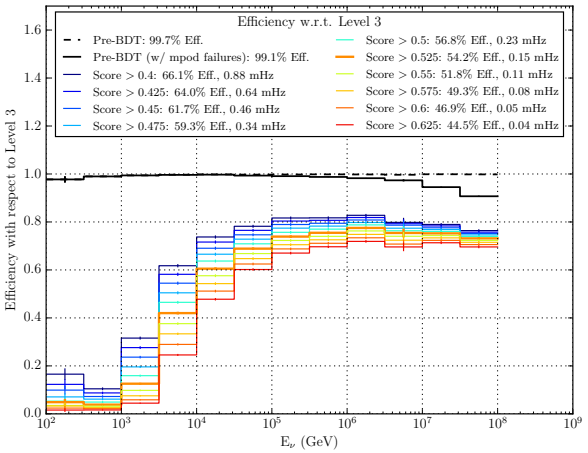

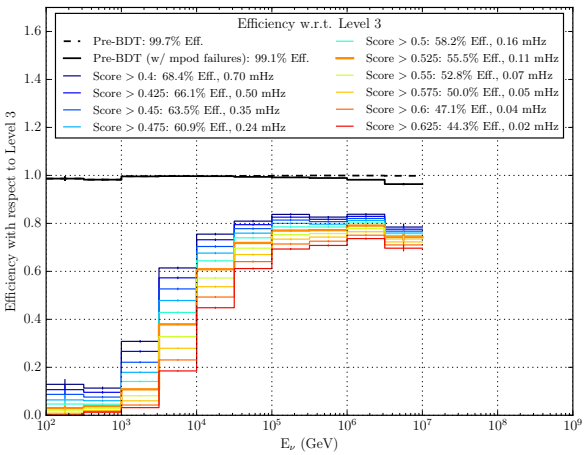

Figure 5.39: E^{-2}-weighted ν_e signal efficiency per energy bin with respect to Level 3 for different possible final cuts on the BDT score. Top: IC79 selection. Middle: IC86I selection. Bottom: IC86II selection.

Cut Level	Signal Efficiency (%)	Background Efficiency (%)	Data Rate (Hz)
Online Filter	–	–	30
Level 3	72	2.5	0.77
Final	54	0.02	1.6×10^{-4}

Table 5.1: Signal and background efficiencies and data rates at different event selection levels averaged over the three search years. Signal is E^{-2}-weighted ν_e simulation. Background is data outside of 2 hours of GRB prompt γ emission.

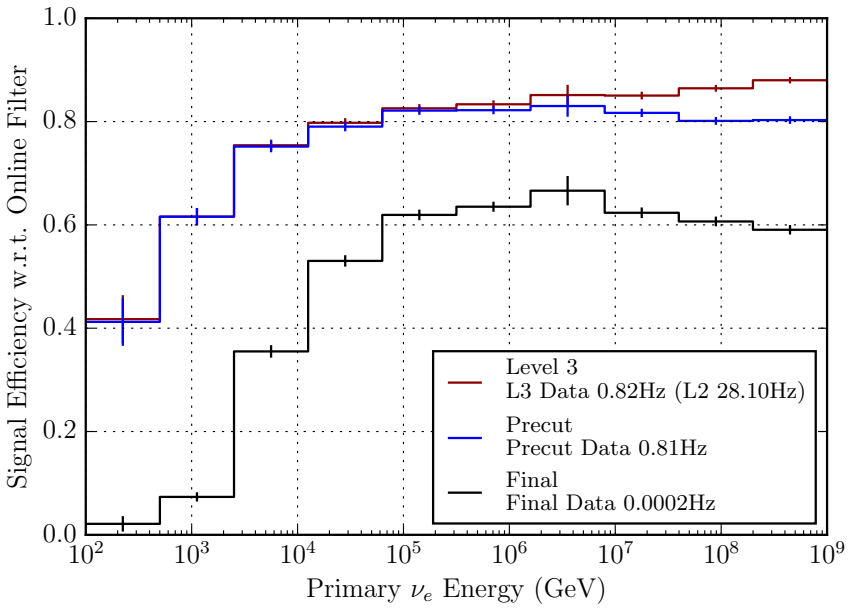

Figure 5.40: E^{-2}-weighted ν_e signal efficiency relative to the online Level 2 filter as a function of neutrino energy. IC79 is shown, while IC86I and IC86II curves are similar.

Compared to the final event samples of IceCube's searches for ν_μ-induced tracks from Northern Hemisphere GRBs, the background in this all-sky all-flavor cascade search requires a cut to a data rate ten times smaller. The disparity between neutrino-induced showers and muon-induced stochastic energy loss showers is less apparent than that between neutrino-induced tracks and detector-edge and coincident muon-induced tracks incorrectly reconstructed as upgoing. In the Northern Hemisphere track searches, most of these muons are able to be removed, leaving only atmospheric neutrinos. The final atmospheric neutrino purity with respect to muons in this search is significantly less ($\sim$40% to $\sim$90%) as a result. Nevertheless, similar sensitivity to the track search is achieved through this search's acceptance of ν_e, ν_τ, and ν_μ signal from GRBs over the entire sky. The top plot of Figure 5.41 compares the effective areas for the two different GRB neutrino searches, while the bottom compares the effective areas for the three cascade search seasons over different detector configurations. The maximum energy in the bottom plot is at the limit of available IC86II simulation at the time of this analysis.

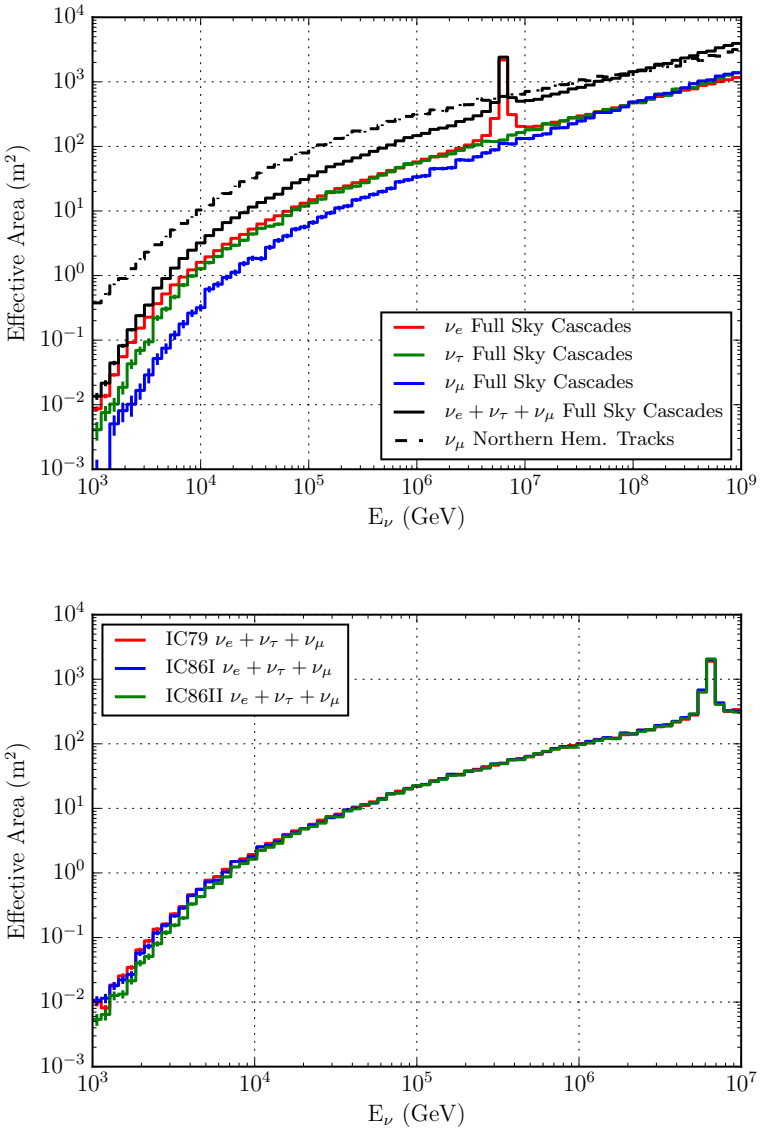

Figure 5.41: Left: three-flavor effective areas for the full-sky shower-like and Northern Hemisphere track-like GRB-coincident event searches with the 79 string detector. Right: effective areas for IC79, IC86I, and IC86II.

Chapter 6

Unbinned Likelihood Method

Once a final sample of events that resemble high energy neutrino-induced electromagnetic or hadronic showers is selected, the likelihood that these events are neutrino signal from observed GRBs must be calculated. This calculation involves a likelihood function that incorporates the probabilities that an event is a signal neutrino from a GRB or a background atmospheric neutrino or muon. These background-like and signal-like probabilities are determined from individually normalized probability distribution functions (PDFs) in time, space, and energy:

$$\begin{aligned} S(\overrightarrow{x_i}) &= P_s^{Time}(t_i) \times P_s^{Space}(\overrightarrow{r_i}) \times P_s^{Energy}(E_i) \\ B(\overrightarrow{x_i}) &= P_b^{Time}(t_i) \times P_b^{Space}(\overrightarrow{r_i}) \times P_b^{Energy}(E_i) \end{aligned} \tag{6.1}$$

where S and B are the probabilities that an event i with properties $\overrightarrow{x}_i$ is signal and background, respectively.

In order to choose the optimal final cut on BDT score and characterize the significance of the result, a test statistic is constructed in the form of a maximum likelihood function. This function incorporates probabilities that observed events are signal and background as well as provides an estimator for the number of observed signal events. The likelihood function combines the signal and background PDFs with the Poisson probability P_N of observing N events, given an expected number

of signal + background events.

This analysis was developed in a blind manner in order to optimally reduce bias [128]. As mentioned in Section 5.4.1, events in the muon-dominated data outside of two hours from any recorded GRB T_{100} are used to characterize the background. The BDTs described in Chapter 5 are trained and the likelihood analysis described in this chapter is developed on these blind data. IceCube data taken within two hours of GRBs are untouched during the development of this analysis and, after thorough review by the collaboration, "unblinded" and analyzed. The results of this unblinding are presented in Chapter 7.

6.1 The Test Statistic

In this analysis, the number of signal events to be measured is unknown ahead of time. The test statistic derived below provides an estimator for the number of observed signal events in the form of a maximum likelihood function that depends on measures of signal and background characteristics.

For a collection of n events, each with properties $\overrightarrow{x_i}$, represented by $\{x_1, x_2, ..., x_n\} = \{\overrightarrow{x_i}\}$ and probability $p(x; a)$, in which a is some unknown parameter, the likelihood function is a product of probabilities.

$$\mathcal{L}(\{\overrightarrow{x_i}\}; a) = p(x_1; a)p(x_2; a)...p(x_n; a) = \prod_{i=1}^{n} p(x; a) \tag{6.2}$$

The first probability function in the likelihood is the probability of observing n events under the assumption that the expected total number of events is N. This

probability is defined by Poisson statistics.

$$P_{\text{Poiss}}(n;N) = \frac{N^n \mathrm{e}^{-N}}{n!} \tag{6.3}$$

The remaining probability functions $\mathcal{P}(\overrightarrow{x_i})$ are the probabilities that each event i has properties $\overrightarrow{x_i}$. One can define $\mathcal{P}$ in the context of expected signal and background, where

$$N = n_s + n_b \tag{6.4}$$

Let the probabilities of observing a signal(s) and background(b) event be defined as

$$p_s = \frac{n_s}{N}, p_b = \frac{n_b}{N} \tag{6.5}$$

Let the probabilities of signal and background events having properties $\overrightarrow{x}$ be defined as $\mathcal{S}(\overrightarrow{x})$ and $\mathcal{B}(\overrightarrow{x})$. Thus, $\mathcal{P}$ can be defined as

$$\mathcal{P}(\overrightarrow{x}) = p_s \mathcal{S}(\overrightarrow{x}) + p_b \mathcal{B}(\overrightarrow{x}) \tag{6.6}$$

So now one may write the likelihood function as

$$\mathcal{L}(\{\overrightarrow{x_i}\}; N) = \frac{N^n \mathrm{e}^{-N}}{n!} \prod_{i=1}^{n} \mathcal{P}(x;a) \tag{6.7}$$

The goal is to maximize $\mathcal{L}$ and since the logarithm is a monotonic function, maxi-

mizing $\ln \mathcal{L}$ maximizes $\mathcal{L}$.

$$\begin{aligned}
\ln \mathcal{L}(\{\overrightarrow{x_i}\}; N) &= \ln \frac{N^n \mathrm{e}^{-N}}{n!} + \sum_{i=1}^{n} \ln \mathcal{P}(\overrightarrow{x_i}) \\
&= n \ln N - N - \ln n! + \sum_{i=1}^{n} \ln \mathcal{P}(\overrightarrow{x_i}) \\
&= -N - \ln n! + \sum_{i=1}^{n} \ln \left[N \mathcal{P}(\overrightarrow{x_i}) \right] \\
&= -N - \ln n! + \sum_{i=1}^{n} \ln \left[n_s \mathcal{S}(\overrightarrow{x}) + n_b \mathcal{B}(\overrightarrow{x_i}) \right]
\end{aligned} \tag{6.8}$$

Now the aim is to manipulate $\mathcal{L}(\{\overrightarrow{x_i}\}; n_s)$ into a useful form for this particular analysis. Since N is an expectation, one determines n_b from off-source data ($\langle n_b \rangle$) and one determines n_s from maximizing $\mathcal{L}$ with respect to it ($\hat{n}_s$). Further, the above likelihood function is simplified by dividing by its null hypothesis

$$\ln \mathcal{L}_0(\{\overrightarrow{x_i}\}) = \ln \mathcal{L}(\{\overrightarrow{x_i}\}; n_s = 0) = -\langle n_b \rangle - \ln n! + \sum_{i=1}^{n} \ln \left[\langle n_b \rangle \mathcal{B}(\overrightarrow{x_i}) \right] \tag{6.9}$$

Dividing the likelihood function by a single scalar has no effect on its maximum value.

$$\begin{aligned}
\ln \mathcal{L}_{\mathcal{R}}(\{\overrightarrow{x_i}\}; n_s) &= \ln \frac{\mathcal{L}(\{\overrightarrow{x_i}\}; n_s)}{\mathcal{L}_0(\{\overrightarrow{x_i}\})} \\
&= -n_s + \sum_{i=1}^{n} \ln \left[n_s \mathcal{S}(\overrightarrow{x_i} + \langle n_b \rangle \mathcal{B}(\overrightarrow{x_i}) \right] - \sum_{i=1}^{n} \ln \left[\langle n_b \rangle \mathcal{B}(\overrightarrow{x_i}) \right] \\
&= -n_s + \sum_{i=0}^{n} \ln \left[\frac{n_s \mathcal{S}(\overrightarrow{x_i})}{\langle n_b \rangle \mathcal{B}(\overrightarrow{x_i})} + 1 \right]
\end{aligned} \tag{6.10}$$

The estimated number of signal events $\hat{n}_s$ maximizes the likelihood function.

$$\left.\frac{\partial \ln \mathcal{L}_{\mathcal{R}}(\{\overrightarrow{x_i}\}\,; n_s)}{\partial n_s}\right|_{n_s=\hat{n}_s} = 0 \tag{6.11}$$

Finally, the analysis test statistic is defined as the logarithm of this maximum value of the likelihood function.

$$T = \ln \mathcal{L}_{\mathcal{R}}(\{\overrightarrow{x_i}\}\,; \hat{n}_s) = -n_s + \sum_{i=0}^{n} \ln\left[\frac{n_s \mathcal{S}(\overrightarrow{x_i})}{\langle n_b \rangle \mathcal{B}(\overrightarrow{x_i})} + 1\right] \tag{6.12}$$

6.2 Probability Distribution Functions

PDFs are calculated in time, space, and energy for signal GRB-emitted neutrinos and background atmospheric muons using the GRBs and data for each of the three data-taking seasons. As described in previous chapters, simulated neutrinos are used for signal and muon-dominated data are used for background. The PDFs capture the likelihood that signal neutrinos should be on-time and on-direction with recorded GRBs and higher energy than background muons. This likelihood then is evaluated in a single test statistic (Equation 6.12) for events in the final data sample of each season.

6.2.1 Time PDFs

The signal time PDF is flat during the gamma-ray emission duration (T_{100} defined in Section 2.3) and has Gaussian tails before T1 and after T2. The width of these Gaussian tails σ_t equals the duration of measured gamma-ray emission up

to 30 s and down to 2 s to account for possible small shifts in the neutrino emission time with respect to that of the photons. Events are accepted out to $\pm 4\sigma_t$ for each GRB time window. The background time PDF is flat throughout the total period of acceptance for each GRB. Examples of the signal time PDF ratios for short, medium, and long duration bursts are given in Figure 6.1.

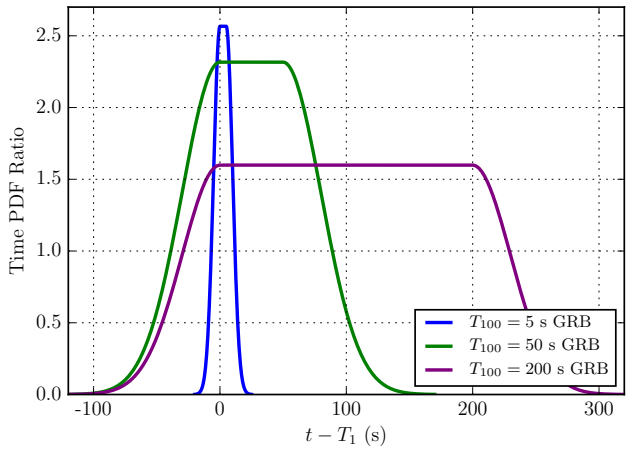

Figure 6.1: Signal / background time PDF ratios for events during and near example GRBs with different measured T_{100} values.

6.2.2 Space PDFs

The signal space PDF is a Kent distribution [129]:

$$P_s^{Space}(\overrightarrow{r_i}, \kappa) = \frac{\kappa}{4\pi \sinh(\kappa)} \mathrm{e}^{\kappa(\hat{r}_i \cdot \hat{r}_{GRB})} \tag{6.13}$$

for which the concentration parameter $\kappa = \frac{1}{\sigma_{GRB}^2 + \sigma_i^2}$ is the reciprocal of the uncertainty in the GRB's localization and the Cramer-Rao uncertainty in the event's reconstructed direction. $\hat{r}_i$ is the reconstructed direction of the event and $\hat{r}_{GRB}$ is

the most precise GRB localization available.

If the most precise GRB localization is from the FermiGBM detector, then its systematic error is included as well. FermiGBM models its systematic error as a sum of 2.6° with 72% weight and 10.4° with 28% weight Gaussian errors [34]. Both of these systematic error components is added in quadrature to the statistical error, listed in the Appendix A tables. For FermiGBM-localized bursts, the two concentration parameters are $\kappa_{2.6} = \frac{1}{(2.6^\circ)^2+\sigma_{GRB}^2+\sigma_i^2}$ and $\kappa_{10.4} = \frac{1}{(10.4^\circ)^2+\sigma_{GRB}^2+\sigma_i^2}$. The signal space PDF then becomes:

$$P_s^{Space}(\overrightarrow{r_i}, \kappa) = 0.72 \times P_s^{Space}(\overrightarrow{r_i}, \kappa_{2.6}) + 0.28 \times P_s^{Space}(\overrightarrow{r_i}, \kappa_{10.4}) \tag{6.14}$$

The background space PDF is a spline fit to the distribution of reconstructed $\cos(\theta_{zenith})$ of all final cut level off-time data events. Because the dominating muon background physically originates from only positive zenith values, higher background weight is given to events reconstructed to originate from the Southern Hemisphere. The negative zenith range of the background space PDF has contributions from both misreconstructed muons as well as Earth-penetrating atmospheric neutrinos. Small variance in the background reconstructed azimuth distribution has negligible impact on this analysis, and so the background space PDF only varies with zenith.

The signal space PDFs are shown in Figure 6.2 for different combined event direction and GRB localization uncertainties. The background space PDFs at final event selection for the IC79, IC86I, and IC86II searches are shown in Figure 6.3.

As discussed in Section 4.2.7, five iterations of the Monopod reconstruction

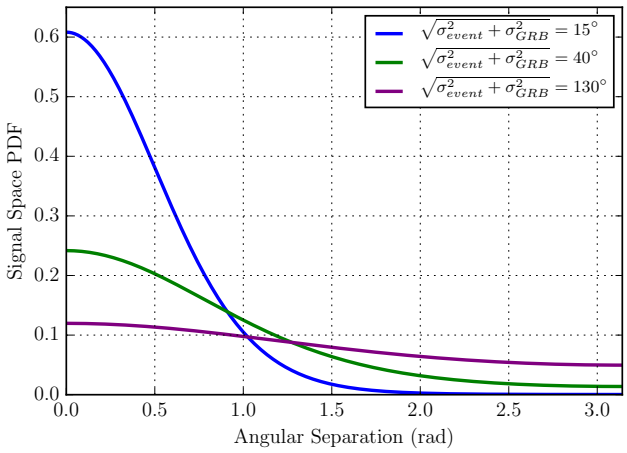

Figure 6.2: Signal space PDFs for three example events and correlated GRBs.

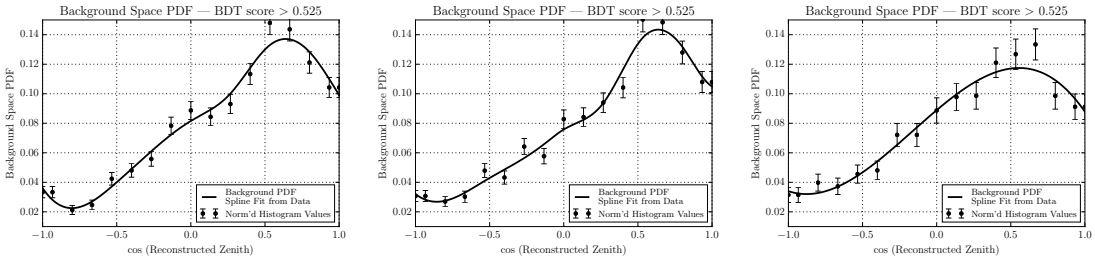

Figure 6.3: Background space PDF, calculated from a spline fit to the zenith distribution of data events at final event selection for the IC79 (left), IC86I (center), and IC86II (right) searches.

achieves the best angular resolution and therefore is used for the signal and background space PDF calculations. Figure 6.4 shows the cumulative point spread function of ν_e, ν_τ, and ν_μ signal at the final event selection, at which all interactions exhibit spherical cascade-like hit patterns. In this plot, each y-axis value is the percentage of events that yield less than or equal to the corresponding angular difference between truth and Monopod reconstruction on the x-axis.

Directional error estimators, including the Cramer-Rao calculation used in this

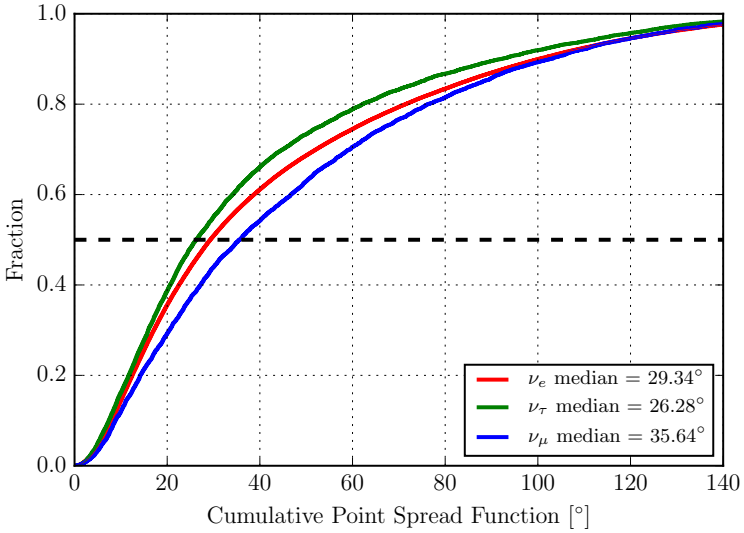

Figure 6.4: Cumulative point spread functions with median angular resolutions shown of simulated astrophysical ν_e, ν_τ, and ν_μ at final event selection.

analysis and described in Section 4.2.8, have been observed to underestimate the degree of misreconstructed direction on IceCube events. These underestimations increase with energy and are likely due to imperfections in the modeling of the ice. To correct σ_{CR}, a rescaling is applied as a function of the Monopod energy. This rescaling is calculated by a spline fit to the ratio of the actual error in reconstructed direction to the Cramer-Rao estimated error, the "pull," versus Monopod energy for E^{-2}-weighted ν_e signal. This spline fit is applied to the 39th percentile pull value, which is the 1σ percentile for the 2D normal distribution.

The corrective spline is calculated in this way for each detector configuration at Level 3, for sufficient statistics. Before the pseudo-search trials and unbinned likelihood analysis are performed, the correction for σ_{CR} is applied to the data and simulated ν_e, ν_τ, ν_μ signal events based on each event's original Cramer-Rao estimation

and reconstructed energy. The ν_e signal $\log_{10}(\sigma_{True}/\sigma_{CR})$ vs. $\log_{10}(\text{Monopod.energy}/GeV)$ distributions before and after the spline correction for each detector are shown in Figures 6.5 and 6.6.

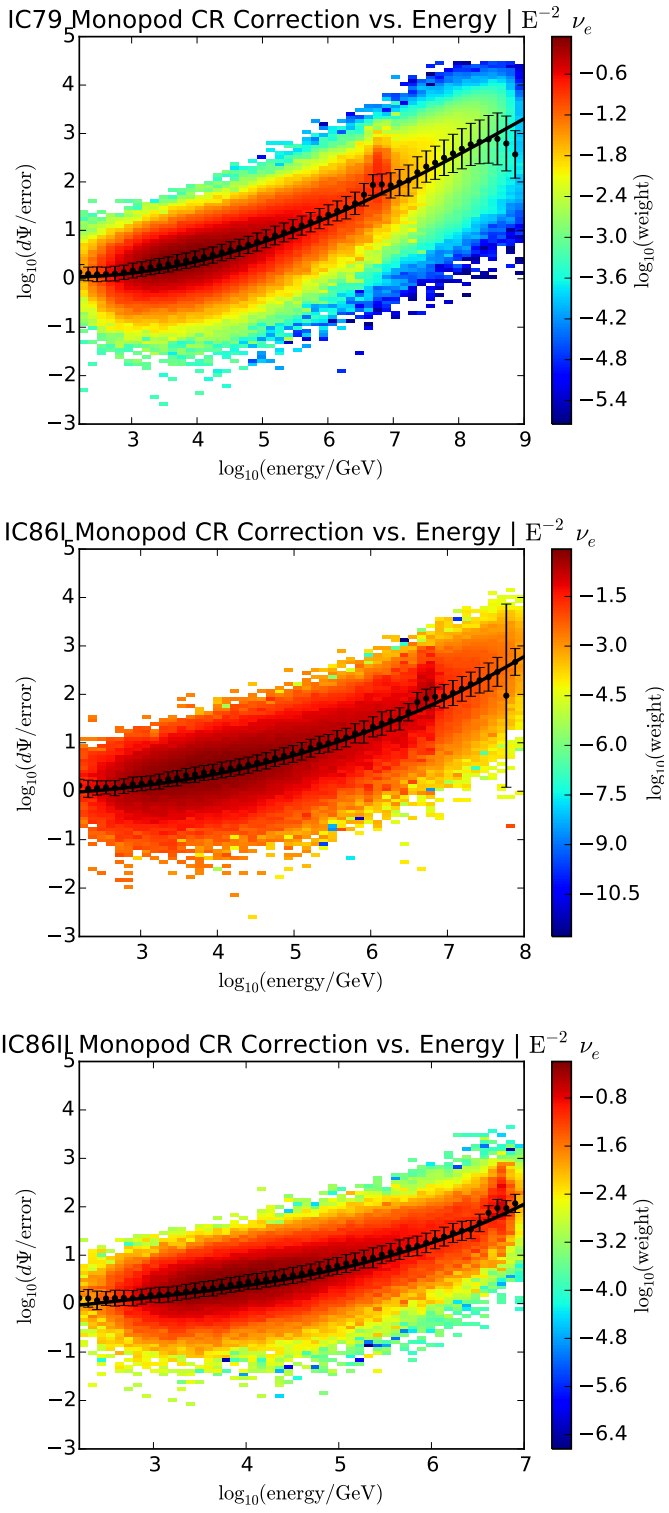

Figure 6.5: Spline correction (black lines) to Cramer-Rao estimated directional uncertainty for E^{-2}-weighted ν_e simulated events at Level 3 event selection, for IC79 (top), IC86I (center), and IC86II (bottom).

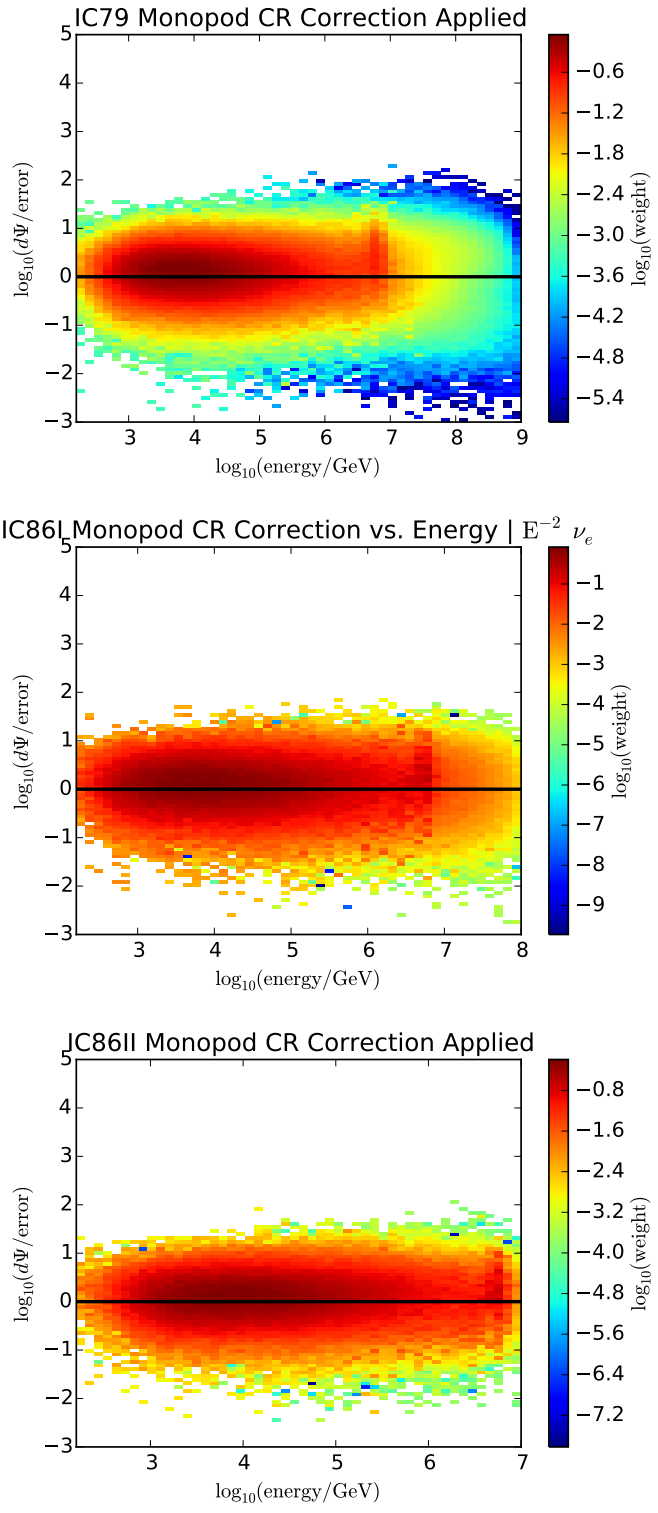

Figure 6.6: Applied spline correction (black lines) to Cramer-Rao estimated directional uncertainty for E^{-2}-weighted ν_e simulated events at Level 3 event selection, for IC79 (top), IC86I (center), and IC86II (bottom).

6.2.3 Energy PDFs

The signal and background energy PDFs are the reconstructed energy distributions of E^{-2}-weighted ν_e simulation and off-time data, respectively. A spline is fit to the ratio of these two PDFs. Few background events in the final sample have reconstructed energies above 1 PeV, and so a constant ratio of signal and background energy PDFs is conservatively assumed at energies above 1 PeV. The signal and background energy PDFs, their spline-fit ratio, and the values that correspond to the two most significant events in the search are shown for the IC79, IC86I, and IC86II searches in Figure 6.7.

As with the space PDFs, five-iteration Monopod is used for the reconstructed energy in the signal and background energy PDFs. The reconstructed energy versus true energy for simulated ν_e signal at the Level 3 event selection is plotted in Figure 6.8 for charged-current (left) and neutral-current (right) interactions in and around the detector volume. The energy resolutions for the three E^{-2}-weighted neutrino flavors at final event selection for charged-current (left) and neutral-current (right) interactions are plotted in Figure 6.9. The reconstructed energy for neutral current interactions is less than that of the primary neutrino because of the energy dissipation to outlets without Cherenkov emission.

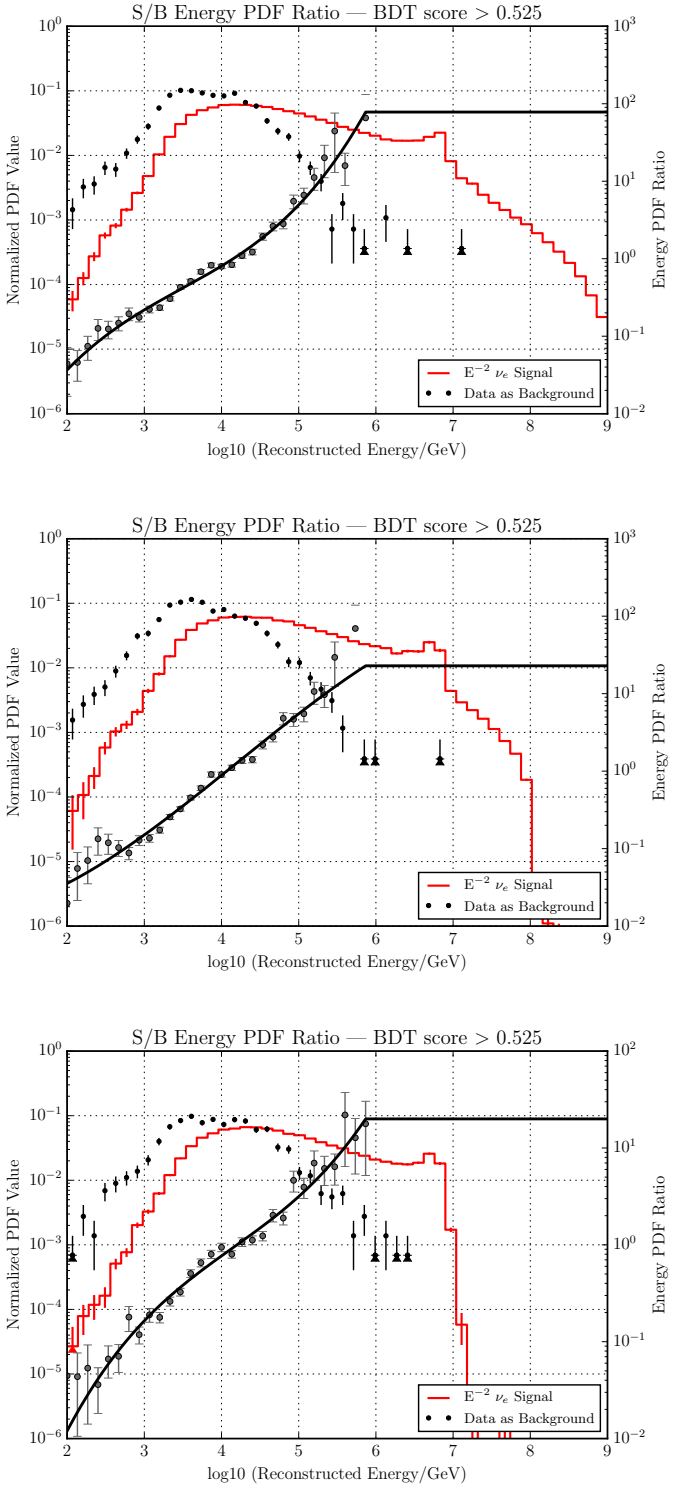

Figure 6.7: IC79 (top), IC86I (middle), and IC86II (bottom) energy PDF ratios. Left vertical axis: Reconstructed energy distributions of data (dots) and E^{-2}-weighted ν_e signal (red line) at final cut level. Right vertical axis: Signal / background energy PDF distribution (black lines) calculated from a spline fit to the ratio of the two energy distributions.

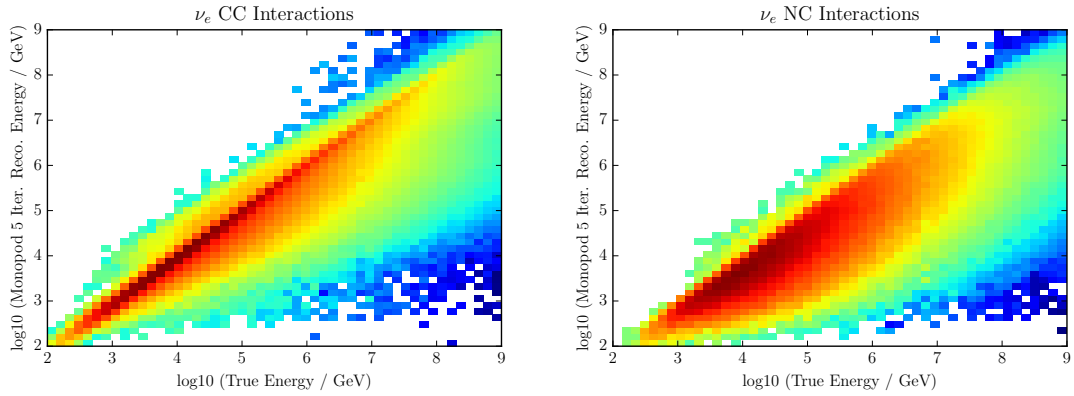

Figure 6.8: Left: Five iteration Monopod reconstructed energy versus Monte Carlo truth energy for E^{-2}-weighted ν_e charged-current (left) and neutral-current (right) interactions in the ice.

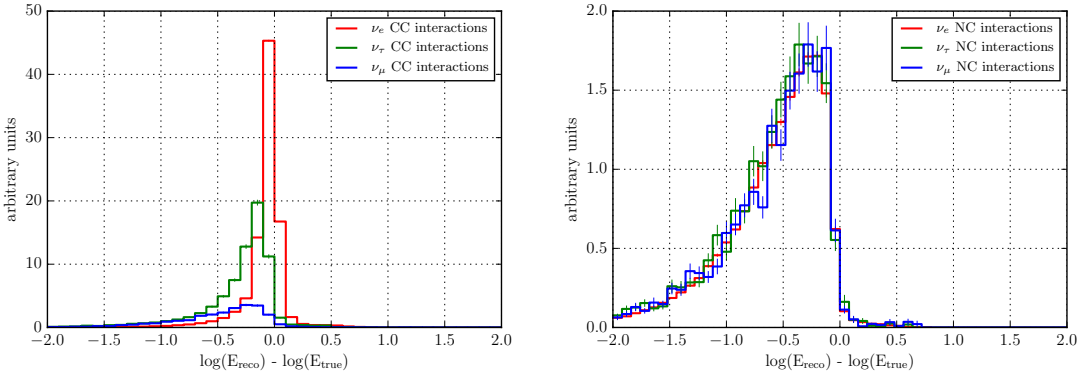

Figure 6.9: Left: Energy resolution per neutrino flavor for charged-current interactions at final selection. Right: Energy resolution per neutrino flavor for neutral-current interactions at final selection.

6.3 Pseudo-Experiment Methodology

To set discovery significance thresholds, first 10^8 pseudo-search trials are performed using only background data for a range of BDT score cuts. As was defined in the BDT training, background events are taken from data (which are dominated by atmospheric muons, even at final selection level) with interaction times outside of two hours from a GRB T_{100}. Each background sample has its own $\langle n_b \rangle_{cut}$ estimated by multiplying the off-time data rate by the summed search windows about all GRB times, $\sum_i^{N_{GRBs}} (T_{100,i} + 8\sigma_{t,i})$. Lower $\langle n_b \rangle_{cut}$ values are expected for tighter BDT score cuts.

In each background-only trial, for each GRB, a pseudo-random number of observed events is chosen within the $T_{100} \pm 4\sigma_t$ search time window about the gamma-ray emission from a Poisson distribution with expectation determined by the background data rate and time window. If the number of events is 0, then T receives no contribution from the search window about that GRB. If the number of events is greater than 0, then each event is constructed using the following steps: (1) choose a random time PDF value; (2) choose a random azimuth within 0 to 2π; (3) choose a reconstructed energy by sampling from the background distribution; (4) choose a reconstructed zenith by sampling from the background distribution of events with similar energy; (5) choose an estimated error in reconstructed direction by sampling from the background distribution of events with similar energy and zenith. Finally, with the signal and background PDF values for every event, the test statistic is calculated for each trial. A distribution like those shown in Figure

6.13 is obtained for every cut on BDT score.

6.4 Sensitivity and Discovery Potentials

The optimal final cut on BDT score is chosen by injecting simulated neutrino signal along with background data and performing 10^4 pseudo-search trials for a range of BDT score cuts. Electron, tau, and muon neutrinos are used for signal injection with equal weight because of the expected 1:1:1 astrophysical flavor ratio at Earth. The background events are selected for each GRB using the same prescription detailed above in Section 6.3 for the background-only trials. The simulated signal events within an 11° circle about each GRB contribute to the likelihood with probabilities proportional to their simulated weights. Signal is increasingly weighted until a certain discovery or limit-setting threshold is reached.

The cuts on BDT score that allow the best possible upper limit, defined as the lowest signal flux required to surpass the median T value in 90% of the trials, and the best discovery potential, defined as the lowest signal flux required to surpass the 5σ T value in 50% of the trials, is determined. The final cut was optimized to set the best possible upper limit while suffering little loss in discovery potential. This final level of event selection is the loosest one that includes possible borderline interesting events while also providing strong limit setting and discovery capabilities. The final cut on BDT score is score > 0.525 for each detector configuration's BDT.

These discovery and limit-setting potentials per BDT score cut are shown in Figure 6.10 for a general E^{-2} spectrum for each of the three search seasons. For

the E^{-2}-weighted spectrum, the IC86I and IC86II the neutrino fluence required for the various discovery thresholds are a few percent larger than what is required for IC79. These differences are due to the limited high energy statistics in the available simulated neutrino datasets in IC86I and IC86II. Additionally, the extremely long GRB111209A during IC86I allows more background in each trial compared to that of the other two seasons. Removing this burst from the optimization reduces the required signal fluence for discovery by 4% without changing the optimal final cut.

The discovery and limit-setting potentials per BDT score cut are shown in Figure 6.11 for the benchmark standard internal shock fireball, the photospheric fireball, and the ICMART fireball spectra plotted in the top panel of Figure 2.9. These curves were calculated using the IC79 datasets. The photospheric model predicts more neutrinos to be detected in IceCube than the standard internal shock model, and therefore requires a lower multiplying factor to surpass a given test statistic threshold. The inverse is true for the ICMART model.

The sensitivity and discovery potential for a given selection on BDT score can be expressed on the so-called Frequentist Plane shown in Figure 6.12. The vertical axis is the per-flavor neutrino signal fluence injected in order to obtain the horizontal axis test statistic value $x\%$ of the time, where x is given by the color scale.

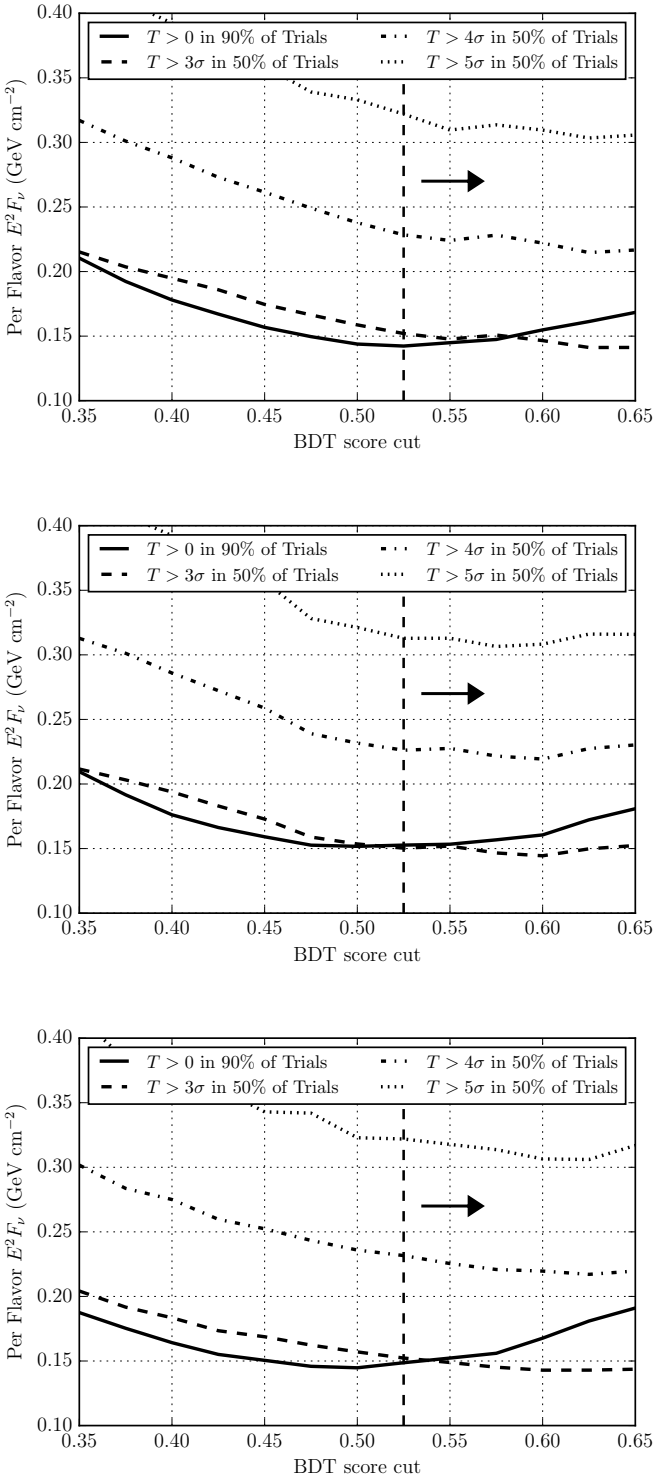

Figure 6.10: Limit setting and discovery potentials per BDT score cut for IC79 (top), IC86I (middle), and IC86II (bottom). Horizontal axis corresponds to a cut on BDT score greater than the given value. The vertical axis corresponds to the E^{-2}-weighted spectrum signal weight needed in order to reach the given threshold. The vertical dashed line represents the final analysis cut of BDT score > 0.525.

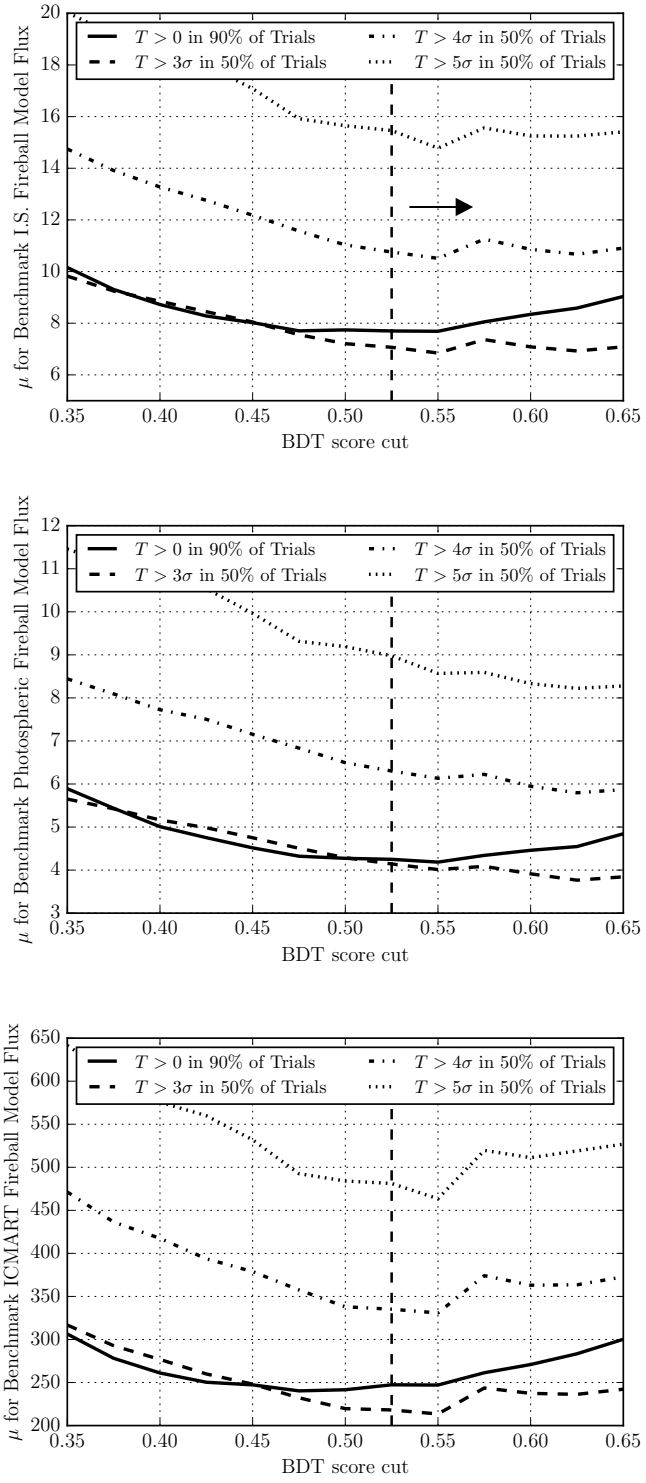

Figure 6.11: IC79 season limit setting and discovery potentials per BDT score cut for internal shock (top), photospheric (middle), and ICMART (bottom) models. Horizontal axis corresponds to a cut on BDT score greater than the given value. Vertical axis corresponds to the multiplying factor μ on the benchmark fireball model neutrino flux shown in Figure 2.9 in order to reach the given threshold. The vertical dashed line represents the final analysis cut of BDT score > 0.525.

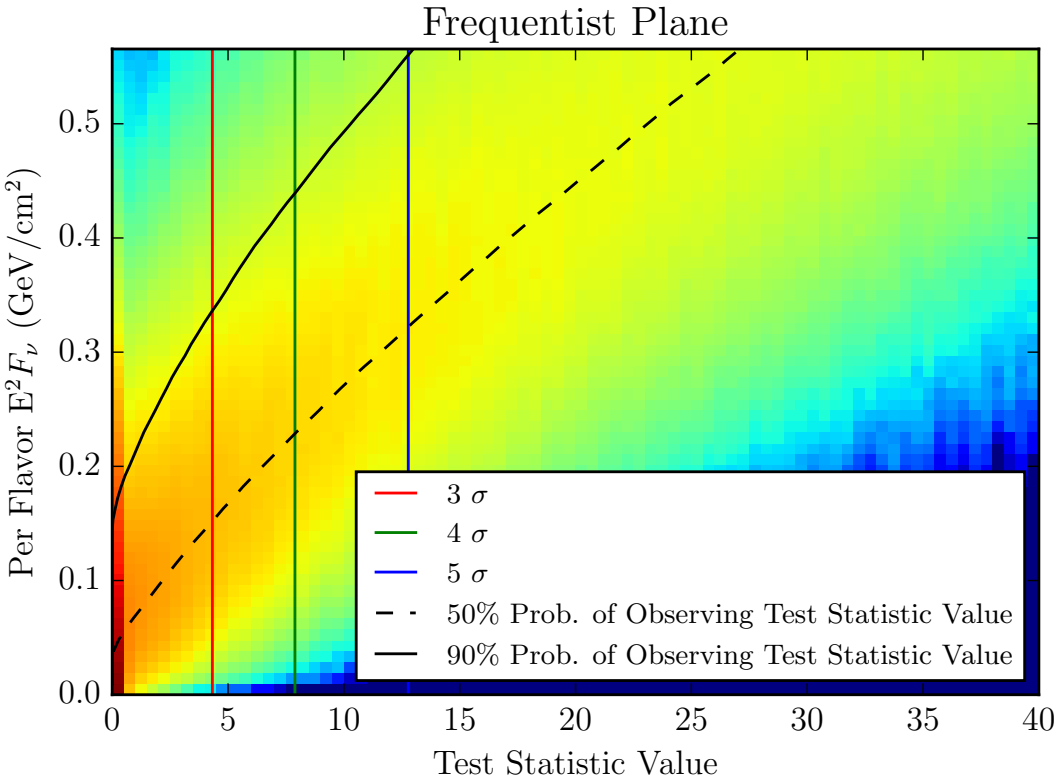

Figure 6.12: Frequentist plane for IC79 signal injection over background at final event selection level. The color corresponds to the probability of observing the test statistic value given the signal strength.

6.5 Per-GRB Optimization Studies

An alternative implementation of the stacked T unbinned likelihood analysis discussed above that gives more significance to individual GRBs has been studied [130]. If a single GRB in a stacked search dominates the neutrino flux, then calculating the test statistic on a per-burst basis improves the discovery potential for such a scenario. The only modification needed to Equation 6.12 is that n_s, $\langle n_b \rangle$, and consequently T are calculated for each burst. Then for each trial or final measurement, the maximum per-burst test statistic $max(T_g)$ is reported. This method also gives higher weight to multiple neutrinos coincident with the same GRB, whereas the stacked T method used in this analysis does not.

The background-only test statistic distributions for the current stacked T method (left) and the $max(T_g)$ method (right) are shown in Figure 6.13. The median null hypothesis value using the current method is zero but it is nonzero using $max(T_g)$ because $\langle n_b \rangle$ is greatly reduced when only applied to a single GRB's T_{100}, which allows many more non-zero test statistic values. In Figure 6.14, the $max(T_g)$ discovery potential curves are worse than those for the stacked T method for an E^{-2} fluence distributed by a sample of bursts over the whole sky. The current stacking analysis combines coincidences across multiple GRBs and thus should do better in this scenario. In Figure 6.15, the $max(T_g)$ method shows to be more powerful than the stacked T method for observing a single random injected signal source. Additionally, a much looser final cut is allowed by the $max(T_g)$ calculation because background contamination is relatively minor for a wide range of event selections.

This search was only optimized using the stacked T methodology. However, future stacked and near-real-time searches will be optimized on the per-burst $max(T_g)$. The results then will have the abilities to be more sensitive to a single burst neutrino fluence and to set strong limits while accruing a minor trials factor penalty.

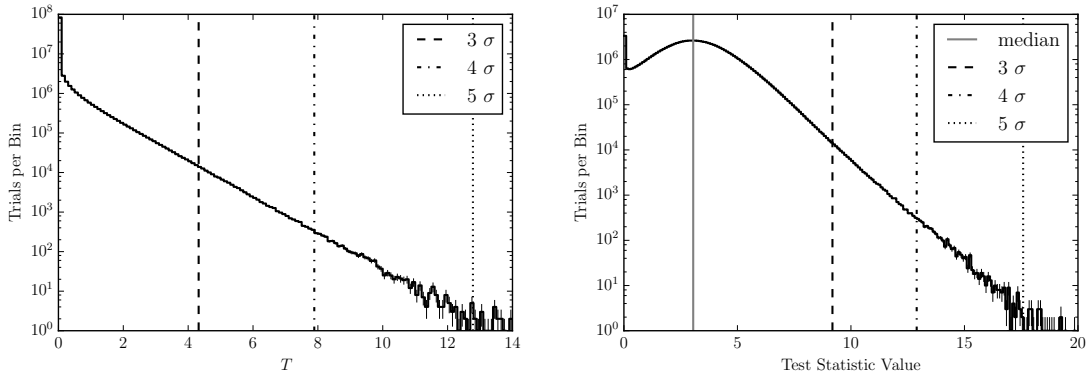

Figure 6.13: Test statistic distributions for 10^8 randomized background-only pseudo-searches at final cut level for the stacked T (left) and the $max(T_g)$ (right) likelihood methods. The vertical lines represent test statistic values for the median and 3σ, 4σ, and 5σ discovery.

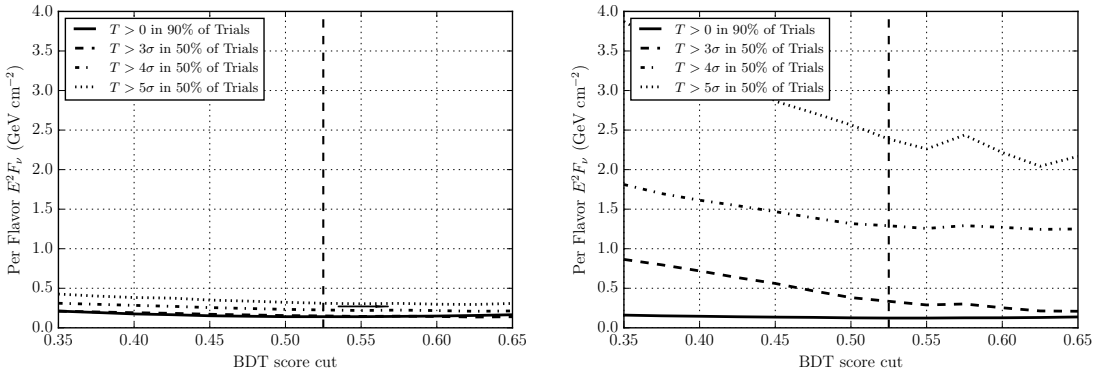

Figure 6.14: Discovery potential versus cut on BDT score for an E^{-2} fluence distributed over the entire sky. Left: stacked T. Right: $max(T_g)$.

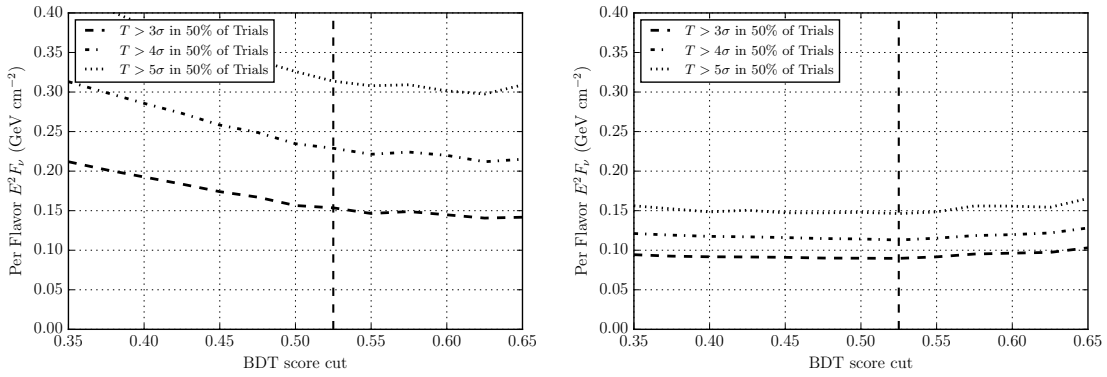

Figure 6.15: Discovery potential versus cut on BDT score for an E^{-2} fluence from a single random burst. Left: stacked T. Right: $max(T_g)$.

6.6 Characteristics of a Discovery

The benchmark internal shock, photospheric, and ICMART fireball model spectra plotted in Figure 2.9 are expected to yield 3.3, 5.4, and 0.1 neutrinos, respectively, over the combined three years of all-flavor shower searches and four years of ν_μ track searches in IceCube. The all-flavor shower search has an average $\langle n_b \rangle$ of 10 events per year for the three search years. This expectation is concentrated at lower energies than the expected signal and is weighted by the time, space, and energy PDFs accordingly in our unbinned likelihood. The expected background during just the T_{100} of each GRB is 3 events per year. An observation of three 1 PeV neutrinos correlated with three GRBs, with the same temporal and spacial properties as IC79 Event 1 and its respective GRB in Table 7.1 and Figure 7.2, would yield a T value over 12 and a 5σ discovery based on the background-only distribution.

Chapter 7

Results

7.1 Three Year Cascade Coincidence Search Results

In the three years of data analyzed, 11 events survived the final selection and were during GRB T_{100}s compared to an expected 9.0 ± 0.2 background events (about 7 atmospheric muons, 1.5 atmospheric ν_μ, 0.5 atmospheric ν_e) estimated from off-time data rates. More than half of the measured on-time events are not correlated with any GRB, considering their estimated uncertainties in reconstructed direction. Five events are found to be correlated in the PDF values with five GRBs: two during IC79 yielding an individual search season $T = 0.009$ and P-value of 0.21, and three during IC86I yielding an individual search season $T = 0.223$ and P-value of 0.11. IC86II had a $T = 0$ and P-value of 1. The estimated number of signal events from the test statistic maximization is 0.20 for the IC79 result and 0.75 for the IC86I result. These estimations are reasonable given that none of the GRB-correlated events are very significant on their own.

Results of multiple detector configurations and signal channels can be combined by adding maximized test statistics for each configuration and channel:

$$T = \sum_c \left\{ -(\hat{n}_s)_c + \sum_{i=0}^{N_c} \ln \left[\frac{(\hat{n}_s)_c \mathcal{S}_c(\overrightarrow{x_i})}{\langle n_b \rangle_c \mathcal{B}_c(\overrightarrow{x_i})} + 1 \right] \right\} \tag{7.1}$$

where c represents each combination of search channel and detector configuration. The combined three year cascade search P-value is 0.32, determined from the combined null hypothesis test statistic distribution shown in Figure 7.1. Therefore, the background is likely to produce such a result one in five times, and this result is not nearly significant enough for a discovery.

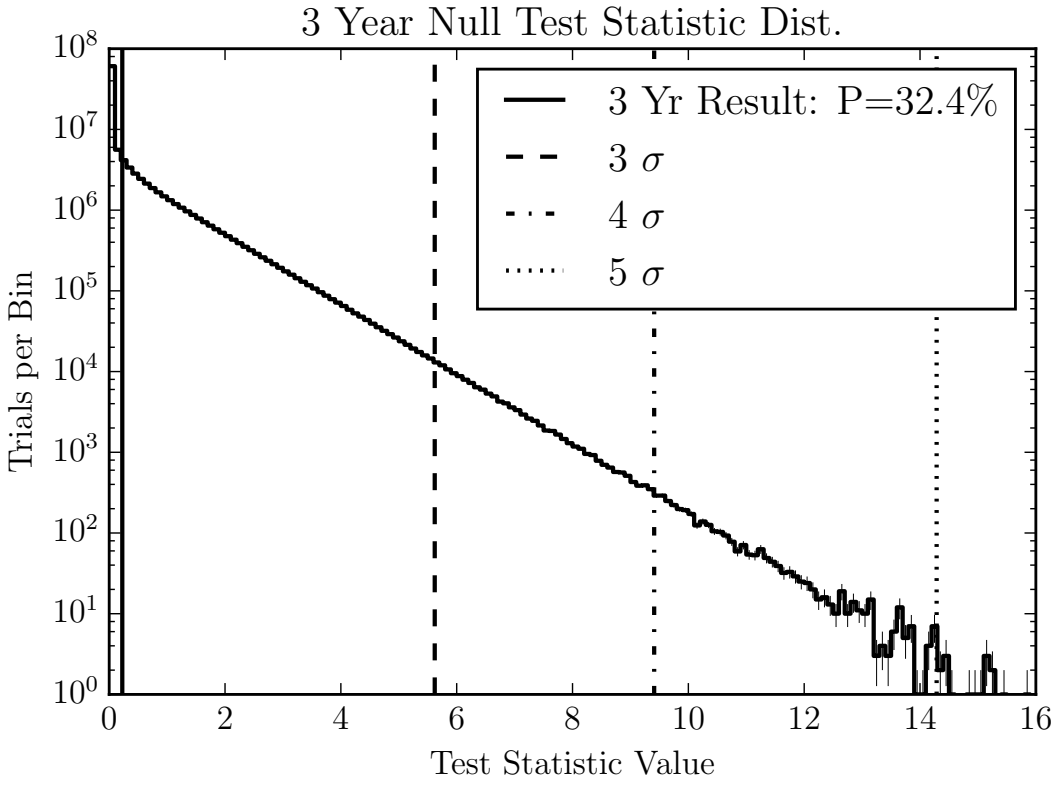

Figure 7.1: Three year cascade search combined null hypothesis test statistic distribution with the combined test statistic as the vertical solid line.

The Northern Hemisphere track searches in four years of data [17] resulted in a single neutrino candidate event correlated with a GRB, and the four year track result combined with the three year cascade result of this work yields a combined P-value of 0.55. Considering the atmospheric neutrino purity of each search, discussed

in Section 5.4.5, the track event is almost certainly a ν_μ while some of the cascade events are likely high energy atmospheric muons. Table 7.1 shows the time, space, and energy data for these events and GRBs. These most significant cascade events all had BDT scores near 0.6.

The first IC79 event occurred on the edge of the detector, imparted 11 TeV in the ice, and was reconstructed to be 0.72σ away from the well localized GRB101213A. The second IC79 event occurred at a corner of the detector configuration, imparted 34 TeV in the ice, and was reconstructed to be 0.94σ away from the poorly localized GRB110101B. The large directional uncertainty of the second event is due to the location of its interaction in the detector, with relatively few DOMs able to record the Cherenkov light.

The first IC86I event occurred inside of the detector, but only imparted 3.4 TeV in the ice, which is relatively small for the expected signal. This event was reconstructed to be 2.1σ away from the fairly well-localized GRB110521B. The second IC86I event occurred on the edge of the detector, imparted 31 TeV in the ice, and was reconstructed to be 2.7σ away from the well-localized GRB111212A. The third IC86I event occurred inside of the detector, imparted 3.8 TeV in the ice, and was reconstructed to be 2.2σ away from the well-localized GRB120114A.

A view of each of these five most significant events' Cherenkov patterns can be seen in Figures 7.6 and 7.7. From this view, it is clear that IC86I Event 3 consists of two coincident muons 20 μs apart, where one loses around a TeV of energy inside of the detector. The other events, while possibly neutrinos, are not of high significance individually, but give a non-zero stacked test statistic collectively.

	Time	Angular Uncertainty	Angular Separation	Fluence/Energy
GRB101213A	$T_{100} = 202$ s	0.0005°		7.4×10^{-6} erg cm^{-2}
IC79 Event 1	$T_1 + 109$ s	32.0°	23°	11 TeV
GRB110101B	$T_{100} = 235$ s	16.5°		6.6×10^{-6} erg cm^{-2}
IC79 Event 2	$T_1 + 141$ s	118°	112°	34 TeV
GRB110521B	$T_{100} = 6.14$ s	1.31°		3.6×10^{-6} erg cm^{-2}
IC86I Event 1	$T_1 + 0.26$ s	16.5°	34.6°	3.4 TeV
GRB111212A	$T_{100} = 68.5$ s	0.0004°		1.4×10^{-6} erg cm^{-2}
IC86I Event 2	$T_1 + 11.7$ s	44.8°	120.2°	30.6 TeV
GRB120114A	$T_{100} = 43.3$ s	0.04°		2.4×10^{-6} erg cm^{-2}
IC86I Event 3	$T_1 + 57.2$ s	7.9°	17.7°	3.8 TeV
GRB100718A[a]	$T_{100} = 39$ s	10.2∘		2.5×10^{-6} erg cm^{-2}
ν_μ Track Event[a]	$T_1 + 15$ s	16°	1.3°	$\gtrsim 10$ TeV

Table 7.1: GRB and Event Properties for the 3 Year Cascade and 4 Year Track Search Coincidences. [a] Corresponds to the ν_μ track search coincidence discussed in [17]

The number of Glashow resonance interactions expected to occur during the summed three season T_{100} time window is about 0.02. This expectation was determined by weighting the ν_e signal simulation to the best-fit astrophysical neutrino spectrum with IceCube [121]. The number expected on-time and on-source is much lower. Nevertheless, a Glashow resonance interaction correlated with a GRB would be a discovery-level event.

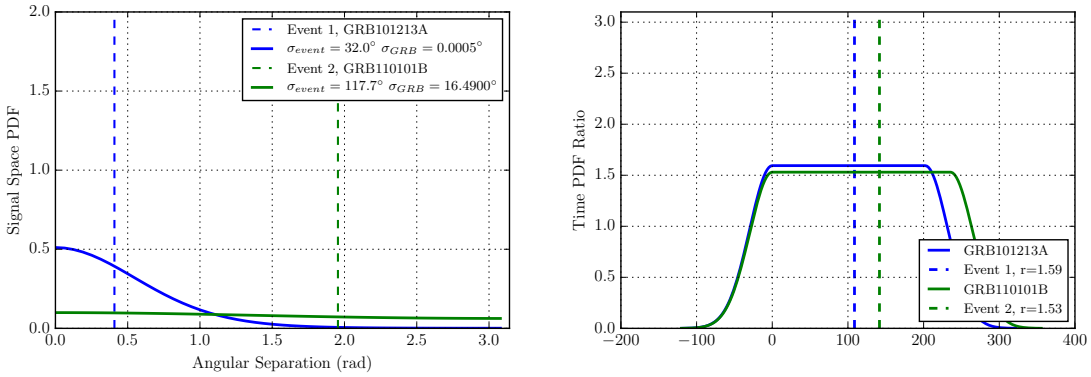

Figure 7.2: Signal space PDF and signal/background time PDF ratio for each of the two most significant IC79 events.

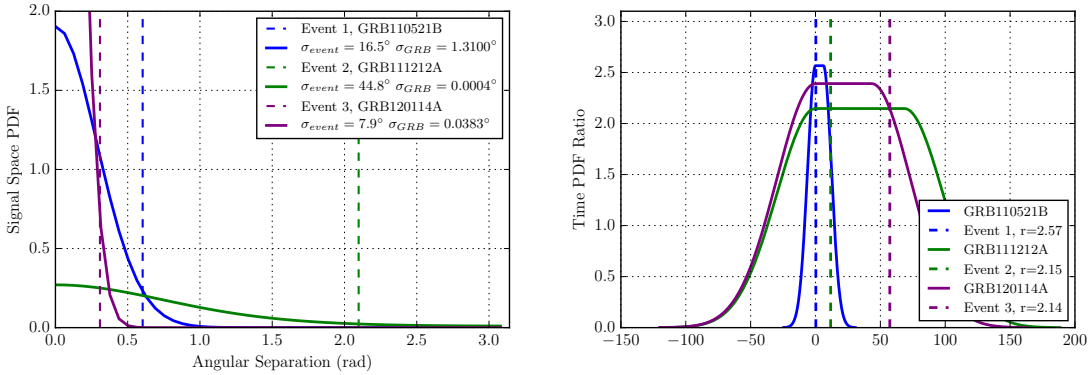

Figure 7.3: Signal space PDF and signal/background time PDF ratio for each of the three most significant IC86I events.

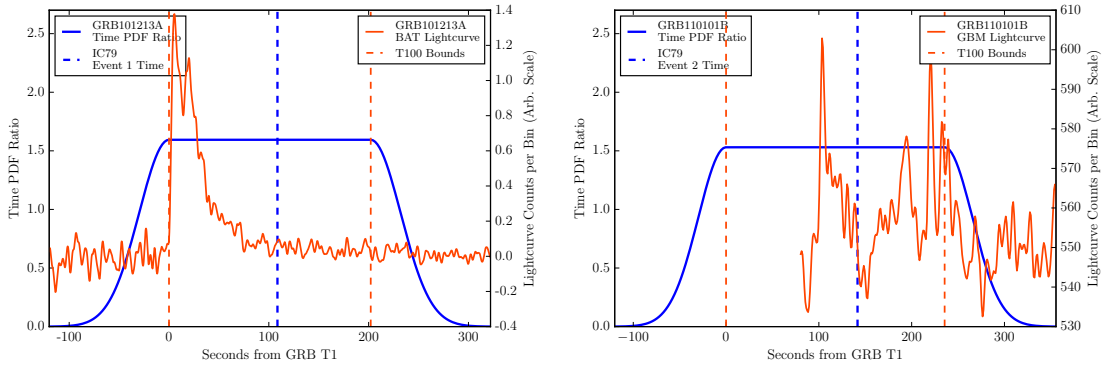

Figure 7.4: Signal/background time PDF ratio and GRB lightcurve for each of the two most significant IC79 events and their corresponding GRBs.

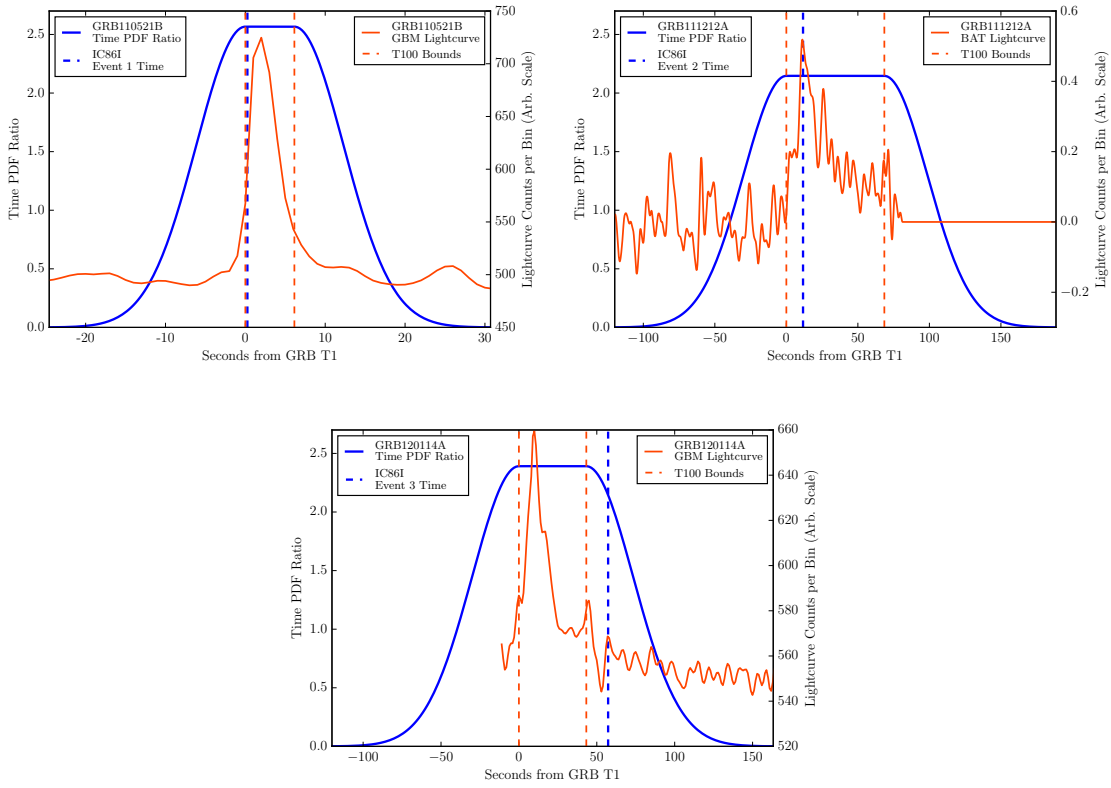

Figure 7.5: Signal/background time PDF ratio and GRB lightcurve for each of the three most significant IC86I events and their corresponding GRBs.

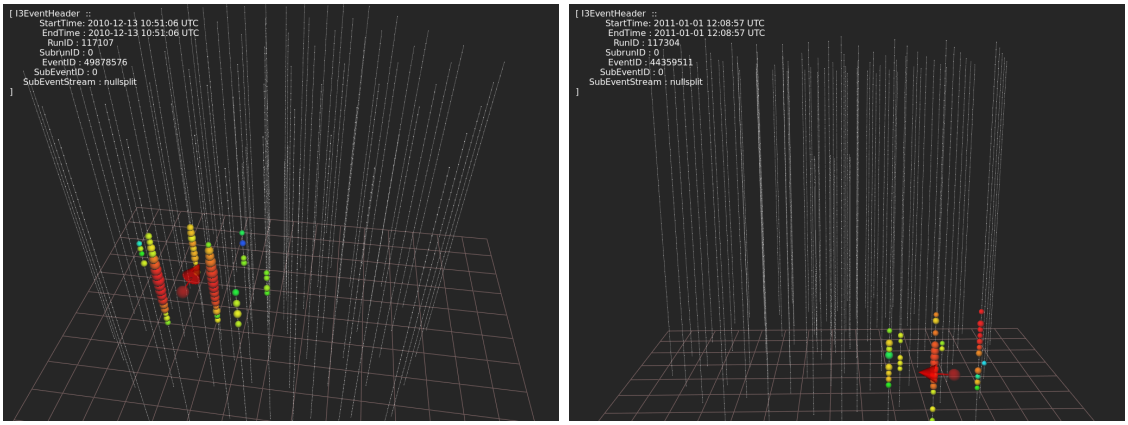

Figure 7.6: Detector views for the two most significant IC79 events (Events 1, 2 in Table 7.1 are left and right, respectively). Red is earlier and blue is later Cherenkov light. DOM sphere size is amount of Cherenkov light collected.

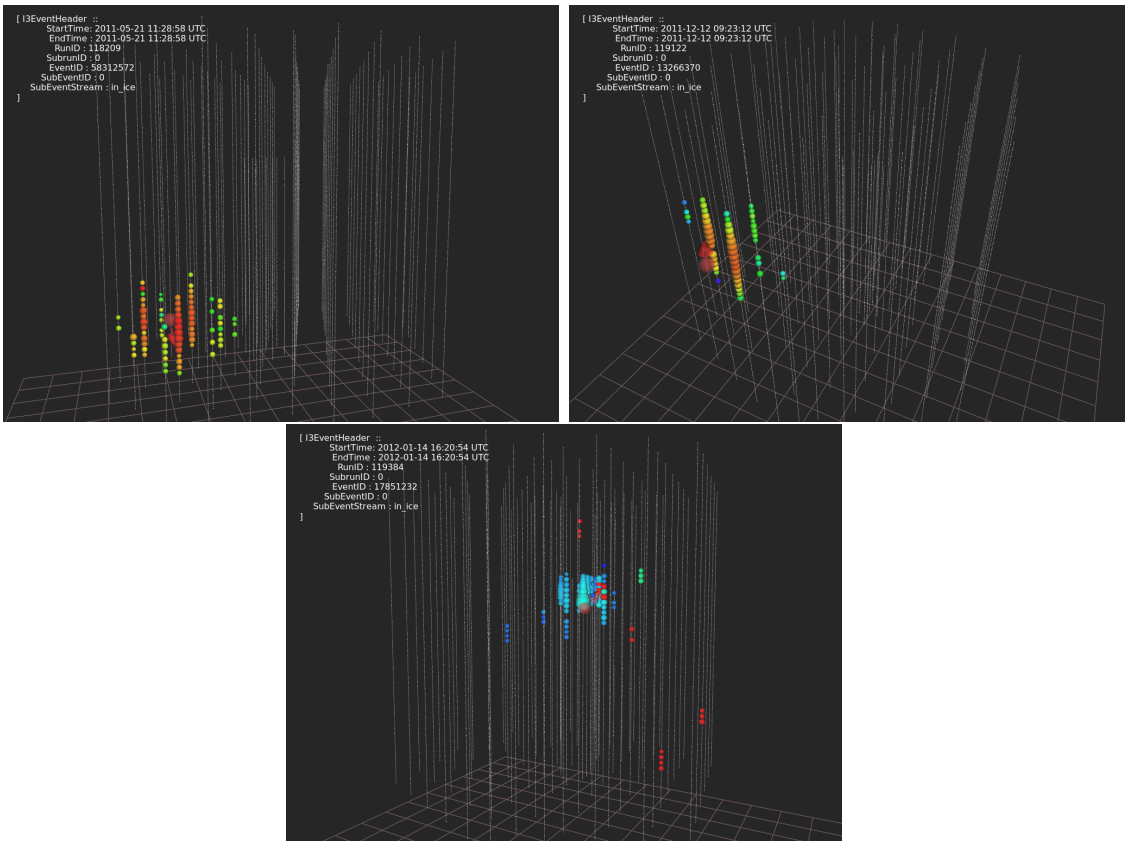

Figure 7.7: Detector views for the three most significant IC86I events (Events 1, 2, 3 in Table 7.1 are left, middle, and right, respectively). Red is earlier and blue is later Cherenkov light. DOM sphere size is amount of Cherenkov light collected.

7.2 Systematic Errors

There are several sources of uncertainty that can contribute to systematic error in the model limits set by this analysis. Uncertainties in the South Pole ice, DOM sensitivity to the Cherenkov light, and > TeV neutrino cross sections must be considered given the simulation's dependence on them. Potential systematic error in the background dataset is small in this analysis because detector data was used; however, the atmospheric muon interaction rate in IceCube varies throughout the year and this must be considered. All of these factors are taken into account by fixing them to their expected extrema, processing the varied datasets through the analysis event selection, and recalculating the upper limits.

The 90% CL best possible ($T > 0$) E^{-2} spectrum upper limit for each dataset was calculated and compared to the limit of the baseline assumptions dataset. For the sources of error that result in a worse limit than the baseline, the relative changes in this flux limit compared to the baseline are added in quadrature. At the time of this writing, the IC86I detector season had the largest amount of ν_e simulated data produced with the systematic variations applied. Additionally, the sensitivity of this analysis does not vary substantially between the three data-taking seasons considered. Therefore, the total systematic error for IC86I is used for the combined limits presented in Sections 7.3.1 and 7.3.2 below.

7.2.1 Ice Model

As is described in Section 4.1, the simulation chain ends with the propagation of Cherenkov light from the shower or muon track and its collection in the PMTs. These simulated light paths rely on a model of the South Pole ice detailing its optical properties [103]. The average properties over 10 m-thick vertical increments are characterized in a table of absorption and effective scattering coefficients [102].

A variance up to 10% is accepted for these coefficients [103]. Simulated ν_e signal interactions with absorption and scattering adjusted to 1.1 and 0.93 times the benchmark is processed through the event selection and the best possible limit is calculated. More absorption reduces the amount of Cherenkov light collected by the DOMs during a particle interaction, requiring a larger signal flux for a non-zero test statistic. Simulated ν_e signal interactions with absorption coefficients adjusted to 1.1 times the benchmark values yield a 90% CL best possible upper limit flux 9.5% greater than the benchmark. More scattering allows more photons to hit the DOMs near a cascade, requiring a smaller signal flux for a non-zero T. Simulated ν_e signal interactions with scattering coefficients adjusted to 1.1 times the benchmark values yield an upper limit flux 2.3% less than the benchmark. Simulated ν_e signal interactions with absorption and scattering coefficients adjusted to 0.93 times the benchmark values yield an upper limit flux 11% less than the benchmark.

More recent studies of the ice discovered anisoptropic scattering properties in it [131]. This slight azimuthal dependence in the scattering of photons is not a result of DOM behavior or bubbles in the melted and re-frozen string holes, but rather

inherent in the glacier as a whole. While the underlying cause of this preferential alignment is currently unknown, it can be incorporated macroscopically in the absorption and scattering tables. ν_e interactions with and without ice anisotropy are processed through the same event selection criteria. The anisotropy-included ice model upper limit is 1.9% greater than that of the no-anisotropy ice model used in this analysis.

7.2.2 Optical Module Sensitivity

The DOM sensitivity to Cherenkov photons was measured in a freezer lab before South Pole deployment. From these studies, a variance of $\pm 10\%$ is accepted as possible [85]. As with the uncertainties in the ice model, simulated ν_e signal interactions with PMT quantum efficiency adjusted to 1.05 and .9 times the benchmark is processed through the event selection and the best possible limit is calculated. Reducing the quantum efficiency reduces the amount of charge recorded for a given amount of Cherenkov light incident on the PMT, and consequently reduces the number of events passing the final event selection. The higher efficiency upper limit is 3.9% greater than that of the benchmark; and the lower efficiency upper limit is 2.7% less than that of the benchmark.

7.2.3 Neutrino Interactions

Uncertainties in $>$ TeV neutrino interactions may also contribute to systematic error in this analysis. Neutrino cross sections from the CTEQ5 model [98] are used

in simulations for this work. The uncertainty on the neutrino-nucleon cross sections is estimated to be $\sim 5\%$ [132]. Larger cross sections would increase the probability of interaction in and near the detector but also decrease the amount of neutrino measured originating from the Northern Hemisphere sky. A conservative 5% is chosen to contribute to the total systematic error on the model upper limits.

7.2.4 Seasonal Rate Variation

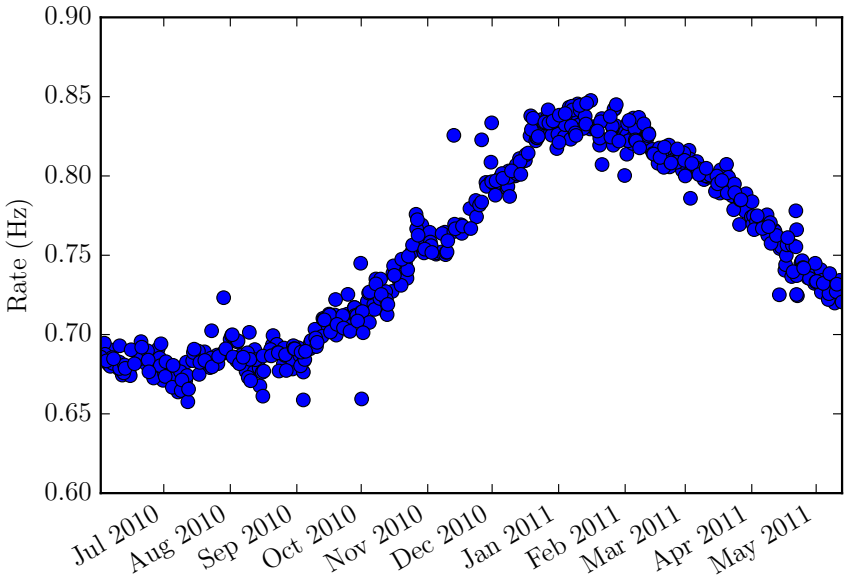

Figure 7.8: Seasonal variation in IC79 data at Level 3 event selection for this analysis.

The total event rate in IceCube changes throughout the year. This variation is due to the changing atmospheric temperature [133]. The warmer sunlit atmosphere is less dense, and so the charged mesons created in cosmic ray interactions are less likely to interact and thus decay to high energy muons more often than during the

colder winter months.

As seen in Figure 7.8, the background rate at Level 3 selection varies by about 10%. The changing rate is difficult to observe in the much lower final level background rate. To quantify this seasonal variation's effect on the result, the expected background rate $\langle n_b \rangle$ is varied by $\pm 10\%$ and the limits are recalculated. Because the background rate at the final event selection level is very low, there is no appreciable change in the upper limits compared to those from the mean $\langle n_b \rangle$ value used in the analysis.

7.2.5 Total Systematic Error

Dataset	Description	% Change w.r.t. Benchmark Limit
10601	Baseline	0
10067	+10% Absorption	+9.5
10068	+10% Scattering	−2.3
10069	−7.1% Scattering and Absorption	−11.2
10413	Anisotropic Ice Model	+1.9
10560	+5% DOM efficiency	+3.9
10439	−10% DOM efficiency	−2.7
–	±10% data rate	0
–	ν interactions	±5

Table 7.2: Systematic error sources and effects assuming an E^{-2}-weighted ν_e signal.

The percent change of the 90% CL best possible ($T > 0$) upper limit compared to that of the benchmark assumptions is shown in Table 7.2.5 for each source of systematic error. The limits per cut on BDT score for the systematics with positive percent change with respect to the benchmark limits are plotted in Figure 7.9. These positive percent changes are added in quadrature and the total 11.6% is applied to the combined upper limits in Sections 7.3.1 and 7.3.2. While the strength of these

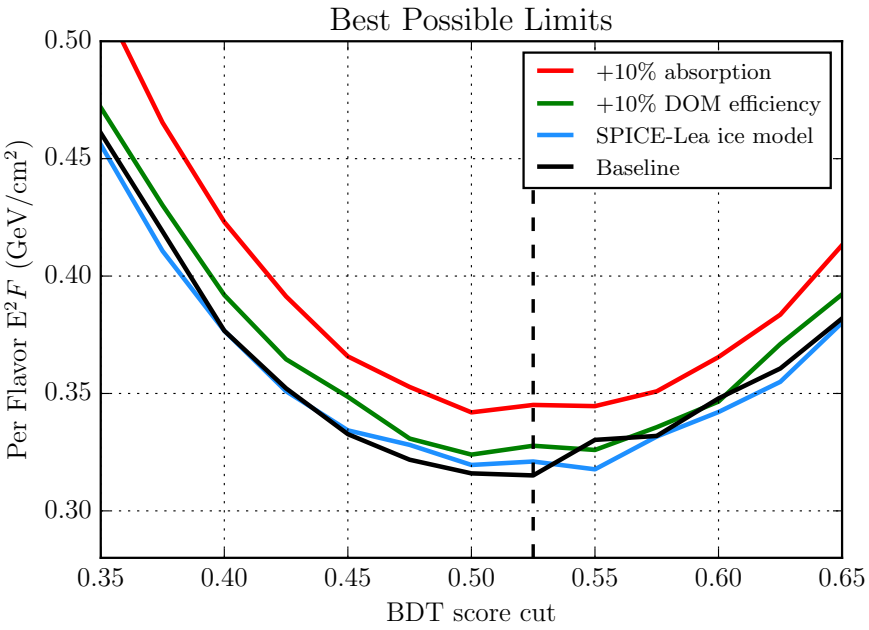

Figure 7.9: Best possible upper limits for the sources of systematic error that degrade the limit compared to the benchmark assumptions.

systematic effects do vary with spectrum shape, as lower energy events yield less photoelectrons with more ice absorption and lower DOM efficiency, the variation is small across the range of spectra considered in the limit calculations of the following sections. Therefore, the total error calculated above for an E^{-2} spectrum is applied to all Γ and break energy spectra limit values.

7.3 GRB Neutrino Production Model Limits

Considering the low significance of these results, 90% CL upper limits are placed on models normalized to the observed flux of UHECRs as well as models normalized to the observed gamma-ray fluence of each GRB. These limits are calculated by combining the three-year cascade search results and four-year Northern

Hemisphere track search results using the multiple configuration and channel test statistic given in equation 7.1. The limit calculations use a Feldman-Cousins approach [134] in which simulated electron, tau, and muon neutrinos are weighted to a certain spectrum and normalization and injected over background in the pseudo-searches; the exclusion confidence level (CL) is the fraction of pseudo-search trials that yield $T \geq T_{observed}$.

7.3.1 Limits Normalized to Cosmic Ray Production in GRBs

Figure 7.10 shows exclusion contours for per-flavor double broken power law spectra, at different first break energies ϵ_b and normalizations $\epsilon_b^2\phi_0$, of the following form:

$$\Phi_\nu(E) = \phi_0 \times \begin{cases} E^{-1}\epsilon_b^{-1}, & E < \epsilon_b \\ E^{-2}, & \epsilon_b \leq E < 10\epsilon_b \\ E^{-4}(10\epsilon_b)^2, & 10\epsilon_b \leq E \end{cases} \tag{7.2}$$

The combined limits largely rule out cosmic ray escape via neutron production [135]. Mechanisms allowing for cosmic ray escape via protons [54] are disfavored as well. The Waxman-Bahcall [54] model has been updated to account for more recent measurements of the UHECR flux [53] and typical gamma break energy [136]. These limits placed on neutrino emission models normalized to the observed UHECR flux are the strongest constraints thus far on the hypothesis that GRBs are the dominant sources of this flux.

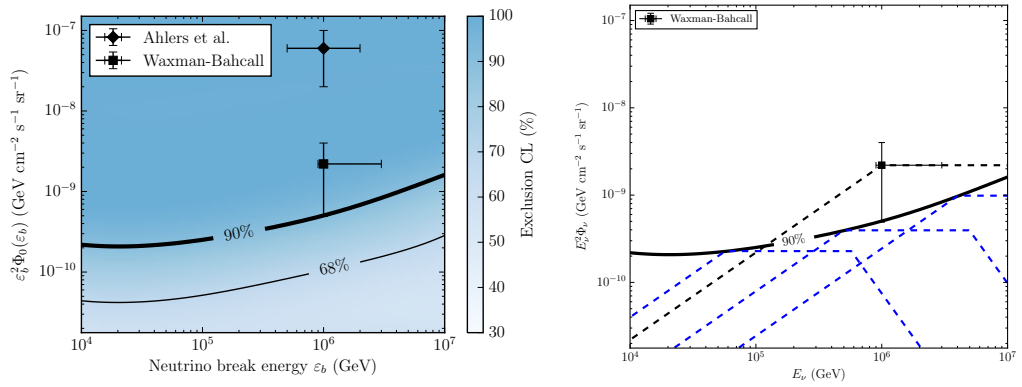

Figure 7.10: Exclusion contours, calculated from the combined three-year all-sky ν_e ν_τ ν_μ shower-like event search and four-year Northern Hemisphere ν_μ track-like event search results, of a per-flavor double broken power law GRB neutrino spectrum of a given flux normalization ϕ_b at first break energy ϵ_b. The right panel shows several of these spectra that are excluded at 90% confidence.

7.3.2 Limits on GRB Fireball Models and Parameter Spaces

The expected number of all-flavor neutrinos from $f_p = 10$, $\Gamma \approx 300$ internal shock, photospheric, and ICMART model fluxes measured by this three-year analysis are 1.45, 2.49, and 0.07, respectively. Similarly, the expected number of muon neutrinos from the three benchmark model fluxes measured by the four-year Northern Hemisphere track analysis are 1.88, 2.99, and 0.06, respectively. Background events are concentrated at much lower energies than these expected neutrinos.

As discussed in Section 2.4.5, the GRB theory community has been very active in light of the null results from IceCube searches for coincident neutrinos. The progression of models and limits is illustrated in Figure 7.11. The analytic benchmark $f_p = 10$, $\Gamma \approx 300$ internal shock fireball model is presented as the grey dashed line and the IceCube limit from 2011 [16] is in solid grey. The current numerically calculated benchmark internal shock fireball model and present limits from this work

combined with previous results is presented in red. This result reaches under this particular model for the first time. The photospheric model in green is ruled out, while the ICMART model in blue is beyond the current detector's reach.

These benchmark parameter models, though, are just one point in the phase space of unmeasured GRB parameters. Figure 7.12 shows exclusion contours in the baryonic loading and bulk Lorentz factor parameter space for the internal shock, photospheric, and ICMART per-burst gamma-ray-normalized fireball models, discussed in Section 2.4. The benchmark model spectra from the top panel of Figure 2.9 and Figures 6.11 and 7.11 are indicated by the intersection of the vertical and horizontal dashed lines.

These limits placed on the latest neutrino emission models normalized to the observed gamma-ray fluence from each GRB constrain parts of the parameter space relevant for the production of UHECR protons. Models that are still allowed require increasingly lower neutrino production efficiencies through large bulk Lorentz boost factors, low baryonic loading, or large dissipation radii.

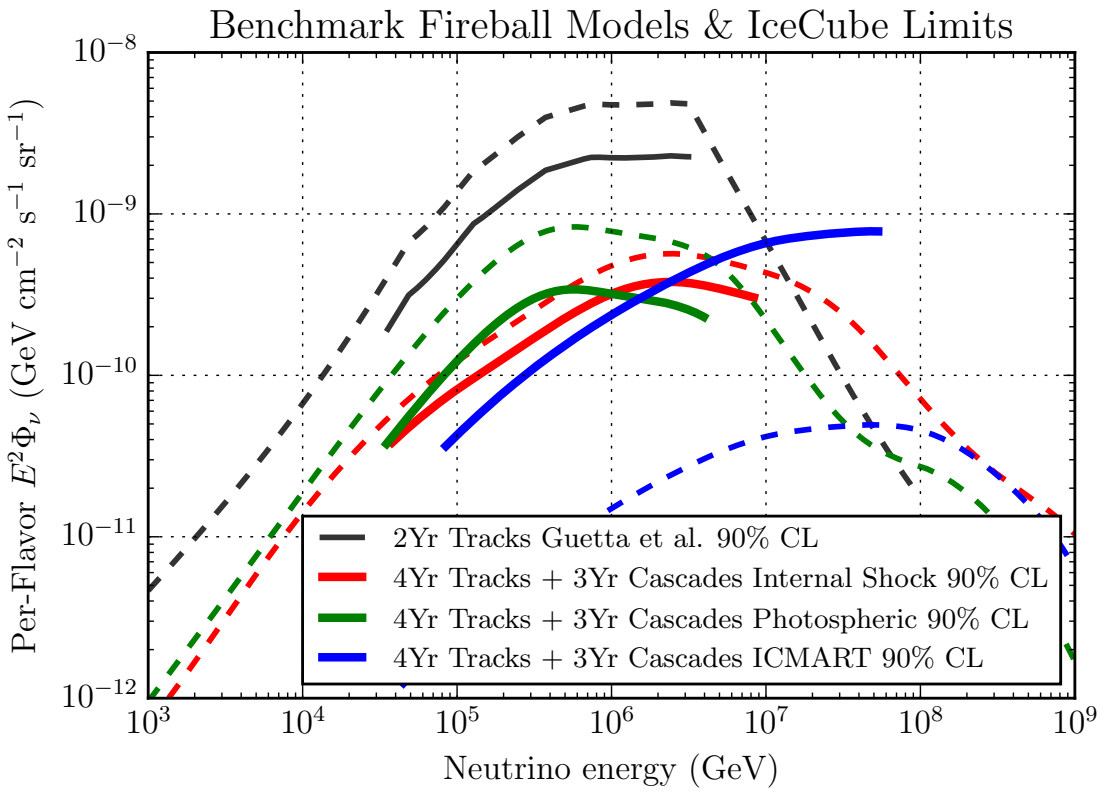

Figure 7.11: Evolution of prompt GRB neutrino flux models and the limits IceCube has placed on them. These models are characterized by benchmark values of $f_p = 10$ and $\Gamma \approx 300$. The dashed lines are the predictions and the solid lines are the limits. The limits are given over the central 90% energies of neutrinos that could be detected by IceCube.

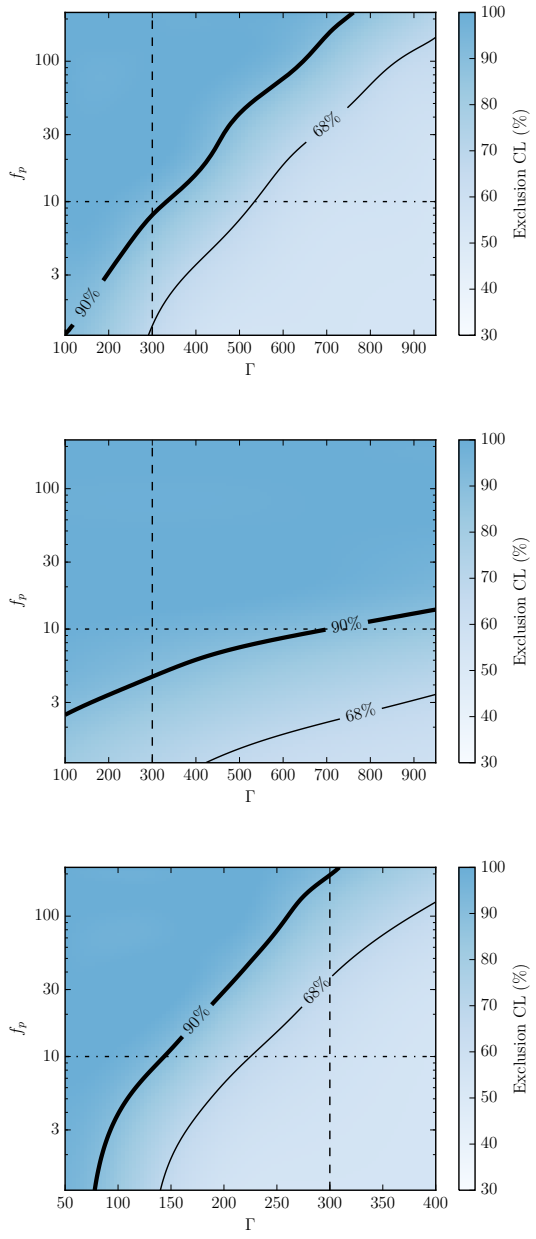

Figure 7.12: Exclusion contours, calculated from the combined three-year all-sky ν_e ν_τ ν_μ shower-like event search and four-year Northern Hemisphere ν_μ track-like event search results, in f_p and Γ GRB parameter space, for three different models of fireball neutrino production. These models differ in the radius at which photohadronic interactions occur. The vertical and horizontal dashed lines indicate the benchmark parameters used for the top of Figure 2.9 and Figures 6.11 and 7.11. Top: Internal Shock. Middle: Photospheric. Bottom: ICMART.

Chapter 8

Conclusions and Outlook

Data from one year of the 79-string and two years of the complete 86-string IceCube detector were analyzed for neutrino signal from 807 GRBs. This search is the first in IceCube for electromagnetic and hadronic showers induced by electron, tau, and muon neutrinos emitted by GRBs. Similar sensitivity to the much lower-background Northern Hemisphere muon neutrino track searches [17] was achieved because of this analysis's acceptance of all neutrino flavors from GRBs over both hemispheres. This wide neutrino net was cast through the effective use of BDT forests to separate neutrino interaction cascades from most of the atmospheric muon flux and an unbinned likelihood method to weight down the remaining background events.

No significant correlations were found and, building upon similar results of the previous track searches, world-leading limits were placed on cosmic ray and neutrino production in GRBs. Cosmic ray emission from GRB fireballs through either the escape and then decay of neutrons or an unspecified method of proton escape are heavily disfavored by the limits presented in Section 7.3.1. Neutrino production models normalized to the measured gamma-ray spectra of individual bursts with no explicit connection to the cosmic ray spectrum have been constrained as well by the limits presented in Section 7.3.2.

Unknown quantities still dominate these model calculations. For instance, the predicted neutrino flux depends strongly on the bulk Lorentz factor Γ. High Γ values in GRBs increase the proton energy threshold for pion production in the observer frame and therefore can explain non-detections even well below the current upper limits. Generally though, Lorentz factors above 2000 are unlikely [21] due to the non-thermal gamma-ray spectra and the observed UHECR energies that must be attained. Multiwavelength observations of GRBs are currently placing constraints on individual burst Lorentz factors [137, 138]. Improved electromagnetic GRB observations will allow for more precise calculations of per-burst neutrino emission models and strengthen the conclusions that can be drawn from this work's upper limits.

As shown in [78], constraints on parameters involved in fireball neutrino production via internal shock collisions can be connected to the requirement that GRBs are the sources of the observed UHECRs in a self-consistent way, assuming a pure proton composition. The unexcluded parameter space in Figure 7.12 allows for protons to efficiently diffuse out of the fireball, assuming a galactic-to-extragalactic source transition at the ankle of the cosmic ray spectrum. Although the allowed parameter space of this model is plausible, the multiwavelength studies discussed above conclude that the average GRB likely exhibits Γ and f_p values that lead to a neutrino flux that would have been observed by this and past analyses.

Although no significant neutrino-GRB correlations were found, Table 7.1 shows several TeV-energy events occurred during the measured prompt emission of GRBs and had reconstructed directions within 2σ of the bursts. The allowed fireball mod-

els expect a similar or fewer number of neutrinos to be seen in IceCube, but at 100 to 1000 times the energy of these events. If each successive year of searching produces similar results, the upper limit gains on these models will lessen and eventually a sufficient lift of signal over background will allow for a significant flux to be measured. An astrophysical neutrino flux has been measured by IceCube [121, 139], but its sources are currently unknown and very unlikely to be due to GRBs [17, 140]. Furthermore, the cascade events of this astrophysical neutrino signal pass the event selection of this analysis and would have yielded a much larger test statistic if they were on time and space with GRBs.

IceCube's acceptance of possible signal will soon increase further with the addition of searches for ν_μ-induced tracks from Southern Hemisphere GRBs with the complete detector. Improved sensitivity through different signal hypotheses and multiple messengers can also be attained. For example, correlating GRB gamma-ray fluence to observed neutrinos through an additional fluence PDF would increase sensitivity to the hypothesized signal if indeed this correlation exists [141]. Additionally, GRBs are proposed to produce another astrophysical messenger: gravitational waves. Correlating GRB neutrinos with a measurement by LIGO [142] would provide a powerful probe of the source parameters, but this dual measurement is only possible for rare nearby short bursts [141].

A near-real-time per-burst analysis using many of the same techniques described in this work will soon allow for rapid observational follow-up of any significant coincidence. Moreoever, the next-generation *IceCube-Gen2* detector will be significantly more sensitive to transient sources of neutrinos [143, 144]. The contin-

ued pursuit of all neutrino flavors from observed GRBs over the entire sky will either reveal a flux that is still lower than our current sensitivity or increasingly disfavor these phenomena as sources of the highest energy cosmic rays.

Appendix A

Gamma-Ray Burst Catalog

This work searches for neutrinos coincident with 807 GRBs over three years of IceCube data, from June 2010 to May 2013. Each burst is named in the format GRBYYMMDDL where YY denotes the last two digits of the year, MM the month, and DD the day. L is a letter, beginning with A, that ensures multiple GRBs that are recorded on the same day have unique names. Alphabetical order of L does not always correspond to the chronological order of the burst measurements because often Fermi GBM does not immediately name its GRBs, instead waiting until the publication of its catalogs. The energy spectrum parameters reported by the satellite detector teams and listed in the tables below have the following units: keV for the gamma-ray energy peak (ϵ_γ) and energy bounds (E_{min}, E_{max}), erg cm^{-2} for the gamma-ray fluence (Fluence$_\gamma$).

Some bursts recorded by satellite detectors are not included in this analysis because IceCube was not in a state to record reliable data during their measurement. For example, GRB110125A was observed by FermiGBM when IceCube was in between calibration runs in which the DOM LED flashers are used; GRB120403A was observed by SwiftBAT when IceCube was down following maintenance of its power supplies; and GRB130112B was observed by FermiGBM when IceCube was down during testing of an upgraded DOMHub. Additionally, the first three GRBs

of the IC86II Table A.3 were observed in the IC86I season but during test runs of the IC86II base processing and filtering.

The procedure used for multiple burst measurements by different detectors is described in Section 2.3. As was done in previous GRB neutrino searches with IceCube [15–17], average values are used when measurements are unavailable. These values are described in Section 2.4.5 and marked with *. Average values from the Fermi GBM First Two Years Catalog [34] are used in the fireball spectrum calculations for GRBs measured only by the Fermi GBM instrument. These values are marked with † and are also within the uncertainties of the GBM First Four Years Catalog [36].

Table A.1: IC79 GRB Parameters

Name	RA (°)	Dec (°)	σ	z	Trigger (UT)	T_1 (s)	T_2 (s)	T_{100} (s)	α_γ	β_γ	ϵ_γ	E_{min}	E_{max}	$Fluence_\gamma$
100604A	248.30	-73.19	3.64°	2.15*	2010-06-04 06:53:34.81	-2.3	11.14	13.44	1.05†	2.25†	205†	8	1000	5.509E-6
100605A	273.43	-67.60	7.67°	2.15*	2010-06-05 18:35:10.74	-1.02	7.17	8.19	1.05†	2.25†	205†	8	1000	7.565E-7
100606A	350.63	-66.24	1.08″	2.15*	2010-06-06 19:12:41.00	0.3	672.3	672.0	1.05	3.05	945	20	2000	3.9E-5
100608A	30.54	20.45	5.33°	2.15*	2010-06-08 09:10:06.34	-7.68	22.53	30.21	1.05†	2.25†	205†	8	1000	1.699E-6
100609A	90.48	42.78	2.53°	2.15*	2010-06-09 18:48:11.33	6.14	236.55	230.41	1.05†	2.25†	205†	8	1000	1.742E-5
100612A	63.53	13.74	2.69°	0.5*	2010-06-12 13:04:21.66	0	0.58	0.58	1.05†	2.25†	205†	8	1000	2.237E-6
100612B	352.00	-1.83	1.58°	2.15*	2010-06-12 17:26:06.13	0.7	9.28	8.58	1.05†	2.25†	205†	8	1000	1.363E-5
100614A	263.50	49.23	1.08″	2.15*	2010-06-14 21:38:26.00	-9	282	291.0	1.88	2.88	200*	15	150	2.7E-6
100614B	224.76	40.87	2.99°	2.15*	2010-06-14 11:57:23.31	-149.76	22.53	172.29	1.05†	2.25†	205†	8	1000	1.963E-5
100615A	177.21	-19.48	1.08″	1.398	2010-06-15 01:59:03.00	0	47.4	47.4	1.24	2.27	85.73	8	1000	8.723E-6
100616A	342.91	3.09	45.74°	0.5*	2010-06-16 18:32:32.90	-0.19	0	0.19	1.05†	2.25†	205†	8	1000	2.758E-7
100619A	84.62	-27.00	1.08″	2.15*	2010-06-19 00:21:07.00	-2.9	105.7	108.6	1.6	2.36	135.3	8	1000	1.129E-5
100620A	80.10	-51.68	1.46°	2.15*	2010-06-20 02:51:29.11	0.19	52.03	51.84	1.05†	2.25†	205†	8	1000	3.716E-6
100621A	315.31	-51.11	1.08″	0.542	2010-06-21 03:03:32.00	-6	204	210.0	1.7	2.45	95	20	2000	3.6E-5
100621B	103.83	37.35	2.81°	2.15*	2010-06-21 10:51:18.26	-6.66	117.25	123.91	1.05†	2.25†	205†	8	1000	7.671E-6
100621C	160.86	14.72	11.41°	0.5*	2010-06-21 12:42:16.43	-0.45	0.58	1.03	1.05†	2.25†	205†	8	1000	1.375E-7
100625A	15.80	-39.09	1.08″	0.5*	2010-06-25 18:32:27.80	0	1.3	1.3	0.1	2.6	371	20	2000	0.83E-6
100625B	338.26	20.29	4.45°	2.15*	2010-06-25 21:22:45.18	-7.42	21.76	29.18	1.05†	2.25†	205†	8	1000	1.401E-6
100628A	225.94	-31.65	0.02°	0.5*	2010-06-28 08:16:40.00	-0.004	0.036	0.04	2.67	4.67	74.1	15	150	2.5E-8
100629A	231.21	27.81	3.32°	0.5*	2010-06-29 19:14:03.35	-0.13	0.7	0.83	1.05†	2.25†	205†	8	1000	1.153E-6
100701B	43.11	-2.22	0.09°	2.15*	2010-07-01 11:45:19.07	0	26.11	26.11	0.95	2.47	1480	8	1000	2.603E-5
100702A	245.69	-56.55	0.01°	0.5*	2010-07-02 01:03:47.00	0.036	0.236	0.2	1.54	2.54	1000*	15	150	1.2E-7
100703A	9.52	-25.71	0.03°	0.5*	2010-07-03 17:43:37.40	0	0.07	0.07	1*	2*	1000*	20	200	7E-7

Table A.1: IC79 GRB Parameters (continued)

Name	RA (°)	Dec (°)	σ	z	Trigger (UT)	T_1 (s)	T_2 (s)	T_{100} (s)	α_γ	β_γ	ϵ_γ	E_{min}	E_{max}	Fluence$_\gamma$
100704A	133.64	-24.20	1.08″	2.15*	2010-07-04 03:35:08.00	-62.3	202.3	264.6	0.76	2.53	178.30	10	1000	1.040E-5
100706A	255.16	46.89	12.23°	0.5*	2010-07-06 16:38:18.92	-0.13	0	0.13	1.05†	2.25†	205†	8	1000	1.316E-7
100707A	358.02	-8.66	1.12°	2.15*	2010-07-07 00:46:38.91	-0.5	102.144	102.644	0.95	2.2	264	20	2000	8.8E-5
100709A	142.53	17.38	4.47°	2.15*	2010-07-09 14:27:32.98	-2.56	97.54	100.1	1.05†	2.25†	205†	8	1000	8.076E-6
100713A	255.21	28.39	0.03°	2.15*	2010-07-13 14:36:06.00	0	20	20.0	1*	2*	200*	20	200	2E-7
100713B	82.06	13.00	3.74°	2.15*	2010-07-13 23:31:34.01	-0.38	7.23	7.61	1.05†	2.25†	205†	8	1000	3.047E-6
100714A	106.37	51.14	3.69°	2.15*	2010-07-14 16:07:23.78	-0.51	35.07	35.58	1.05†	2.25†	205†	8	1000	3.251E-6
100714B	307.94	61.30	9.69°	2.15*	2010-07-14 16:27:20.08	-3.33	2.3	5.63	1.05†	2.25†	205†	8	1000	1.558E-6
100715A	299.27	-54.71	9.32°	2.15*	2010-07-15 11:27:17.64	-1.02	13.82	14.84	1.05†	2.25†	205†	8	1000	2.552E-6
100717A	287.06	-0.66	8.84°	2.15*	2010-07-17 08:55:06.21	-0.58	5.38	5.96	1.05†	2.25†	205†	8	1000	4.263E-7
100717B	304.31	19.53	9.19°	2.15*	2010-07-17 10:41:47.12	-0.13	2.3	2.43	1.05†	2.25†	205†	8	1000	3.328E-7
100718A	298.47	41.43	10.24°	2.15*	2010-07-18 19:06:22.58	-2.82	35.84	38.66	1.05†	2.25†	205†	8	1000	2.535E-6
100718B	121.83	-46.18	5.93°	2.15*	2010-07-18 03:50:09.61	-21.62	11.02	32.64	1.05†	2.25†	205†	8	1000	2.747E-6
100719A	112.32	-5.86	0.02°	2.15*	2010-07-19 03:30:57.00	-3.9	35.1	39.0	1.69	2.69	200*	15	150	5.3E-7
100719B	304.87	-67.14	15.41°	0.5*	2010-07-19 07:28:17.62	-1.54	0.06	1.6	1.05†	2.25†	205†	8	1000	3.868E-7
100719D	113.30	5.40	1.00°	2.15*	2010-07-19 23:44:04.13	1.54	23.36	21.82	1.05†	2.25†	205†	8	1000	5.194E-5
100722A	238.77	-15.61	1.07°	2.15*	2010-07-22 02:18:37.24	0	7.17	7.17	1.01	2.54	68.1	8	1000	9.5E-9
100722B	31.81	56.23	8.06°	0.5*	2010-07-22 06:58:24.72	-1.22	0.06	1.28	1.05†	2.25†	205†	8	1000	1.039E-7
100724A	194.54	-11.10	1.08″	1.288	2010-07-24 00:42:19.00	0.1	1.6	1.5	1.92	2.92	1000*	15	150	1.6E-7
100724B	120.04	76.74	1.10°	2.15*	2010-07-24 00:42:04.70	-4.1	230.608	234.708	0.84	1.84	467.8	8	1000	2.44E-4
100725A	166.48	-26.67	1.08″	2.15*	2010-07-25 07:12:52.00	-4.8	172	176.8	1.23	2.23	200*	15	150	2.0E-6
100725B	290.03	76.96	1.08″	2.15*	2010-07-25 11:24:34.00	-4.8	226.1	230.9	1.89	2.89	200*	15	150	6.8E-6
100727A	154.18	-21.39	1.08″	2.15*	2010-07-27 05:42:17.00	-82	29.8	111.8	1.71	2.71	200*	8	1000	2.03E-6
100728A	88.76	-15.26	0.72″	1.567	2010-07-28 02:18:24.00	-84.3	334	418.3	0.75	3.04	344.3	8	1000	1.291E-4
100728B	163.49	-45.47	0.36″	2.106	2010-07-28 10:31:54.97	-2.05	14.2	16.25	0.8	2.2	104	8	1000	2.4E-6
100730A	339.79	-22.23	5.40°	2.15*	2010-07-30 11:06:14.97	-1.54	62.34	63.88	1.05†	2.25†	205†	8	1000	6.058E-6
100802A	2.47	47.76	1.08″	2.15*	2010-08-02 05:45:36.00	-3.3	531.7	535.0	1.17	3.17	149	10	1000	2.24E-6
100804A	248.97	27.45	1.00°	2.15*	2010-08-04 02:29:26.35	0.13	6.72	6.59	1.05†	2.25†	205†	8	1000	1.068E-5
100805A	299.88	52.63	0.36″	2.15*	2010-08-05 04:12:42.00	-1.4	17.1	18.5	1.76	2.76	200*	15	150	5.1E-7
100805B	22.80	34.19	7.65°	0.5*	2010-08-05 07:12:12.48	-0.1	-0.03	0.07	1.05†	2.25†	205†	8	1000	2.043E-7
100805C	112.72	-35.93	3.75°	2.15*	2010-08-05 20:16:29.53	0	58.43	58.43	1.05†	2.25†	205†	8	1000	1.061E-5
100807A	55.30	67.67	1.08″	2.15*	2010-08-07 09:13:13.00	-6.1	3.1	9.2	2.32	3.32	200*	15	150	3.4E-7
100810A	124.77	-1.61	5.65°	2.15*	2010-08-10 01:10:34.24	-1.86	0.7	2.56	1.05†	2.25†	205†	8	1000	3.937E-7
100811A	345.87	15.86	6.04°	0.5*	2010-08-11 02:35:49.36	-0.06	0.32	0.38	1.05†	2.25†	205†	8	1000	2.930E-6
100811B	108.14	62.19	3.57°	2.15*	2010-08-11 18:44:09.30	-52.99	25.09	78.08	1.05†	2.25†	205†	8	1000	4.675E-6
100814A	22.47	-18.00	1.08″	2.15*	2010-08-14 03:50:08.51	-1.5	238	239.5	0.64	2.02	106.4	10	1000	1.98E-5
100814B	122.82	18.49	2.60°	2.15*	2010-08-14 08:25:25.75	-0.77	6.66	7.43	0.62	2.49	81.0	10	1000	4.7E-6
100816A	351.74	26.58	1.08″	0.8034	2010-08-16 00:37:50.94	0	11.448	11.448	0.31	2.77	136.70	10	1000	3.84E-6
100816B	102.12	-26.66	1.06°	2.15*	2010-08-16 00:12:41.41	-21.76	40.64	62.4	1.05†	2.25†	205†	8	1000	2.530E-5
100819A	279.60	-50.04	3.86°	2.15*	2010-08-19 11:56:35.26	-4.86	7.68	12.54	1.05†	2.25†	205†	8	1000	3.322E-6
100820A	258.79	-18.51	2.14°	2.15*	2010-08-20 08:56:58.47	-0.77	8.19	8.96	1.05†	2.25†	205†	8	1000	2.993E-6
100823A	20.70	5.83	1.44″	2.15*	2010-08-23 17:25:33.00	0	25	25.0	2.19	3.19	200*	15	150	4.1E-7
100825A	253.44	-56.57	6.34°	2.15*	2010-08-25 06:53:48.67	-1.28	2.05	3.33	1.05†	2.25†	205†	8	1000	1.378E-6
100826A	279.59	-22.13	1.60°	2.15*	2010-08-26 22:58:29.73	0	130.56	130.56	1.31	2.1	606	20	10000	3.0E-4

Table A.1: IC79 GRB Parameters (continued)

Name	RA (°)	Dec (°)	σ	z	Trigger (UT)	T_1 (s)	T_2 (s)	T_{100} (s)	α_γ	β_γ	ϵ_γ	E_{min}	E_{max}	Fluence$_\gamma$
100827A	193.90	71.89	5.68°	0.5*	2010-08-27 10:55:49.33	-0.13	0.45	0.58	1.05†	2.25†	205†	8	1000	1.029E-6
100829A	90.41	30.31	0.27°	2.15*	2010-08-29 21:02:07.94	0	10.24	10.24	1.44	9.4	278	20	2000	1.40E-5
100829B	115.45	-3.99	4.66°	2.15*	2010-08-29 08:59:07.02	0.26	95.23	94.97	1.05†	2.25†	205†	8	1000	7.290E-6
100831A	161.26	33.65	10.16°	2.15*	2010-08-31 15:37:25.94	-23.3	16.9	40.2	1.05†	2.25†	205†	8	1000	2.930E-6
100901A	27.27	22.76	1.44′′	1.408	2010-09-01 13:34:10.00	-2.4	471.8	474.2	1.52	2.52	200*	15	150	2.1E-6
100902A	48.63	30.98	1.08′′	2.15*	2010-09-02 19:31:54.00	-49.5	409.6	459.1	1.98	2.98	200*	15	150	3.2E-6
100902B	306.04	42.31	7.20°	2.15*	2010-09-02 23:45:19.22	-4.1	18.18	22.28	1.05†	2.25†	205†	8	1000	2.107E-6
100904A	172.91	-16.18	0.02°	2.15*	2010-09-04 01:33:43.00	-14.5	23	37.5	1.67	2.67	200*	15	150	1.3E-6
100905A	31.55	14.93	1.08′′	2.15*	2010-09-05 15:08:14.00	-1.6	2.1	3.7	1.09	2.09	200*	15	150	1.7E-7
100905B	262.65	13.08	4.00°	2.15*	2010-09-05 21:46:22.99	-4.61	6.91	11.52	1.05†	2.25†	205†	8	1000	1.854E-6
100906A	28.68	55.63	0.72′′	1.727	2010-09-06 13:49:27.00	-0.2	142.264	142.464	1.34	1.98	106.0	10	1000	2.64E-5
100907A	177.29	-40.63	6.90°	2.15*	2010-09-07 18:01:11.64	-1.54	3.84	5.38	1.05†	2.25†	205†	8	1000	7.333E-7
100909A	73.95	54.65	0.02°	2.15*	2010-09-09 09:04:00.00	0	60	60.0	1*	2*	200*	20	200	10E-6
100910A	238.10	-34.62	1.02°	2.15*	2010-09-10 19:37:43.96	1.34	15.17	13.83	0.92	2.26	143	10	1000	1.48E-5
100911A	151.32	58.99	11.77°	2.15*	2010-09-11 19:35:39.91	-0.77	4.86	5.63	1.05†	2.25†	205†	8	1000	8.679E-7
100915A	315.69	65.67	1.08′′	2.15*	2010-09-15 01:31:05.00	-36.3	72.2	108.5	1.5	3.5	265.2	15	150	1.5E-6
100915B	85.39	25.09	0.02°	2.15*	2010-09-15 05:49:39.62	-5.6	4	9.6	1.35	3.35	83.49	10	1000	4.82E-7
100916A	151.96	-59.38	3.48°	2.15*	2010-09-16 18:41:12.49	-0.26	12.54	12.8	1.05†	2.25†	205†	8	1000	1.784E-6
100917A	289.25	-17.12	0.02°	2.15*	2010-09-17 05:03:25.00	-2.1	76	78.1	1.67	2.67	200*	15	150	8.6E-7
100918A	308.41	-45.96	1.00°	2.15*	2010-09-18 20:42:18.01	18.43	104.45	86.02	1.05†	2.25†	205†	8	1000	8.924E-5
100919A	163.24	6.02	1.81°	2.15*	2010-09-19 21:12:16.28	-38.4	11.2	49.6	1.05†	2.25†	205†	8	1000	5.760E-6
100922A	356.98	-25.19	15.03°	2.15*	2010-09-22 14:59:43.01	-1.02	3.33	4.35	1.05†	2.25†	205†	8	1000	4.246E-7
100923A	106.12	39.60	5.35°	2.15*	2010-09-23 20:15:10.67	-0.77	50.94	51.71	1.05†	2.25†	205†	8	1000	3.917E-6
100924A	0.67	7.00	0.01°	2.15*	2010-09-24 03:58:08.00	-15.1	128.9	144.0	1.59	2.59	200*	10	1000	3.33E-6
100925A	254.74	-15.24	0.03°	2.15*	2010-09-25 08:05:05.00	0	10	10.0	1*	2*	200*	10*	10000*	1.00E-5*
100926A	222.75	-72.35	3.81°	2.15*	2010-09-26 14:17:03.94	-24.06	8.19	32.25	1.05†	2.25†	205†	8	1000	6.973E-6
100926B	43.58	-11.10	12.00°	2.15*	2010-09-26 16:39:54.52	-3.07	34.82	37.89	1.05†	2.25†	205†	8	1000	1.374E-6
100928A	223.04	-28.54	0.02°	2.15*	2010-09-28 02:19:52.00	0.9	4.4	3.5	1.79	2.79	200*	15	150	3.5E-7
100929A	166.33	62.29	13.39°	2.15*	2010-09-29 05:38:52.49	-2.3	5.89	8.19	1.05†	2.25†	205†	8	1000	4.955E-7
100929B	243.62	33.33	23.83°	2.15*	2010-09-29 07:33:04.05	-0.51	4.1	4.61	1.05†	2.25†	205†	8	1000	3.249E-7
100929C	183.03	-24.94	7.79°	0.5*	2010-09-29 21:59:45.82	-0.13	0.19	0.32	1.05†	2.25†	205†	8	1000	7.614E-7
101002A	323.35	-27.47	16.36°	2.15*	2010-10-02 06:41:26.95	-4.35	2.82	7.17	1.05†	2.25†	205†	8	1000	4.396E-7
101003A	175.85	2.49	7.39°	2.15*	2010-10-03 05:51:08.01	-1.79	8.19	9.98	1.05†	2.25†	205†	8	1000	2.231E-6
101008A	328.88	37.07	1.08′′	2.15*	2010-10-08 16:43:15.00	-4	106.6	110.6	1.42	2.42	200*	10	1000	2.016E-6
101010A	47.19	43.56	18.63°	2.15*	2010-10-10 04:33:46.83	-11.01	54.02	65.03	1.05†	2.25†	205†	8	1000	1.551E-6
101011A	48.29	-65.98	0.72′′	2.15*	2010-10-11 16:58:35.00	-0.4	84.2	84.6	0.49	2.49	296.6	8	1000	5.24E-6
101013A	292.08	-49.64	1.60°	2.15*	2010-10-13 09:52:42.88	0.58	15.94	15.36	1.05†	2.25†	205†	8	1000	6.410E-6
101014A	26.94	-51.07	1.00°	2.15*	2010-10-14 04:11:52.62	1.41	450.82	449.41	1.27	2.07	181.40	10	1000	2.072E-4
101015A	73.16	15.46	5.94°	2.15*	2010-10-15 13:24:02.67	-2.05	498.5	500.55	1.05†	2.25†	205†	8	1000	3.737E-5
101016A	133.04	-4.62	2.81°	2.15*	2010-10-16 05:50:16.07	-1.54	2.3	3.84	1.05†	2.25†	205†	8	1000	2.444E-6
101017A	291.39	-35.15	1.44′′	2.15*	2010-10-17 10:32:41.69	0	117	117.0	1.18	3.18	600	20	2000	6.7E-5
101017B	27.47	-26.55	4.92°	2.15*	2010-10-17 14:51:29.48	-1.02	46.85	47.87	1.05†	2.25†	205†	8	1000	1.775E-6
101020A	189.61	23.13	0.03°	2.15*	2010-10-20 23:40:41.00	-50	159	209.0	2.04	3.04	200*	15	150	2.6E-6
101021A	0.87	-23.71	1.33°	2.15*	2010-10-21 00:13:25.36	-51.46	69.31	120.77	1.05†	2.25†	205†	8	1000	2.230E-5

Table A.1: IC79 GRB Parameters (continued)

Name	RA (°)	Dec (°)	σ	z	Trigger (UT)	T_1 (s)	T_2 (s)	T_{100} (s)	α_γ	β_γ	ϵ_γ	E_{min}	E_{max}	Fluence$_\gamma$
101021B	0.46	47.34	12.81°	0.5*	2010-10-21 01:30:31.66	-0.51	1.02	1.53	1.05†	2.25†	205†	8	1000	2.926E-7
101023A	317.96	-65.39	1.08″	2.15*	2010-10-23 22:50:12.00	-11	137.3	148.3	1.07	2.5	200	20	2000	6.6E-5
101024A	66.51	-77.27	1.08″	2.15*	2010-10-24 11:39:33.60	-7.68	16.77	24.45	1.4	3.4	56.25	10	1000	1.2E-6
101025A	240.19	-8.49	24.35°	2.15*	2010-10-25 03:30:18.64	-1.79	12.54	14.33	1.05†	2.25†	205†	8	1000	2.788E-7
101026A	263.70	-0.37	7.57°	0.5*	2010-10-26 00:49:16.14	-0.13	0.13	0.26	1.05†	2.25†	205†	8	1000	9.295E-7
101027A	79.02	43.97	11.39°	0.5*	2010-10-27 05:30:30.76	-1.28	0.06	1.34	1.05†	2.25†	205†	8	1000	1.438E-7
101030A	166.38	-16.38	1.08″	2.15*	2010-10-30 15:56:30.72	-69.63	46.8	116.43	1.82	2.82	200*	15	150	2.0E-6
101031A	184.12	-7.47	15.87°	0.5*	2010-10-31 14:59:32.73	-0.06	0.32	0.38	1.05†	2.25†	205†	8	1000	2.217E-7
101101A	13.55	45.75	3.06°	2.15*	2010-11-01 17:51:34.02	-2.3	1.02	3.32	1.05†	2.25†	205†	8	1000	6.500E-7
101102A	284.68	-37.03	7.85°	2.15*	2010-11-02 20:10:07.43	-1.79	41.73	43.52	1.05†	2.25†	205†	8	1000	1.722E-6
101104A	161.02	-7.08	8.53°	0.5*	2010-11-04 19:26:14.05	-0.51	0.77	1.28	1.05†	2.25†	205†	8	1000	8.934E-7
101107A	168.33	22.43	4.09°	2.15*	2010-11-07 00:16:25.12	2.3	378.12	375.82	1.05†	2.25†	205†	8	1000	7.258E-6
101112A	292.22	39.36	0.02°	2.15*	2010-11-12 22:10:24.00	0	15.448	15.448	0.79	2.02	105.8	8	1000	2.96E-6
101112B	100.10	9.62	5.13°	2.15*	2010-11-12 23:36:55.81	-9.47	73.47	82.94	1.05†	2.25†	205†	8	1000	8.572E-6
101113A	29.08	0.21	2.67°	2.15*	2010-11-13 11:35:36.40	-0.26	12.03	12.29	1.05†	2.25†	205†	8	1000	3.062E-6
101114A	303.19	14.03	0.02°	2.15*	2010-11-14 00:32:50.00	-2.2	6.6	8.8	1.15	3.15	296	10*	10000*	4.7E-6
101116A	32.00	-81.20	7.26°	0.5*	2010-11-16 11:32:26.74	-0.13	0.45	0.58	1.05†	2.25†	205†	8	1000	3.044E-7
101117A	57.19	-26.87	1.75°	2.15*	2010-11-17 11:54:45.75	-2.05	48.13	50.18	1.05†	2.25†	205†	8	1000	8.241E-6
101117B	173.00	-72.66	0.36″	2.15*	2010-11-17 19:13:23.00	-0.1	8.6	8.7	1.5	2.5	200*	15	150	1.1E-6
101119A	226.49	59.61	16.19°	0.5*	2010-11-19 16:27:02.66	-0.32	0.32	0.64	1.05†	2.25†	205†	8	1000	1.694E-7
101123A	131.38	5.56	0.34°	2.15*	2010-11-23 22:51:34.97	41.47	162.272	120.802	0.75	2.14	476	10	1000	1.283E-4
101126A	84.77	-22.55	1.00°	2.15*	2010-11-26 04:44:27.48	0	43.84	43.84	1.05†	2.25†	205†	8	1000	3.101E-5
101127A	290.31	7.89	23.17°	2.15*	2010-11-27 02:13:59.07	-3.33	26.11	29.44	1.05†	2.25†	205†	8	1000	6.961E-7
101127B	70.95	-11.32	6.55°	2.15*	2010-11-27 02:27:30.90	-5.12	55.55	60.67	1.05†	2.25†	205†	8	1000	3.085E-6
101128A	145.47	-35.20	5.70°	2.15*	2010-11-28 07:44:04.24	-2.82	5.38	8.2	1.05†	2.25†	205†	8	1000	8.356E-7
101129A	155.92	-17.64	0.03°	2.15*	2010-11-29 15:39:30.76	0	2	2.0	0.4	2.4	1210	20	5000	3.5E-6
101129B	271.54	1.01	8.22°	0.5*	2010-11-29 17:25:25.34	-0.06	0.51	0.57	1.05†	2.25†	205†	8	1000	8.079E-7
101130A	61.80	-16.75	0.20°	2.15*	2010-11-30 09:39:26.18	0	65.792	65.792	0.6	2.6	190	20	1000	3.1E-6
101130B	274.61	26.62	23.61°	2.15*	2010-11-30 01:45:54.35	-2.3	2.56	4.86	1.05†	2.25†	205†	8	1000	2.336E-7
101201A	1.96	-16.20	0.02°	2.15*	2010-12-01 10:01:49.74	0	112.64	112.64	1.5	3.5	275.70	10	1000	2.41E-5
101202A	254.02	58.48	6.13°	2.15*	2010-12-02 03:41:53.84	0	18.43	18.43	1.05†	2.25†	205†	8	1000	1.408E-6
101204A	167.54	-20.42	1.08″	2.15*	2010-12-04 23:53:29.00	0	10	10.0	1.3	2.3	200*	15	150	1.2E-6
101204B	191.91	55.67	10.37°	0.5*	2010-12-04 08:14:18.60	-0.06	0.06	0.12	1.05†	2.25†	205†	8	1000	2.817E-7
101205A	322.10	-39.10	11.10°	2.15*	2010-12-05 07:24:24.86	-3.84	4.1	7.94	1.05†	2.25†	205†	8	1000	3.905E-7
101206A	164.08	-38.11	3.50°	2.15*	2010-12-06 00:52:17.53	0	34.82	34.82	1.05†	2.25†	205†	8	1000	5.841E-6
101207A	175.75	8.72	3.73°	2.15*	2010-12-07 12:51:41.31	5.63	67.07	61.44	1.05†	2.25†	205†	8	1000	6.648E-6
101208A	212.40	4.04	11.70°	0.5*	2010-12-08 04:52:56.92	-0.19	0	0.19	1.05†	2.25†	205†	8	1000	3.098E-7
101208B	280.94	-59.02	1.41°	2.15*	2010-12-08 11:57:01.20	-0.64	1.41	2.05	1.05†	2.25†	205†	8	1000	3.843E-6
101211A	31.84	10.06	11.25°	2.15*	2010-12-11 11:37:54.52	-2.82	10.75	13.57	1.05†	2.25†	205†	8	1000	1.634E-6
101213A	241.31	21.90	1.08″	0.414	2010-12-13 10:49:19.00	-1	201.1	202.1	1.1	2.35	309.7	10	1000	1.40E-5
101214A	0.69	-28.27	5.56°	2.15*	2010-12-14 17:57:03.97	-1.41	0.83	2.24	1.05†	2.25†	205†	8	1000	2.371E-7
101214B	181.13	-31.06	5.73°	2.15*	2010-12-14 23:50:00.97	-0.77	10.75	11.52	1.05†	2.25†	205†	8	1000	1.092E-6
101216A	284.27	-20.97	2.12°	0.5*	2010-12-16 17:17:52.54	0	1.92	1.92	1.05†	2.25†	205†	8	1000	3.044E-6
101219A	74.59	-2.53	0.01°	0.718	2010-12-19 02:31:29.00	0	5.6	5.6	0.22	2.22	490	20	10000	3.6E-6

Table A.1: IC79 GRB Parameters (continued)

Name	RA (°)	Dec (°)	σ	z	Trigger (UT)	T_1 (s)	T_2 (s)	T_{100} (s)	α_γ	β_γ	ϵ_γ	E_{min}	E_{max}	Fluence$_\gamma$
101219B	12.23	-34.57	1.08″	0.5519	2010-12-19 16:27:53.00	10	66.66	56.66	0.33	2.12	70	10	1000	5.5E-6
101220A	241.57	46.14	1.25°	2.15*	2010-12-20 13:49:58.13	2.3	74.75	72.45	1.05†	2.25†	205†	8	1000	9.596E-6
101220B	2.70	27.20	1.48°	2.15*	2010-12-20 20:43:54.12	-1.02	30.72	31.74	1.05†	2.25†	205†	8	1000	5.288E-6
101223A	250.55	48.22	4.34°	2.15*	2010-12-23 20:00:18.10	-41.22	14.85	56.07	1.05†	2.25†	205†	8	1000	2.455E-6
101224A	285.94	45.71	0.02°	0.5*	2010-12-24 05:27:13.86	-0.06	1.66	1.72	0.83	2.83	330	10	1000	2.4E-7
101224B	289.14	-55.25	4.82°	2.15*	2010-12-24 13:52:58.23	-0.13	44.61	44.74	1.05†	2.25†	205†	8	1000	3.892E-6
101224C	290.16	34.46	8.86°	2.15*	2010-12-24 14:43:32.93	-2.56	23.04	25.6	1.05†	2.25†	205†	8	1000	2.606E-6
101224D	325.17	-38.66	8.29°	2.15*	2010-12-24 23:57:34.94	-9.73	8.96	18.69	1.05†	2.25†	205†	8	1000	1.355E-6
101225A	0.20	44.60	0.72″	0.40	2010-12-25 18:37:45.00	0	963	963.0	1.82	2.82	200*	15	150	3E-6
101225B	60.68	32.77	1.81°	2.15*	2010-12-25 09:02:53.50	20.54	101.76	81.22	1.05†	2.25†	205†	8	1000	2.016E-5
101227A	186.79	-83.55	7.16°	2.15*	2010-12-27 04:40:28.72	-0.77	94.72	95.49	1.05†	2.25†	205†	8	1000	3.431E-6
101227B	240.50	-24.50	1.62°	2.15*	2010-12-27 09:45:06.57	0.77	154.11	153.34	1.05†	2.25†	205†	8	1000	1.375E-5
101227C	150.87	-49.44	2.59°	2.15*	2010-12-27 12:51:46.19	-0.13	28.74	28.87	1.05†	2.25†	205†	8	1000	6.441E-6
101231A	191.71	17.64	1.41°	2.15*	2010-12-31 01:36:50.61	0	23.62	23.62	1.05†	2.25†	205†	8	1000	1.683E-5
110101A	264.26	36.54	11.17°	2.15*	2011-01-01 04:50:20.48	-2.3	1.28	3.58	1.05†	2.25†	205†	8	1000	2.499E-7
110101B	105.50	34.58	16.49°	2.15*	2011-01-01 12:08:21.58	-103.43	132.1	235.53	1.05†	2.25†	205†	8	1000	6.629E-6
110102A	245.88	7.61	0.36″	2.15*	2011-01-02 18:52:25.00	-49.2	294.9	344.1	1.22	2.3	267	20	5000	5.4E-5
110105A	85.11	-17.12	2.03°	2.15*	2011-01-05 21:02:39.60	-7.68	115.71	123.39	1.05†	2.25†	205†	8	1000	2.092E-5
110106A	79.31	64.17	1.08″	0.093	2011-01-06 15:25:16.00	-1	3.9	4.9	1.71	2.71	200*	15	150	3.0E-7
110106B	134.15	47.00	1.08″	0.618	2011-01-06 21:26:16.08	-16.9	24.5	41.4	1.61	2.61	200*	10	1000	5.90E-6
110108A	11.62	-9.64	2.67°	2.15*	2011-01-08 23:26:18.52	-1.02	50.43	51.45	1.05†	2.25†	205†	8	1000	2.511E-6
110112A	329.93	26.46	1.80″	0.5*	2011-01-12 04:12:18.00	-0.1	0.5	0.6	2.14	3.14	1000*	15	150	3.0E-8
110112B	10.60	64.41	0.03°	2.15*	2011-01-12 22:24:54.00	0	2.34	2.34	0.72	2.72	495	10	1000	3.53E-7
110118A	226.57	-39.55	4.07°	2.15*	2011-01-18 20:34:18.79	-6.14	28.42	34.56	1.05†	2.25†	205†	8	1000	2.966E-6
110119A	348.59	5.99	1.08″	2.15*	2011-01-19 22:20:58.00	-86.4	217.5	303.9	0.6	1.95	126.3	10	1000	1.36E-5
110120A	61.60	-12.00	0.40°	2.15*	2011-01-20 15:59:39.22	-0.7	44.216	44.916	0.6	2.6	680	20	5000	3.1E-5
110123A	246.97	28.03	1.16°	2.15*	2011-01-23 19:17:45.04	0.7	18.56	17.86	0.64	1.96	280	10	1000	2.61E-5
110124A	53.83	36.35	9.14°	2.15*	2011-01-24 18:49:09.07	-3.33	2.05	5.38	1.05†	2.25†	205†	8	1000	1.589E-7
110130A	111.51	38.25	6.75°	2.15*	2011-01-30 05:31:52.58	-0.26	47.1	47.36	1.05†	2.25†	205†	8	1000	2.902E-6
110201A	137.49	88.61	0.01°	2.15*	2011-02-01 09:35:08.00	-2.8	13.3	16.1	1.09	2.09	200*	15	150	7.0E-7
110204A	1.82	-17.40	4.03°	2.15*	2011-02-04 04:17:11.37	-3.84	24.83	28.67	1.05†	2.25†	205†	8	1000	3.096E-6
110205A	164.63	67.53	1.08″	2.22	2011-02-05 02:02:41.00	0	330	330.0	1.52	3.52	222	20	1200	3.66E-5
110205B	359.73	-80.44	9.24°	2.15*	2011-02-05 00:39:04.65	-2.82	3.58	6.4	1.05†	2.25†	205†	8	1000	1.953E-7
110206A	92.36	-58.81	0.02°	2.15*	2011-02-06 18:08:05.00	0	20	20.0	1*	2*	200*	10*	10000*	1.00E-5*
110206B	333.70	1.61	15.47°	2.15*	2011-02-06 04:50:36.06	-6.4	5.89	12.29	1.05†	2.25†	205†	8	1000	7.904E-7
110207A	12.54	-10.79	0.01°	2.15*	2011-02-07 11:17:20.29	-1.02	108.3	109.32	1.09	3.09	450	10	1000	4.4E-6
110207B	179.00	-58.43	9.03°	2.15*	2011-02-07 23:00:26.41	-0.77	6.91	7.68	1.05†	2.25†	205†	8	1000	3.423E-7
110208A	22.46	-20.59	1.08″	2.15*	2011-02-08 21:10:46.00	-1.5	40.7	42.2	2.08	3.08	200*	15	150	2.7E-7
110209A	329.70	-21.93	10.63°	2.15*	2011-02-09 03:58:08.30	-3.78	1.86	5.64	1.05†	2.25†	205†	8	1000	6.733E-7
110210A	13.06	7.78	1.08″	2.15*	2011-02-10 09:52:41.00	-102.9	153.6	256.5	1.73	2.73	200*	15	150	9.6E-7
110212A	69.03	43.72	0.01°	2.15*	2011-02-12 01:09:08.00	-1.8	2.6	4.4	0.78	2.78	44.6	15	150	2.4E-7
110212B	311.33	-74.50	4.33°	0.5*	2011-02-12 13:12:33.52	-0.05	0.02	0.07	1.05†	2.25†	205†	8	1000	6.349E-7
110213A	42.96	49.27	1.08″	1.46	2011-02-13 05:17:29.00	-31.2	32.8	64.0	1.28	2.4	89	20	2000	1.0E-5
110213B	41.77	0.95	0.30°	1.083	2011-02-13 14:31:33.00	0	50	50.0	1.52	3.52	123	20	1400	1.77E-5

Table A.1: IC79 GRB Parameters (continued)

Name	RA (°)	Dec (°)	σ	z	Trigger (UT)	T_1 (s)	T_2 (s)	T_{100} (s)	α_γ	β_γ	ϵ_γ	E_{min}	E_{max}	Fluence$_\gamma$
110213C	6.28	27.54	10.82°	0.5*	2011-02-13 21:00:51.34	-0.13	0.19	0.32	1.05†	2.25†	205†	8	1000	3.273E-8
110220A	185.49	16.58	6.06°	2.15*	2011-02-20 18:16:21.63	-1.79	31.23	33.02	1.05†	2.25†	205†	8	1000	2.114E-6
110221A	15.18	66.05	1.24°	2.15*	2011-02-21 05:51:19.36	-1.54	11.52	13.06	1.05†	2.25†	205†	8	1000	2.246E-6
110223A	345.85	87.56	1.08″	2.15*	2011-02-23 20:56:59.00	0.1	8.1	8.0	1*	2*	200*	15	150	1.6E-7
110223B	150.23	-68.30	1.08″	2.15*	2011-02-23 21:25:48.00	-45	20	65.0	1.65	2.65	200*	15	150	6.1E-7
110226A	199.29	35.77	7.07°	2.15*	2011-02-26 23:44:31.13	-2.3	11.78	14.08	1.05†	2.25†	205†	8	1000	1.896E-6
110227A	148.72	-54.04	11.93°	0.5*	2011-02-27 00:12:28.23	-0.19	1.54	1.73	1.05†	2.25†	205†	8	1000	1.638E-7
110227B	25.24	15.89	7.45°	2.15*	2011-02-27 05:30:10.82	-1.02	17.41	18.43	1.05†	2.25†	205†	8	1000	2.398E-6
110227C	232.73	-9.94	4.99°	2.15*	2011-02-27 10:04:12.55	-11.26	14.34	25.6	1.05†	2.25†	205†	8	1000	2.421E-6
110228A	10.27	-45.67	2.56°	2.15*	2011-02-28 00:15:58.91	-30.72	13.76	44.48	1.05†	2.25†	205†	8	1000	5.144E-6
110228B	245.09	16.41	4.74°	2.15*	2011-02-28 18:59:50.39	-3.84	13.31	17.15	1.05†	2.25†	205†	8	1000	9.601E-7
110301A	229.35	29.40	1.00°	2.15*	2011-03-01 05:08:43.07	0	5.7	5.7	0.81	2.7	106.80	10	1000	3.65E-5
110302A	122.35	2.91	6.84°	2.15*	2011-03-02 01:01:51.73	-11.2	27.14	38.34	1.05†	2.25†	205†	8	1000	3.730E-6
110304A	322.93	33.27	4.23°	2.15*	2011-03-04 01:42:33.80	-0.26	19.26	19.52	1.05†	2.25†	205†	8	1000	3.456E-6
110305A	260.88	-15.80	1.08″	2.15*	2011-03-05 06:38:01.00	-0.9	12.1	13.0	1.62	2.62	200*	15	150	8.0E-7
110307A	193.12	15.64	7.58°	2.15*	2011-03-07 23:19:08.26	-1.79	0.51	2.3	1.05†	2.25†	205†	8	1000	5.750E-7
110311A	117.59	34.29	9.68°	2.15*	2011-03-11 19:29:21.42	-1.79	4.61	6.4	1.05†	2.25†	205†	8	1000	1.119E-6
110312A	157.48	-5.26	1.08″	2.15*	2011-03-12 17:55:37.00	24.1	64.9	40.8	2.32	3.32	200*	15	150	8.2E-7
110315A	279.19	17.54	0.72″	2.15*	2011-03-15 23:57:04.00	-66.8	38.8	105.6	1.77	2.77	200*	15	150	4.1E-6
110316A	46.70	-67.58	17.80°	2.15*	2011-03-16 03:19:41.86	-3.01	-0.06	2.95	1.05†	2.25†	205†	8	1000	1.150E-7
110318A	338.29	-15.28	0.01°	2.15*	2011-03-18 13:14:19.00	-13	10.6	23.6	0.8	2.74	107.00	10	1000	8.05E-6
110318B	211.68	-51.58	1.08″	2.15*	2011-03-18 15:27:09.00	-1.7	3.7	5.4	1.09	2.09	200*	15	150	2.9E-7
110319A	356.50	-66.01	1.08″	2.15*	2011-03-19 02:16:41.00	-0.3	31.3	31.6	1.31	3.31	21.9	15	150	1.4E-6
110319B	326.09	-56.77	0.01°	2.15*	2011-03-19 19:34:02.00	-3.5	28.67	32.17	1.39	2.39	200*	15	150	1.0E-6
110319C	207.96	-51.58	4.94°	2.15*	2011-03-19 15:04:45.46	-2.3	13.04	15.34	1.05†	2.25†	205†	8	1000	1.562E-6
110321A	13.31	-21.81	11.83°	2.15*	2011-03-21 08:17:42.48	-4.1	26.62	30.72	1.05†	2.25†	205†	8	1000	1.120E-6
110322A	99.04	-48.90	4.72°	2.15*	2011-03-22 13:23:42.81	-4.1	32	36.1	1.05†	2.25†	205†	8	1000	3.560E-6
110328A	251.21	57.58	1.08″	2.15*	2011-03-28 12:57:45.00	0	10	10.0	1.72	2.72	200*	15	150	3.0E-6
110328B	117.65	43.10	1.70°	2.15*	2011-03-28 12:29:19.19	1.02	142.34	141.32	1.11	1.94	369	10	1000	2.6E-5
110331A	6.66	25.99	4.66°	2.15*	2011-03-31 14:29:06.84	-0.06	3.14	3.2	1.05†	2.25†	205†	8	1000	2.641E-7
110401A	268.56	26.87	3.76°	2.15*	2011-04-01 22:04:19.63	-0.64	1.73	2.37	0.66	2.36	1194	10	1000	1.51E-6
110402A	197.40	61.25	1.08″	2.15*	2011-04-02 00:12:58.00	-1.5	83.5	85.0	1.03	3.03	1395	10*	10000*	1.6E-5
110406A	17.34	35.81	0.17°	2.15*	2011-04-06 03:44:06.67	0	9.216	9.216	1.24	2.3	326	20	10000	4.8E-5
110407A	186.03	15.71	1.44″	2.15*	2011-04-07 14:06:41.00	-2.9	158.8	161.7	0.73	2.73	57.9	15	150	1.7E-6
110407B	97.41	-11.95	1.00°	2.15*	2011-04-07 23:56:57.06	0.83	9.86	9.03	1.05†	2.25†	205†	8	1000	2.643E-5
110410A	30.94	-15.95	3.67°	2.15*	2011-04-10 03:10:52.43	-11.01	50.94	61.95	1.05†	2.25†	205†	8	1000	6.412E-6
110410B	337.17	-21.96	17.39°	2.15*	2011-04-10 18:31:19.88	-4.74	3.33	8.07	1.05†	2.25†	205†	8	1000	9.522E-7
110411A	291.44	67.71	1.08″	2.15*	2011-04-11 19:34:11.00	-11.9	86.3	98.2	1.51	3.51	41.0	15	150	3.3E-6
110411B	210.30	-64.99	6.28°	2.15*	2011-04-11 15:05:15.35	-3.84	19.71	23.55	1.05†	2.25†	205†	8	1000	3.584E-6
110412A	133.49	13.49	0.02°	2.15*	2011-04-12 07:33:21.00	13.7	40.4	26.7	0.7	2.7	87	10	1000	2.2E-6
110414A	97.87	24.36	1.08″	2.15*	2011-04-14 07:42:14.00	-38.4	135.6	174.0	1*	2*	200*	15	150	3.5E-6
110420A	2.16	-37.89	0.36″	2.15*	2011-04-20 11:02:24.00	-0.1	16	16.1	1.71	3.71	43	10*	10000*	6.54E-6
110420B	320.05	-41.28	0.02°	0.5*	2011-04-20 22:42:11.73	-0.06	0.1	0.16	0.12	2.12	296.8	10	1000	2.65E-7
110421A	277.23	50.80	1.71°	2.15*	2011-04-21 18:10:39.92	-2.56	37.89	40.45	1.05†	2.25†	205†	8	1000	1.060E-5

Table A.1: IC79 GRB Parameters (continued)

Name	RA (°)	Dec (°)	σ	z	Trigger (UT)	T_1 (s)	T_2 (s)	T_{100} (s)	α_γ	β_γ	ϵ_γ	E_{min}	E_{max}	Fluence$_\gamma$
110422B	226.69	43.02	21.52°	0.5*	2011-04-22 00:41:48.56	-0.13	0.19	0.32	1.05†	2.25†	205†	8	1000	8.065E-8
110424A	293.31	-11.12	12.35°	0.5*	2011-04-24 18:11:36.65	-0.06	0.61	0.67	1.05†	2.25†	205†	8	1000	4.652E-8
110426A	219.93	-8.72	1.28°	2.15*	2011-04-26 15:06:26.61	14.59	370.95	356.36	2.28	3.28	200*	10	1000	4.54E-5
110428A	5.30	64.80	0.15°	2.15*	2011-04-28 09:18:30.00	-2	12.568	14.568	0.2	2.88	175.60	10	1000	2.27E-5
110428B	128.44	19.94	2.94°	2.15*	2011-04-28 08:07:05.24	-53.76	47.87	101.63	1.05†	2.25†	205†	8	1000	1.579E-5
110430A	147.06	67.95	2.53°	2.15*	2011-04-30 09:00:13.40	1.02	33.54	32.52	1.05†	2.25†	205†	8	1000	7.067E-6
110503A	132.78	52.21	0.36′′	1.613	2011-05-03 17:35:45.00	-6.6	16.3	22.9	0.98	2.7	219	20	5000	2.6E-5
110503B	70.51	-10.90	4.29°	2.15*	2011-05-03 03:28:26.12	-0.26	7.68	7.94	1.05†	2.25†	205†	8	1000	1.865E-6
110505A	16.81	-32.30	3.09°	2.15*	2011-05-05 04:52:56.43	-0.38	3.71	4.09	1.05†	2.25†	205†	8	1000	2.034E-6
110509A	180.81	-34.00	4.60°	2.15*	2011-05-09 03:24:38.79	-11.01	57.86	68.87	1.05†	2.25†	205†	8	1000	3.761E-6
110509B	74.65	-26.98	8.30°	0.5*	2011-05-09 11:24:15.58	-0.32	0.32	0.64	1.05†	2.25†	205†	8	1000	5.257E-7
110511A	214.10	-45.42	10.62°	2.15*	2011-05-11 14:47:12.69	-2.56	3.33	5.89	1.05†	2.25†	205†	8	1000	4.894E-7

Table A.2: IC86I GRB Parameters

Name	RA (°)	Dec (°)	σ	z	Trigger (UT)	T_1 (s)	T_2 (s)	T_{100} (s)	α_γ	β_γ	ϵ_γ	E_{min}	E_{max}	Fluence$_\gamma$
110517A	296.09	-73.76	8.97°	0.5*	2011-05-17 10:52:35.41	-0.06	0.51	0.57	1.05†	2.25†	205†	8	1000	9.890E-8
110517B	190.15	6.29	2.11°	2.15*	2011-05-17 13:44:47.60	-0.26	22.78	23.04	1.05†	2.25†	205†	8	1000	8.740E-6
110518A	67.18	-34.20	0.20°	2.15*	2011-05-18 20:38:10.77	0	35.072	35.072	1.29	2.3	229	20	10000	6.5E-5
110519A	261.64	-23.43	0.01°	2.15*	2011-05-19 02:12:16.00	-4.7	37.8	42.5	2.09	3.09	200*	15	150	4.0E-6
110520A	134.34	56.43	1.08′′	2.15*	2011-05-20 20:28:48.00	-1.2	16.6	17.8	1.13	2.13	200*	15	150	1.1E-6
110520B	71.01	-85.93	12.41°	2.15*	2011-05-20 07:14:26.24	-10.5	1.79	12.29	1.05†	2.25†	205†	8	1000	1.043E-6
110521A	120.13	45.83	1.08′′	2.15*	2011-05-21 15:51:31.00	0.2	18.8	18.6	0.9	1.9	200*	15	150	4.4E-7
110521B	57.54	-62.34	1.31°	2.15*	2011-05-21 11:28:58.88	0	6.14	6.14	1.05†	2.25†	205†	8	1000	3.608E-6
110522A	228.91	55.53	5.56°	2.15*	2011-05-22 06:08:17.45	-8.7	19.46	28.16	1.05†	2.25†	205†	8	1000	2.109E-6
110522B	184.46	49.33	6.40°	2.15*	2011-05-22 07:06:01.93	-5.12	22.02	27.14	1.05†	2.25†	205†	8	1000	1.057E-6
110522C	180.57	-26.81	12.50°	2.15*	2011-05-22 15:11:56.61	-0.26	57.86	58.12	1.05†	2.25†	205†	8	1000	3.044E-6
110523A	219.03	-15.42	4.50°	2.15*	2011-05-23 08:15:54.58	-1.28	43.26	44.54	1.05†	2.25†	205†	8	1000	2.227E-6
110526A	102.48	-16.42	5.84°	0.5*	2011-05-26 17:09:01.81	-0.13	0.32	0.45	1.05†	2.25†	205†	8	1000	8.457E-7
110528A	44.79	-6.87	2.48°	2.15*	2011-05-28 14:58:44.30	-1.02	68.61	69.63	1.05†	2.25†	205†	8	1000	4.595E-6
110529A	118.33	67.91	1.50°	2.15*	2011-05-29 00:48:40.25	0	2.5	2.5	0.88	2.05	1161	10	1000	2.32E-6
110529B	172.60	8.79	2.10°	2.15*	2011-05-29 06:17:41.01	0.26	46.08	45.82	1.05†	2.25†	205†	8	1000	6.779E-6
110530A	282.07	61.93	0.72′′	2.15*	2011-05-30 15:31:02.00	-4.5	17.4	21.9	2.06	3.06	200*	15	150	3.3E-7
110531A	190.51	11.85	11.06°	2.15*	2011-05-31 10:45:10.56	-4.86	33.79	38.65	1.05†	2.25†	205†	8	1000	2.295E-6
110601A	310.71	11.48	3.00°	2.15*	2011-06-01 16:20:16.08	0	52.21	52.21	1.05†	2.25†	205†	8	1000	1.237E-5
110604A	271.00	18.47	0.05°	2.15*	2011-06-04 14:49:45.67	0	37.376	37.376	1.1	3.2	166	20	5000	3.1E-5
110605A	14.95	52.46	1.00°	2.15*	2011-06-05 04:23:32.30	1.54	84.23	82.69	1.05†	2.25†	205†	8	1000	1.925E-5
110605B	242.09	-3.14	10.13°	0.5*	2011-06-05 18:42:49.04	-0.26	1.28	1.54	1.05†	2.25†	205†	8	1000	4.385E-7
110609B	317.63	-38.16	4.71°	2.15*	2011-06-09 10:12:06.16	-6.66	26.37	33.03	1.05†	2.25†	205†	8	1000	2.353E-6
110610A	308.18	74.83	1.08′′	2.15*	2011-06-10 15:22:06.00	-53	24	77.0	0.93	2.23	170.0	10	1000	8.70E-6
110613A	336.86	-3.47	2.79°	2.15*	2011-06-13 15:08:46.30	-0.26	39.94	40.2	1.05†	2.25†	205†	8	1000	3.256E-6
110616A	274.45	-34.02	11.96°	2.15*	2011-06-16 15:33:25.23	-4.61	7.94	12.55	1.05†	2.25†	205†	8	1000	1.295E-6
110618A	176.81	-71.69	0.50°	2.15*	2011-06-18 08:47:36.38	-3.07	246.632	249.702	1.4	3.4	569	20	5000	1.1E-4

Table A.2: IC86I GRB Parameters (continued)

Name	RA (°)	Dec (°)	σ	z	Trigger (UT)	T_1 (s)	T_2 (s)	T_{100} (s)	α_γ	β_γ	ϵ_γ	E_{min}	E_{max}	Fluence$_\gamma$
110618B	147.05	-7.48	2.10°	2.15*	2011-06-18 18:14:16.31	-0.51	89.09	89.6	1.05†	2.25†	205†	8	1000	9.781E-6
110622A	133.96	19.46	1.79°	2.15*	2011-06-22 03:47:19.10	6.08	76.48	70.4	1.05†	2.25†	205†	8	1000	5.427E-5
110624A	65.02	-15.95	17.34°	2.15*	2011-06-24 21:44:25.56	-1.28	2.24	3.52	1.05†	2.25†	205†	8	1000	2.781E-7
110625A	286.75	6.75	0.01°	2.15*	2011-06-25 21:08:22.00	-1	146.3	147.3	1.05	2.7	190	20	10000	6.1E-5
110625B	315.33	-39.44	4.60°	2.15*	2011-06-25 13:53:24.57	-0.51	35.07	35.58	1.05†	2.25†	205†	8	1000	3.523E-6
110626A	131.91	5.56	7.66°	2.15*	2011-06-26 10:44:54.21	-0.77	5.63	6.4	1.05†	2.25†	205†	8	1000	1.163E-6
110629A	69.37	25.01	4.82°	2.15*	2011-06-29 04:09:58.20	0	61.7	61.7	1.05†	2.25†	205†	8	1000	2.428E-6
110702A	5.62	-37.66	4.75°	2.15*	2011-07-02 04:29:28.92	-10.75	23.62	34.37	1.05†	2.25†	205†	8	1000	7.988E-6
110703A	155.39	-29.30	3.76°	2.15*	2011-07-03 13:22:15.58	-4.22	2.5	6.72	1.05†	2.25†	205†	8	1000	9.739E-7
110705B	122.96	28.80	3.08°	2.15*	2011-07-05 08:43:43.42	0.26	19.46	19.2	1.05†	2.25†	205†	8	1000	8.943E-6
110706A	100.08	6.14	8.03°	2.15*	2011-07-06 04:51:04.03	-1.54	10.5	12.04	1.05†	2.25†	205†	8	1000	3.269E-6
110706B	94.15	-50.77	2.04°	2.15*	2011-07-06 11:26:15.76	-2.56	70.66	73.22	1.05†	2.25†	205†	8	1000	6.716E-6
110706C	9.06	31.73	4.11°	2.15*	2011-07-06 17:27:56.34	0.13	17.02	16.89	1.05†	2.25†	205†	8	1000	2.341E-6
110706D	347.47	7.11	2.58°	2.15*	2011-07-06 23:26:51.41	-14.72	18.5	33.22	1.05†	2.25†	205†	8	1000	6.554E-6
110708A	340.12	53.96	0.02°	2.15*	2011-07-08 04:43:22.00	0	50	50.0	1*	2*	200*	20	200	2E-6
110708B	170.38	-50.57	0.16°	2.15*	2011-07-08 13:59:46.39	0	47.616	47.616	0.78	2.4	294	20	10000	9.4E-5
110709A	238.89	40.92	1.08′′	2.15*	2011-07-09 15:24:29.00	-4.3	65.5	69.8	1.03	3.03	356	20	5000	3.7E-5
110709B	164.65	-23.45	0.72′′	2.15*	2011-07-09 21:32:44.00	-12	850.3	862.3	1	3.0	278	10*	10000*	1.1E-6
110709C	155.38	23.12	1.53°	2.15*	2011-07-09 11:06:53.37	0	24.06	24.06	1.05†	2.25†	205†	8	1000	6.909E-6
110709D	156.21	-41.79	10.84°	2.15*	2011-07-09 20:40:50.09	-1.79	3.58	5.37	1.05†	2.25†	205†	8	1000	7.974E-7
110710A	229.09	48.40	3.87°	2.15*	2011-07-10 22:53:50.60	-4.86	17.86	22.72	1.05†	2.25†	205†	8	1000	9.317E-6
110715A	237.68	-46.24	1.44′′	0.82	2011-07-15 13:13:49.00	-3	24.432	27.432	1.23	2.7	120	20	10000	2.3E-5
110716A	329.68	-76.98	3.86°	2.15*	2011-07-16 00:25:19.97	-3.07	4.1	7.17	1.05†	2.25†	205†	8	1000	1.355E-6
110717A	308.47	-7.85	7.45°	0.5*	2011-07-17 04:19:50.66	-0.02	0.1	0.12	1.05†	2.25†	205†	8	1000	2.512E-7
110717B	312.84	-14.84	1.20°	2.15*	2011-07-17 07:39:55.86	5.38	95.75	90.37	1.05†	2.25†	205†	8	1000	4.245E-5
110719A	24.58	34.59	1.44′′	2.15*	2011-07-19 06:09:11.00	-2	42.9	44.9	1.63	2.63	200*	15	150	1.8E-6
110720A	198.65	-44.29	2.60°	2.15*	2011-07-20 04:14:32.38	-0.13	11.07	11.2	1.05†	2.25†	205†	8	1000	5.628E-6
110721A	333.40	-39.00	0.75°	2.15*	2011-07-21 04:47:43.76	0	29.624	29.624	0.94	1.77	372.50	10	1000	3.52E-5
110722A	215.06	5.00	1.99°	2.15*	2011-07-22 16:39:16.68	-0.51	72.96	73.47	1.05†	2.25†	205†	8	1000	2.114E-5
110722B	8.28	62.74	4.66°	2.15*	2011-07-22 17:01:45.91	-4.61	9.73	14.34	1.05†	2.25†	205†	8	1000	1.799E-6
110725A	270.14	-25.20	9.06°	2.15*	2011-07-25 05:39:42.06	-1.02	19.2	20.22	1.05†	2.25†	205†	8	1000	1.309E-6
110726A	286.72	56.07	0.36′′	1.036	2011-07-26 01:30:40.00	-0.9	5	5.9	0.64	2.64	46.5	15	150	2.2E-7
110726B	317.71	2.47	3.82°	2.15*	2011-07-26 05:03:59.49	-3.84	26.11	29.95	1.05†	2.25†	205†	8	1000	4.361E-6
110729A	353.39	4.97	1.36°	2.15*	2011-07-29 03:25:05.93	2.08	410.66	408.58	1.05†	2.25†	205†	8	1000	4.640E-5
110730A	263.08	-22.78	4.28°	2.15*	2011-07-30 00:11:54.74	-7.94	20.48	28.42	1.05†	2.25†	205†	8	1000	1.257E-6
110730B	335.10	-2.89	3.80°	2.15*	2011-07-30 15:50:43.76	-8.7	25.15	33.85	1.05†	2.25†	205†	8	1000	7.969E-6
110731A	280.50	-28.54	0.36′′	2.83	2011-07-31 11:09:30.00	-1.5	80.3	81.8	0.8	2.98	304	10	1000	2.218E-5
110801A	89.44	80.96	0.36′′	1.858	2011-08-01 19:49:42.00	-24.2	385	409.2	1.84	3.84	140	15	150	7.3E-6
110801B	248.27	-57.06	7.30°	0.5*	2011-08-01 08:01:43.09	-0.13	0.26	0.39	1.05†	2.25†	205†	8	1000	3.537E-7
110802A	44.45	32.59	0.12°	0.5*	2011-08-02 15:19:16.19	0	0.6	0.6	0.63	2.63	3451	20	10000	1.3E-5
110803A	300.42	-11.44	7.49°	2.15*	2011-08-03 18:47:25.43	-156.68	30.21	186.89	1.05†	2.25†	205†	8	1000	2.951E-6
110806A	112.04	2.38	2.42°	2.15*	2011-08-06 22:25:31.12	0.26	28.67	28.41	1.05†	2.25†	205†	8	1000	7.190E-6
110807A	278.70	-8.76	0.03°	2.15*	2011-08-07 19:57:46.00	0	10	10.0	1*	2*	200*	10*	10000*	1.00E-5*
110808A	57.27	-44.20	1.80′′	2.15*	2011-08-08 06:18:54.00	-7.4	40.6	48.0	2.32	3.32	200*	15	150	3.3E-7

Table A.2: IC86I GRB Parameters (continued)

Name	RA (°)	Dec (°)	σ	z	Trigger (UT)	T_1 (s)	T_2 (s)	T_{100} (s)	α_γ	β_γ	ϵ_γ	E_{min}	E_{max}	Fluence$_\gamma$
110808B	266.18	-37.74	0.07°	0.5*	2011-08-08 15:44:55.24	0	0.5	0.5	1.07	2.5	4238	20	10000	1.6E-5
110809A	172.17	-13.93	1.84°	2.15*	2011-08-09 11:03:34.00	-4.35	8.19	12.54	1.05†	2.25†	205†	8	1000	3.905E-6
110812A	358.41	72.21	0.03°	2.15*	2011-08-12 00:20:08.00	0	30	30.0	1*	2*	200*	10*	10000*	1.00E-5*
110812B	77.76	1.71	2.49°	2.15*	2011-08-12 21:35:08.61	-2.3	8.96	11.26	1.05†	2.25†	205†	8	1000	1.174E-6
110813A	61.24	34.56	1.00°	2.15*	2011-08-13 05:40:50.93	-1.79	20.99	22.78	1.05†	2.25†	205†	8	1000	4.768E-6
110815A	85.30	32.44	0.11°	2.15*	2011-08-15 09:40:55.97	0	19.2	19.2	0.85	2.5	251	20	10000	5.0E-5
110817A	336.04	-45.84	1.54°	2.15*	2011-08-17 04:35:12.12	0	5.95	5.95	1.05†	2.25†	205†	8	1000	1.195E-5
110818A	317.34	-63.98	0.72″	2.15*	2011-08-18 20:37:49.00	-14.2	117.4	131.6	1.33	3.33	256.3	10	1000	8.2E-6
110819A	139.49	-76.64	3.19°	2.15*	2011-08-19 15:57:54.97	-0.51	15.87	16.38	1.05†	2.25†	205†	8	1000	3.036E-6
110820A	343.19	70.30	1.44″	2.15*	2011-08-20 17:38:27.00	-7.07	264.9	271.97	1.92	2.92	200*	15	150	8.2E-7
110820B	157.58	-54.60	0.50°	2.15*	2011-08-20 21:27:48.05	0	191.488	191.488	1.22	2.1	481	20	10000	2.5E-4
110820C	90.51	21.63	3.96°	2.15*	2011-08-20 11:25:44.35	-4.1	7.17	11.27	1.05†	2.25†	205†	8	1000	7.981E-7
110824A	152.05	1.32	1.68°	2.15*	2011-08-24 00:13:09.94	0	76.61	76.61	1.05†	2.25†	205†	8	1000	1.485E-5
110825A	44.90	15.40	0.34°	2.15*	2011-08-25 02:27:03.00	-3	61.11	64.11	1.23	2.04	233.6	10	1000	5.45E-5
110825B	251.31	-80.28	5.18°	2.15*	2011-08-25 06:22:11.44	-16.38	34.69	51.07	1.05†	2.25†	205†	8	1000	2.179E-6
110827A	164.06	53.82	0.02°	2.15*	2011-08-27 00:01:52.00	-2.9	6.3	9.2	1.24	2.24	200*	15	150	1.8E-7
110828A	110.58	-23.81	1.04°	2.15*	2011-08-28 13:48:14.72	-1.12	43.55	44.67	1.05†	2.25†	205†	8	1000	2.721E-6
110831A	352.35	33.66	5.86°	2.15*	2011-08-31 06:45:26.61	-20.22	78.66	98.88	1.05†	2.25†	205†	8	1000	4.421E-6
110901A	141.28	-15.79	3.37°	2.15*	2011-09-01 05:31:44.06	-7.68	14.85	22.53	1.05†	2.25†	205†	8	1000	1.506E-6
110903A	197.06	58.98	0.02°	2.15*	2011-09-03 02:39:33.12	0	422	422.0	0.69	2.7	295	20	10000	4.2E-5
110903B	164.21	42.08	1.18°	2.15*	2011-09-03 00:13:06.29	-1.02	27.65	28.67	1.05†	2.25†	205†	8	1000	1.521E-5
110904A	359.69	35.90	2.63°	2.15*	2011-09-04 02:58:15.96	-0.13	83.78	83.91	1.05†	2.25†	205†	8	1000	1.110E-5
110904B	190.40	-28.85	6.11°	2.15*	2011-09-04 03:54:36.02	-1.28	50.18	51.46	1.05†	2.25†	205†	8	1000	3.464E-6
110904C	323.74	23.94	1.68°	2.15*	2011-09-04 12:44:19.33	-2.56	17.92	20.48	1.05†	2.25†	205†	8	1000	3.812E-6
110905A	278.96	-19.27	0.03°	2.15*	2011-09-05 05:48:40.00	590	963	373.0	1.53	2.53	200*	15	150	7.8E-7
110906A	296.89	-26.21	0.04°	2.15*	2011-09-06 12:25:13.00	0	94	94.0	1*	2*	200*	10*	10000*	1.00E-5*
110906B	26.32	17.65	4.03°	2.15*	2011-09-06 07:15:13.42	-5.38	18.56	23.94	1.05†	2.25†	205†	8	1000	3.796E-6
110909A	347.34	-24.22	1.98°	2.15*	2011-09-09 02:46:58.19	-12.29	8.45	20.74	1.05†	2.25†	205†	8	1000	4.920E-5
110911A	258.58	-66.98	50.00°	2.15*	2011-09-11 01:41:41.57	-4.61	4.35	8.96	1.05†	2.25†	205†	8	1000	5.938E-7
110915A	310.82	-0.72	2.16″	2.15*	2011-09-15 13:20:44.00	-2.74	92.1	94.84	0.94	2.94	183	15	150	1.35E-5
110915B	77.55	1.93	0.04°	2.15*	2011-09-15 18:24:19.00	0	18	18.0	1*	2*	200*	10*	10000*	1.00E-5*
110916A	4.11	40.36	21.86°	0.5*	2011-09-16 00:23:01.65	-1.41	0.38	1.79	1.05†	2.25†	205†	8	1000	4.226E-7
110918A	32.58	-27.28	0.06°	0.982	2011-09-18 21:27:02.86	0	69.376	69.376	1.2	2	150	20	10000	7.5E-4
110919A	279.97	66.43	1.00°	2.15*	2011-09-19 15:12:15.78	10.5	45.57	35.07	1.05†	2.25†	205†	8	1000	2.683E-5
110920A	87.57	38.76	5.00°	2.15*	2011-09-20 08:07:16.41	-0.51	9.22	9.73	1.05†	2.25†	205†	8	1000	2.687E-6
110920B	209.82	-27.56	1.00°	2.15*	2011-09-20 13:05:43.81	5.12	165.89	160.77	1.05†	2.25†	205†	8	1000	1.723E-4
110921A	294.10	36.33	1.08″	2.15*	2011-09-21 13:51:20.00	-31.55	16.45	48.0	1.39	3.39	139	10	1000	4.2E-6
110921B	6.09	-5.83	7.31°	2.15*	2011-09-21 10:38:48.20	-68.61	80.9	149.51	1.05†	2.25†	205†	8	1000	5.897E-6
110921C	17.97	-27.75	1.00°	2.15*	2011-09-21 21:52:45.09	0.9	18.56	17.66	1.05†	2.25†	205†	8	1000	3.631E-5
110923A	323.40	-10.89	3.69°	2.15*	2011-09-23 20:01:58.13	0	46.4	46.4	1.05†	2.25†	205†	8	1000	4.092E-6
110924A	234.75	-66.31	0.03°	2.15*	2011-09-24 09:03:20.00	0	10	10.0	1*	2*	200*	10*	10000*	1.00E-5*
110926A	69.44	10.43	3.27°	2.15*	2011-09-26 02:33:36.64	-0.77	74.5	75.27	1.05†	2.25†	205†	8	1000	1.198E-5
110928A	257.73	36.54	1.44″	2.15*	2011-09-28 01:51:31.00	-0.53	27.88	28.41	1.09	2.09	200*	15	150	6.9E-7
110928B	153.40	34.29	1.42°	2.15*	2011-09-28 04:19:51.41	-119.3	28.93	148.23	1.05†	2.25†	205†	8	1000	1.415E-5

Table A.2: IC86I GRB Parameters (continued)

Name	RA (°)	Dec (°)	σ	z	Trigger (UT)	T_1 (s)	T_2 (s)	T_{100} (s)	α_γ	β_γ	ϵ_γ	E_{min}	E_{max}	Fluence$_\gamma$
110929A	288.19	-62.21	4.03°	2.15*	2011-09-29 04:28:53.58	-0.51	4.61	5.12	1.05†	2.25†	205†	8	1000	2.197E-6
110930A	187.31	-53.66	5.05°	2.15*	2011-09-30 13:32:31.19	-6.91	30.98	37.89	1.05†	2.25†	205†	8	1000	6.232E-6
111001A	340.01	-15.33	15.11°	0.5*	2011-10-01 19:17:58.58	-0.26	0.13	0.39	1.05†	2.25†	205†	8	1000	1.901E-7
111003A	276.76	-62.32	1.11°	2.15*	2011-10-03 11:10:00.23	0.51	17.15	16.64	0.94	2.94	231.5	10	1000	1.83E-5
111005A	223.31	-19.72	0.02°	2.15*	2011-10-05 08:05:14.00	-5.23	23.06	28.29	2.03	3.03	200*	15	150	6.2E-7
111005B	340.30	75.80	5.28°	2.15*	2011-10-05 09:33:03.38	-11.26	19.46	30.72	1.05†	2.25†	205†	8	1000	2.055E-6
111008A	60.45	-32.71	1.08′′	5.0	2011-10-08 22:12:58.00	-2.64	68.8	71.44	1.36	3.36	149	20	2000	9.0E-6
111008B	220.75	-5.67	4.34°	2.15*	2011-10-08 23:49:01.29	-4.1	38.4	42.5	1.05†	2.25†	205†	8	1000	3.034E-6
111009A	183.04	-56.82	1.08°	2.15*	2011-10-09 06:45:40.17	-0.26	20.48	20.74	1.05†	2.25†	205†	8	1000	1.203E-5
111010A	87.09	43.98	3.18°	2.15*	2011-10-10 05:40:34.56	-3.58	78.85	82.43	1.05†	2.25†	205†	8	1000	1.101E-5
111010B	183.54	-31.70	7.08°	2.15*	2011-10-10 15:50:21.80	-1.02	7.68	8.7	1.05†	2.25†	205†	8	1000	8.706E-7
111010C	69.80	41.88	1.67°	2.15*	2011-10-10 17:00:35.29	1.54	54.53	52.99	1.05†	2.25†	205†	8	1000	1.256E-5
111010D	77.02	-14.96	7.68°	2.15*	2011-10-10 21:34:13.68	-14.66	3.9	18.56	1.05†	2.25†	205†	8	1000	9.588E-7
111011A	37.96	-12.53	6.77°	0.5*	2011-10-11 02:15:09.90	-0.06	1.41	1.47	1.05†	2.25†	205†	8	1000	4.205E-7
111012A	154.01	68.09	2.08°	2.15*	2011-10-12 10:56:37.44	1.02	21.76	20.74	1.05†	2.25†	205†	8	1000	1.645E-5
111012B	97.22	67.05	1.71°	2.15*	2011-10-12 19:27:39.10	-0.51	7.42	7.93	1.05†	2.25†	205†	8	1000	3.294E-6
111015A	220.65	-58.41	1.96°	2.15*	2011-10-15 10:15:12.98	-0.64	92.1	92.74	1.05†	2.25†	205†	8	1000	2.420E-5
111016A	153.83	27.46	1.08′′	2.15*	2011-10-16 18:37:04.00	35.41	614.48	579.07	1.95	2.95	200*	15	150	4.0E-6
111016B	290.50	-4.58	0.18°	2.15*	2011-10-16 22:41:40.72	0	145.408	145.408	0.78	2.78	378	20	5000	1.37E-4
111017A	8.10	-7.01	1.00°	2.15*	2011-10-17 15:45:23.72	0.26	11.33	11.07	0.91	2.7	692.5	10	1000	2.26E-5
111018A	271.49	-3.91	1.08′′	2.15*	2011-10-18 17:26:24.00	-4.08	37.3	41.38	2.18	3.18	200*	15	150	4.0E-7
111018B	106.08	66.14	7.15°	2.15*	2011-10-18 14:16:48.87	-0.77	7.42	8.19	1.05†	2.25†	205†	8	1000	1.112E-6
111018C	124.18	81.29	7.46°	2.15*	2011-10-18 18:50:14.71	-6.4	23.3	29.7	1.05†	2.25†	205†	8	1000	1.763E-6
111020A	287.05	-38.01	1.08′′	0.5*	2011-10-20 06:33:49.00	-0.04	0.39	0.43	1.37	2.37	1000*	15	150	6.5E-8
111022A	275.87	-23.67	0.01°	2.15*	2011-10-22 16:07:04.00	-17.69	18.57	36.26	1.01	3.01	64.7	15	150	2.0E-6
111022B	108.97	49.68	1.08′′	2.15*	2011-10-22 17:13:04.00	-47.84	53.8	101.64	1.59	2.59	200*	15	150	9.0E-7
111022C	104.50	-33.11	9.32°	0.5*	2011-10-22 20:29:23.70	-0.13	0.06	0.19	1.05†	2.25†	205†	8	1000	1.260E-7
111024A	222.18	25.84	0.15°	0.5*	2011-10-24 07:21:27.00	0	0	0.0	1*	2*	1000*	10*	10000*	1.00E-5*
111024B	162.74	-44.94	2.57°	2.15*	2011-10-24 17:19:02.88	-6.14	62.46	68.6	1.05†	2.25†	205†	8	1000	1.578E-5
111024C	91.23	-1.75	13.15°	0.5*	2011-10-24 21:30:02.24	-0.26	1.54	1.8	1.05†	2.25†	205†	8	1000	2.320E-7
111025A	325.62	-35.52	2.73°	2.15*	2011-10-25 01:52:45.74	-0.51	51.2	51.71	1.05†	2.25†	205†	8	1000	2.981E-6
111026A	244.26	-47.44	0.02°	2.15*	2011-10-26 06:47:29.00	-0.09	4.07	4.16	1.69	2.69	200*	15	150	1.7E-7
111029A	44.78	57.11	1.44′′	2.15*	2011-10-29 09:44:40.00	19.6	28.92	9.32	0.77	2.77	36.2	15	150	3.9E-7
111103A	327.11	-10.53	0.01°	2.15*	2011-11-03 10:35:13.00	-0.42	12.14	12.56	0.43	2.43	152.2	10	1000	3.20E-6
111103B	265.69	1.61	1.08′′	2.15*	2011-11-03 10:59:03.00	-6.55	250.78	257.33	0.97	2.97	372	20	5000	2.0E-5
111103C	201.58	-43.16	10.99°	0.5*	2011-11-03 22:45:05.72	-0.06	0.26	0.32	1.05†	2.25†	205†	8	1000	2.818E-7
111105A	153.48	7.28	14.24°	2.15*	2011-11-05 10:57:36.08	-9.98	33.54	43.52	1.05†	2.25†	205†	8	1000	1.681E-6
111107A	129.48	-66.52	1.08′′	2.893	2011-11-07 00:50:25.48	-1.54	31.83	33.37	1.38	3.38	108	10	1000	1.392E-6
111107B	315.46	-38.53	3.53°	2.15*	2011-11-07 01:49:46.02	0.19	77.38	77.19	1.05†	2.25†	205†	8	1000	1.041E-5
111109A	118.20	-41.58	1.44′′	2.15*	2011-11-09 02:57:46.00	-5.6	8.4	14.0	1.86	2.86	200*	15	150	2.4E-7
111109B	133.73	-33.35	7.38°	2.15*	2011-11-09 10:52:32.25	-2.56	2.3	4.86	1.05†	2.25†	205†	8	1000	3.049E-7
111109C	129.98	44.65	1.50°	2.15*	2011-11-09 20:57:16.66	-4.61	5.06	9.67	1.05†	2.25†	205†	8	1000	6.692E-6
111112A	223.72	28.81	3.83°	0.5*	2011-11-12 21:47:48.16	-0.06	0.13	0.19	1.05†	2.25†	205†	8	1000	7.667E-7
111113A	225.39	2.19	0.10°	0.5*	2011-11-13 05:10:13.62	0	0.16	0.16	0.53	2.53	1480	20	10000	7.7E-6

Table A.2: IC86I GRB Parameters (continued)

Name	RA (°)	Dec (°)	σ	z	Trigger (UT)	T_1 (s)	T_2 (s)	T_{100} (s)	α_γ	β_γ	ϵ_γ	E_{min}	E_{max}	Fluence$_\gamma$
111113B	4.32	-7.52	3.96°	2.15*	2011-11-13 09:50:11.76	-1.02	14.34	15.36	1.05†	2.25†	205†	8	1000	3.103E-6
111114A	268.08	-20.01	5.72°	2.15*	2011-11-14 05:35:45.35	-1.54	20.48	22.02	1.05†	2.25†	205†	8	1000	1.112E-6
111117A	12.70	23.02	0.02°	0.5*	2011-11-17 12:13:41.00	-0.016	1.45	1.466	0.69	2.69	370	10	1000	6.7E-7
111117B	27.16	-16.11	6.22°	2.15*	2011-11-17 12:38:00.76	-1.28	22.53	23.81	1.05†	2.25†	205†	8	1000	1.423E-6
111120A	344.60	-37.34	5.17°	2.15*	2011-11-20 13:20:24.05	-21.25	77.38	98.63	1.05†	2.25†	205†	8	1000	6.728E-6
111121A	154.76	-46.67	1.08′′	2.15*	2011-11-21 16:26:24.00	-0.34	141.08	141.42	0.44	3	1780	20	10000	2.3E-5
111123A	154.85	-20.64	1.08′′	3.1516	2011-11-23 18:13:21.00	-8.7	481.3	490.0	1.68	2.68	200*	15	150	7.3E-6
111124A	94.06	4.63	9.42°	2.15*	2011-11-24 07:24:10.09	-0.77	8.19	8.96	1.05†	2.25†	205†	8	1000	6.263E-7
111126A	276.06	51.46	0.03°	0.5*	2011-11-26 18:57:42.00	0	0.8	0.8	1.1	2.1	1000*	15	150	7E-8
111127A	103.70	3.50	2.09°	2.15*	2011-11-27 19:27:01.70	-0.77	18.24	19.01	1.05†	2.25†	205†	8	1000	8.643E-6
111129A	307.43	-52.71	1.08′′	2.15*	2011-11-29 16:18:14.00	-6.29	2.88	9.17	2.56	3.56	200*	15	150	1.8E-7
111201A	190.49	32.99	0.02°	2.15*	2011-12-01 14:22:45.26	-1.79	15.1	16.89	1.6	2.6	200*	15	150	10E-7
111203A	53.22	33.47	3.23°	2.15*	2011-12-03 01:17:04.03	-44.54	11.01	55.55	1.05†	2.25†	205†	8	1000	4.647E-6
111203B	242.83	-22.15	13.30°	2.15*	2011-12-03 14:36:45.38	-2.82	19.2	22.02	1.05†	2.25†	205†	8	1000	6.948E-7
111204A	336.63	-31.38	1.44′′	2.15*	2011-12-04 13:37:28.00	33	81	48.0	1.83	2.83	200*	15	150	4.7E-7
111205A	134.49	-31.97	0.10°	2.15*	2011-12-05 13:10:50.30	0	80.384	80.384	0.82	2.82	998	20	10000	1.7E-4
111207A	92.92	-39.00	0.03°	2.15*	2011-12-07 14:16:59.00	-1	3	4.0	1*	2*	200*	10*	10000*	1.00E-5*
111207B	164.88	-17.94	9.98°	0.5*	2011-12-07 12:17:16.20	-0.9	-0.13	0.77	1.05†	2.25†	205†	8	1000	2.621E-7
111208A	290.21	40.67	0.02°	2.15*	2011-12-08 08:28:10.79	-4.1	36.86	40.96	1.5	2.5	200*	15	150	10E-7
111209A	14.34	-46.80	0.72′′	0.677	2011-12-09 07:12:08.00	-1900	4400	6300.0	1.31	3.31	310	10*	10000*	4.86E-4
111210A	191.48	-7.17	1.44′′	2.15*	2011-12-10 14:37:03.00	-2.33	0.36	2.69	1.3	2.3	200*	15	150	1.6E-7
111211A	153.09	11.18	0.03°	0.478	2011-12-11 22:17:33.00	0	25	25.0	2.77	3.77	200*	20	5000	9.2E-6
111212A	310.43	-68.61	1.08′′	2.15*	2011-12-12 09:23:07.00	-5.77	62.74	68.51	1.67	2.67	200*	15	150	1.4E-6
111215A	349.56	32.49	0.72′′	2.15*	2011-12-15 14:04:08.00	-116.4	960.1	1076.5	1.7	2.7	200*	15	150	4.5E-6
111215B	222.40	16.44	0.08°	2.15*	2011-12-15 20:28:02.72	0	77.5	77.5	1.03	2.3	413	20	10000	5.3E-5
111216A	185.99	5.83	1.37°	2.15*	2011-12-16 09:20:31.51	2.3	86.08	83.78	1.05†	2.25†	205†	8	1000	4.168E-5
111220A	267.60	-56.05	1.39°	2.15*	2011-12-20 11:40:26.24	-6.14	32.9	39.04	1.05†	2.25†	205†	8	1000	5.356E-5
111221A	10.16	-29.77	1.92°	2.15*	2011-12-21 17:43:30.81	-0.51	26.62	27.13	1.05†	2.25†	205†	8	1000	3.059E-6
111222A	179.22	69.07	0.36′′	0.5*	2011-12-22 14:51:55.02	-0.06	0.26	0.32	0.35	2.35	762	20	3000	7.2E-6
111225A	13.15	51.57	0.36′′	0.297	2011-12-25 03:50:37.00	-14.28	111.24	125.52	1.7	2.7	200*	15	150	1.3E-6
111226A	21.50	3.87	1.00°	2.15*	2011-12-26 19:04:58.28	-6.14	68.61	74.75	1.05†	2.25†	205†	8	1000	1.145E-5
111228A	150.07	18.30	0.72′′	0.714	2011-12-28 15:44:43.00	-12.82	115.43	128.25	1.9	2.7	34	10	1000	1.8E-5
111228B	330.65	14.47	3.57°	2.15*	2011-12-28 10:52:50.52	0.1	3.04	2.94	1.05†	2.25†	205†	8	1000	2.747E-6
111230A	150.19	33.43	2.78°	2.15*	2011-12-30 16:23:08.60	-12.8	15.36	28.16	1.05†	2.25†	205†	8	1000	2.896E-6
111230B	242.61	-22.12	2.02°	2.15*	2011-12-30 19:39:32.14	-0.64	12.1	12.74	1.05†	2.25†	205†	8	1000	3.512E-6
120101A	185.87	52.91	8.77°	0.5*	2012-01-01 08:30:06.91	-0.1	0.03	0.13	1.05†	2.25†	205†	8	1000	1.092E-7
120102B	341.15	-23.16	3.58°	2.15*	2012-01-02 09:59:01.27	-10.24	9.98	20.22	1.05†	2.25†	205†	8	1000	2.553E-6
120105A	203.69	40.07	2.80°	2.15*	2012-01-05 14:00:35.90	-8.19	14.34	22.53	1.05†	2.25†	205†	8	1000	1.468E-6
120106A	66.11	64.04	0.72′′	2.15*	2012-01-06 14:16:24.00	-6.24	60.24	66.48	1.53	2.53	200*	15	150	9.7E-7
120107A	246.40	-69.93	0.50°	2.15*	2012-01-07 09:12:12.45	0	27	27.0	0.91	2.11	188.90	10	1000	6.81E-6
120109A	251.33	30.80	11.33°	2.15*	2012-01-09 19:46:01.94	-2.05	36.61	38.66	1.05†	2.25†	205†	8	1000	1.919E-6
120111A	95.34	5.00	5.38°	2.15*	2012-01-11 01:13:27.63	-2.05	74.75	76.8	1.05†	2.25†	205†	8	1000	3.968E-6
120114A	317.90	57.04	0.02°	2.15*	2012-01-14 16:20:05.68	-7.94	35.33	43.27	1.4	2.4	200*	15	150	1.00E-5*
120114B	263.23	-75.64	11.05°	2.15*	2012-01-14 10:23:39.21	-0.13	2.62	2.75	1.05†	2.25†	205†	8	1000	1.487E-7

Table A.2: IC86I GRB Parameters (continued)

Name	RA (°)	Dec (°)	σ	z	Trigger (UT)	T_1 (s)	T_2 (s)	T_{100} (s)	α_γ	β_γ	ϵ_γ	E_{min}	E_{max}	Fluence$_\gamma$
120118A	195.40	-61.64	0.03°	2.15*	2012-01-18 06:04:44.00	0	60	60.0	1*	2*	200*	20	200	2E-7
120118C	166.57	47.87	7.17°	2.15*	2012-01-18 21:32:45.81	-0.51	16.64	17.15	1.05†	2.25†	205†	8	1000	1.616E-6
120119C	65.96	-33.92	4.42°	2.15*	2012-01-19 08:29:29.82	-7.94	8.45	16.39	1.05†	2.25†	205†	8	1000	2.610E-6
120120A	134.72	35.47	5.71°	2.15*	2012-01-20 10:21:25.41	0	32.26	32.26	1.05†	2.25†	205†	8	1000	1.503E-6
120121A	249.35	-23.96	1.08″	2.15*	2012-01-21 09:42:19.00	-11	18.33	29.33	1.23	2.23	200*	15	150	1.1E-6
120121B	235.67	-39.34	7.86°	2.15*	2012-01-21 02:25:53.80	-3.33	15.1	18.43	1.05†	2.25†	205†	8	1000	1.955E-6
120121C	208.90	-1.34	1.61°	2.15*	2012-01-21 06:00:45.24	-5.63	31.49	37.12	1.05†	2.25†	205†	8	1000	1.154E-5
120129A	30.44	59.28	3.83°	2.15*	2012-01-29 13:55:46.24	0.32	5.328	5.008	0.76	2.9	326	20	10000	2.7E-5
120129B	26.52	-8.51	15.04°	0.5*	2012-01-29 07:29:14.05	-0.64	0.64	1.28	1.05†	2.25†	205†	8	1000	8.932E-8
120130A	150.04	-17.45	3.69°	2.15*	2012-01-30 16:47:10.88	-0.64	27.14	27.78	1.05†	2.25†	205†	8	1000	6.612E-6
120130B	64.96	9.48	5.55°	2.15*	2012-01-30 21:44:54.33	-1.28	2.3	3.58	1.05†	2.25†	205†	8	1000	5.248E-7
120130C	323.30	58.56	1.00°	2.15*	2012-01-30 22:30:34.47	-5.12	33.79	38.91	1.05†	2.25†	205†	8	1000	1.041E-5
120202A	203.51	22.77	0.03°	2.15*	2012-02-02 21:40:17.00	0	100	100.0	1*	2*	200*	20	200	7E-7
120205A	243.42	25.90	23.83°	0.5*	2012-02-05 06:51:05.31	-0.58	0	0.58	1.05†	2.25†	205†	8	1000	1.109E-7
120206A	73.45	58.41	2.25°	2.15*	2012-02-06 22:46:16.69	-0.26	9.22	9.48	1.05†	2.25†	205†	8	1000	5.876E-6
120210A	54.65	-58.52	5.51°	0.5*	2012-02-10 15:35:43.28	-0.06	1.28	1.34	1.05†	2.25†	205†	8	1000	6.445E-7
120211A	87.75	-24.77	1.08″	2.15*	2012-02-11 11:58:28.00	-2.34	64.1	66.44	1.5	2.5	200*	15	150	8.1E-7
120212A	43.10	-18.02	1.08″	2.15*	2012-02-12 09:11:23.50	-2.05	7.17	9.22	1.83	2.83	200*	10	1000	1.407E-7
120212B	303.40	-48.10	7.47°	0.5*	2012-02-12 08:27:47.59	-0.83	0.03	0.86	1.05†	2.25†	205†	8	1000	5.087E-8
120213A	301.01	65.41	1.44″	2.15*	2012-02-13 00:27:19.00	-6.31	74.46	80.77	2.37	3.37	200*	15	150	1.9E-6
120213B	183.49	5.76	4.20°	2.15*	2012-02-13 14:32:44.61	-3.07	10.75	13.82	1.05†	2.25†	205†	8	1000	2.678E-6
120217A	122.44	36.77	3.23°	2.15*	2012-02-17 19:23:50.57	-0.51	5.38	5.89	1.05†	2.25†	205†	8	1000	1.746E-6
120217B	298.73	32.70	1.50°	2.15*	2012-02-17 21:41:57.77	-0.22	2.4	2.62	1.05†	2.25†	205†	8	1000	4.858E-6
120218A	319.76	-25.46	0.02°	2.15*	2012-02-18 00:49:22.00	-20.6	8.9	29.5	1.75	2.75	200*	15	150	5.3E-6
120219A	129.79	51.03	1.08″	2.15*	2012-02-19 14:30:08.00	-7.83	90.06	97.89	0.6	2.6	51.6	15	150	5.4E-7
120219B	274.85	-31.11	10.94°	2.15*	2012-02-19 13:31:23.11	-1.15	6.98	8.13	1.05†	2.25†	205†	8	1000	5.578E-7
120220A	206.13	-57.36	7.39°	2.15*	2012-02-20 05:02:21.60	-5.38	15.87	21.25	1.05†	2.25†	205†	8	1000	1.237E-6
120222A	299.55	26.49	2.76°	0.5*	2012-02-22 00:29:36.13	-0.06	1.02	1.08	1.05†	2.25†	205†	8	1000	1.728E-6
120222B	340.00	-36.41	5.70°	2.15*	2012-02-22 02:51:54.09	-5.12	24.32	29.44	1.05†	2.25†	205†	8	1000	2.451E-6
120223A	219.61	-7.46	2.74°	2.15*	2012-02-23 22:23:48.94	-0.51	13.82	14.33	1.05†	2.25†	205†	8	1000	3.879E-6
120224A	40.94	-17.76	1.08″	2.15*	2012-02-24 04:39:56.00	-1.08	8.26	9.34	2.25	3.25	200*	15	150	2.4E-7
120224B	118.42	41.34	4.60°	2.15*	2012-02-24 06:46:28.52	1.79	62.72	60.93	1.05†	2.25†	205†	8	1000	9.123E-6
120224C	331.06	10.18	3.59°	2.15*	2012-02-24 21:33:07.39	0.26	29.44	29.18	1.05†	2.25†	205†	8	1000	2.599E-6
120226A	300.05	48.81	0.50°	2.15*	2012-02-26 20:54:19.72	0	78.086	78.086	1.01	2.5	279	20	5000	7.5E-5
120226B	87.59	52.35	1.15°	2.15*	2012-02-26 10:44:16.39	-3.26	11.33	14.59	1.05†	2.25†	205†	8	1000	5.848E-6
120227A	84.76	8.50	6.33°	2.15*	2012-02-27 09:22:45.97	-0.77	18.94	19.71	1.05†	2.25†	205†	8	1000	3.742E-6
120227B	256.73	-88.86	1.21°	2.15*	2012-02-27 17:24:41.05	0.26	17.66	17.4	1.05†	2.25†	205†	8	1000	2.195E-5
120302A	122.43	29.64	0.02°	2.15*	2012-03-02 01:55:30.00	0	85.15	85.15	1.62	2.62	200*	10	1000	3.84E-6
120302B	24.09	9.71	13.87°	0.5*	2012-03-02 17:19:59.08	-0.13	1.47	1.6	1.05†	2.25†	205†	8	1000	1.187E-7
120304A	127.15	-61.12	1.00°	2.15*	2012-03-04 01:27:48.72	-0.26	9.73	9.99	1.05†	2.25†	205†	8	1000	5.046E-6
120304B	277.28	-46.22	1.00°	2.15*	2012-03-04 05:57:47.78	-0.26	5.12	5.38	1.05†	2.25†	205†	8	1000	1.144E-5
120305A	47.54	28.49	1.08″	0.5*	2012-03-05 19:37:30.00	0	0.136	0.136	1	2.0	1000*	15	150	2.0E-7
120308A	219.09	79.69	1.08″	2.15*	2012-03-08 06:13:38.00	-24.15	58.2	82.35	1.71	2.71	200*	15	150	1.2E-6
120308B	30.75	55.22	1.19°	2.15*	2012-03-08 14:06:05.77	-21.5	4.1	25.6	1.05†	2.25†	205†	8	1000	6.721E-6

Table A.2: IC86I GRB Parameters (continued)

Name	RA (°)	Dec (°)	σ	z	Trigger (UT)	T_1 (s)	T_2 (s)	T_{100} (s)	α_γ	β_γ	ϵ_γ	E_{min}	E_{max}	Fluence$_\gamma$
120311A	273.09	14.30	1.44″	2.15*	2012-03-11 05:33:38.00	-1.38	3.22	4.6	2.3	3.3	200*	15	150	3.0E-7
120311B	258.56	-13.05	1.08″	2.15*	2012-03-11 15:08:10.00	-13.88	21.63	35.51	1.96	2.96	200*	15	150	1.0E-6
120312A	251.81	23.88	0.02°	2.15*	2012-03-12 16:06:28.00	-1.42	15.87	17.29	1.72	2.72	200*	15	150	5.7E-7
120314A	17.89	-48.73	17.82°	0.5*	2012-03-14 09:52:34.67	-1.28	0	1.28	1.05†	2.25†	205†	8	1000	1.642E-7
120316A	57.02	-56.29	0.47°	2.15*	2012-03-16 00:11:02.00	0	28.16	28.16	0.92	2.92	539	20	10000	2.3E-5
120319A	69.85	-45.44	3.67°	2.15*	2012-03-19 23:35:04.21	-4.61	67.84	72.45	1.05†	2.25†	205†	8	1000	2.420E-6
120320A	212.52	8.70	1.44″	2.15*	2012-03-20 11:56:15.00	-0.01	29.86	29.87	0.31	2.31	62.8	15	150	5.9E-7
120323A	340.41	29.72	0.12°	2.15*	2012-03-23 12:10:15.97	0	4.38	4.38	0.82	2.01	64.8	10	1000	1.080E-5
120323B	211.10	-45.23	3.79°	2.15*	2012-03-23 03:52:49.27	-0.77	3.58	4.35	1.05†	2.25†	205†	8	1000	1.408E-6
120324A	291.08	24.13	1.08″	2.15*	2012-03-24 05:59:11.00	-150.5	142.5	293.0	1.02	2.3	445	20	10000	4.5E-5
120326A	273.90	69.26	1.08″	1.798	2012-03-26 01:20:29.00	-67.9	22.56	90.46	0.98	2.53	46.45	10	1000	3.539E-6
120327A	246.86	-29.41	1.08″	2.81	2012-03-27 02:55:16.00	-15.79	74.58	90.37	1.52	2.52	200*	15	150	3.6E-6
120327B	170.41	23.76	13.00°	0.5*	2012-03-27 10:01:49.23	-0.19	0.06	0.25	1.05†	2.25†	205†	8	1000	1.141E-7
120328A	241.61	-39.34	1.08″	2.15*	2012-03-28 03:06:19.00	-17.27	20.61	37.88	1.87	2.87	200*	15	150	4.7E-7
120328B	229.04	25.30	1.08°	2.15*	2012-03-28 06:26:20.95	3.84	56.176	52.336	0.75	2	177.90	10	1000	7.74E-5
120331A	26.37	-54.84	6.51°	2.15*	2012-03-31 01:19:06.64	-2.82	13.57	16.39	1.05†	2.25†	205†	8	1000	6.774E-7
120401A	58.08	-17.64	1.44″	2.15*	2012-04-01 05:24:15.00	-92.97	52.72	145.69	1.66	2.66	200*	15	150	9.1E-7
120402B	223.73	-10.40	2.61°	2.15*	2012-04-02 16:04:00.76	-2.08	18.14	20.22	1.35	2.44	37.2	10	1000	3.4E-6
120403B	55.28	-89.01	1.44″	2.15*	2012-04-03 20:33:56.00	-3	5.3	8.3	1.51	3.51	182	4	10000*	4.6E-7
120410A	159.63	-17.00	8.60°	0.5*	2012-04-10 14:02:00.19	-1.02	0.06	1.08	1.05†	2.25†	205†	8	1000	2.907E-7
120411A	38.07	-7.24	8.45°	2.15*	2012-04-11 22:12:25.65	0	38.91	38.91	1.05†	2.25†	205†	8	1000	1.464E-6
120412A	29.44	-24.67	13.47°	2.15*	2012-04-12 01:18:42.15	-4.1	5.63	9.73	1.05†	2.25†	205†	8	1000	1.246E-6
120412B	38.91	7.06	2.80°	2.15*	2012-04-12 22:04:40.56	0	101.19	101.19	1.05†	2.25†	205†	8	1000	7.029E-6
120415A	213.54	16.73	4.36°	2.15*	2012-04-15 01:49:57.68	-0.51	12.03	12.54	1.05†	2.25†	205†	8	1000	2.230E-6
120415B	190.69	4.91	6.88°	0.5*	2012-04-15 21:23:41.03	-0.26	0.7	0.96	1.05†	2.25†	205†	8	1000	1.305E-7
120415C	150.46	61.27	4.96°	2.15*	2012-04-15 22:59:19.13	-4.35	8.19	12.54	1.05†	2.25†	205†	8	1000	2.314E-6
120419A	187.40	-63.02	0.03°	2.15*	2012-04-19 12:56:25.00	0	20	20.0	1*	2*	200*	20	200	2E-7
120420A	47.89	-52.19	5.44°	2.15*	2012-04-20 05:58:07.26	-0.77	24.83	25.6	1.05†	2.25†	205†	8	1000	2.878E-6
120420B	109.26	10.76	1.11°	2.15*	2012-04-20 20:35:13.07	0	254.92	254.92	1.05†	2.25†	205†	8	1000	4.325E-5
120422A	136.91	14.02	1.08″	0.28	2012-04-22 07:12:03.00	-0.8	6	6.8	1.19	2.19	200*	15	150	2.3E-7
120426A	111.54	-65.63	0.30°	2.15*	2012-04-26 02:09:14.33	0.22	3.1	2.88	0.61	3.2	140	20	10000	1.9E-5
120429A	165.98	-8.76	15.40°	0.5*	2012-04-29 00:04:07.26	-0.19	1.47	1.66	1.05†	2.25†	205†	8	1000	2.794E-7
120429B	133.04	-32.23	5.34°	2.15*	2012-04-29 11:37:03.74	-1.02	14.34	15.36	1.05†	2.25†	205†	8	1000	2.368E-6
120430A	47.25	18.52	5.75°	2.15*	2012-04-30 23:30:43.35	-2.3	12.29	14.59	1.05†	2.25†	205†	8	1000	5.557E-7
120504A	329.94	46.83	4.06°	2.15*	2012-05-04 11:13:39.94	-0.51	41.47	41.98	1.05†	2.25†	205†	8	1000	3.363E-6
120506A	172.22	-33.72	9.33°	2.15*	2012-05-06 03:05:02.12	-0.77	1.54	2.31	1.05†	2.25†	205†	8	1000	2.872E-7
120510A	44.05	72.89	2.88″	2.15*	2012-05-10 08:47:44.00	0	130	130.0	2.05	3.05	200*	20	1200	3.82E-6
120510B	186.93	-55.24	3.75°	2.15*	2012-05-10 21:36:26.10	1.79	64.26	62.47	1.05†	2.25†	205†	8	1000	6.014E-6
120511A	226.93	-60.49	2.07°	2.15*	2012-05-11 15:18:47.92	-0.13	45.12	45.25	1.05†	2.25†	205†	8	1000	1.140E-5
120512A	325.56	13.64	0.01°	2.15*	2012-05-12 02:41:40.00	0	40	40.0	1.03	2.5	470.5	100	1000	9.33E-6
120514A	283.00	-4.26	1.08″	2.15*	2012-05-14 01:12:49.00	-8.75	165.55	174.3	2.3	3.3	200*	100	1000	1.62E-6

Table A.3: IC86II GRB Parameters

Name	RA (°)	Dec (°)	σ	z	Trigger (UT)	T_1 (s)	T_2 (s)	T_{100} (s)	α_γ	β_γ	ϵ_γ	E_{min}	E_{max}	Fluence$_\gamma$
120426B	285.49	-13.68	3.83°	2.15*	2012-04-26 14:02:22.36	0	30.98	30.98	1.05†	2.25†	205†	8	1000	3.658E-6
120427A	224.94	29.31	0.22°	2.15*	2012-04-27 01:17:27.79	0.26	12.448	12.188	0.77	2.9	133	20	10000	7.8E-6
120427B	114.70	50.21	26.65°	2.15*	2012-04-27 03:40:37.87	-2.3	20.48	22.78	1.05†	2.25†	205†	8	1000	6.805E-7
120519A	178.37	22.41	0.63°	2.15*	2012-05-19 17:18:14.64	-0.5	5.2	5.7	0.5	2.5	740	20	10000	3.7E-6
120520A	45.86	35.28	8.30°	2.15*	2012-05-20 22:46:24.66	-4.74	1.02	5.76	1.05†	2.25†	205†	8	1000	4.409E-7
120521A	148.72	-49.42	1.08′′	0.5*	2012-05-21 05:59:42.00	0.02	0.56	0.54	0.98	1.98	1000*	15	150	7.8E-8
120521B	197.01	-52.76	1.08′′	2.15*	2012-05-21 09:07:48.00	-1.39	95.14	96.53	0.34	2.34	213	10	1000	3.11E-6
120521C	214.29	42.15	1.08′′	6.0	2012-05-21 23:22:07.00	-1.03	31.84	32.87	1.73	2.73	200*	15	150	1.1E-6
120522A	166.00	-62.09	0.08°	2.15*	2012-05-22 03:11:07.38	0	78.086	78.086	0.88	2.88	381	20	10000	2.5E-5
120522B	56.07	54.85	2.02°	2.15*	2012-05-22 08:39:16.84	-11.52	16.64	28.16	1.05†	2.25†	205†	8	1000	9.324E-6
120524A	358.15	-15.61	10.45°	0.5*	2012-05-24 03:12:54.68	-0.13	0.58	0.71	1.05†	2.25†	205†	8	1000	2.527E-7
120526A	66.28	-32.23	1.04°	2.15*	2012-05-26 07:16:40.77	3.07	46.72	43.65	1.05†	2.25†	205†	8	1000	1.162E-4
120528A	295.13	6.50	5.98°	2.15*	2012-05-28 10:36:00.22	-0.77	15.62	16.39	1.05†	2.25†	205†	8	1000	3.792E-6
120528B	77.59	-37.80	0.06°	2.15*	2012-05-28 18:11:48.00	0	26	26.0	0.41	2.41	201	10*	10000*	2.9E-6
120528C	12.93	-0.95	0.06°	2.15*	2012-05-28 21:21:58.00	0	30	30.0	1*	2*	200*	10*	10000*	1.00E-5*
120530A	175.96	78.83	3.27°	2.15*	2012-05-30 02:53:41.86	0	77.06	77.06	1.05†	2.25†	205†	8	1000	7.173E-6
120531A	290.40	1.22	11.03°	2.15*	2012-05-31 09:26:38.36	-2.82	22.53	25.35	1.05†	2.25†	205†	8	1000	9.099E-7
120602A	87.92	-39.35	0.04°	2.15*	2012-06-02 05:00:00.23	0	70	70.0	0.77	2.8	300	20	10000	3.6E-4
120603A	198.79	4.33	0.64°	2.15*	2012-06-03 10:32:09.85	-0.06	5.3	5.36	0.4	2.4	560	20	10000	1.0E-6
120604A	163.87	-7.40	9.34°	2.15*	2012-06-04 05:16:31.31	-2.82	7.68	10.5	1.05†	2.25†	205†	8	1000	1.235E-6
120604B	113.58	-2.79	11.91°	2.15*	2012-06-04 08:13:40.16	-2.56	9.47	12.03	1.05†	2.25†	205†	8	1000	1.510E-6
120605A	243.61	41.51	2.62°	2.15*	2012-06-05 10:52:15.90	-0.64	17.47	18.11	1.05†	2.25†	205†	8	1000	3.253E-6
120608A	229.98	-26.12	2.52°	0.5*	2012-06-08 11:43:51.83	-0.19	0.77	0.96	1.05†	2.25†	205†	8	1000	4.834E-7
120608B	313.26	12.64	5.08°	2.15*	2012-06-08 18:38:33.04	-14.34	10.5	24.84	1.05†	2.25†	205†	8	1000	3.174E-6
120609A	67.32	13.00	7.54°	0.5*	2012-06-09 13:54:35.62	-0.77	1.02	1.79	1.05†	2.25†	205†	8	1000	4.196E-7
120611A	324.68	-44.79	5.28°	2.15*	2012-06-11 02:36:00.52	-9.22	40.7	49.92	1.05†	2.25†	205†	8	1000	4.526E-6
120612A	126.72	-17.57	1.08′′	2.15*	2012-06-12 02:05:19.00	16.9	125.4	108.5	1.36	2.36	200*	15	150	1.3E-6
120612B	211.88	34.56	7.08°	2.15*	2012-06-12 16:19:45.55	-10.5	52.74	63.24	1.05†	2.25†	205†	8	1000	2.062E-6
120612C	39.67	-37.91	10.65°	0.5*	2012-06-12 16:29:44.56	-0.19	0.06	0.25	1.05†	2.25†	205†	8	1000	7.051E-7
120614A	312.73	65.16	0.12°	2.15*	2012-06-14 05:49:10.00	0	45	45.0	1*	2*	200*	10*	10000*	1.00E-5*
120616A	79.69	56.44	8.54°	0.5*	2012-06-16 15:06:50.64	-0.05	0	0.05	1.05†	2.25†	205†	8	1000	2.576E-7
120617A	22.31	33.80	0.25°	0.5*	2012-06-17 15:02:47.03	0	0.5	0.5	0.95	2.95	180	20	10000	2.1E-6
120618A	77.31	75.85	2.59°	2.15*	2012-06-18 03:03:49.88	-0.13	17.47	17.6	1.05†	2.25†	205†	8	1000	5.580E-6
120618B	213.57	-2.11	4.80°	2.15*	2012-06-18 22:03:34.31	-20.48	27.14	47.62	1.05†	2.25†	205†	8	1000	3.629E-6
120619A	190.74	-25.02	2.79°	0.5*	2012-06-19 21:13:16.91	-0.26	0.7	0.96	1.05†	2.25†	205†	8	1000	4.242E-7
120622A	205.43	-1.71	0.21°	2.15*	2012-06-22 03:21:46.00	0	39	39.0	1*	2*	200*	10*	10000*	1.00E-5*
120624A	4.77	7.17	0.44°	2.15*	2012-06-24 07:24:22.98	0	3.58	3.58	0.83	3.4	3700	10	1000	6.5E-6
120624B	170.89	8.93	0.01°	2.15*	2012-06-24 22:19:30.98	-20	289.952	309.952	0.85	2.36	566	10	1000	1.916E-4
120625A	51.26	51.07	1.17°	2.15*	2012-06-25 02:50:46.04	-0.26	7.17	7.43	1.05†	2.25†	205†	8	1000	1.022E-5
120629A	176.16	-0.60	8.88°	0.5*	2012-06-29 13:34:11.68	-0.38	0.32	0.7	1.05†	2.25†	205†	8	1000	5.192E-8
120630A	352.30	42.49	0.03°	0.5*	2012-06-30 23:17:33.00	-0.1	0.6	0.7	1.04	2.04	1000*	15	150	6.1E-8
120701A	80.34	-58.53	0.01°	2.15*	2012-07-01 07:50:41.00	0	15.4	15.4	1.05	2.05	200*	15	150	1.4E-6
120701B	182.73	-45.70	14.79°	0.5*	2012-07-01 15:41:48.32	-0.96	0.06	1.02	1.05†	2.25†	205†	8	1000	8.357E-8
120703A	339.36	-29.72	0.72′′	2.15*	2012-07-03 17:25:22.00	-7.27	32.6	39.87	0.98	2.08	238.5	10	1000	9.154E-6

Table A.3: IC86II GRB Parameters (continued)

Name	RA (°)	Dec (°)	σ	z	Trigger (UT)	T_1 (s)	T_2 (s)	T_{100} (s)	α_γ	β_γ	ϵ_γ	E_{min}	E_{max}	Fluence$_\gamma$
120703B	69.49	34.74	2.60°	2.15*	2012-07-03 10:01:11.69	-0.51	64	64.51	1.05†	2.25†	205†	8	1000	1.108E-5
120703C	210.51	46.26	5.15°	2.15*	2012-07-03 11:56:56.87	-2.05	75.52	77.57	1.05†	2.25†	205†	8	1000	2.597E-6
120707A	291.87	-32.77	2.11°	2.15*	2012-07-07 19:12:17.43	1.52	66.6	65.08	1.17	2.31	174	10	1000	1.1E-4
120709A	320.23	-51.13	0.50°	2.15*	2012-07-09 21:11:40.37	-0.13	27.832	27.962	0.94	2	643	20	10000	1.8E-5
120710A	120.39	-31.14	4.76°	2.15*	2012-07-10 02:23:17.05	0	131.84	131.84	1.05†	2.25†	205†	8	1000	5.338E-6
120711A	94.70	-70.90	0.16°	3	2012-07-11 02:45:55.81	0	46.336	46.336	0.94	2.4	973	10	1000	1.942E-4
120711B	331.71	60.00	0.03°	2.15*	2012-07-11 03:11:02.58	-12.1	51.4	63.5	1.75	2.75	200*	15	150	5.6E-7
120711C	127.88	-31.83	11.03°	2.15*	2012-07-11 10:42:54.57	-1.28	86.27	87.55	1.05†	2.25†	205†	8	1000	1.862E-6
120712A	169.59	-20.03	1.08″	4.15	2012-07-12 13:42:27.00	-4.57	18.74	23.31	0.6	1.8	124	10	1000	4.43E-6
120713A	161.68	40.66	16.71°	2.15*	2012-07-13 05:25:29.14	-3.07	10.75	13.82	1.05†	2.25†	205†	8	1000	1.130E-6
120714A	167.98	-30.63	1.08″	2.15*	2012-07-14 07:46:46.00	-0.74	17.78	18.52	1.62	2.62	200*	15	150	8.2E-7
120714B	355.41	-46.20	0.03°	0.3984	2012-07-14 21:18:46.57	-23	154	177.0	1.52	2.52	200*	15	150	1.2E-6
120715A	272.15	58.79	3.73°	2.15*	2012-07-15 01:35:15.57	-4.86	24.83	29.69	1.05†	2.25†	205†	8	1000	2.195E-6
120716A	313.09	9.56	0.17°	2.48	2012-07-16 17:05:03.91	-1.02	234	235.02	0.48	2.19	115	10	1000	1.47E-5
120716B	304.53	59.41	5.09°	2.15*	2012-07-16 13:51:02.13	-5.89	19.07	24.96	1.05†	2.25†	205†	8	1000	5.223E-6
120719A	204.29	-43.45	1.37°	2.15*	2012-07-19 03:30:00.82	0.77	75.78	75.01	1.05†	2.25†	205†	8	1000	1.355E-5
120722A	230.50	13.25	1.44″	0.9586	2012-07-22 12:53:26.00	-0.3	47.5	47.8	1.9	2.9	200*	15	150	1.2E-6
120724A	245.18	3.51	1.08″	1.48	2012-07-24 06:39:02.00	-30	100	130.0	0.53	2.53	27.6	15	150	6.8E-7
120727A	163.26	25.09	15.27°	0.5*	2012-07-27 08:29:39.08	-0.9	0	0.9	1.05†	2.25†	205†	8	1000	1.091E-7
120727B	37.76	16.36	1.00°	2.15*	2012-07-27 16:20:19.53	-0.22	10.27	10.49	1.05†	2.25†	205†	8	1000	9.235E-6
120728A	137.09	-54.44	1.08″	2.15*	2012-07-28 22:25:12.74	-1.54	31.23	32.77	1.66	3.66	119.80	10	1000	5.29E-6
120728B	103.77	-45.89	0.47°	2.15*	2012-07-28 10:25:34.98	0	250	250.0	1	2.9	95	20	10000	1.20E-4
120729A	13.07	49.94	1.08″	0.80	2012-07-29 10:56:14.00	-3.08	101.94	105.02	1.49	2.49	200*	10	1000	5.1E-6
120801A	245.73	-47.37	2.39°	2.15*	2012-08-01 22:05:21.19	-7.17	472.07	479.24	1.05†	2.25†	205†	8	1000	3.340E-5
120802A	44.84	13.77	1.80″	3.796	2012-08-02 08:00:51.00	-35.68	28.02	63.7	1.21	3.21	57.2	15	150	1.9E-6
120803A	269.53	-6.73	0.03°	2.15*	2012-08-03 07:22:16.00	0.4	11.4	11.0	0.86	1.86	200*	15	150	3.0E-7
120803B	314.24	53.30	1.08″	2.15*	2012-08-03 11:06:06.00	-2.67	49.16	51.83	0.84	2.84	117.8	15	150	2.5E-6
120804A	233.95	-28.78	1.08″	0.5*	2012-08-04 00:54:14.00	-0.16	0.83	0.99	1.34	3.34	135	15	150	1.45E-6
120805A	216.54	5.83	1.80″	2.15*	2012-08-05 21:28:09.00	-15.39	32.61	48.0	1.2	2.2	200*	15	150	8.2E-7
120805B	30.13	-21.51	10.11°	0.5*	2012-08-05 16:56:21.72	-0.96	0.9	1.86	1.05†	2.25†	205†	8	1000	1.879E-7
120806A	308.99	6.33	4.25°	2.15*	2012-08-06 00:10:08.87	-0.26	26.37	26.63	1.05†	2.25†	205†	8	1000	4.902E-6
120807A	241.26	-47.48	1.08″	2.15*	2012-08-07 07:09:37.00	-0.24	24.07	24.31	1.81	2.81	200*	15	150	2.9E-7
120811A	257.18	-22.73	0.03°	2.15*	2012-08-11 02:35:18.00	-14.16	169.06	183.22	1.95	2.95	200*	15	150	1.1E-6
120811B	43.66	-31.68	0.23°	0.5*	2012-08-11 00:20:30.29	-0.13	1.33	1.46	0.14	2.14	1130	20	10000	4.6E-6
120811C	199.68	62.30	1.08″	2.671	2012-08-11 15:34:52.00	-9.7	42.9	52.6	1.4	3.4	42.9	15	150	3.0E-6
120814A	26.19	22.45	3.71°	0.5*	2012-08-14 04:49:12.58	-0.38	0.51	0.89	1.05†	2.25†	205†	8	1000	3.831E-7
120814B	90.57	33.13	10.68°	0.5*	2012-08-14 19:16:06.75	-0.19	0	0.19	1.05†	2.25†	205†	8	1000	1.284E-7
120815A	273.96	-52.13	1.08″	2.358	2012-08-15 02:13:58.00	-0.24	11.97	12.21	2.29	3.29	200*	15	150	4.9E-7
120816A	282.14	-6.94	1.08″	2.15*	2012-08-16 19:18:34.00	-1.97	6.66	8.63	2.54	3.54	200*	15	150	4.3E-7
120816B	341.15	2.16	2.51°	0.5*	2012-08-16 23:58:18.85	0	0.768	0.768	0.61	2.61	2320	20	10000	9.7E-5
120817A	250.69	-38.35	1.08″	2.15*	2012-08-17 06:49:42.00	-2.24	30.77	33.01	1.97	2.97	200*	15	150	6.9E-7
120817B	8.31	-26.43	0.05°	2.15*	2012-08-17 04:02:29.72	-0.03	4.08	4.11	0.82	2.82	1740	20	10000	4.1E-6
120817C	259.97	-9.07	7.14°	2.15*	2012-08-17 01:22:09.78	-6.4	30.46	36.86	1.05†	2.25†	205†	8	1000	1.040E-6
120819A	235.91	-7.31	1.08″	2.15*	2012-08-19 13:10:14.00	4.42	82.88	78.46	1.49	2.49	200*	15	150	1.4E-6

Table A.3: IC86II GRB Parameters (continued)

Name	RA (°)	Dec (°)	σ	z	Trigger (UT)	T_1 (s)	T_2 (s)	T_{100} (s)	α_γ	β_γ	ϵ_γ	E_{min}	E_{max}	Fluence$_\gamma$
120819B	171.54	49.42	7.94°	2.15*	2012-08-19 01:08:26.77	-5.63	60.67	66.3	1.05†	2.25†	205†	8	1000	1.334E-6
120820A	186.64	-12.31	4.81°	2.15*	2012-08-20 14:02:21.99	-17.41	90.11	107.52	1.05†	2.25†	205†	8	1000	6.981E-6
120821A	255.27	-40.52	0.02°	2.15*	2012-08-21 13:23:45.00	0	12	12.0	1*	2*	200*	20	200	3E-7
120822A	181.72	80.56	7.70°	0.5*	2012-08-22 15:03:56.40	-1.28	0.26	1.54	1.05†	2.25†	205†	8	1000	1.085E-7
120824A	70.92	17.63	3.00°	2.15*	2012-08-24 14:16:00.73	-8.19	103.43	111.62	1.05†	2.25†	205†	8	1000	5.919E-6
120827A	222.74	-71.89	1.67°	2.15*	2012-08-27 05:10:25.01	-1.66	3.39	5.05	1.05†	2.25†	205†	8	1000	3.367E-6
120830A	88.42	-28.81	0.86°	0.5*	2012-08-30 07:07:03.53	-0.38	0.9	1.28	0.4	2.4	1212.00	10	1000	3.253E-6
120830B	337.87	-80.04	3.46°	2.15*	2012-08-30 05:04:52.74	0.45	16.51	16.06	1.05†	2.25†	205†	8	1000	7.515E-6
120831A	144.02	-16.21	8.54°	0.5*	2012-08-31 21:37:31.88	-0.26	0.13	0.39	1.05†	2.25†	205†	8	1000	2.515E-7
120905A	355.96	16.99	1.80°	2.15*	2012-09-05 15:46:21.17	-7.17	188.42	195.59	1.05†	2.25†	205†	8	1000	1.957E-5
120907A	74.75	-9.31	1.08′′	2.15*	2012-09-07 00:24:24.51	-1.92	17.76	19.68	0.75	2.75	154.50	6	10000*	7.8E-7
120908A	230.64	-25.79	0.29°	2.15*	2012-09-08 22:31:00.02	-4.61	62.34	66.95	1.21	3.21	205.9	10	1000	1.7E-5
120908B	268.67	-35.79	1.50°	2.15*	2012-09-08 20:57:30.95	0.58	47.42	46.84	1.05†	2.25†	205†	8	1000	1.270E-5
120909A	275.74	-59.45	0.72′′	3.93	2012-09-09 01:41:09.00	0	149.17	149.17	1.23	3.23	335	10*	10000*	2.3E-5
120911A	357.98	63.10	1.08′′	2.15*	2012-09-11 07:08:33.99	-4.48	24.1	28.58	0.36	2.36	64.2	10	1000	2.34E-6
120911B	172.03	-37.51	0.30°	2.15*	2012-09-11 06:25:14.00	0	132	132.0	1.01	2.72	1200	10	1000	1.973E-4
120913A	146.40	26.96	0.01°	2.15*	2012-09-13 20:18:22.89	-3.07	38.8	41.87	1.25	3.25	26	10	1000	0.38E-8
120913B	213.66	-14.51	0.01°	2.15*	2012-09-13 23:55:58.00	-51.7	111.79	163.49	1.19	1.97	163	10	1000	2.9E-5
120914A	267.94	1.82	5.35°	2.15*	2012-09-14 03:26:42.11	-1.28	8.96	10.24	1.05†	2.25†	205†	8	1000	7.350E-7
120915A	283.56	-1.11	6.54°	2.15*	2012-09-15 11:22:04.22	-2.3	3.58	5.88	1.05†	2.25†	205†	8	1000	3.829E-7
120916A	205.63	36.70	0.50°	2.15*	2012-09-16 04:07:46.69	-2	54.19	56.19	0.99	1.9	312.40	10	1000	1.95E-5
120916B	82.04	-19.22	11.13°	0.5*	2012-09-16 02:02:15.91	-0.32	1.02	1.34	1.05†	2.25†	205†	8	1000	8.154E-8
120918A	181.04	-32.76	0.01°	2.15*	2012-09-18 11:16:10.00	-2.86	23.9	26.76	1	3.0	85.5	15	150	3.7E-6
120919A	214.77	-45.56	0.09°	2.15*	2012-09-19 07:24:38.60	0	25.78	25.78	0.76	2.15	162	10	1000	1.679E-5
120919B	302.63	-37.49	0.27°	2.15*	2012-09-19 01:14:23.07	2.05	134.56	132.51	0.9	2.3	250	20	10000	3.1E-5
120919C	303.53	-66.16	11.89°	2.15*	2012-09-19 19:35:41.80	-3.33	18.69	22.02	1.05†	2.25†	205†	8	1000	1.031E-6
120920A	27.12	-26.12	7.84°	2.15*	2012-09-20 00:04:32.73	-2.3	26.88	29.18	1.05†	2.25†	205†	8	1000	1.193E-6
120921A	96.42	-64.77	3.20°	2.15*	2012-09-21 21:03:03.77	-0.26	5.38	5.64	1.05†	2.25†	205†	8	1000	2.478E-6
120922A	234.75	-20.18	1.08′′	3.1	2012-09-22 22:30:28.00	-22.58	215.73	238.31	1.6	2.3	37.7	180	10000*	6.5E-6
120923A	303.80	6.22	1.08′′	2.15*	2012-09-23 05:16:06.00	-2.93	26.64	29.57	0.29	2.29	44.4	15	150	3.2E-7
120926A	318.39	58.38	1.51°	2.15*	2012-09-26 08:02:56.57	-0.64	3.65	4.29	1.05†	2.25†	205†	8	1000	2.478E-6
120926B	59.72	-37.20	3.76°	2.15*	2012-09-26 10:13:16.04	-2.3	57.86	60.16	1.05†	2.25†	205†	8	1000	4.383E-6
120926C	24.61	-45.58	21.32°	2.15*	2012-09-26 18:04:35.10	-1.54	1.54	3.08	1.05†	2.25†	205†	8	1000	1.878E-7
121001A	276.03	-5.67	1.08′′	2.15*	2012-10-01 18:23:02.00	-30	143	173.0	1.34	2.34	200*	15	150	1.7E-6
121004A	137.46	-11.02	9.44°	0.5*	2012-10-04 05:03:18.19	-0.51	1.02	1.53	1.05†	2.25†	205†	8	1000	3.794E-7
121005A	195.17	-2.09	9.48°	2.15*	2012-10-05 00:42:51.89	-31.23	65.54	96.77	1.05†	2.25†	205†	8	1000	3.731E-6
121005B	149.73	25.40	5.39°	2.15*	2012-10-05 08:09:12.86	0	141.57	141.57	1.05†	2.25†	205†	8	1000	5.169E-6
121008A	340.97	-3.10	9.00°	2.15*	2012-10-08 10:10:50.66	-0.32	3.14	3.46	1.05†	2.25†	205†	8	1000	3.918E-7
121011A	260.21	41.11	1.44′′	0.58	2012-10-11 11:15:30.26	-10	80.1	90.1	1.09	3.09	1160	10	1000	1.00E-5
121011B	182.81	44.11	1.49°	2.15*	2012-10-11 22:32:20.08	0	2.5	2.5	0.45	1.9	670	20	10000	2.8E-6
121012A	33.42	14.58	6.78°	0.5*	2012-10-12 17:22:16.39	-0.13	0.32	0.45	0.47	2.47	540	10	1000	1.15E-6
121014A	166.65	-29.11	0.02°	2.15*	2012-10-14 20:11:56.00	-12.21	67.79	80.0	1.91	2.91	200*	15	150	1.1E-6
121014B	320.01	-53.43	17.20°	0.5*	2012-10-14 15:19:00.58	-0.58	-0.19	0.39	1.05†	2.25†	205†	8	1000	9.619E-8
121017A	288.83	-1.60	1.08′′	2.15*	2012-10-17 19:23:28.00	-2.72	2.53	5.25	1.74	2.74	200*	15	150	6.6E-7

Table A.3: IC86II GRB Parameters (continued)

Name	RA (°)	Dec (°)	σ	z	Trigger (UT)	T_1 (s)	T_2 (s)	T_{100} (s)	α_γ	β_γ	ϵ_γ	E_{min}	E_{max}	Fluence$_\gamma$
121019A	43.47	62.14	7.52°	2.15*	2012-10-19 05:35:09.23	-2.56	11.78	14.34	1.05†	2.25†	205†	8	1000	5.886E-7
121023A	313.86	-4.38	4.76°	0.5*	2012-10-23 07:44:16.95	-0.13	0.38	0.51	1.05†	2.25†	205†	8	1000	7.727E-7
121024A	70.47	-12.29	0.72″	2.298	2012-10-24 02:56:12.00	-8.27	75.73	84.0	1.41	2.41	200*	15	150	1.1E-6
121025A	248.38	27.67	2.16″	2.15*	2012-10-25 07:46:30.00	0	20	20.0	1*	2*	200*	10*	10000*	1.00E-5*
121027A	63.60	-58.83	1.08″	1.773	2012-10-27 07:32:29.00	-9.34	65.33	74.67	1.82	2.82	200*	15	150	2.0E-6
121027B	4.31	-47.54	2.61°	2.15*	2012-10-27 00:54:19.37	-65.54	101.38	166.92	1.05†	2.25†	205†	8	1000	7.395E-6
121028A	271.90	-2.29	1.08″	2.15*	2012-10-28 05:04:31.00	-0.8	3.8	4.6	1.79	2.79	200*	15	150	3.7E-7
121028B	52.56	-25.07	7.68°	2.15*	2012-10-28 06:43:13.09	-1.79	9.22	11.01	1.05†	2.25†	205†	8	1000	9.978E-7
121029A	226.77	-28.20	1.65°	2.15*	2012-10-29 08:24:18.00	-2	20	22.0	0.57	2.82	176	10	1000	7.82E-6
121031A	170.77	-3.52	1.08″	2.15*	2012-10-31 22:47:15.27	-27.39	293.31	320.7	0.87	2.87	142.3	10	1000	1.99E-5
121102A	270.90	-16.96	0.72″	2.15*	2012-11-02 02:27:00.00	0	37.25	37.25	1.88	2.88	200*	15	150	1.9E-6
121102B	258.47	14.09	12.15°	2.15*	2012-11-02 01:32:47.94	-1.54	0.51	2.05	1.05†	2.25†	205†	8	1000	5.672E-7
121104A	72.14	14.08	4.05°	2.15*	2012-11-04 15:02:15.49	-1.02	58.11	59.13	1.05†	2.25†	205†	8	1000	4.446E-6
121108A	83.19	54.47	1.08″	2.15*	2012-11-08 17:47:39.00	-0.15	137.98	138.13	2.28	3.28	200*	15	150	9.6E-7
121109A	6.84	-42.57	10.37°	2.15*	2012-11-09 08:06:56.63	-6.91	15.23	22.14	1.05†	2.25†	205†	8	1000	5.336E-6
121112A	78.98	-55.44	15.56°	0.5*	2012-11-12 19:20:44.27	-0.13	1.15	1.28	1.05†	2.25†	205†	8	1000	2.232E-7
121113A	313.17	59.82	2.06°	2.15*	2012-11-13 13:02:43.53	1.54	97.03	95.49	1.05†	2.25†	205†	8	1000	2.685E-5
121116A	180.88	-74.79	6.98°	0.5*	2012-11-16 11:00:24.60	-0.7	0.64	1.34	1.05†	2.25†	205†	8	1000	2.398E-7
121117A	31.61	7.42	0.36″	2.15*	2012-11-17 08:50:56.00	0	158.6	158.6	1.16	2.16	200*	15	150	1.4E-6
121117B	279.14	44.93	4.32°	2.15*	2012-11-17 00:25:37.73	-270.34	61.44	331.78	1.05†	2.25†	205†	8	1000	1.063E-5
121118A	299.38	65.65	1.14°	2.15*	2012-11-18 13:48:54.26	-0.26	33.54	33.8	1.05†	2.25†	205†	8	1000	6.777E-6
121118B	171.70	-3.06	0.74°	2.15*	2012-11-18 22:27:06.66	-30	70	100.0	1.18	3.05	599	20	10000	8.5E-5
121119A	311.65	-16.92	8.13°	2.15*	2012-11-19 13:53:14.13	-0.26	2.05	2.31	1.05†	2.25†	205†	8	1000	8.815E-7
121122A	35.26	45.14	3.71°	2.15*	2012-11-22 21:14:52.55	0.51	20.616	20.106	0.68	3.1	178	10	1000	5.46E-5
121122B	52.67	46.47	12.89°	2.15*	2012-11-22 13:31:27.52	-1.28	7.42	8.7	1.05†	2.25†	205†	8	1000	8.146E-7
121122C	355.45	6.34	2.66°	2.15*	2012-11-22 20:52:49.03	0	125.44	125.44	1.05†	2.25†	205†	8	1000	9.070E-6
121123A	307.32	-11.86	0.36″	2.15*	2012-11-23 10:02:41.00	-6.34	419	425.34	0.25	3	85	10	1000	2.20E-5
121123B	30.52	-18.79	1.61°	2.15*	2012-11-23 10:35:55.71	2.3	44.8	42.5	1.05†	2.25†	205†	8	1000	1.423E-5
121124A	87.93	49.55	14.64°	0.5*	2012-11-24 14:32:07.30	-0.13	0.13	0.26	1.05†	2.25†	205†	8	1000	5.660E-8
121125A	228.53	55.31	1.08″	2.15*	2012-11-25 08:32:27.00	-6.31	77.64	83.95	1.38	3.38	196	10	1000	9.5E-6
121125B	177.53	38.54	5.24°	2.15*	2012-11-25 11:14:47.49	-2.3	10.56	12.86	1.05†	2.25†	205†	8	1000	8.568E-7
121127A	176.44	-52.41	0.08°	2.15*	2012-11-27 21:55:57.29	0	3.51	3.51	0.55	1.55	200*	100	1000	9.34E-7
121201A	13.47	-42.94	1.08″	3.6	2012-12-01 12:25:42.00	-24	71	95.0	1.9	2.9	200*	15	150	7.8E-7
121202A	256.80	23.95	0.72″	2.15*	2012-12-02 04:20:05.00	-2.18	20.84	23.02	1.14	3.14	135.4	10	1000	2.0E-6
121205A	238.59	-49.71	11.72°	2.15*	2012-12-05 12:10:04.71	-0.38	2.43	2.81	1.05†	2.25†	205†	8	1000	1.335E-7
121209A	326.79	-8.23	1.08″	2.15*	2012-12-09 21:59:11.00	-2.16	44.28	46.44	1.43	2.43	200*	15	150	2.9E-6
121210A	202.54	17.77	8.25°	2.15*	2012-12-10 01:56:01.53	-1.54	11.26	12.8	1.05†	2.25†	205†	8	1000	2.024E-6
121211B	72.37	8.63	5.23°	2.15*	2012-12-11 16:41:02.77	-0.51	8.45	8.96	1.05†	2.25†	205†	8	1000	1.340E-6
121212A	177.79	78.04	1.08″	2.15*	2012-12-12 06:56:12.00	0	10	10.0	2.65	3.65	200*	15	150	1.2E-7
121216A	13.88	-85.44	14.15°	2.15*	2012-12-16 10:03:16.45	-2.05	7.17	9.22	1.05†	2.25†	205†	8	1000	3.850E-7
121217A	153.71	-62.35	1.08″	0.8	2012-12-17 07:17:47.00	-17.7	783.8	801.5	1.2	3.2	264	10	1000	1.11E-5
121217B	153.71	-62.35	1.80″	2.15*	2012-12-17 07:30:01.58	-807.42	21.25	828.67	1.05†	2.25†	205†	8	1000	6.767E-6
121220A	31.07	48.28	8.30°	2.15*	2012-12-20 07:28:13.24	-1.28	3.84	5.12	1.05†	2.25†	205†	8	1000	4.532E-7
121221A	214.26	33.55	4.22°	2.15*	2012-12-21 21:59:29.97	-3.07	35.84	38.91	1.05†	2.25†	205†	8	1000	5.039E-6

Table A.3: IC86II GRB Parameters (continued)

Name	RA (°)	Dec (°)	σ	z	Trigger (UT)	T_1 (s)	T_2 (s)	T_{100} (s)	α_γ	β_γ	ϵ_γ	E_{min}	E_{max}	Fluence$_\gamma$
121223A	50.11	21.37	2.74°	2.15*	2012-12-23 07:11:19.81	0	11.01	11.01	1.05†	2.25†	205†	8	1000	7.017E-6
121225A	264.86	-66.07	0.17°	2.15*	2012-12-25 09:50:24.00	0	33	33.0	1*	2*	200*	10*	10000*	1.00E-5*
121225B	308.91	-34.35	1.25°	2.15*	2012-12-25 10:01:03.17	-16	70	86.0	1.08	2.14	277.6	10	1000	7.16E-5
121226A	168.62	-30.41	0.02°	0.5*	2012-12-26 19:09:43.00	-0.36	0.8	1.16	1.51	2.51	1000*	15	150	1.4E-7
121229A	190.10	-50.59	1.08′′	2.707	2012-12-29 05:00:21.00	0	64	64.0	2.43	3.43	200*	15	150	4.6E-7
121229B	315.59	-11.94	4.58°	2.15*	2012-12-29 12:47:33.36	0	23.04	23.04	1.05†	2.25†	205†	8	1000	3.508E-6
121231A	335.47	-17.78	6.46°	2.15*	2012-12-31 10:41:23.25	-5.63	27.14	32.77	1.05†	2.25†	205†	8	1000	2.937E-6
130102A	311.42	49.82	1.08′′	2.15*	2013-01-02 18:10:53.00	12.51	100.43	87.92	1.39	2.39	200*	15	150	7.2E-7
130102B	309.58	-72.38	0.17°	2.15*	2013-01-02 04:41:42.00	0	30	30.0	2.85	3.85	200*	10*	10000*	3.46E-6
130104A	174.09	25.92	2.44°	2.15*	2013-01-04 17:18:07.05	-1.79	24.58	26.37	1.05†	2.25†	205†	8	1000	5.668E-6
130106A	66.67	29.74	4.99°	2.15*	2013-01-06 19:53:22.07	-2.56	8.7	11.26	1.05†	2.25†	205†	8	1000	1.586E-6
130106B	28.76	63.38	1.87°	2.15*	2013-01-06 23:52:25.79	-1.02	69.38	70.4	1.05†	2.25†	205†	8	1000	1.543E-5
130109A	17.45	19.24	3.72°	2.15*	2013-01-09 04:56:26.26	-3.58	5.38	8.96	1.05†	2.25†	205†	8	1000	2.535E-6
130112A	236.03	52.19	4.93°	2.15*	2013-01-12 06:52:07.52	-29.7	5.63	35.33	1.05†	2.25†	205†	8	1000	2.614E-6
130114A	310.19	-15.32	10.86°	2.15*	2013-01-14 00:27:04.55	-2.05	6.66	8.71	1.05†	2.25†	205†	8	1000	1.113E-6
130115A	171.09	22.62	2.78°	2.15*	2013-01-15 17:10:39.18	-3.84	9.73	13.57	1.05†	2.25†	205†	8	1000	2.718E-6
130116A	38.24	15.75	29.85°	2.15*	2013-01-16 09:58:14.22	-4.1	62.72	66.82	1.05†	2.25†	205†	8	1000	9.271E-7
130117A	341.24	2.81	6.17°	2.15*	2013-01-17 02:05:11.42	1.79	80.64	78.85	1.05†	2.25†	205†	8	1000	2.849E-6
130118A	278.30	40.98	6.70°	2.15*	2013-01-18 11:33:29.36	-5.63	15.94	21.57	1.05†	2.25†	205†	8	1000	8.278E-7
130121A	211.31	-49.49	1.14°	2.15*	2013-01-21 20:01:59.97	1.79	180.48	178.69	1.05†	2.25†	205†	8	1000	4.345E-5
130122A	194.28	59.02	1.08′′	2.15*	2013-01-22 23:44:09.00	-12.6	67.4	80.0	1.34	2.34	200*	15	150	7.4E-7
130127A	251.05	-17.07	8.46°	0.5*	2013-01-27 17:50:23.93	-0.26	0.19	0.45	0.03	2.4	700	10	1000	4.9E-7
130127B	301.21	-57.21	10.01°	2.15*	2013-01-27 07:09:53.16	-3.84	15.62	19.46	1.05†	2.25†	205†	8	1000	1.022E-6
130131A	171.13	48.08	1.08′′	2.15*	2013-01-31 13:56:22.00	-0.95	52.15	53.1	2.12	3.12	200*	15	150	3.1E-7
130131B	173.96	15.04	1.08′′	2.539	2013-01-31 19:10:08.00	-0.28	4.37	4.65	1.15	2.15	200*	15	150	3.4E-7
130131C	189.63	-14.48	1.00°	2.15*	2013-01-31 12:15:13.39	3.58	151.04	147.46	1.05†	2.25†	205†	8	1000	3.920E-5
130204A	105.64	41.92	7.07°	0.5*	2013-02-04 11:36:51.70	-0.13	0.06	0.19	1.05†	2.25†	205†	8	1000	2.809E-7
130206A	140.39	-58.19	0.02°	2.15*	2013-02-06 19:36:30.45	-2.56	89.03	91.59	1.1	3.1	132.6	10	1000	3.3E-6
130208A	181.60	50.93	4.67°	2.15*	2013-02-08 16:24:23.84	-1.02	40.45	41.47	1.05†	2.25†	205†	8	1000	2.255E-6
130209A	33.59	-27.58	1.00°	2.15*	2013-02-09 23:03:41.79	0.13	10.05	9.92	1.05†	2.25†	205†	8	1000	5.900E-6
130211A	147.52	-42.33	0.02°	2.15*	2013-02-11 03:36:32.00	-1.56	32	33.56	1.81	2.81	200*	15	150	6.4E-7
130213A	99.09	-8.10	10.62°	2.15*	2013-02-13 21:43:55.96	-5.63	9.73	15.36	1.05†	2.25†	205†	8	1000	9.874E-7
130214A	325.02	-1.83	12.77°	2.15*	2013-02-14 03:17:05.66	-3.33	93.44	96.77	1.05†	2.25†	205†	8	1000	1.585E-6
130214B	56.93	-0.29	1.60°	2.15*	2013-02-14 19:12:21.00	-3.58	10.18	13.76	1.05†	2.25†	205†	8	1000	5.983E-6
130215A	43.49	13.39	0.02°	0.597	2013-02-15 01:31:25.44	-7	139.11	146.11	1	1.6	155	10	1000	2.02E-5
130215B	3.11	59.38	2.10°	2.15*	2013-02-15 15:34:16.19	6.91	65.02	58.11	1.05†	2.25†	205†	8	1000	2.149E-5
130216A	67.90	14.67	0.01°	2.15*	2013-02-16 22:15:24.00	-6.16	4.31	10.47	0.7	2.6	152	10	1000	6.231E-6
130216B	58.87	2.04	0.02°	2.15*	2013-02-16 18:58:11.69	-6.27	9.02	15.29	1.6	2.2	91	10	1000	4.8E-6
130217A	96.72	6.80	8.19°	2.15*	2013-02-17 16:31:19.12	-11.26	3.58	14.84	1.05†	2.25†	205†	8	1000	1.100E-6
130218A	69.31	-69.13	2.28°	2.15*	2013-02-18 06:16:25.56	-6.14	30.98	37.12	1.05†	2.25†	205†	8	1000	9.433E-6
130219A	303.73	40.83	1.21°	2.15*	2013-02-19 18:35:51.73	-2	116	118.0	1.08	2.28	200*	10	1000	3.18E-5
130219B	169.29	-22.25	2.20°	2.15*	2013-02-19 04:44:07.57	5.38	173.38	168.0	1.05†	2.25†	205†	8	1000	3.186E-5
130219C	211.60	12.22	16.68°	0.5*	2013-02-19 15:01:13.95	-1.09	0.45	1.54	1.05†	2.25†	205†	8	1000	2.027E-7
130220A	306.20	31.74	1.14°	2.15*	2013-02-20 23:08:48.20	0.26	6.66	6.4	1.05†	2.25†	205†	8	1000	7.235E-6

Table A.3: IC86II GRB Parameters (continued)

Name	RA (°)	Dec (°)	σ	z	Trigger (UT)	T_1 (s)	T_2 (s)	T_{100} (s)	α_γ	β_γ	ϵ_γ	E_{min}	E_{max}	Fluence$_\gamma$
130224A	205.90	59.72	2.62°	2.15*	2013-02-24 08:53:02.38	-35.84	35.07	70.91	1.05†	2.25†	205†	8	1000	4.962E-6
130228A	265.83	55.93	0.50°	2.15*	2013-02-28 02:40:02.17	-9.86	101.89	111.75	1.05†	2.25†	205†	8	1000	1.241E-5
130228B	240.75	-55.21	1.28°	2.15*	2013-02-28 05:05:57.05	0	15.42	15.42	1.05†	2.25†	205†	8	1000	1.748E-5
130304A	98.93	53.57	1.20°	2.15*	2013-03-04 09:49:53.10	0.83	68.67	67.84	1.05†	2.25†	205†	8	1000	3.701E-5
130305A	116.77	52.04	0.02°	2.15*	2013-03-05 11:39:11.37	1.28	38.096	36.816	0.67	2.4	640	10	1000	5.7E-5
130305B	73.32	-1.56	1.76°	2.15*	2013-03-05 12:37:47.72	1.28	119.81	118.53	1.05†	2.25†	205†	8	1000	1.520E-6
130306A	279.48	-11.68	0.02°	2.15*	2013-03-06 23:47:25.57	-17.66	370.1	387.76	1.5	3.5	212	20	10000	2.9E-4
130307A	156.00	23.00	0.36°	0.5*	2013-03-07 03:01:44.47	-0.06	0.32	0.38	0.78	2.78	1670	10	1000	1.43E-6
130307B	319.52	10.77	4.42°	2.15*	2013-03-07 05:42:19.33	-12.29	51.2	63.49	1.05†	2.25†	205†	8	1000	3.972E-6
130310A	141.91	-17.43	0.22°	2.15*	2013-03-10 20:09:41.50	4.1	20.1	16.0	1.01	2.27	2100	10	1000	1.4E-5
130313A	236.44	-0.35	0.03°	0.5*	2013-03-13 16:08:11.00	-0.02	0.23	0.25	1.37	2.37	1000*	15	150	3.1E-8
130314A	206.21	46.77	1.41°	2.15*	2013-03-14 03:31:16.30	1.54	144.39	142.85	1.05†	2.25†	205†	8	1000	1.460E-5
130315A	157.54	-51.79	0.01°	2.15*	2013-03-15 12:45:32.00	-3.3	268	271.3	1.81	2.81	200*	15	150	4.9E-6
130318A	200.74	8.12	9.94°	2.15*	2013-03-18 10:56:31.18	-2.82	135.17	137.99	1.05†	2.25†	205†	8	1000	3.407E-6
130320A	192.68	-14.47	1.51°	2.15*	2013-03-20 07:08:44.82	0	22.784	22.784	0.78	2.78	295	20	10000	2.6E-5
130320B	195.54	-71.26	0.49°	2.15*	2013-03-20 13:24:11.73	0	384.768	384.768	1	2	340	20	10000	7.8E-5
130324A	255.43	0.05	6.03°	2.15*	2013-03-24 01:00:24.75	-6.27	31.49	37.76	1.05†	2.25†	205†	8	1000	1.904E-6
130325A	122.78	-18.90	0.25°	2.15*	2013-03-25 04:51:54.30	0.58	10.448	9.868	0.73	2.18	202.20	10	1000	8.25E-6
130325B	30.44	62.06	16.14°	0.5*	2013-03-25 00:07:46.82	-0.06	0.58	0.64	1.05†	2.25†	205†	8	1000	5.656E-8
130327A	92.04	55.72	1.08′′	2.15*	2013-03-27 01:47:34.00	-4.38	5.62	10.0	2.26	3.26	200*	15	150	2.3E-7
130327B	218.09	-69.51	0.17°	2.15*	2013-03-27 08:24:04.75	-1	43.704	44.704	0.56	3.4	334	10	1000	5.176E-5
130331A	164.47	29.64	2.43°	2.15*	2013-03-31 13:35:44.87	-0.51	13.31	13.82	1.05†	2.25†	205†	8	1000	9.331E-6
130403A	199.90	-46.68	8.26°	2.15*	2013-04-03 20:46:47.41	-7.94	14.85	22.79	1.05†	2.25†	205†	8	1000	1.094E-6
130404A	30.75	1.54	7.24°	2.15*	2013-04-04 10:15:40.05	-1.54	1.79	3.33	1.05†	2.25†	205†	8	1000	8.425E-7
130404B	146.58	-42.16	1.08°	2.15*	2013-04-04 20:10:04.03	0.32	34.88	34.56	1.05†	2.25†	205†	8	1000	8.355E-6
130404C	28.29	56.49	18.23°	0.5*	2013-04-04 21:02:11.03	-0.13	0.83	0.96	1.05†	2.25†	205†	8	1000	2.202E-7
130406A	157.78	-62.05	2.09°	2.15*	2013-04-06 06:55:03.46	-0.51	7.42	7.93	1.05†	2.25†	205†	8	1000	2.924E-6
130406B	109.66	-27.86	7.66°	2.15*	2013-04-06 08:00:36.77	-5.12	83.71	88.83	1.05†	2.25†	205†	8	1000	3.211E-6
130406C	138.21	42.83	14.84°	2.15*	2013-04-06 08:29:36.58	-1.28	1.28	2.56	1.05†	2.25†	205†	8	1000	2.976E-7
130407A	248.10	10.51	0.06°	2.15*	2013-04-07 23:37:01.00	0	25	25.0	1*	2*	200*	10*	10000*	1.00E-5*
130407B	53.53	44.17	9.29°	2.15*	2013-04-07 19:12:43.06	-5.63	26.37	32.0	1.05†	2.25†	205†	8	1000	1.746E-6
130408A	134.41	-32.36	1.08′′	3.758	2013-04-08 21:51:38.00	-2	33.5	35.5	0.7	2.3	272	20	10000	1.2E-5
130408B	118.77	66.34	3.93°	2.15*	2013-04-08 15:40:22.85	-4.86	4.35	9.21	1.05†	2.25†	205†	8	1000	2.052E-6
130409A	30.52	44.10	2.22°	2.15*	2013-04-09 23:01:59.66	0.26	26.37	26.11	1.05†	2.25†	205†	8	1000	7.871E-6
130416A	99.28	24.70	14.34°	2.15*	2013-04-16 16:34:07.06	-2.82	0.26	3.08	1.05†	2.25†	205†	8	1000	2.807E-7
130416B	51.21	-18.25	4.86°	0.5*	2013-04-16 18:28:53.30	-0.05	0.14	0.19	1.05†	2.25†	205†	8	1000	9.385E-7
130419A	355.28	9.90	0.03°	2.15*	2013-04-19 13:30:29.00	40.09	169.51	129.42	1.43	2.43	200*	15	150	7.8E-7
130420A	196.11	59.42	1.08′′	1.297	2013-04-20 07:28:29.00	-19.7	189.9	209.6	1	3.0	56	10	1000	1.4E-5
130420B	183.13	54.39	1.08′′	2.15*	2013-04-20 12:56:32.99	-7.17	15	22.17	0.24	2.24	91	10	1000	1.04E-7
130420D	117.06	-69.03	4.01°	2.15*	2013-04-20 10:08:09.20	-2.43	24.9	27.33	1.05†	2.25†	205†	8	1000	3.771E-6
130425A	6.21	-70.18	2.50°	2.15*	2013-04-25 07:51:16.23	-1.86	77.216	79.076	1.29	2.46	167	20	10000	5.9E-5
130427A	173.14	27.70	2.16′′	0.34	2013-04-27 07:47:57.00	-51.05	223.5	274.55	0.789	3.06	830	10	1000	1.975E-3
130427B	314.90	-22.55	1.08′′	2.78	2013-04-27 13:20:41.00	-1.29	32.71	34.0	1.64	2.64	200*	15	150	1.5E-6
130502B	66.65	71.08	0.09°	2.15*	2013-05-02 07:51:12.76	0	37	37.0	0.75	2.47	323.00	10	1000	1.21E-4

Bibliography

[1] G.T. Zatsepin and V.A. Kuzim. Upper limit of the spectrum of cosmic rays. *JETP Lett.*, 4:78–80, 1966.

[2] RU Abbasi, T Abu-Zayyad, M Allen, JF Amman, G Archbold, K Belov, JW Belz, SY Ben Zvi, DR Bergman, SA Blake, et al. First observation of the Greisen-Zatsepin-Kuzmin suppression. *Physical Review Letters*, 100(10):101101, 2008.

[3] J Abraham, P Abreu, M Aglietta, EJ Ahn, D Allard, J Allen, J Alvarez-Muniz, M Ambrosio, L Anchordoqui, S Andringa, et al. Measurement of the energy spectrum of cosmic rays above 10 18 ev using the pierre auger observatory. *Physics Letters B*, 685(4):239–246, 2010.

[4] Markus Ackermann, M Ajello, A Allafort, L Baldini, J Ballet, G Barbiellini, MG Baring, D Bastieri, K Bechtol, R Bellazzini, et al. Detection of the characteristic pion-decay signature in supernova remnants. *Science*, 339(6121):807–811, 2013.

[5] W.I. Axford. The origins of high-energy cosmic rays. *ApJS*, 90:937, 1994.

[6] Kenneth Greisen. End to the cosmic-ray spectrum? *Physical Review Letters*, 16(17):748, 1966.

[7] F. Reines and C.L. Cowan. A proposed experiment to detect the free neutrino. *Physical Review*, 90:492, 1953.

[8] F. Reines and C.L. Cowan. The neutrino. *Nature*, 178:446, 1956.

[9] C.L. Cowan. Detection of the free neutrino: a confirmation. *Science*, 124:103, 1956.

[10] B. Pontecorvo. *J.E.T.P.*, 33:429, 1957.

[11] D.H. Perkins. *Introduction to High Energy Physics, 4th Ed.* Cambridge University Press, 2000.

[12] et al. Fukuda, Y. Measurements of the solar neutrino flux from superkamiokande's first 300 days. *Physical Review Letters*, 81:1158, 1998.

[13] Abraham Achterberg, M Ackermann, J Adams, J Ahrens, K Andeen, J Auffenberg, JN Bahcall, X Bai, B Baret, SW Barwick, et al. Search for neutrino-induced cascades from gamma-ray bursts with AMANDA. *The Astrophysical Journal*, 664(1):397, 2007.

[14] Abbasi, R. et al. Search for muon neutrinos from gamma-ray bursts with the IceCube neutrino telescope. *Astrophys. J.*, 710:346–359, 2010.

[15] et al. Abbasi. Limits on neutrino emission from gamma-ray bursts with the 40 string icecube detector. *Phys. Rev. Lett.*, 106:141101, 2011.

[16] Abbasi, R. et al. An absence of neutrinos associated with cosmic-ray acceleration in gamma-ray bursts. *Nature*, 484:351, 2012.

[17] MG Aartsen, M Ackermann, J Adams, JA Aguilar, M Ahlers, M Ahrens, D Altmann, T Anderson, C Arguelles, TC Arlen, et al. Search for prompt neutrino emission from gamma-ray bursts with IceCube. *The Astrophysical Journal Letters*, 805(1):L5, 2015.

[18] Eleonora Presani. Search for neutrinos from gamma-ray bursts with ANTARES. *arXiv preprint arXiv:1104.4033*, 2011.

[19] C Bigongiari, U Emanuele, Juan Pablo Gómez González, Juan José Hernández Rey, Guillaume Lambard, Salvatore Mangano, J Ruiz Rivas, Francisco Salesa Greus, Agustín Sánchez Losa, Harold Yepes Ramírez, et al. First search for neutrinos in correlation with gamma-ray bursts with the ANTARES neutrino telescope. *Journal Of Cosmology And Astroparticle Physics, 2013, vol. 03, p. 006*, 2013.

[20] Silvia Adrián-Martínez, Andreas Albert, Imen Al Samarai, Michel André, M Anghinolfi, G Anton, S Anvar, M Ardid, T Astraatmadja, J-J Aubert, et al. Search for muon neutrinos from gamma-ray bursts with the ANTARES neutrino telescope using 2008 to 2011 data. *Astronomy & Astrophysics*, 559:A9, 2013.

[21] Meszaros. Gamma-ray bursts. *Rep. Prog. Phys.*, 69:2259–2321, 2006.

[22] Klebesadel R, Strong I and Olsen R. *Astrophys. J.*, 541:L51, 1973.

[23] Noami Greenberg-Slovin (Translator) Govert Schilling (Author). *Flash!: The Hunt for the Biggest Explosions in the Universe*. Cambridge University Press, 2002.

[24] Ruderman M. *Ann. N.Y. Acad. Sci.*, 262:164, 1975.

[25] Fishman G. and Meegan C. *Annu. Rev. Astron. Astrophys.*, 33:415, 1995.

[26] K. Hurley. Receding from our grasp. *Nature*, 357:112–113, 1992.

[27] NASA Burst and Transient Source Explorer - BATSE, 2004. http://www.batse.msfc.nasa.gov/batse/.

[28] Costa E. et al. *Nature*, 387:783, 1997.

[29] van Paradijs J. et al. *Nature*, 386:686, 1997.

[30] MacFadyen A. and Woosley S. *Astrophys. J.*, 524:262, 1999.

[31] Eichler D., Livio M., Prian T. and Schramm D. *Nature*, 340:126, 1989.

[32] L. Anchordoqui et al. Ultrahigh energy cosmic rays: The state of the art before the auger observatory. *Int. J. Mod. Phys. A*, 18:2229, 2003.

[33] William S Paciesas, Charles A Meegan, Andreas von Kienlin, PN Bhat, Elisabetta Bissaldi, Michael S Briggs, J Michael Burgess, Vandiver Chaplin, Valerie Connaughton, Roland Diehl, et al. The fermi gbm gamma-ray burst catalog: the first two years. *The Astrophysical Journal Supplement Series*, 199(1):18, 2012.

[34] Adam Goldstein, J Michael Burgess, Robert D Preece, Michael S Briggs, Sylvain Guiriec, Alexander J van der Horst, Valerie Connaughton, Colleen A Wilson-Hodge, William S Paciesas, Charles A Meegan, et al. The fermi gbm gamma-ray burst spectral catalog: the first two years. *The Astrophysical Journal Supplement Series*, 199(1):19, 2012.

[35] Andreas von Kienlin, Charles A. Meegan, William S. Paciesas, P.N. Bhat, Elisabetta Bissaldi, et al. The Second Fermi GBM Gamma-Ray Burst Catalog: The First Four Years. *ApJS*, 211:13, 2014.

[36] David Gruber, Adam Goldstein, Victoria Weller von Ahlefeld, P. Narayana Bhat, Elisabetta Bissaldi, et al. The Fermi GBM Gamma-Ray Burst Spectral Catalog: Four Years Of Data. *ApJS*, 211:12, 2014.

[37] M Ackermann, M Ajello, K Asano, Magnus Axelsson, L Baldini, J Ballet, G Barbiellini, D Bastieri, K Bechtol, R Bellazzini, et al. The first fermi-lat gamma-ray burst catalog. *The Astrophysical Journal Supplement Series*, 209(1):11, 2013.

[38] Neil Gehrels, G Chincarini, P Giommi, KO Mason, JA Nousek, AA Wells, NE White, SD Barthelmy, DN Burrows, LR Cominsky, et al. The swift gamma-ray burst mission. *The Astrophysical Journal*, 611(2):1005, 2004.

[39] Scott D Barthelmy, Louis M Barbier, Jay R Cummings, Ed E Fenimore, Neil Gehrels, Derek Hullinger, Hans A Krimm, Craig B Markwardt, David M Palmer, Ann Parsons, et al. The burst alert telescope (bat) on the swift midex mission. *Space Science Reviews*, 120(3-4):143–164, 2005.

[40] David N Burrows, JE Hill, JA Nousek, JA Kennea, A Wells, JP Osborne, AF Abbey, A Beardmore, K Mukerjee, ADT Short, et al. The swift x-ray telescope. *Space Science Reviews*, 120(3-4):165–195, 2005.

[41] David N Burrows, JE Hill, JA Nousek, JA Kennea, A Wells, JP Osborne, AF Abbey, A Beardmore, K Mukerjee, ADT Short, et al. The swift x-ray telescope. *Space Science Reviews*, 120(3-4):165–195, 2005.

[42] RL Aptekar, DD Frederiks, SV Golenetskii, VN Ilynskii, EP Mazets, VN Panov, ZJ Sokolova, MM Terekhov, LO Sheshin, TL Cline, et al. Konus-w gamma-ray burst experiment for the ggs wind spacecraft. *Space Science Reviews*, 71(1-4):265–272, 1995.

[43] Christoph Winkler, TJ-L Courvoisier, G Di Cocco, N Gehrels, A Giménez, S Grebenev, W Hermsen, JM Mas-Hesse, F Lebrun, Niels Lund, et al. The integral mission. *Astronomy & Astrophysics*, 411(1):L1–L6, 2003.

[44] Masaru Matsuoka, Kazuyoshi Kawasaki, Shiro Ueno, Hiroshi Tomida, Mitsuhiro Kohama, Motoko Suzuki, Yasuki Adachi, Masaki Ishikawa, Tatehiro Mihara, Mutsumi Sugizaki, et al. The maxi mission on the iss: Science and instruments for monitoring all-sky x-ray images. *Publications of the Astronomical Society of Japan*, 61(5):999–1010, 2009.

[45] Kazutaka Yamaoka, Akira Endo, Teruaki Enoto, Yasushi Fukazawa, Ryuji Hara, Yoshitaka Hanabata, Soojing Hong, Tsuneyoshi Kamae, Chie Kira, Natsuki Kodaka, et al. Design and in-orbit performance of the suzaku wide-band all-sky monitor. *Publications of the Astronomical Society of Japan*, 61(sp1):S35–S53, 2009.

[46] M Feroci, E Costa, P Soffitta, E Del Monte, G Di Persio, I Donnarumma, Y Evangelista, M Frutti, I Lapshov, F Lazzarotto, et al. Superagile: The hard x-ray imager for the agile space mission. *Nuclear Instruments and Methods in Physics Research Section A: Accelerators, Spectrometers, Detectors and Associated Equipment*, 581(3):728–754, 2007.

[47] K Hurley, S Golenetskii, R Aptekar, E Mazets, V Palshin, D Frederiks, IG Mitrofanov, D Golovin, A Kozyrev, M Litvak, et al. The third interplanetary network. In *Gamma Ray Bursts 2010*, volume 1358, pages 385–388. AIP Publishing, 2011.

[48] GCN: Gamma-ray Coordinates Network, gcn.gsfc.nasa.gov.

[49] J. A. Aguilar. 32nd ICRC Conf. Proc., 2011.

[50] GRBweb, grbweb.icecube.wisc.edu.

[51] T. Piran. The physics of gamma-ray bursts. *Rev. Mod. Phys.*, 72:1143, 2004.

[52] D.B. Fox and P. Meszaros. Grb fireball physics: Prompt and early emission. *New J. Phys.*, 8:199, 2006.

[53] Boaz Katz, Ran Budnik, and Eli Waxman. The energy production rate & the generation spectrum of uhecrs. *Journal of Cosmology and Astroparticle Physics*, 2009(03):020, 2009.

[54] Eli Waxman and John Bahcall. High energy neutrinos from cosmological gamma-ray burst fireballs. *Phys. Rev. Lett.*, 78:2292–2295, 1997.

[55] Eli Waxman. Astrophysical sources of high energy neutrinos. *Nuclear Physics B*, 118:353–362, 2003.

[56] F. Halzen M. Ahlers, M.C. Gonzalez-Garcia. Grbs on probation: testing the uhe cr paradigm. *Astropart. Phys.*, 35:429–455, 2011.

[57] Svenja Hümmer, Philipp Baerwald, and Walter Winter. Neutrino emission from gamma-ray burst fireballs, revised. *Phys. Rev. Lett.*, 108:231101, Jun 2012.

[58] Bing Zhang and Pawan Kumar. Model-dependent high-energy neutrino flux from gamma-ray bursts. *Phys. Rev. Lett.*, 110:121101, Mar 2013.

[59] M.J. Rees and P. Meszaros. Dissipative photosphere models of gamma-ray bursts and x-ray flashes. *Astrophys. J.*, 628:847, 2005.

[60] K. Murase. Prompt high-energy neutrinos from gamma-ray bursts in photospheric and synchrotron self-compton scenarios. *Phys. Rev. D*, 78:101302, 2008.

[61] B. Zhang and H. Yan. The internal-collision-induced magnetic reconnection and turbulence (icmart) model of gamma-ray bursts. *Astrophys. J.*, 726:90, 2011.

[62] Mauricio Bustamante, Philipp Baerwald, Kohta Murase, and Walter Winter. Neutrino and cosmic-ray emission from multiple internal shocks in gamma-ray bursts. *Nature communications*, 6, 2015.

[63] MJ Rees and P Mészáros. Relativistic fireballs: energy conversion and time-scales. *Monthly Notices of the Royal Astronomical Society*, 258(1):41P–43P, 1992.

[64] Martin J Rees and P Mészáros. Unsteady outflow models for cosmological gamma-ray bursts. *arXiv preprint astro-ph/9404038*, 1994.

[65] D Band, J Matteson, L Ford, B Schaefer, D Palmer, B Teegarden, T Cline, M Briggs, W Paciesas, G Pendleton, et al. Batse observations of gamma-ray burst spectra. i-spectral diversity. *The Astrophysical Journal*, 413:281–292, 1993.

[66] Ignacio Taboada and Michelangelo V. D'Agostino. Correlating prompt grb photons with neutrinos. 2008. arXiv:astro-ph/0711.2277v1.

[67] P. Meszaros and M. Rees. *Astrophys. J.*, 405:278, 1993.

[68] B. Paczynski and G.H. Xu. *Astrophys. J.*, 427:708, 1994.

[69] Thomas K. Gaisser. *Cosmic Rays and Particle Physics*. Cambridge University Press, Cambridge, UK, 1990.

[70] Enrico Fermi. On the origin of the cosmic radiation. *Phys. Rev.*, 75:1169–1174, 1949.

[71] D. Guetta, D. Hooper, J. Alvarez-Muniz, F. Halzen and E. Reuveni. *Astrophart. Phys.*, 20:429, 2004.

[72] F. Halzen and D. Saltzberg. *Phys. Rev. Lett.*, 81:4305, 1998.

[73] Abbasi, R. et al. Limits on the neutrino emission from gamma-ray bursts with the 40 string IceCube detector. *Phys. Rev. Lett.*, 106:141101, 2011.

[74] M. Lyutikov and R. Blandford. 2003. arXiv:astro-ph/0312347.

[75] D. Lazzati and M.C. Begelman. *Astrophys. J.*, 725:1137, 2010.

[76] Markus Ahlers. Fireballet - a fireball emission tool. 2012. IceCube Collaboration Internal Report.

[77] A. Mucke et al. *Comput. Phys. Commun.*, 124:290, 2000. [arXiv:astro-ph/9903478].

[78] Philipp Baerwald, Mauricio Bustamante, and Walter Winter. Are gamma-ray bursts the sources of ultra-high energy cosmic rays? *APh*, 62:66–91, 2014.

[79] E. Waxman. *Astrophys. J.*, 452:L1, 1995.

[80] J. P. Rachen and P. Mészáros. In C. A. Meegan et al., editors, *Gamma-Ray Bursts, 4th Hunstville Symp.*, volume 428 of *AIP Conf. Proc.*, pages 776–780, 1998.

[81] R.U. Abbasi et al. [HiRes Collaboration]. *Phys. Rev. Lett.*, 100:101101, 2008.

[82] R.U. Abbasi et al. [HiRes Collaboration]. *Phys. Rev. Lett.*, 104:161101, 2010.

[83] A. Ishihara, Proceedings of TEXAS 2010, Heidelberg, Germany.

[84] A. Achterberg, M. Ackermann, J. Adams, J. Ahrens, K. Andeen, D. W. Atlee, J. Baccus, J. N. Bahcall, X. Bai, and et al. First year performance of the IceCube neutrino telescope. *APh*, 26:155–173, October 2006.

[85] Abbasi, et al. Calibration and characterization of the IceCube photomultiplier tub. *Nuclear Instruments and Methods in Physics Research A*, 618:139–152, 2010.

[86] R Abbasi, Yasser Abdou, T Abu-Zayyad, M Ackermann, J Adams, JA Aguilar, M Ahlers, MM Allen, D Altmann, K Andeen, et al. The design and performance of IceCube deepcore. *Astroparticle physics*, 35(10):615–624, 2012.

[87] Abbasi, et al. The IceCube data acquisition system: System capture, digitization, and timestamping. *Nuclear Instruments and Methods in Physics Research A*, 601:294–316, 2009.

[88] S. Kleinfelder. Gigahertz waveform sampling and digitization circuit design and implementation. *Nuclear Science, IEEE Transactions on*, 50(4):955 – 962, aug. 2003.

[89] See <tf.nist.gov/timefreq/time/oneway.htm> and <www.nist.gov/pml/div688/grp40/gpsarchive.cfm>.

[90] Charles L Lawson and Richard J Hanson. *Solving least squares problems*, volume 161. SIAM, 1974.

[91] Whitehorn, N., Doctoral Dissertation.

[92] Sheldon L Glashow. Resonant scattering of antineutrinos. *Physical Review*, 118(1):316, 1960.

[93] MG Aartsen, R Abbasi, Yasser Abdou, M Ackermann, J Adams, JA Aguilar, M Ahlers, D Altmann, J Auffenberg, X Bai, et al. First observation of pev-energy neutrinos with IceCube. *Physical review letters*, 111(2):021103, 2013.

[94] Vernon Barger, John Learned, and Sandip Pakvasa. IceCube pev cascade events initiated by electron-antineutrinos at glashow resonance. *Physical Review D*, 87(3):037302, 2013.

[95] B. Voigt. Sensitivity of the IceCube detector for ultra high energetic electron neutrino events. *PhD thesis*, 2008.

[96] Dmitry Chirkin and Wolfgang Rhode. Propagating leptons through matter with muon monte carlo (mmc). *arXiv preprint hep-ph/0407075*, 2004.

[97] A. Gazizov and M. Kowalski. Anis: High energy neutrino generator for neutrino telescopes. *Computer Physics Communications*, 172(3):203 – 213, 2005.

[98] HL Lai, J Huston, S Kuhlmann, J Morfin, F Olness, JF Owens, J Pumplin, and WK Tung. Global qcd analysis of parton structure of the nucleon: Cteq5 parton distributions. *The European Physical Journal C-Particles and Fields*, 12(3):375–392, 2000.

[99] A. M. Dziewonski and D. L. Anderson. Preliminary Reference Earth Model. *Phys. Earth Planet. Inter.*, 25:297–356, June 1981.

[100] M. Honda, T. Kajita, K. Kasahara, S. Midorikawa, and T. Sanuki. Calculation of Atmospheric Neutrino Flux Using the Interaction Model Calibrated with Atmospheric Muon Data. *Phys. Rev. D*, 75:043006–+, February 2007.

[101] D. Heck, J. Knapp, J. N. Capdevielle, G. Schatz, and T. Thouw. CORSIKA: A Monte Carlo Code to Simulate Extensive Air Showers. Technical Report FZKA 6019, Forschungszentrum Karlsruhe, Germany, February 1998.

[102] J. Lundberg, P. Miočinović, K. Woschnagg, T. Burgess, J. Adams, S. Hundertmark, P. Desiati, and P. Niessen. Light Tracking Through Ice and Water: Scattering and Absorption in Heterogeneous Media with PHOTONICS. *Nucl. Instrum. Meth. A*, 581:619–631, November 2007.

[103] Markus Ackermann, J Ahrens, X Bai, M Bartelt, SW Barwick, RC Bay, T Becka, JK Becker, K-H Becker, P Berghaus, et al. Optical properties of deep glacial ice at the south pole. *Journal of Geophysical Research: Atmospheres (1984–2012)*, 111(D13), 2006.

[104] J Ahrens, X Bai, R Bay, SW Barwick, T Becka, JK Becker, K-H Becker, E Bernardini, D Bertrand, A Biron, et al. Muon track reconstruction and data selection techniques in AMANDA. *Nuclear Instruments and Methods in Physics Research Section A: Accelerators, Spectrometers, Detectors and Associated Equipment*, 524(1):169–194, 2004.

[105] MG Aartsen, R Abbasi, Yasser Abdou, M Ackermann, J Adams, JA Aguilar, M Ahlers, D Altmann, J Auffenberg, X Bai, et al. Improvement in fast particle track reconstruction with robust statistics. *Nuclear Instruments and Methods in Physics Research Section A: Accelerators, Spectrometers, Detectors and Associated Equipment*, 736:143–149, 2014.

[106] Stephen Boyd and Lieven Vandenberghe. *Convex optimization*. Cambridge university press, 2004.

[107] Kowalski, M., Doctoral Dissertation.

[108] Michael JD Powell. An efficient method for finding the minimum of a function of several variables without calculating derivatives. *The computer journal*, 7(2):155–162, 1964.

[109] MG Aartsen, R Abbasi, M Ackermann, J Adams, JA Aguilar, M Ahlers, D Altmann, C Arguelles, J Auffenberg, X Bai, et al. Energy reconstruction methods in the IceCube neutrino telescope. *Journal of Instrumentation*, 9(03):P03009, 2014.

[110] TA Gabriel, Donald E Groom, PK Job, NV Mokhov, and GR Stevenson. Energy dependence of hadronic activity. *Nuclear Instruments and Methods in Physics Research Section A: Accelerators, Spectrometers, Detectors and Associated Equipment*, 338(2):336–347, 1994.

[111] Sea Agostinelli, John Allison, K al Amako, J Apostolakis, H Araujo, P Arce, M Asai, D Axen, S Banerjee, G Barrand, et al. Geant4a simulation toolkit. *Nuclear instruments and methods in physics research section A: Accelerators, Spectrometers, Detectors and Associated Equipment*, 506(3):250–303, 2003.

[112] R Abbasi, Yasser Abdou, T Abu-Zayyad, J Adams, JA Aguilar, M Ahlers, K Andeen, J Auffenberg, X Bai, M Baker, et al. First search for atmospheric and extraterrestrial neutrino-induced cascades with the IceCube detector. *Physical Review D*, 84(7):072001, 2011.

[113] Middell, E., Doctoral Dissertation.

[114] Eike Middell. Search for atmospheric neutrino induced particle showers with IceCube 40. In *International Cosmic Ray Conference*, volume 4, page 246, 2011.

[115] Fred James and MINUIT Roos. Minuit-a system for function minimization and analysis of the parameter errors and correlations. *Computer Physics Communications*, 10(6):343–367, 1975.

[116] Leif Rädel and Christopher Wiebusch. Calculation of the cherenkov light yield from electromagnetic cascades in ice with geant4. *Astroparticle Physics*, 44:102–113, 2013.

[117] H. Cramer. *Mathematical Methods of Statistics*. Princeton Univ. Press, 1945.

[118] C.R. Rao. Information and the accuracy attainable in the estimation of statistical parameters. *Bulletin of Cal. Math. Soc.*, 37:81, 1945.

[119] Klaus Wiebe. Resolution estimator for cascades. 2014. IceCube Collaboration Internal Report.

[120] MG Aartsen, R Abbasi, M Ackermann, J Adams, JA Aguilar, M Ahlers, D Altmann, C Arguelles, TC Arlen, J Auffenberg, et al. Search for neutrino-induced particle showers with IceCube-40. *Physical Review D*, 89(10):102001, 2014.

[121] MG Aartsen, M Ackermann, J Adams, JA Aguilar, M Ahlers, M Ahrens, D Altmann, T Anderson, C Arguelles, TC Arlen, et al. Observation of high-energy astrophysical neutrinos in three years of IceCube data. *Physical review letters*, 113(10):101101, 2014.

[122] MG Aartsen, M Ackermann, J Adams, JA Aguilar, M Ahlers, M Ahrens, D Altmann, T Anderson, C Arguelles, TC Arlen, et al. Atmospheric and astrophysical neutrinos above 1 tev interacting in IceCube. *Physical Review D*, 91(2):022001, 2015.

[123] Gareth James, Daniela Witten, Trevor Hastie, and Robert Tibshirani. *An introduction to statistical learning*. Springer, 2013.

[124] Yoav Freund and Robert E Schapire. A decision-theoretic generalization of on-line learning and an application to boosting. *Journal of computer and system sciences*, 55(1):119–139, 1997.

[125] Richman, M., pybdt software package.

[126] Nikolai V Smirnov. On the estimation of the discrepancy between empirical curves of distribution for two independent samples. *Bull. Math. Univ. Moscou*, 2(2), 1939.

[127] William Feller. On the Kolmogorov-Smirnov limit theorems for empirical distributions. *The annals of mathematical statistics*, pages 177–189, 1948.

[128] Aaron Roodman. Blind analysis in particle physics. *arXiv preprint physics/0312102*, 2003.

[129] John T Kent. The Fisher-Bingham distribution on the sphere. *Journal of the Royal Statistical Society. Series B (Methodological)*, pages 71–80, 1982.

[130] Ryan Maunu. Modifications to the prompt grb test statistic. 2015. IceCube Collaboration Internal Report.

[131] MG Aartsen, R Abbasi, Y Abdou, M Ackermann, J Adams, JA Aguilar, M Ahlers, D Altmann, J Auffenberg, X Bai, et al. The IceCube neutrino observatory part vi: Ice properties, reconstruction and future developments. *arXiv preprint arXiv:1309.7010*, 2013.

[132] Jonathan Pumplin, Daniel Robert Stump, Joey Huston, Hung-Liang Lai, Pavel Nadolsky, and Wu-Ki Tung. New generation of parton distributions with uncertainties from global qcd analysis. *Journal of High Energy Physics*, 2002(07):012, 2002.

[133] Serap Tilav, Paolo Desiati, Takao Kuwabara, Dominick Rocco, Florian Rothmaier, Matt Simmons, Henrike Wissing, et al. Atmospheric variations as observed by IceCube. *arXiv preprint arXiv:1001.0776*, 2010.

[134] G. J. Feldman and R. D. Cousins. *PhRvD*, 57:3873–3889, 1998.

[135] M. Ahlers, M.C. Gonzalez-Garcia, and F. Halzen. GRBs on probation: testing the UHE CR paradigm with IceCube. *APh*, 35:87–94, 2011.

[136] A. Goldstein, J.M. Burgess, R.D. Preece, et al. *ApJS*, 199:19, 2012.

[137] JL Racusin, SR Oates, P Schady, DN Burrows, M de Pasquale, D Donato, N Gehrels, S Koch, J McEnery, T Piran, et al. Fermi and swift gamma-ray burst afterglow population studies. *The Astrophysical Journal*, 738(2):138, 2011.

[138] Tanmoy Laskar, Edo Berger, Raffaella Margutti, Daniel Perley, B Ashley Zauderer, Re'em Sari, and Wen-fai Fong. Energy injection in gamma-ray burst afterglows. *arXiv preprint arXiv:1504.03702*, 2015.

[139] IceCube Collaboration et al. Evidence for high-energy extraterrestrial neutrinos at the IceCube detector. *Science*, 342(6161):1242856, 2013.

[140] M. G. Aartsen, K. Abraham, M. Ackermann, J. Adams, J. A. Aguilar, M. Ahlers, M. Ahrens, D. Altmann, T. Anderson, M. Archinger, and et al. The Detection of a Type IIn Supernova in Optical Follow-up Observations of IceCube Neutrino Events. *The Astrophysical Journal*, 811:52, September 2015.

[141] Marka Bartos. Can a single high-energy neutrino from gamma-ray bursts be a discovery? *arXiv:1409.1217*, 2014.

[142] BP Abbott, R Abbott, R Adhikari, P Ajith, Bruce Allen, G Allen, RS Amin, SB Anderson, WG Anderson, MA Arain, et al. Ligo: the laser interferometer gravitational-wave observatory. *Reports on Progress in Physics*, 72(7):076901, 2009.

[143] MG Aartsen, M Ackermann, J Adams, JA Aguilar, M Ahlers, M Ahrens, D Altmann, T Anderson, G Anton, C Arguelles, et al. IceCube-Gen2: A vision for the future of neutrino astronomy in antarctica. *arXiv preprint arXiv:1412.5106*, 2014.

[144] Markus Ahlers and Francis Halzen. Pinpointing extragalactic neutrino sources in light of recent IceCube observations. *Physical Review D*, 90(4):043005, 2014.